UNIVERSITÀ
DEGLI STUDI
DI PADOVA

Sede Amministrativa: Università degli Studi di Padova

Dipartimento di Fisica e Astronomia

SCUOLA DI DOTTORATO DI RICERCA IN ASTRONOMIA

CICLO XXIV

FROM 8(m) TO 8(mm): WAVEFRONT SENSING FROM COSMOLOGICAL TO HUMAN SCALES

Direttore della Scuola: Ch.mo Prof. Giampaolo Piotto
Supervisore: Ch.mo Prof. Roberto Ragazzoni

Dottoranda: Valentina Viotto

Abstract

The largest Field of View Wavefront Sensor ever realized, namely one of the Ground-Layer Wavefront Sensors on-board LINC-NIRVANA, the Fizeau interferometric focal station of the Large Binocular Telescope, has been completed in the Astronomical Observatory of Padova. This Thesis includes a detailed description of such a sensor, starting from the optical concepts behind it, going through the definition of the alignment procedures ensuring the compliance of each sub-system with its optical tolerances, and concluding with the complete set of results of the system verification as a whole. At the same time, a similar wavefront sensor, but with a single line of sight, has been realized as a laboratory demonstrator for a system to perform the quality test of artificial Intra-Ocular Lenses (IOL), used in the transplant of human damaged crystalline lens. Such a demonstrator has been designed, procured, aligned and fully characterized, with the goal to retrieve high resolution aberrations of the IOL with a compact, easy to procure and user-friendly system.

Riassunto

Questa Tesi descrive il sensore di turbolenza di terra (Ground-layer Wavefront Sensor, GWS) di LINC-NIRVANA, l'interferometro di Fizeau che si sta realizzando fra Italia e Germania al fine di sfruttare appieno le potenzialità della configurazione interferometrica del Large Binocular Telescope. Il GWS, interamente assemblato ed allineato presso l'Osservatorio Astronomico di Padova, è il sensore di fronte d'onda con il più ampio campo di vista mai realizzato finora (6' di diametro), all'interno del quale possono essere selezionate fino a 12 stelle di guida naturali, ai fini della misura della turbolenza atmosferica di bassa quota. In questo elaborato è inclusa una descrizione dettagliata di tale sensore, partendo dai concetti di ottica che ne costituiscono le fondamenta, per passare allo studio delle procedure per l'allineamento dei diversi sottosistemi, che ne assicurano la conformità alle tolleranze calcolate in fase di disegno ottico, fino a concludere con l'analisi dei risultati ottenuti dalle verifiche effettuate sul sensore. Contemporaneamente, si è proceduto alla realizzazione di un secondo sensore di fronte d'onda, basato sul medesimo concetto ottico ma limitato ad un'unica linea di vista. Tale sensore è il prototipo di un sistema ottico per la misura della qualità ottica di lenti intraoculari artificiali (Intra-Ocular Lens, IOL) da trapianto, utilizzate per la sostituzione del cristallino umano nelle operazioni chirurgiche per la correzione della cataratta. Tale prototipo è stato disegnato, realizzato, allineato e completamente caratterizzato, al fine di misurare le aberrazioni introdotte dalle IOL con un sistema che sia il più possibile compatto, di semplice utilizzo e prodotto con componenti di facile reperibilità e limitato costo.

Contents

Introduction **7**

1 Adaptive Optics **9**
1.1 Telescope theoretical resolution . . . 9
1.2 The Earth's atmosphere . . . 11
1.2.1 Seeing parameters . . . 15
1.2.2 Other parameters . . . 16
1.3 Classical Adaptive Optics . . . 18
1.3.1 Tip-tilt sensing: the Quad-Cell wavefront sensor . . . 20
1.3.2 High order sensing . . . 21
1.4 Multi-Conjugated Adaptive Optics . . . 28
1.4.1 References . . . 30
1.4.2 Wavefront Sensors for MCAO . . . 32
1.4.3 Multiple Field of View Concept . . . 34
1.4.4 Ground-Layer Adaptive Optics . . . 36
1.5 Wavefront reconstruction . . . 37

2 8m: LINC-NIRVANA and the GWS **41**
2.1 Interferometry with the LBT . . . 43
2.2 Science with Linc-Nirvana . . . 45
2.2.1 LINC mode . . . 47
2.3 Adaptive Optics serving interferometry . . . 48
2.4 Linc-Nirvana system overview . . . 52
2.4.1 Ground-layer Wavefront Sensor . . . 54
2.4.2 Main sub-units description . . . 55
2.4.3 Main mechanical structure . . . 59
2.4.4 GWS first light: pathfinder at the LBT . . . 61

3 Ground layer Wavefront Sensor Error Budget **63**
3.1 GWS components . . . 63
3.2 GWS internal alignment . . . 64
3.3 Thermal effects . . . 65
3.4 GWS misalignment with respect to LN optical bench . . . 65
3.5 Bearing contribution . . . 70
3.5.1 Bearing Wobble . . . 70
3.5.2 Bearing Runout . . . 70

3.5.3 Bearing non-uniform rotation . . . 71
3.6 Flexures . . . 72
3.6.1 GWS flexures . . . 72
3.6.2 Bearing flexures . . . 72
3.6.3 Star Enlargers flexures . . . 73
3.6.4 Annular mirror flexures . . . 74
3.7 Overall Error Budget . . . 74

4 Star Enlargers **77**
4.1 Star Enlargers alignment concept . . . 77
4.2 Star Enlargers AIV . . . 78
4.2.1 Measurements and conclusions . . . 83

5 Pupil Re-Imager **85**
5.1 Pupil Re-Imager assembly . . . 86
5.1.1 Mounting of the mechanical supports for both the folding and the parabolic mirrors . . . 86
5.1.2 Glue the mirrors on their pads . . . 86
5.1.3 Flat mirror mount positioning . . . 87
5.1.4 Prime focus corrector positioning . . . 89
5.1.5 Parabolic mirror positioning . . . 89
5.1.6 CCD holding structure positioning . . . 89
5.2 Pupil Re-Imager Alignment concept . . . 90
5.3 Pupil Re-Imager alignment . . . 94
5.3.1 Phase 1: On axis reference definition on the test camera . . . 95
5.3.2 Phase 2: Alignment on axis between the objective and the parabola . . . 100
5.3.3 Phase 3: Alignment of the two flat mirrors . . . 101
5.3.4 Phase 4: Alignment of the PR-I . . . 104
5.3.5 Phase 5: final focus adjustment of the PR-I . . . 105
5.3.6 Phase 6: final PR-I optical quality check . . . 107

6 Ground layer Wavefront Sensor AIV **109**
6.1 GWS assembly . . . 109
6.1.1 Optical bench positioning . . . 114
6.2 GWS internal alignment . . . 114
6.2.1 PR-I flat mirror alignment . . . 115
6.2.2 Star Enlargers alignment inside the GWS . . . 116
6.2.3 Other verifications . . . 124
6.3 System test as a whole and next steps . . . 128
6.4 Conclusions . . . 132

7 8mm: IntraOcular Lenses test demonstrator **133**
7.1 Astro vs Ophto . . . 134
7.1.1 The human eye: our personal optical system . . . 134
7.2 IOL quality test demonstrator . . . 135
7.2.1 The demonstrator concept . . . 135
7.2.2 The real setup . . . 136

7.2.3 Setup details . . . 137
7.3 WFS linearity range . . . 139
7.3.1 Characterization of the relation between Zernike defocus coefficient, diopters and focal lengths . . . 139
7.3.2 Defocus measurements linearity and sensitivity . . . 141
7.3.3 Tip-tilt measurements linearity and sensitivity . . . 143
7.4 Wavefront computation and conversion in nanometers . . . 144
7.5 Calibration lines . . . 146
7.5.1 Through focus reliable range for the calibration lines determination . 146
7.6 Wavefront analysis . . . 151
7.6.1 Static aberration . . . 151
7.6.2 Measurement of the aberrations introduced by the IOL holder . . . 153
7.7 Test IOL WF measurements repeatability . . . 154
7.8 IOL focal length measurement . . . 157
7.9 Comments to the results and conclusions . . . 157

8 Conclusions **161**

Introduction

From an astronomical point of view, one of the most attractive challenges in the technological framework is trying to get sharper and sharper images of the sky. The goal is to apply direct imaging also to researches which need to clearly resolve and study small or far objects and structures even in crowded areas (small structures on the planets surfaces, solar active regions, orbits of stars close to our Galaxy center, and so on..). Since the entrance pupil of a telescope practically selects a portion of the wavefronts coming from the astronomical objects, such a spatial selection translates into an uncertainty, directly deriving from Heisenberg's principle, on the propagation direction of the selected photons, resulting in the enlargement of the point-like image, which is now said to be diffraction-limited, on the focal plane. The diffraction effect is one of the reasons, together with the wide collecting areas, pushing the astronomical community to build large and extremely-large class telescopes. For ground based telescopes with diameters larger than a few tens of centimeters, however, the resolution is normally limited by the seeing, an atmospheric characteristic due to spatial and temporal non-homogeneities in the refraction index of the air, causing a distortion in the wavefronts passing through it. The goal of Adaptive Optics is to sense the wavefronts reaching the ground and retrieve the distortion introduced on them by the atmosphere, in order to correct them through one or more deformable mirrors, with a number of actuators calibrated on the minimum spatial scale on which the wavefront is expected to be corrected, and changing their shape with a frequency higher than the typical atmospheric properties variation timescale (Chapter 1). In this framework, wavefront sensing can be considered as the heart of modern optical systems aiming to compensate static or dynamic aberrations in order to achieve extremely sharp images. Depending on the kind of aberrations and the level of precision of measurements, this can take the name of Active Optics, Adaptive Optics or even more exotic labels like Extreme Adaptive Optics, e.g. for planet finding, or Multi Conjugated Adaptive Optics, for wide field coverage, and others as well. It has been pointed out that similar classes of needs are involved in ophthalmology. It is surprising how similar can be the concepts, and in some cases the related hardware, for wavefront sensing applied to an 8m class telescope so as to achieve deep images of the remote Universe and the sensing of the human pupil, barely reaching 8mm in diameter, three orders of magnitude smaller, in order to assess, for example, which kind of artificial lenses has to be produced to surgically replace a damaged crystalline lens.

In my PhD thesis I will focus on the optical design, procurement, assembly, integration and verification of a few wavefront sensing units.

The main work has been done on the large field of view (up to 6 arcmin in diameter) wavefront sensors serving LINC-NIRVANA (Chapter 2), a Fizeau interferometric focal station on-board LBT, a 2x8.4m telescope. I first focused on these sensors' error budget (Chapter 3), exploring all the possible error sources, so as to define a detailed alignment procedure, and then perform

it on the first of these wavefront sensors, starting from its units (Chapters 4 and 5), to finally realize its whole integration and alignment (Chapter 6).
Considerations similar to the ones about astronomy could be made about the application of AO to the study of the human eye, both for research and defects diagnosis and treatment. That's because the eye is an optical system in all respects, composed of two lenses, named the cornea and the crystalline lens, like a basic telescope, and a fluid, called the vitreous humor, which has a physiological protection and retaining function but also introduces distortions on the light passing through it. That's why ophthalmology can take advantage of the same AO techniques serving astronomy to improve its diagnostic power in detecting lens diseases and, at the diffraction limit, resolving retinal structures. During my PhD, a laboratory demonstrator for a pyramid wavefront sensor, similar to those already used at TNG, VLT, LBT and Calar Alto Observatories, has been realized, to characterize artificial crystallines (Chapter 7).

Chapter 1

Adaptive Optics

1.1 Telescope theoretical resolution

One of the most important characteristics of a telescope is its capability to separate different sources when their separation on the sky is getting smaller and smaller, namely the angular resolution of the telescope itself. The telescope aperture, during the observations, selects a portion of the incoming wavefronts, which is properly focused onto the focal plane of the telescope where, in the simple case of imaging, the detector is acquiring images. In geometrical optics, the point-like source image is a point again. Due to the wave nature of light, however, this is far from the actual result one could achieve in the real world from an even perfect optical system, because of *diffraction*. Diffraction is a particular type of interference, originating when a wavefront reaches an obstruction. The result is that the wave, once the obstacle is crossed, starts propagating in directions which are different from the one of the incoming wavefront, accordingly to the Huygens principle.

If we neglect the atmosphere, the wavefront coming from a star and reaching a telescope aperture is flat. The selection of a portion of such a wavefront, made by the telescope stop, defines an area inside which the photons have to go through, to reach the focal plane. According to Heisenberg uncertainty principle, an uncertainty is then introduced on the direction of the photons motion, which translates into a point-like source image enlargement.

The same result can be obtained without introducing quantum considerations.

Let's consider the system shown in Figure 1.1, in which flat wavefronts hit an ideal infinitely extended slit of width b. Accordingly to Huygens principle, the secondary wavefronts, generated by each point along the slit, interfere one with each other, producing light and dark alternated bands on a screen.

We can describe the incoming wavefront as $y = A\sin(\omega t - kx)$, where A is the amplitude, ω the temporal frequency and $k = 2\pi/\lambda$ the wave number. The secondary wave emitted by the source ds, namely the slit element at a distance s from the center of the slit itself, can be formalized as

$$dy_s = \frac{Ads}{x}\sin[\omega t - k(x + \Delta)] = \frac{Ads}{x}\sin[\omega t - k(x + s\sin\phi)]$$

where Δ and ϕ are shown in Figure 1.1.

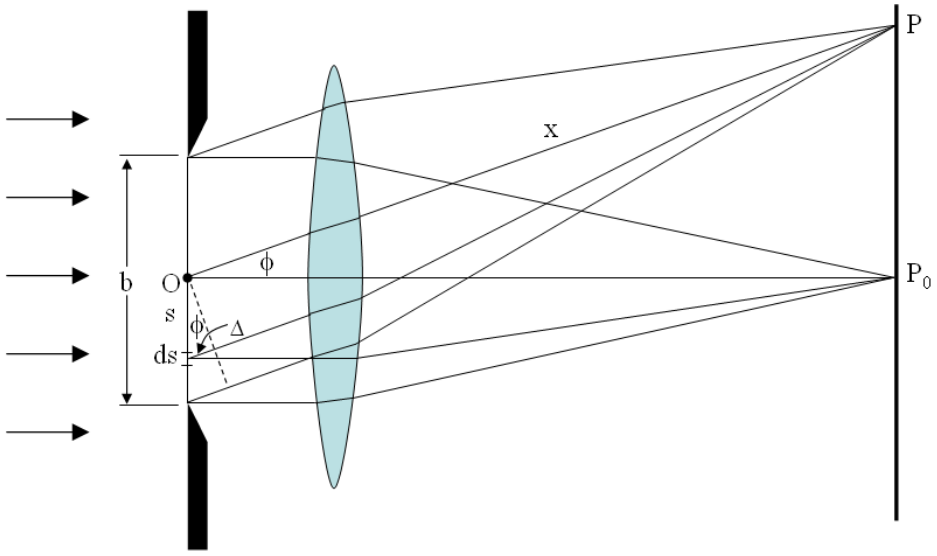

Figure 1.1: Diffraction through a slit.

If $dy = dy_{-s} + dy_s$, one can derive the following:

$$dy = \frac{Ads}{x}[\sin(\omega t - kx - ks\sin\phi) + \sin(\omega t - kx + ks\sin\phi)] = \frac{Ads}{x}[2\cos(ks\sin\phi)\sin(\omega t - kx)]. \tag{1.1}$$

Since, for the Huygens principle, the secondary waves sum up, then the transmitted wave expression can be found integrating 1.1 in the range $[0, b/2]$:

$$y = \int_0^{b/2} dy = A_0 \frac{\sin\beta}{\beta}\sin(\omega t - kx) \tag{1.2}$$

where $A_0 = \frac{ab}{x}$ and $\beta = \frac{kb}{2}\sin\phi = \frac{\pi b}{\lambda}\sin\phi$. If the wavefront reaches the slit with an inclination i, the resulting transmitted wave is the same, replacing $\beta = \frac{\pi b}{\lambda}(\sin i + \sin\phi)$.

From the previous considerations, one can see that the intensity of the re-imaged spot on the detector (namely the square of the resulting wave amplitude: $I = A_0^2\frac{\sin^2\beta}{\beta^2}$) depends on parameter β, which is linked to the angle ϕ and, then, to the position onto the detector. The resulting image, indeed, has a well-defined 2D structure, which can be retrieved with Equation 1.2. The maximum of the image intensity I will correspond to the position in which $\frac{\sin^2\beta}{\beta^2} = 1$, that is to say $\beta = 0$ and, so, $\phi = 0$. The central maximum of the diffraction pattern will, then, appear at position P_0 in Figure 1.1. Analogously, one can derive the diffraction pattern minima and secondary maxima, correspondingly, respectively, to the case in which $\beta = \pm m\pi$, where m is the order of the minimum, and $\tan\beta = \beta$ ($\pm 1.43\pi$, $\pm 2.46\pi$, ecc..). Concerning ϕ, the minima occur when $\phi \simeq m\lambda/b$.

In the circular aperture case, the concept is the same. The diffraction pattern consists of a central bright disk, surrounded by a series of dark and bright rings, which get fainter and fainter as the distance from the central maximum increases. This is the Airy pattern (shown in Figure 1.2).

The concept of angular resolution can be introduced in this framework, since the diffraction patterns of close sources overlap. According to Rayleigh's criterion, two sources are just

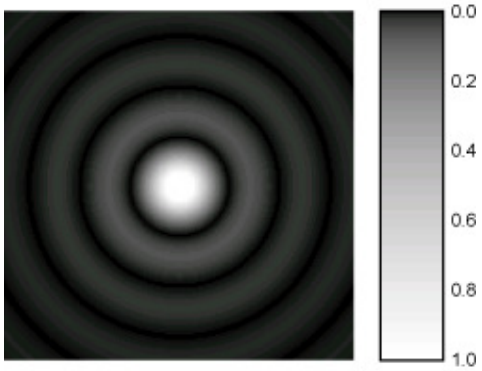

Figure 1.2: Airy diffraction pattern.

resolved when the maximum of the diffraction pattern of one of them is overlapped to the first minimum of the other, that is to say when the angular distance between the sources is $\theta = \lambda/b$.

Considering an ideal telescope outside the atmosphere, the minimum angular distance between two resolved sources corresponds to the radius of the first dark ring of the Airy pattern, namely:

$$\theta_{Airy} = 1.22\frac{\lambda}{D} \tag{1.3}$$

where D is the telescope aperture diameter and λ the reference wavelength which is observed.

Switching to the real world case, the image of a star on the focal plane of a telescope presents several distortions, due to the optical aberrations to which the system is subject. We can summarize the overall resulting point-like source image dimension as follows:

$$\theta_{tot}^2 = \theta_{Airy}^2 + \theta_{al}^2 + \theta_{opt}^2 + \theta_{opt}^2(t) \tag{1.4}$$

where θ_{opt} is a term due to the aberrations introduced by the optics constituting the instrument itself, θ_{al} contains the errors in the instrument alignment and in the optical surfaces production and $\theta_{opt}(t)$ is a term taking into account the atmosphere action ($t < 1s$, to be minimized with Adaptive Optics) and the mechanical distortions, like flexures and long-term temperature variation effects ($t > 1s$, Active Optics regime).

When $\theta_{tot} = \theta_{Airy}$, the image is labeled as "diffraction limited".

1.2 The Earth's atmosphere

Modern astronomy must consider the Earth atmosphere as part of each ground-based optical system looking at the sky, because of its absorbing and deforming effects on the incoming wavefronts. In addition to the presence of dust, the atmospheric absorption is mainly due to the interaction between the light and the atoms and molecules of the atmosphere, via scattering or actual radiation absorption, which usually occurs only at discrete wavelengths. Since we mentioned also molecules, however, because of the high numbers of degrees of freedom, mainly vibrational and rotational, the energy levels are so close one to each other that

the absorption can occur in a quite wide wave band. There are some regions of the electromagnetic spectrum, called "windows", to whose wavelengths the Earth's atmosphere is quite transparent; these regions are situated in the Visible and in the Radio domains, and in some InfraRed regions, where they are spaced out by molecular absorption bands.

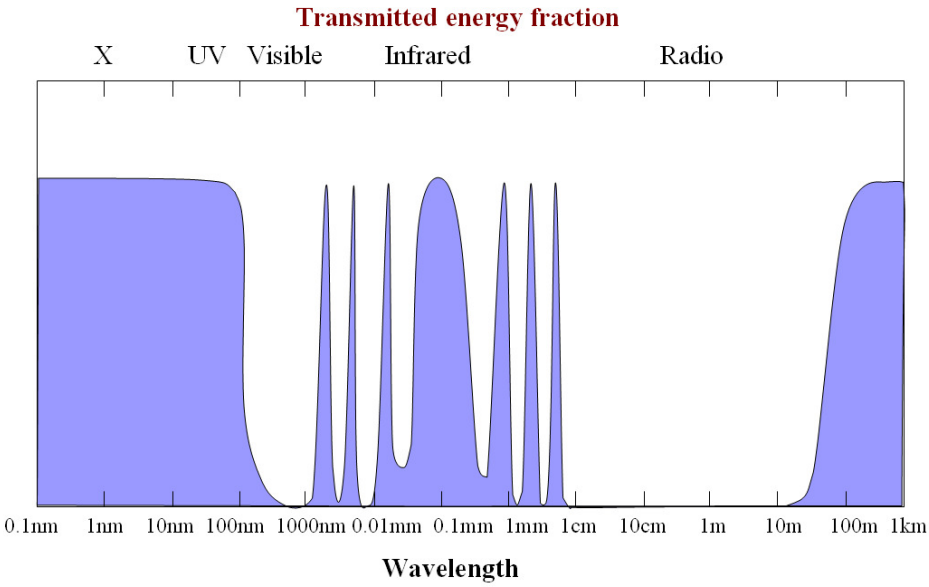

Figure 1.3: Atmospheric mean absorption.

As we already mentioned, the second effect of the atmosphere on the electromagnetic radiation coming from on-sky sources is the distortion of the wavefronts, which is due to the fact that the atmosphere is an inhomogeneous medium, constituted of regions with different and time-varying optical properties.

The main parameter we're interested in is the refractive index. When a wavefront goes through a discontinuity surface between two media with different refraction index, its direction of propagation changes, as quantified by the Snell equation:

$$n_1 \sin \psi_1 = n_2 \sin \psi_2$$

where n_1 and n_2 are the refraction indexes of the two media and ψ_1 and ψ_2 are the angles between the direction of propagation of the waves and the normal to the discontinuity surface.

The refraction index value in vacuum conditions is $n_{vacuum} = 1$ and the air, close to the Earth's surface, has a refraction index which deviates from n_{vacuum} only at the forth decimal place. If we imagine the atmosphere as composed by several shells with a refraction index which is continuously increasing as the height from the Earth's surface decreases, each wave coming from an astronomical object will always bend toward the Earth's surface normal, accordingly to the Snell law. Unfortunately, the atmosphere not only bends the waves propagation trajectories, because the refraction index is not only characterized by a vertical gradient, but also by a continuous spatial and temporal horizontal variation on small scales. This phenomenon, called *seeing*, continuously bends the waves trajectories and causes the wavefronts perturbation. The refraction index value depends upon the physical characteris-

tics of the medium, as quantified by the Chauchy's equation:

$$n - 1 = \frac{77 \times 10^{-6}}{T}(1 + 7.52 \times 10^{-3}\lambda^{-2})(P + 4810\frac{p}{T}) \tag{1.5}$$

where $T(K)$ and $P(mbar)$ are temperature and pressure of the air, respectively, and $p(mbar)$ is the pressure of the water vapor, which is negligible, as a low order approximation, for the Visible and InfraRed bands, especially for the sites selected to build the modern large and very large telescopes. The main term of Equation 1.5 can be recognized in the Gladstone equation:

$$n - 1 = 77 \times 10^{-6}\frac{P}{T}$$

from which one can deduce that the temperature variations are far more relevant than the pressure ones, from the refractive index variation point of view; the partial derivations, indeed, give $\partial n/\partial P \sim (1/10)\partial n/\partial T$. Since the atmosphere is a fluid medium, two main regimes can be identified, depending on the motion transmission mechanism: the laminar regime and the turbulent regime. In the first case, layers with different chemical and physical characteristics are flowing one on the other without mixing, and they are reducing the small perturbations which could arise. In the turbulent regime, instead, the fluid motion feeds vortices on a wide spatial scale (*external scale*, L_0), whose kinetic energy does not dissipate because of viscosity friction, but it is transferred to smaller scale vortices, in a so-called *inertial regime*.

The vortices, then, degrade up to the complete energy dissipation due to molecular motion, through which energy is converted into heat by the viscous friction, when a peculiar length scale is reached (*dissipative regime*); such a characteristic scale is called *Kolmogorov scale* (or *internal scale*, l_0).

The width of the inertial range, between internal and external scales, depends on the *Reynolds number*:

$$Re(L) = \frac{Lv_L}{\nu} \tag{1.6}$$

where L is the characteristic spatial scale of the system, v_L represents the fluid characteristic speed at the scale L and ν is the kinematic viscosity parameter, i.e. a coefficient depending upon several fluid properties. When the Reynolds parameter exceeds the critical value Re_{cr}, depending only on the geometrical characteristics of the flow, then the fluid enters the turbulent regime and the separation between the two characteristic scales grows. In the atmosphere $\nu \approx 15 \times 10^{-6}\, m^2/s$, $L_0 > 15\, m$ ($l_0 \approx 1 \div 10\, mm$) and $v_{L_0} > 1\, m/s$, so $Re(L_0) > 10^6$. Since the typical value of Re_{cr} is about 2000, the Reynolds parameter of the Earth's atmosphere is always several orders of magnitude above the critical value, corresponding to a clearly turbulent regime and to a very wide inertial range. The first modern theory on turbulence has been formalized by A. N. Kolmogorov in 1941 and it describes, through a statistical approach applied to velocity fields, the shape of the energy spectrum in the stationary inertial regime [15]. The resulting energy to be associated to the vortices, in the considered hypothesis, is proportional to the physical width of the vortex itself, to the 5/3 power:

$$E_k \propto k^{-5/3} \tag{1.7}$$

where $k = 2\pi/L$. Moreover, the refraction index fluctuations have been found to be proportional to the vortices dimensions, whose spatial scale changes according to the site selected for the observations and to the height of the turbulent layer.

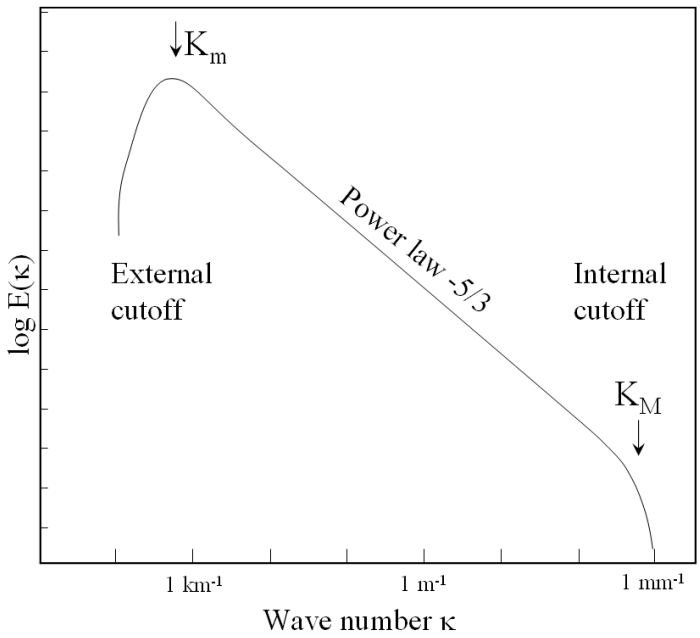

Figure 1.4: Power spectrum of the energy to be associated to the vortices in the turbulent regime. The range between the internal and external scales behaves as predicted by the *Kolmogorov law* 1.7. $K_m = 2\pi/L_0$ e $K_M = 2\pi/l_0$.

To quantify the amount of turbulence of the atmosphere, some *structural parameters* have been defined. They are linked to the time and spatial variability of the temperature or the refraction index. In particular, the temperature structural parameter, C_T^2, depends on the statistical variance of the temperature difference between two points at a relative distance of one meter, in a determinate site and at a certain height from the ground: $C_T^2 = \sigma_{\Delta T}^2 / r^{2/3}$ where r is the distance between the two considered points (one meter) and ΔT is the statistical variable "temperature difference". Accordingly to the *Gladstone equation*, the refractive index structural parameter can be retrieved as:

$$C_n^2 = \frac{\partial n}{\partial T} C_T^2 = \left(77 \times 10^{-6} \frac{P}{T^2}\right)^2 C_T^2$$

The vertical distribution of such a parameter describes the perturbation acting on the wavefront in a certain astronomical site. On average, C_n^2 decreases with height, but it presents some peaks under particular conditions: when two air masses in relative motion cross each other, in mechanical turbulence conditions and in regions characterized by high temperature gradient (e.g. thermal inversions, see Figure 1.5).

Examples of such conditions are usually found at less than 1000 m from the ground, because of meteorological events, in the troposphere at ($\sim$ 5000 m) and in correspondence of the so-called *tropopause* at a $\sim$ 10000 m height, where a thermal inversion occurs. To go more in detail, some turbulent layers can be found in all the ground-based astronomical sites, with different strength. Typically, the most perturbing turbulent layer extends up to some tens of meters from the ground; it's called the *ground layer* and it's due to the thermal exchange between the atmosphere and the ground, which, during the night, gives back part of the energy

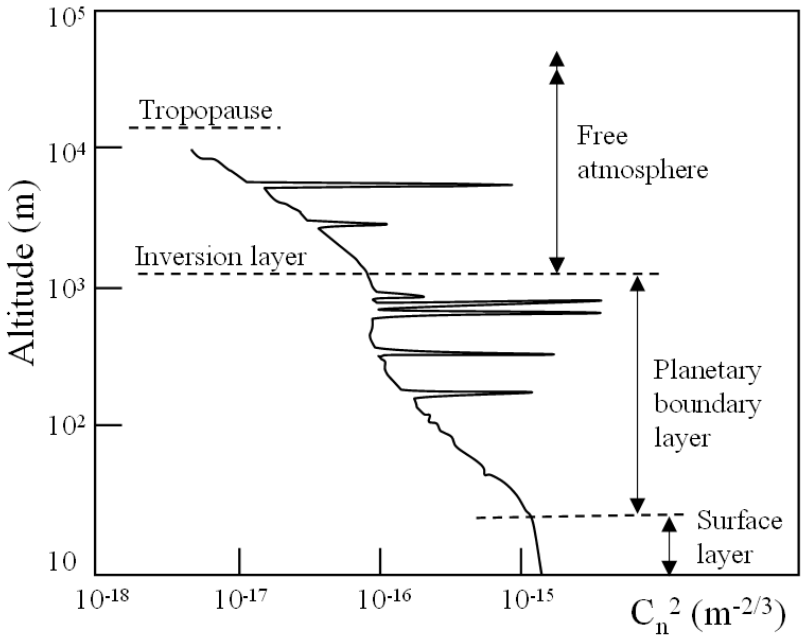

Figure 1.5: Example of vertical behavior of the atmosphere structure parameter.

accumulated during the day. From the ground layer up to about 1km of height, there is an intermediate layer called the *boundary layer*, generated by the air flow, ascending because of the average temperature gradient of the atmosphere. In the overlying "free atmosphere" the turbulence is generated by meteorological events: winds, air masses movements and quick thermal gradient variations. An example of these variations is the thermal inversion at about 10 km from the ground; warm air masses rise up from the lower part of the atmosphere, their adiabatic expansion implies their cooling down (the atmospheric average pressure decreases with altitude), and, when the water vapor condensation temperature is reached, the latent heat of condensation warms the air and stops the temperature decrease while the air masses are still rising. There are also other thermal inversion zones inside the atmosphere, but they stand at a height in which the air is more rarefied and can introduce only a small perturbation on the wavefronts, since their average refractive index is very close to one and its fluctuations are small.

1.2.1 Seeing parameters

To describe the degradation of astronomical images due to the effects of the atmosphere, some other parameters, depending upon the wavelength, have to be introduced. The most important is the *Fried parameter*, r_0, corresponding to the length scale, in the wavefront plane, after which the wavefront itself statistically varies more than a radian:

$$r_0 = [0.43\frac{4\pi^2}{\lambda^2}(\cos\phi)^{-1}\int_0^\infty C_n^2(z)dz]^{-\frac{3}{5}} \propto \lambda^{6/5} \tag{1.8}$$

where ϕ is the zenithal distance, e.g. the angle between the normal to the Earth's surface and the observed direction, λ is the considered wavelength and C_n^2 the refraction index structural parameter. The Fried parameter can be interpreted also as the average size of a turbulent

cell, or an air ball with a homogeneous refractive index. This parameter corresponds also to the diffraction limited aperture with the same resolution of a telescope focusing the perturbed wavefronts; this is true because if a telescope has an aperture wider than the Fried parameter and it is not equipped with an Adaptive Optics system, its angular resolution is limited to $\frac{\lambda}{r_0}$, which is the value to be attributed to the *seeing*. The Fried parameter depends on the refractive index structural parameter, and its dependence upon wavelength can be approximated as $r_0 \sim \lambda^{6/5}$. Because of this, InfraRed images are less affected by seeing, since its typical value is higher. However the Airy disk width is proportional to the wavelength, so the resolution is not drastically better in the Visible or InfraRed bands, if no Adaptive Optics systems are present. A typical value of r_0, in the K band, is $r_0 \sim 30\,cm$.

A second very important parameter, concerning the wavefront distortion due to the atmosphere, is the *isoplanatic angle*, θ_0, i.e. the angle subtended by the FoV inside which the wavefront phase statistically changes less than one radian:

$$\theta_0 = 0.314\frac{r_0}{\bar{h}} \propto \lambda^{6/5} \tag{1.9}$$

where $\bar{h}$ is the mean height of the turbulent layers. This angle corresponds to the FoV inside which the perturbation introduced by the atmosphere affects the wavefronts in a very similar way, and its typical value is a few arcseconds.

The time scale of the variability of the atmospheric distortion can be defined with a parameter, called the *coherence time*, representing the typical timescale in which the wavefront phase changes of one radian, and it corresponds to the time slot inside which the PSF remains raughly constant inside the isoplanatic patch:

$$\tau_0 = \frac{r_0}{v} \propto \lambda^{6/5} \tag{1.10}$$

where v is the mean wind speed at the altitude of the turbulence. The coherence time is usually some tens of milliseconds in the IR domain and, as with all the atmospheric parameters introduced above, it depends on the observation site and the considered turbulent layer. The inverse of τ_0 corresponds to the *Greenwood frequency*, $f_G = \tau_0^{-1} = v/r_0$.

The wavefront aberrations translate into scintillation, image motion and deformation on the telescope focal plane. Such effects, integrated in time, result in point-like sources images enlargement and a decrease in the instrument resolving power.

1.2.2 Other parameters

Other very important parameters, which are essential for Adaptive Optics, have to be mentioned: the *Strehl Ratio* and the *Signal to Noise Ratio*. Such parameters are used to quantify the performance of a generic optical system.

Strehl Ratio

The Strehl Ratio (SR) is defined as the ratio between the peak intensities of the observed PSF and of the diffraction limited image, ideally obtained with the same instrument:

$$SR = \frac{PSF_{seeing}(0,0)}{PSF_{dl}(0,0)} \tag{1.11}$$

where PSF_{seeing} is the observed PSF intensity, while PSF_{dl} is the diffraction limited PSF one.

Obviously, the highest SR value is $SR = 1$, when the wavefront goes through a perfect optical system, and it is not perturbed at all. In all real cases, $SR < 1$ and the smaller its value, the worse the image quality.

Signal to Noise Ratio

The Signal to Noise Ratio (SNR) is another parameter used to quantify the quality of the images which can be retrieved with an instrument. The source radiation is considered as the "signal". The "noise" is a radiation flux which only partially depends on the astronomical source, but it mingles with the signal, reducing the image quality which can be obtained with an optical system. The noise is composed by several contributions. First of all, the *Poisson noise* is a contribution which is intrinsic in the photon nature, due to the statistical fluctuation in the photon number (i.e. in the flux) measurements. One of the main noise sources, concerning astronomical images, is the *sky background*, that is to say the noise due to the diffuse light coming from the night sky. When you observe a FoV in the sky, part of the photons detected by the detector are coming from sources which are different from the target. It could be a contribution due to the Sun light reflected by the moon, if visible, or the emission coming from extragalactic unresolved sources, in addition to the integrated Milky Way starlight. Moreover, the interplanetary dust reflects a fraction of the Visible Sun light, producing the *zodiacal light*. Such a component has a distribution which is a function of the FoV coordinates with respect to the ecliptic. The maxima of such an emission can be found on the ecliptic plane, in the solar direction and in the opposite one. The zodiacal light generates almost 70% of the total sky background on a moonless night.

Another noise source is the radiation emission from the Earth's atmosphere (*airglow*), which is limited to discrete wavelengths and is due to transitions between the electronic, rotational and vibrational energy levels of the molecules constituting the medium, together with the electronic recombination and the diffusing effect of such molecules on the sun light. Such contribution intensity depends upon the geographic coordinates of the observing site and its maxima can be found at the sub-polar latitudes and at the equator.

The optical system itself is, moreover, introducing some noise, since it emits black body thermal radiation with a peak in the InfraRed band (*thermal noise*).

Concerning the noise which is intrinsic in the detector, let's consider the noise sources which are typical of CCDs. The CCD (*Charge Coupled Device*) is an integration-based detector. When a photon hits the sensitive area, it generates an electric charge because of the photoelectric effects, that is to say that it transmits an amount of energy to the Silicon atoms (Silicon is the main constituent of the CCD, working in the Visible and InfraRed bands) which is enough to separate the electrons from the nucleus. The free charges are accumulated during the integration time. Then such charges are read and translated into *counts*, an operative unit of measurement for the flux. The number of charges translated into a single count is said *gain*.

The main noise which affects the CCDs is the *ReadOut Noise* (RON), introduced by the readout amplifier when trying to measure a very small packet of charge. Moreover, the charge reading is performed with a pixel-to-pixel charge transfer along a line and then along a column, as long as the output node is reached. This process introduces errors due to delays in the charges transfer or to some spurious counts generation. All these effects translates

into a minimum counts threshold, in the best cases a constant one, introduced on the images. Another CCD noise is the *dark current*, due to the electric charges released because of thermal agitation of the electrons inside the CCD itself. Statistically, some electrons reach, thanks to thermal agitation, enough energy to separate from the Silicon nucleus, generating a current which is said "dark" since it's not due to a photon arrival on the CCD. Such thermal noise can be reduced cooling the detector sensitive area down.

1.3 Classical Adaptive Optics

The goal of Adaptive Optics (AO) is the correction of the aberrations introduced by the atmosphere on the wavefront, by means of one ore more optical correctors inserted into the optical path before the scientific camera or spectrograph.

Atmospheric perturbations have three main effects on the wavefront:

- **Piston**: mean value of the wavefront profile across the telescope pupil (not relevant for single telescopes);
- **Tip-tilt**: mean inclination of the wavefront, selected by the telescope aperture, that is to say the first derivative of the wavefront shape. The effect of such aberration is the motion of the image in the focal plane;
- **High order aberrations**: deformations of the wavefront on smaller scales. The perturbed wavefront reaches the telescope aperture with small deformations, down to the r_0 scale, as shown in Figure 1.6. Considering a point-like source, each wavefront area, which is locally flat, focuses at a different position in the focal plane, forming separate spots. The overall effect is the superimposition of such spots, resulting in the target image enlargement.

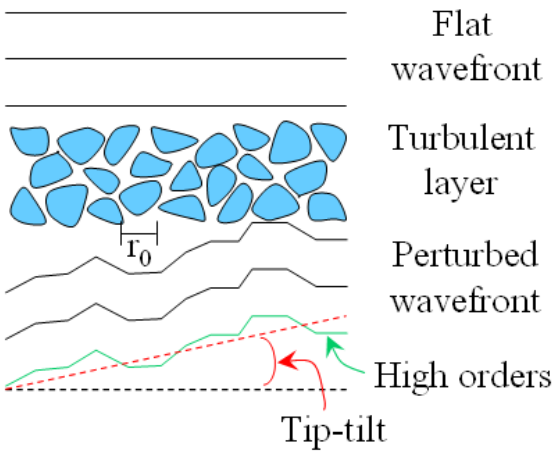

Figure 1.6: Starting from the incoming wavefront shape, tip-tilt and high order aberrations are shown. The mean dimension of the air masses with a constant refraction index is r_0, the Fried parameter.

After the integration in time of the light coming from the point-like source, both the atmospheric perturbation effects translate into image enlargement and so into the decrease of the telescope resolving power from λ/D (diffraction limited) to λ/r_0, where r_0 is the Fried parameter. Considering small aperture telescopes ($D < r_0$) the dominating effect is the motion of the image in the focal plane, due to the tip-tilt, since the wavefront area selected by the aperture is smaller than the wavefront region which is locally flat. With big telescopes ($D >> r_0$), instead, high order perturbations are dominating. The telescope aperture, indeed, is wide enough to contain the scale r_0 several times. Because of this, the selected wavefront will be perturbed on small scales. The mean tilt on such a large scale, instead, is statistically lower than on smaller scales.

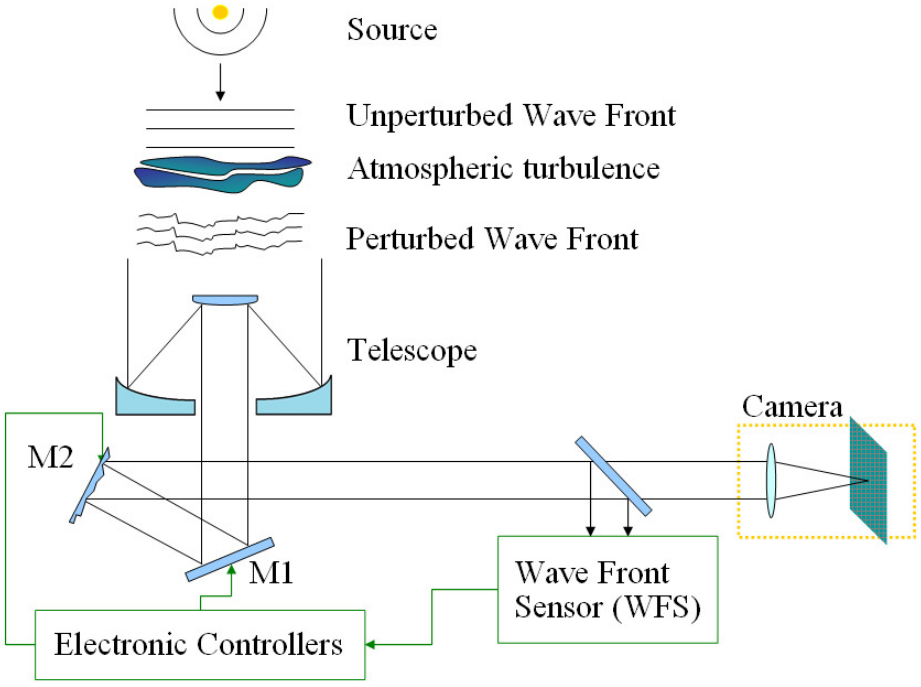

Figure 1.7: Scheme of a telescope equipped with a classic AO system. The wavefront perturbed by the atmospheric turbulence hits the telescope collecting area The light beam is reflected by the flat mirror, M1, and the deformable one, M2, before being split between the WFS and the imaging camera. The WFS retrieves the wavefront shape and sends the information about the proper correction to be applied to the wavefront to the electronics controlling the mirrors.

The goal of AO is to allow diffraction limited imaging, that is, to correct the aberrations introduced by the atmosphere. To correct the tip-tilt, a flat mirror, to be properly tilted accordingly to the wavefront sensor signal, is usually introduced inside the optical path, to reproduce the opposite of the incoming wavefront mean inclination. The high order perturbation correction is performed with a Deformable Mirror (DM), which can reproduce the opposite of the retrieved small scale distortions of the wavefront, pushing and pulling actuators below the mirror surface. The separation of tip-tilt is necessary to keep the required actuators' stroke under a value which is reachable with the currently existing DMs, usually

limited to few tens of micrometers.

The deformable mirror is controlled by the electronics of the system, which elaborates the signals retrieved by the WaveFront Sensor (WFS), which is the heart of an AO system. The WFS looks at a reference point-like source (usually a star) inside the astronomical target isoplanatic patch and reconstructs the distortion the wavefront has been subjected to before reaching the sensor itself.

1.3.1 Tip-tilt sensing: the Quad-Cell wavefront sensor

To evaluate the tip-tilt of the wavefronts, the so-called Quad-Cell WFS can be used, splitting the light coming from a reference target into four beams. Such a sensor is positioned on the focal plane of the system and its center is placed at the location on which the diffraction limited PSF should focus, in the absence of aberrations. The WFS can measure the spot movements, which are directly proportional to the first derivative of the incoming wavefront shape.

The concept of the Quad-Cell sensor is shown in Figure 1.8, from which it is easy to understand how a shift of the spot along the x and y axis can be quantified through two simple expressions:

$$X\ signal: \quad S_x = \frac{B + D - (A + C)}{A + B + C + D}$$

$$Y\ signal: \quad S_y = \frac{A + B - (C + D)}{A + B + C + D}$$

in which A, B, C and D are the integrated fluxes reaching the respective quadrants of the sensor and S_x and S_y are proportional to the first derivative of the wavefront, computed along two orthogonal directions, for small shifts of the spot.

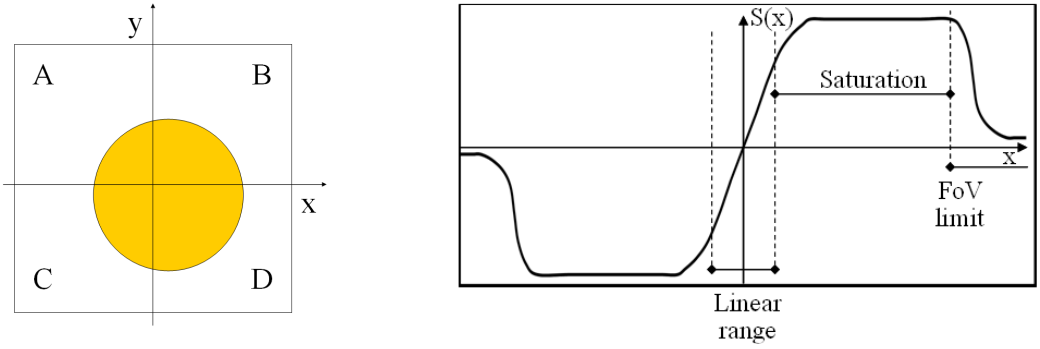

Figure 1.8: *Left*: Quad-Cell WFS concept; *right*: S_x signal as a function of the spot shift along the x axis.

In Figure 1.8, on the right, the S_x signal behavior as a function of the shift of the spot along the x axis is shown (an analogous graph can be shown for the S_y signal as a function of y). The useful range, with the aim of measure the tip-tilt, is the one in which S_x and S_y are increasing linearly. This happens when the light of the spot hits all the four quadrants of the WFS. Let's consider the following example: if the spot shown in Figure 1.8 illuminated only quadrants B and D, then the y signal $S_y = (B - D)/(B + D)$ would still be in its linear

regime, giving the true inclination of the wavefront in the y direction, while the x signal would have reached its saturation value $S_x, sat = 1$.

Obviously, the linear range width is related to the spot dimension: the smaller the spot, the more sensitive the sensor, because the S_x and S_y slopes in the linear regime are steeper and a smaller shift of the spot barycenter is enough to retrieve an high tilt signal.

To realize a Quad-Cell WFS several approaches can be used. Let's see some examples:

- It is possible to use a 2×2 lenslet array, positioned on the focal plane, with the aim to re-image 4 pupils, the integrated flux of which depending on the amount of light reaching the respective lens (i.e. the respective quadrant). Then, the 4 beams fluxes are measured by 4 detectors.
- A similar effect can be obtained taking advantage of the optical properties of a refractive pyramid, positioned in the focal plane, splitting the light spot into four beams, as in the previous case. The beams can then be collimated and reach a CCD or be focused on four avalanche photo-diodes. A detailed description of how the pyramid works can be found in Section 1.3.2.
- The 4 quadrants splitting can be realized by software, directly on a spot image, acquired by a CCD.

The information retrieved with a Quad-Cell WFS can be sent to a flat mirror positioned along the optical path, inside the instrument, to correct the incoming wavefront mean inclination.

1.3.2 High order sensing

To detect small scale deformations in the incoming wavefront, it's necessary to operate a spatial sampling of the wavefront itself. The pupil, whose diameter is D, is then divided into $N \times N$ sub-apertures, with a $d = D/N$ size.

Once the wavefront is properly sampled, it is possible to apply the Quad-Cell concept to retrieve the mean local tilt inside each sub-aperture, using several different approaches.

Generally speaking, remembering the Fried parameter definition, the number of sub-apertures optimizing the system spatial sampling will be $N \sim D/r_0$. Since we want to describe with a high precision the incoming wavefront shape, it is evident that a high number of sub-apertures would be preferable; however, if the spatial scale below which the deformation are negligible is, as already said, r_0, then it would be useless to oversample the pupil, since this would lead to a decreasing of the light illuminating each sub-aperture (translating into a SNR decreasing), without giving any additional information.

Shack-Hartmann wavefront sensor

The Shack-Hartmann WFS takes advantage of a technique originally used to verify the optical quality of telescopes mirrors, the so-called *Hartmann test*, consisting in positioning a properly perforated mask just above the telescope aperture. In such a way, each small hole samples a small area of the whole aperture and, once the pupil is re-imaged by collimating optics, on such image one will see many small fixed pupils, each one corresponding to one of the holes on the mask. If, however, we move to the focal plane, we will find only one image of the source, independently on the shape of the introduced mask. Moving, again, on a plane

positioned between the pupil image and the focal plane, we will find as many spots as the holes on the mask, moving independently one from each other (if a time-varying perturbation is introduced on wavefronts), accordingly to the local tilt of the wavefront.

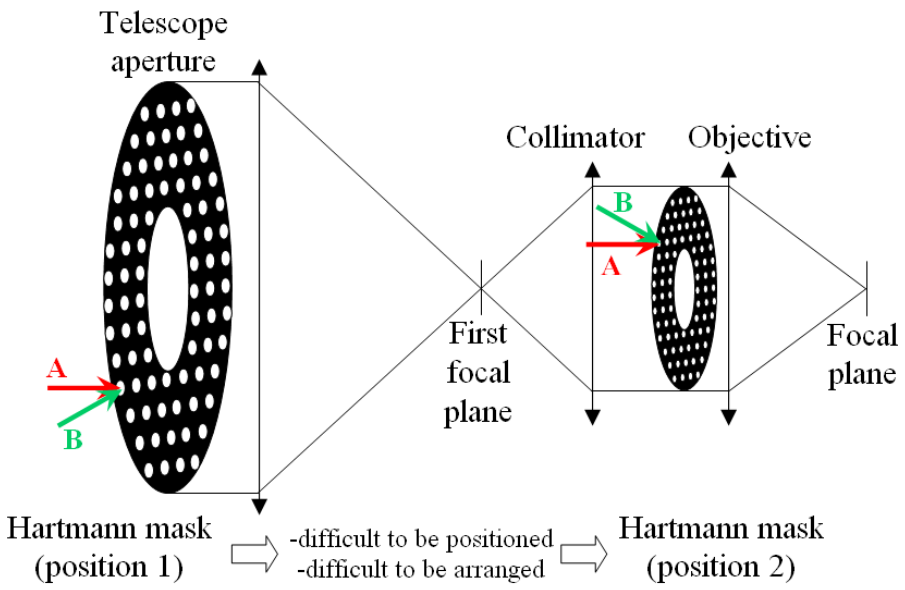

Figure 1.9: WFS using the Hartmann mask. In the picture 2 masks are displayed: their presence is mutually exclusive.

If the Hartmann concept was used for a WFS as described above, however, the sensor would have several limitations. First of all, the insertion of a mask like the one shown in Figure 1.9 makes the system lose a lot of light coming from the reference source and, consequently, only very bright stars could be selected as references, considerably reducing the system sky coverage. Second, the selected areas corresponding to the holes on the mask are often not representative of the local mean tilt of the wavefront (see Figure 1.10).

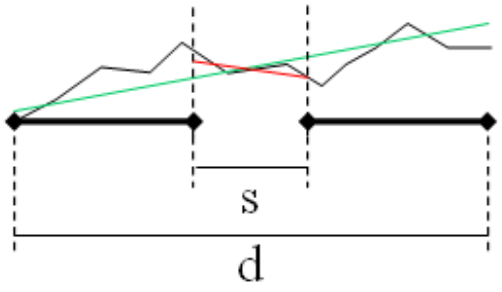

Figure 1.10: Example of a wavefront sampling which is not representative of the mean inclination of the wavefront. s represents the diameter of one of the holes in the Hartmann mask (the red line shows the detected mean tilt) mask and d the subaperture selected by one of the lenslet on the Shack-Hartmann array (the green line shows the detected mean tilt).

Both these problems have been solved, in the Shack-Hartmann (SH) WFS, substituting the perforated mask with a lenslet array, positioned on a pupil plane inside the optical path, as shown in Figure 1.11. The detector is, then, positioned in the focal plane.

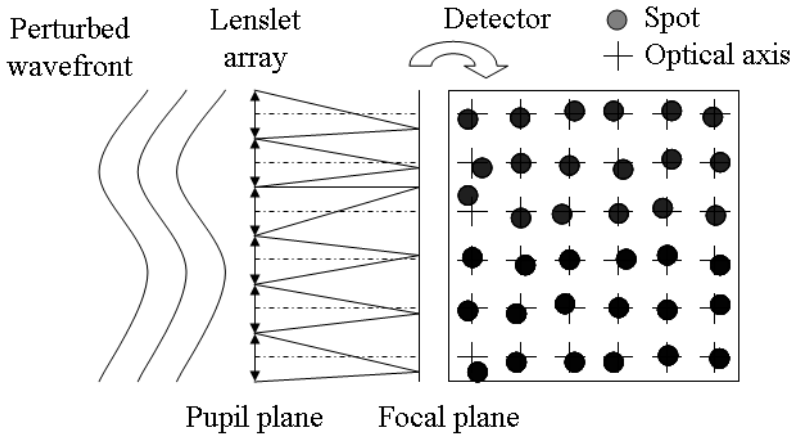

Figure 1.11: Shack-Hartmann WFS scheme.

In this configuration, the WFS receives all the flux collected by the telescope aperture, since the pupil is not masked. Moreover, the measured tip-tilt actually corresponds to the mean inclination of the wavefront in the selected sub-aperture, as shown in Figure 1.10. As many Quad-Cell WFSs as the total number of spots (corresponding to the lenslet number in the array) are positioned in the focal plane. If the wavefront is perfectly flat and its inclination is zero, each spot barycenter will be focused on the optical axis of the corresponding lens, but if, on the contrary, the wavefront is perturbed, the image focused by each lens will move on the focal plane, accordingly to the local inclination of the wavefront itself. The SH WFS sensitivity is fixed and depends upon the spot radius, which is linked to the lenslet dimension.

Obviously, since each spot is created by one lenslet, its angular dimension will no longer be $\theta = \frac{\lambda}{D}$, with D the telescope diameter, but it will become $\theta_{SH} = \frac{\lambda}{d}$, where d is the dimension of the incoming wavefront area selected by a single lens. If the number of sub-apertures is $N \times N$, then $d = D/N$, so the spot dimension will become $\theta_{SH} \frac{\lambda}{D/N}$. To optimize the sampling, accordingly to the mean value of the Fried parameter of the astronomical site, $N \sim D/r_0$, and the spots are expected to move quite independently from each other (even if the low-order aberration effects, i.e. deformations on scales larger than r_0, will be similar for adjacent sub-apertures).

Let's quantify now the Shack-Hartmann WFS error. Considering M photons reaching the telescope entrance pupil in an integration time τ_0 (frozen wavefronts) and a lenslet array $N \times N$, each sub-aperture collects about $n^* = M/N^2$ photons. The uncertainty to be associated to the measurement of the spot barycenter position depends on the number of incoming photons, in a perfect optical system, dominated by Poisson errors. Because of this uncertainty, which is intrinsic in the photon nature, the number of photons collected by the optical system is inside the range $M \pm \sqrt{M}$. This error propagates in the Quad-Cell signals expressions, resulting in:

$$S_x = \frac{\theta}{2} \cdot \frac{\frac{M}{2} \pm \sqrt{\frac{M}{2}} - \left(\frac{M}{2} \pm \sqrt{\frac{M}{2}} \right)}{M \pm \sqrt{M}} = \pm \frac{\theta}{2} \cdot \frac{\sqrt{M}}{M \pm \sqrt{M}} \sim \pm \frac{\theta}{2} \cdot \frac{1}{\sqrt{M}}$$

which result in an uncertainty: $\epsilon = \frac{spot\ dimension}{2\sqrt{\#\ photons}}$. It is then evident that the Shack-Hartmann WFS presents an optical advantage with respect to a WFS using the Hartmann mask, since a higher number of collected photons translates into a lower error to be associated to the spot position measurement and, consequently, to the local tilt determination. The uncertainty to be associated to the SH WFS is then:

$$\epsilon_{SH} = \frac{\lambda}{D/N} \cdot \frac{1}{2\sqrt{n^*}} = \frac{\lambda}{r_0} \cdot \frac{1}{2\sqrt{n^*}} \tag{1.12}$$

where $N = D/r_0$ is assumed as the number of sub-apertures across the diameter. Let's now consider a flat wavefront, only affected by tip-tilt aberration. All the spots in the SH WFS will move by the same amount in the same direction. The uncertainty on the signal will then be

$$\epsilon_{SH_{tilt}} = \frac{\lambda}{Nr_0} \cdot \frac{1}{2\sqrt{n^*}} = \frac{\lambda}{D} \cdot \frac{1}{2\sqrt{n^*}} \tag{1.13}$$

Summarizing, the SH WFS can retrieve the wavefront aberration concerning both low and high orders, but it presents also some technical difficulties. The lenslet array is constituted by a lot of optical surfaces, which need to be produced within quite tight specifications, concerning both the surface accuracy and the optical power. But the main difficulty is represented by the conjunctions between the lenses, since the wider is the gap, the higher the amount of light which is lost and diffused because of diffraction, also introducing noise on the CCD. Everything is made even more complicated by the fact that the alignment of such an array with respect to the detector is not straightforward.

Curvature WFS

The curvature WFS concept is completely different from the previously described WFS, since it measures the curvature of the incoming wavefront, and not its inclination. It was invented by F. Roddier in 1981 [23].

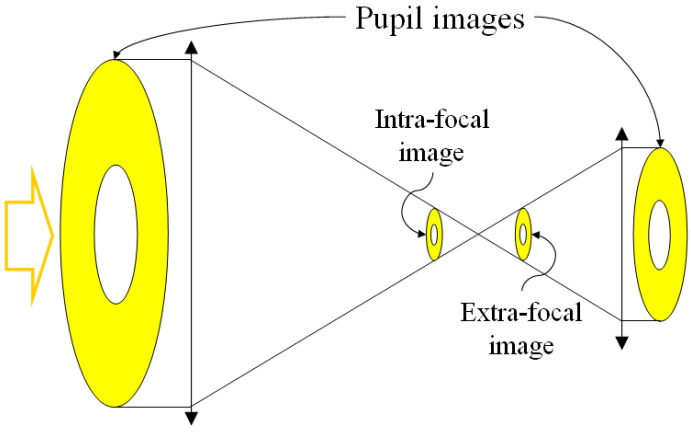

Figure 1.12: Curvature WFS concept.

The concept behind the curvature WFS is shown in Figure 1.12, where the so-called *intra-focal* and *extra-focal* images are represented, corresponding to de-focused images of the source. Considering the geometric optics approximation, a positive curvature wavefront produces an

intra-focal image (which is retrieved before the focal plane, along the optical axis) which is brighter than the extra-focal one (imaged after the focal plane. On the contrary, a negative curvature wavefront translates into just the opposite effect. The curvature WFS takes advantage of such dependency of the de-focused images intensities from the curvature of the incoming wavefront.

Two detectors are positioned at the extra-focal and the intra-focal images (a beam splitter can be used to separate two channels) and the acquired images are compared. The normalized difference between the intensities of the intra-focal and extra-focal images is proportional to the wavefront Laplacian:

$$\frac{I_i(r) - I_e(r)}{I_i(r) + I_e(r)} \propto \nabla^2 W \tag{1.14}$$

where I_i and I_e are the intra-focal and extra-focal images intensities, respectively, W is the wavefront and ∇^2 the Laplacian, corresponding to the divergence of the gradient of the field to which it's applied.

It is possible to realize a curvature WFS using only one detector, positioned in a pupil plane, and avoiding the splitting of the light.

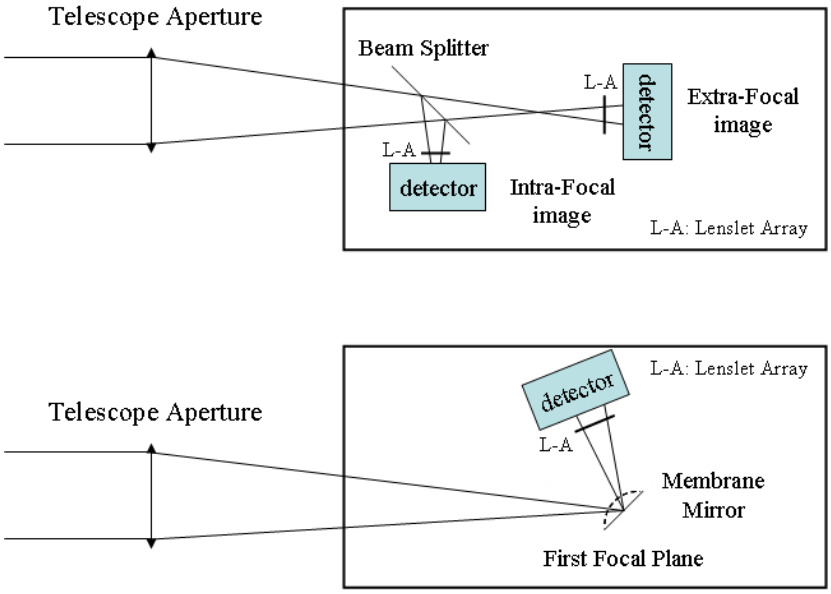

Figure 1.13: Curvature WFS realization. *Top*: configuration with a beam splitter allowing the separation of two channels for the intra and extra-focal images. *Bottom*: a membrane mirror is inserted on the focal plane of the system, in order to alternatively increase and reduce the optical path before a lenslet array (L-A) spatially sampling and focusing the beam on a detector.

In Figure 1.13, if a weakly divergent lens is positioned on the focal plane, the pupil plane is slightly shifted toward the detector, while if a convergent lens is inserted the pupil plane moves in the opposite direction. If, then, a lenslet array is positioned in the pupil plane, focusing on a detector, and a positive and a negative lenses are alternately inserted in the focal plane before the array, with a frequency which is twice the Greenwood one, the detector will alternately acquire an intra-focal and an extra-focal image. Since the observable of such

a system is the total intensity of the spot, photon counting detectors can be used. The same result can be obtained without the introduction of mechanical arms or wheels inserting and removing the lenses on the focal plane at a sufficiently high frequency, since it is possible to fold the beam positioning a reflecting membrane, vibrating at the Greenwood frequency, in the focal plane. Such a membrane will alternately act as a positive and negative lens. Obviously, the detector should acquire images at a frequency equal to $2f_G$, that is to say about every 5 ms. Since the pupil plane is sampled by the lenslet array, the comparison of the intensities can be done in corresponding intra and extra-focal images of the spot produced by the light selected by a sub-aperture, to compute the high order deformation. The main difference with respect to the previously described WFSs, as already said, is that the curvature WFS measures the wavefront curvature inside each sub-aperture, so the retrieved information is about the second derivative of the wavefront shape.

The difficulty in positioning a large number of detectors in a quite small space limits the number of sub-apertures sampling the pupil. Consequently, the curvature WFS cannot retrieve very high order aberrations. Moreover, such WFSs are insensitive to the mean tip-tilt of the wavefront, since its second derivative is zero. On the other hand, the curvature WFS presents the advantage with respect to the SH WFS of allowing a tuning of the system gain, by simply changing the membrane vibration amplitude.

Pyramid wavefront sensor

The idea of using a refractive pyramid to split the light in the focal plane of a WFS was first proposed by Ragazzoni [19] and has been validated and applied in the past years to several working systems, used at TNG, VLT and Calar Alto Observatories, up to the recent results of the first light AO system at LBT [6]. The concept is quite simple, and it is based on the Foucault knife-edge test, introduced in 1858 by L. Foucault to measure conic shapes of optical mirrors and then used for more than a century to determine longitudinal and transverse aberrations which affect an optical system [10].

In the Pyramid wavefront sensor, a square-based refractive pyramid, positioned on the system focal plane at the location of the reference star image, splits the light into four beams (namely the four areas of a Quad-Cell WFS) which are then re-imaged into four pupil images on a detector. The four pupils are separated if the objective focal length is properly tuned with the pyramid vertex angle; the distance between the centers of the pupils ($d_{centers}$) can be retrieved as follows:

$$d_{centers} = \beta(n-1)f_{obj} \tag{1.15}$$

where β is the pyramid vertex angle, as defined in Figure 1.14, n its refraction index, and f_{obj} the objective focal length.

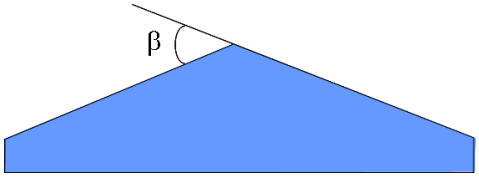

Figure 1.14: Pyramid vertex angle definition.

Once the light coming from the reference star is divided into 4 beams, the tip-tilt signal

is computed exactly as described for the quad-cell WFS, comparing the intensities of the 4 pupil images.

One of the Pyramid WFS advantages is that, since 4 pupils are re-imaged on a detector, as shown in Figure 1.15, the wavefront sub-apertures are defined at the level of the CCD. In particular, if four corresponding sub-apertures are defined onto the 4 pupil images (corresponding to the colored squares in Figure 1.16), the local tilt can be retrieved in the selected sub-aperture, using the usual analytic expressions for S_x and S_y. It can be done because the light corresponding to the considered sub-aperture is divided into 4 parts by the pyramid. In such a way, the high order wavefront reconstruction can be performed.

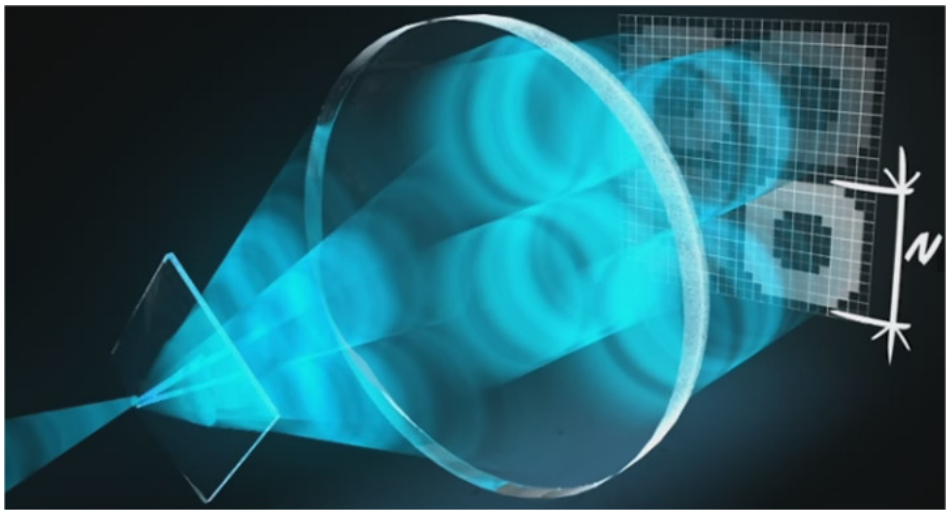

Figure 1.15: Pyramid wavefront sensor concept. Picture credits: Marco Dima

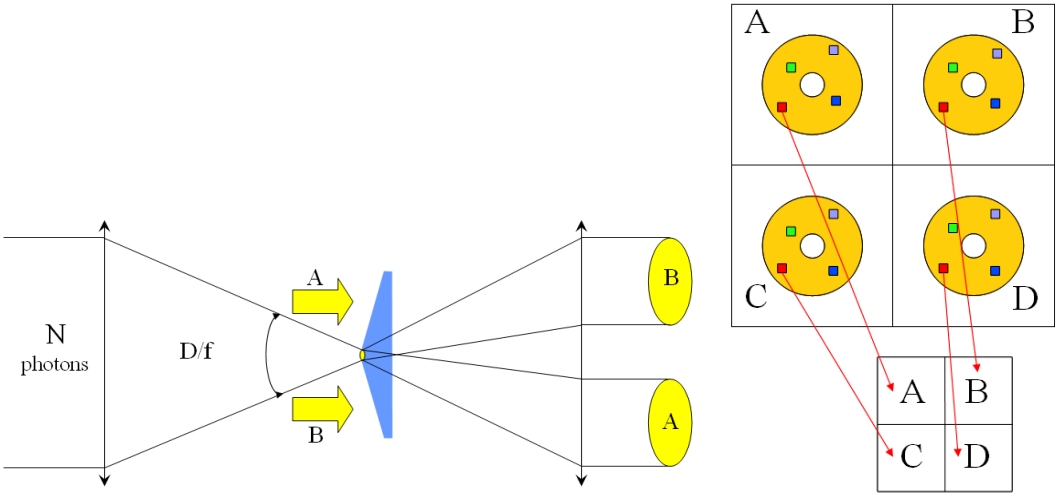

Figure 1.16: Four pupil re-imaging in the pyramid WFS. The tip-tilt can be computed for the overall aperture or,using the same expressions, the local tilt of a sub-aperture on the pupil.

Another advantage of the pyramid WFS is given by the Poisson error reduction with respect to a Shack-Hartmann WFS. The spot dimension on the pin of the pyramid, in closed

loop, is λ/D so, the associated error will be:

$$\epsilon_{P_{tilt}} = \frac{\lambda}{D} \cdot \frac{1}{2\sqrt{M}} = \frac{\epsilon_{SH_{tilt}}}{N}$$

where λ is the working wavelength, D the telescope diameter, M the number of incoming photons, N the number of lens in the SH array, sampling a pupil diameter, and $\epsilon_{SH_{tilt}}$ the SH WFS Poisson error, as retrieved in 1.13.

Additional advantages:

- The Gain can be varied. When the AO system is activated, the DM is guided by the electronics accordingly to the information retrieved by the WFS, up to the loop closing, when the spot dimension on the pin of the pyramid, starting from the seeing-limited value of $\theta_{seeing} = \lambda/r_0$, tends to its diffraction-limited value $\theta_{dl} = \lambda/D$. Because of this reason, the WFS sensitivity to the spot movements (i.e. the tilt, being it global or local) increases, allowing a wider dynamical range in the first AO iterations and a higher sensitivity when the loop is closed. Moreover, when the loop is closed, the SNR increases considerably, consequently translating into an increasing of the theoretical limiting magnitude of the WFS [20].

- Since the spatial sampling is done at the level of the detector, it's easy to change the number of sub-apertures, accordingly to the seeing value. The real gain in this can be achieved when a detector allowing a direct rebin of the pixels before the charge reading is used, since it can considerably reduce the Read-Out Noise. In this case, a rebin matching the sub-apertures dimension can be chosen, to optimize the sampling accordingly to r_0, dividing the pupil image into D/r_0 sub-apertures and minimizing the RON;

- The pyramid and the pupil re-imager are quite easy to be aligned to the CCD, if compared to a whole lenslet array.

The pyramid WFS concept has been applied all to the WFSs inside LINC-NIRVANA, as described in Chapter 2.

1.4 Multi-Conjugated Adaptive Optics

The main limit of the classical adaptive optics is the size of the corrected field of view. The light coming from the science target and the reference star goes through slightly different cylinders of atmosphere before reaching the telescope entrance pupil and undergo different distortions, mainly when very high strong turbulent layers are present. This effect is called *angular anisoplanatism*. Because of this limitation, the reference object is required to be very close to the science target. Of course the smaller the corrected FoV, the more difficult to find a suitable reference (for classic AO the typical limiting magnitude is $\sim 15 - 16$ mag). This finally limits the sky coverage which can be achieved with classical AO systems, barely reaching $\sim 5\%$. In each case, it is not possible to correct for a considerably wide FoV, which is a limit for several science cases. The Multi-Conjugated Adaptive Optics (MCAO) technique was initially introduced by Beckers in 1988 [1] and it is based on the concept of using more

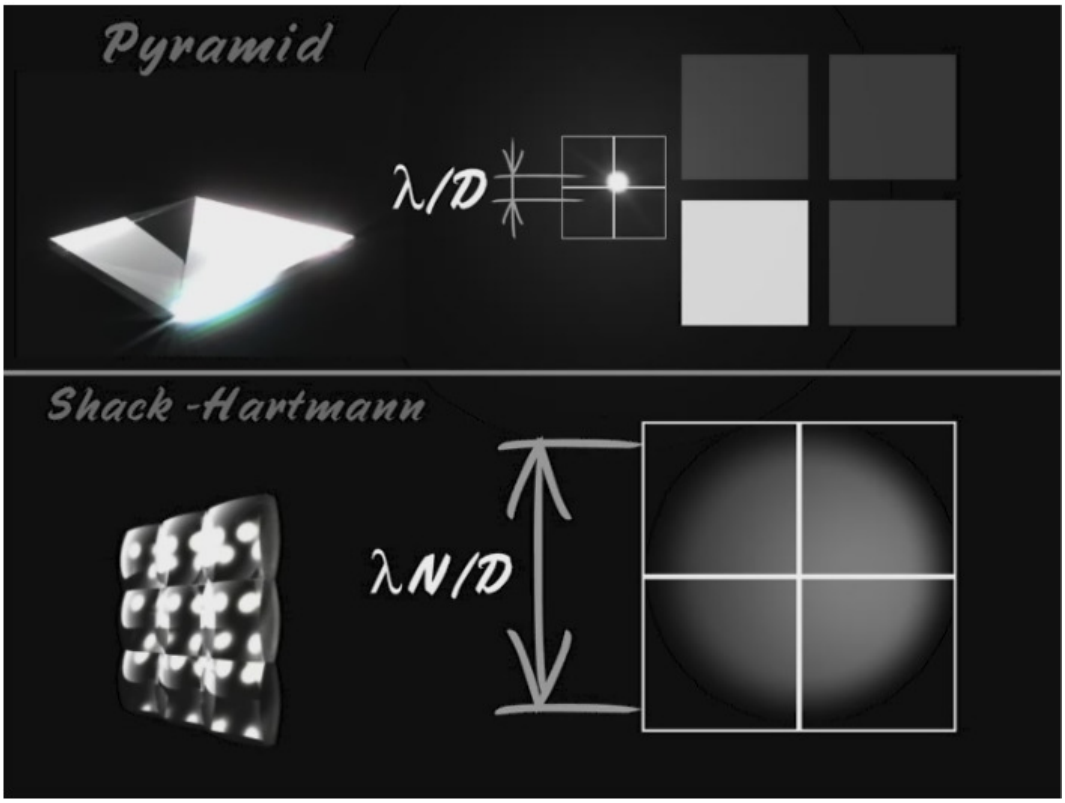

Figure 1.17: Comparison of Pyramid and SH wavefront sensors sensitivities. Picture credits: Marco Dima

than one guide star as a reference, to sense the turbulence effect in various directions, to obtain a 3D map of the atmospheric perturbation.

The single guide star observation (that is to say a small FoV) gives a depth of focus which is infinite, while if more references are used at the same time the FoV increases and, consequently, the depth of focus decreases. Because of this reason, an MCAO WFS allows to focus at a given altitude and sense the turbulence inside a limited atmospheric layer. Consequently, more than one DM can/must be introduced in the system to correct the perturbations introduced by the atmosphere at different heights. Ideally, a DM would be required for each atmospheric layer to be sensed and whose effects need to be corrected, but of course this is limited by complexity and cost constraints. Generally speaking, however, each astronomical site is characterized by the presence of some strong turbulent layers whose heights are mapped by site testing before the AO system optical design is realized. Of course, a continuous component is present too, together with many weak peaks in the C_n^2 profile. In each site, however, the Ground Layer is the strongest one, introducing the main part of aberration on the incoming wavefronts.

The conjugation heights of the DMs are independent from the WFS choice and are selected in order to minimize the residual of the atmospheric perturbations after a perfect AO correction; because of this, the DMs' conjugation heights do not necessarily coincide with strong turbulent layers, but can be located between them.

1.4.1 References

Generally speaking, the scientific target cannot often be used as a reference since it usually is too faint. On the other hand, it is not granted that guide stars with a high SNR can be found inside the isoplanatic angle, θ_0 (note that this value depends also on the working wavelength), centered on the science target. In classical AO systems, reference stars with a brightness higher than about 16 magnitudes are needed (this value fine tuning depends on the WFS concept and design). These constraints lead to a limited sky coverage, that is to say the fraction of the whole sky in which the classical AO systems can work granting a high Strehl Ratio corrected image. Obviously, the sky coverage changes in different areas of the sky, since the probability to find a suitable reference depends on the galactic coordinates of the region which is considered. In particular, the lowest sky coverage occurs at the galactic poles (0.1% in the V-band and 0.5% in the K-band), since the statistical density of stars is lower than in all the other directions. On the other hand, the maximum sky coverage will be given for the galactic equatorial areas (1% in V-band and 4% in K-band).

The main adopted solutions to increase the sky coverage are listed in the following:

- to create an artificial reference at the required position in the sky. These are the so-called Laser Guide Stars [8], for which two kinds of source can be adopted:
  - Rayleigh LGS: a laser beam is sent in the lower part of the atmosphere ($\sim$ 20 km) and the back-diffused light emitted because of Rayleigh scattering is observed as a source.
  - Sodium LGS: a $\lambda = 589\,nm$ laser beam can excite the sodium molecules which can be found in a particular atmospheric layer situated at about $\sim$ 90 km height; the Sodium molecules emit at the same wavelength, creating an artificial source.

  The LGSs are subjected to some not-negligible limitations. First of all, they're not sensitive to tip-tilt, since the laser beam, during it's path starting from the laser (on the ground) and finally reaching the detector (on the ground, again), goes twice through the same part of atmosphere in a time interval which is lower than the mean time scale of the variation of mean inclination introduced by the atmosphere to the wavefronts. The resulting tip-tilt is close to zero (only differential tilts can be retrieved). This has always been clear for the tip-tilt, but recent studies made on real LGS systems, which are under construction or already working at the moment for the Extremely Large Telescopes, reveal that such problems have to be extended to all the low order aberrations, at least up to the tenth Zernike polynomial. Moreover, because of the finite altitude of the source, the WFs which reach the telescope are not approximately flat but still spherical (also without considering aberrations) and they cross a conical atmospheric portion which is not covering the whole cylinder which is affecting the science target wavefronts (cone effect). In addition, the Sodium layer which is excited to form the laser source is about 10 km thick (thickness varying with time), resulting into an elongated source, which is not point-like anymore, as shown in Figure 1.18. Finally, telescopes are not designed to focus at 10-100 km, and this fact introduces large static aberrations which, even if they can be characterized and removed from the retrieved wavefront shape, can saturate the WFS.

- To use more than one reference star (also LGSs): properly combining the light coming from different guide stars, it's possible to achieve a good correction over a wide FoV,

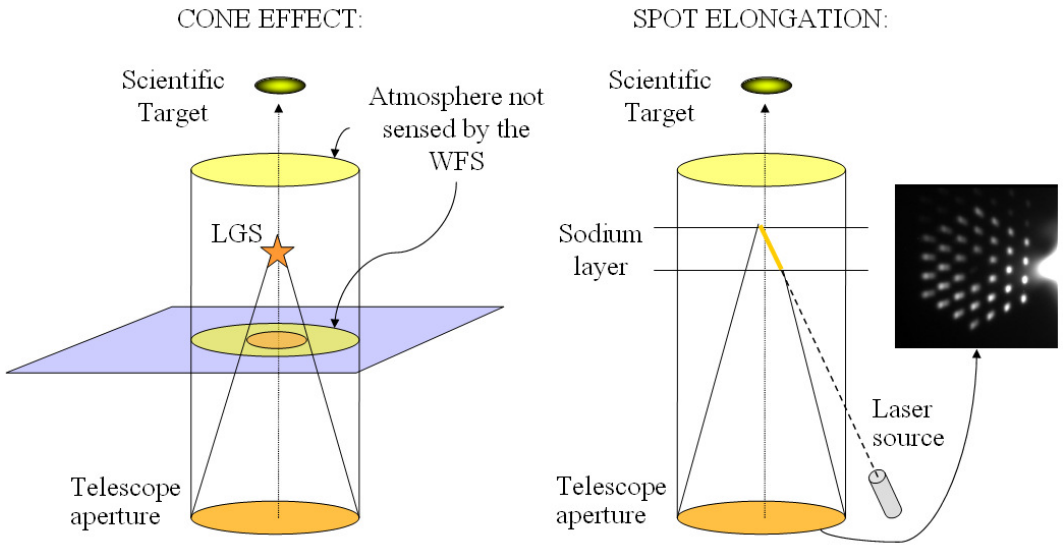

Figure 1.18: Conceptual representations of the cone effect and the spot elongation effect, to which the LGSs are subjected. On the left, the different portions of atmosphere sensed by the WFS and passed through by the science target light are shown. On the right, a schematic view of the LGS elongation problem is shown, together with a typical spot array (in SH WFS mode) of a Sodium LGS on a segmented telescope (Keck I).

since the light coming from the references allows the sensing of a wide volume of atmosphere, up to the maximum height at which the atmosphere is considered to introduce a non-negligible perturbation. In Figure 1.19 the telescope entrance pupil projections in the references directions are shown to partially overlap up to the higher turbulent layer, covering the whole metapupil (the projection of the entrance pupil of the telescope, considering the FoV to be corrected, at a given height). In such a way, the needed information on the whole volume of atmosphere passed through by the light coming from the scientific FoV can be retrieved. In Figure 1.19, the Natural Guide Stars (NGS) case is shown. However, the same concept can be used also for LGSs, which can be put in the FoV in the needed configuration. Obviously, the number of LGSs needed to cover the whole metapupil is higher than the one of NGSs, because of the cone effect.

Let's now consider a practical example. Each of the arms of the LBT has a primary mirror 8.4 m wide, with an entrance pupil of 8.25 m in diameter. Considering a FoV of 2' to be corrected and a maximum turbulent layer height of 10 km, the metapupil enlargement at 10 km for a 2' FoV is 5.82 m, resulting in an overall metapupil $\sim$14 m width. Once the FoV is fixed, the larger is the entrance pupil of the telescope, the better the superposition between the atmospheric cylinder passed through by the light coming from the reference stars.

If a complete sensing of the metapupil at 10 km of height is required, the 14 m metapupil has to be completely filled with the entrance pupil projections, in the guide stars directions.

In Figure 1.20, (a), the 14 m metapupil filling, optimized in a way to minimize the number of references, is shown. It is clear that at least 6 guide stars are required. To completely fill the larger metapupil (17 m wide), forming at 15 km of height (Figure 1.20, (b)), at least 7 references are required. Generally speaking, when NGSs are used, the probability to find a

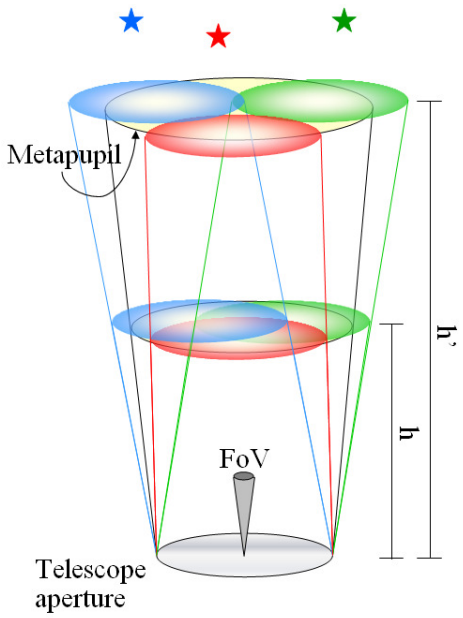

Figure 1.19: Telescope entrance pupil projection in the directions of several NGSs. One can see how, for high atmospheric layers, the scientific field pupil projection (the metapupil) is barely covered by the pupil projections in the NGSs directions. The last completely sensed layer is at an height **h**. For higher layers, the metapupil is no more covered.

large number of references in the required FoV is quite low and decreases when a constraint on the asterism (that is to say the guide stars disposition inside the FoV) is introduced. Because of this, the number of NGSs needed to fill the metapupil will often be larger than the theoretical minimum. If the references are LGSs, on the contrary, their number can be optimized, since their asterism is defined ad hoc.

1.4.2 Wavefront Sensors for MCAO

There are two different approaches to the Multi-Conjugated Adaptive Optics concept: *star-oriented* (SO) and *layer-oriented* (LO).

The star oriented technique consists of a set of WFSs, each sensing the light coming from a different reference star. In other words, optically speaking, the characteristics of each WFS are the same as a classical AO WFS. The limiting magnitude of the references, for example, is the same required for the classical AO technique. The information on the incoming wavefronts (both tip-tilt and high orders) obtained by the WFSs are combined together to retrieve the 3-dimensional properties of the atmosphere, through linear reconstruction algorithms converting, by convolving the computed data with the metapupil shape, the WFSs measurements into signals to be sent to the DMs.

The WFSs synchronization is quite easy to be reached, but the huge amount of acquired data requires a non-negligible computation time, together with a high computation power of the wavefront computer.

In the layer-oriented technique, each WFS retrieves its information from all the reference stars and guides a dedicated DM, which is conjugated at the same height as the WFS itself.

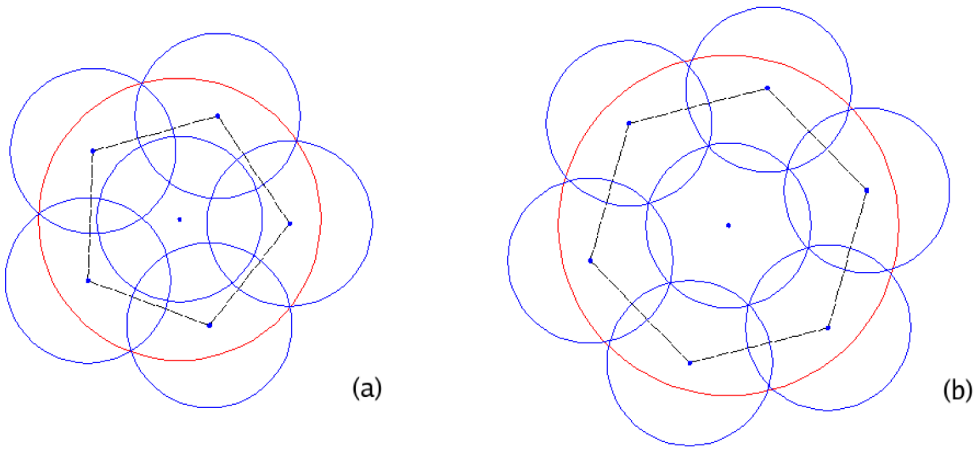

Figure 1.20: Metapupil filling for a telescope with an entrance pupil 8.25 m wide (as LBT), considered in the case of a 10 km (a) or a 15 km (b) height. In red, the entrance pupil projection is shown for a 2' FoV (metapupil). This metapupil is completely filled by the projections of the entrance pupil in the directions of the reference stars.

This can be done only when pupil plane WFSs are used (that is to say, WFSs in which the detector is positioned at the level of a pupil image), like the pyramid WFS.

Optically, the light coming from each of the four faces of the pyramids, is superimposed (by properly align all the pyramids vertices) on four common pupil images in the pupil plane. The detector of each WFS is then moved along the optical axis in order to focus at the height to which the corresponding DM is conjugated, in order to retrieve only the perturbations introduced by the layers of interest [21]. On the Ground-layer Wavefront Sensor (GWS), four circular images of the entrance pupil of the telescope will form, while on WFSs conjugated to higher layers the images of the corresponding union of the pupil projections in the reference stars directions will be focused, as shown in Figure 1.22.

This approach grants all the advantages given by the use of refractive pyramids listed in Section 1.3.2 and requires a lower number of WFSs, corresponding to the number of DMs,with respect to the star-oriented technique. This method introduces also an additional advantage, which is the optical superimposition of the light on the wavefronts, allowing to increase the SNR and reduce the overall RON, since only one detector has to be readout. The optical sum of the light coming from all the references also allows fainter guide stars, increasing the limiting magnitude, together with the sky coverage.

The main advantage of the layer-oriented approach, however, is the possibility to tune the temporal and spatial sampling to match the atmospheric parameters, according to the conjugation height of the WFS, characterized by a certain r_0 and wind speed. This fact can introduce a further increasing in the SNR, avoiding oversampling, since the Fried parameter, for example, can vary by an order of magnitude between different turbulent layers. Moreover, in the LO technique, each WFS is separately closing the loop, as in the classic AO, with a dedicated DM, while the SO technique requires for a complete 3D reconstruction of the atmosphere, with the higher time and spatial sampling, but only a fraction of the retrieved information is then translated into signals for the DMs. Because of this reason, the gain concerning the computation complexity reduction is huge.

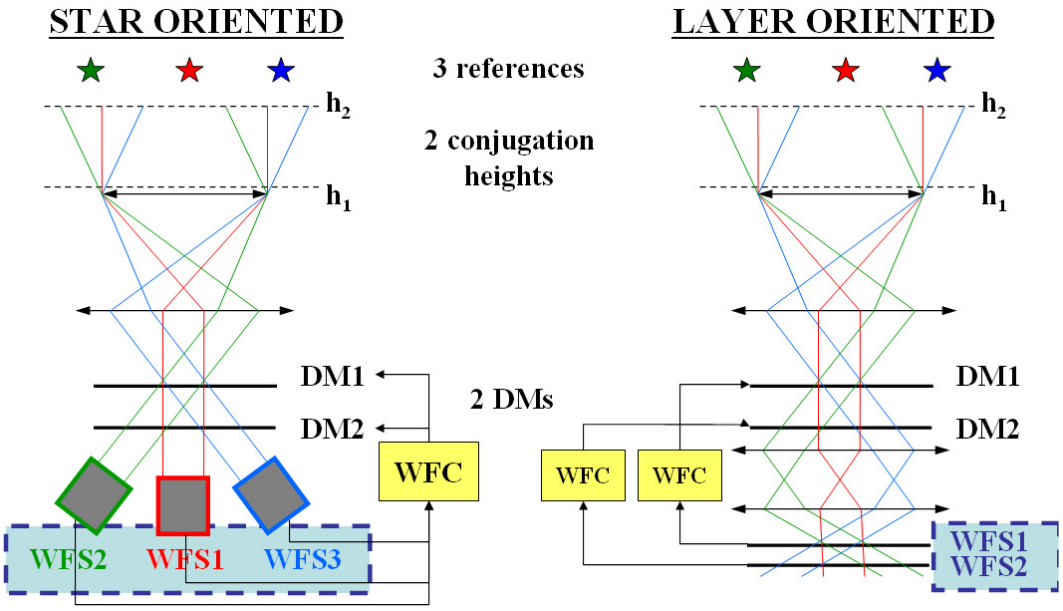

Figure 1.21: A schematic comparison between the star-oriented and the layer-oriented approaches is shown. The Star-oriented concept is shown on the left, where each of three WFSs is looking at a different guide star. The wavefront computer computes the 3-dimensional structure of the whole atmospheric volume which is crossed by the light coming from the references, with the temporal and spatial sampling which is required by the most turbulent layer considered. On the right, the layer-oriented technique is shown, in which the light coming from all the references optically superimposes on to two different WFSs, sensing the aberrations introduced on the wavefronts at a pre-determined height, with the sampling which is required by the atmospheric parameters characterizing each layer. In both cases, the computed reconstruction instructions are sent to two DMs.

LO approach limitations are due to different aspects, some of which can be overcome. Since the FoV size in the focal plane and the metapupil images diameter on the detector are inversely proportional one to each other, the increasing in the FoV would require either for wide re-imaging optics or very big detectors, characterized by high readout time, up to not reach the required time sampling. Finally, in MCAO systems it is necessary to separate the light to be sent to the various WFSs and this can be easily done introducing beam splitters, but decreasing the number of photons reaching each WFS, which translates into a SNR decreasing. To split the light coming from the references in a more convenient way, the Multiple Field of View approach has been introduced.

1.4.3 Multiple Field of View Concept

As already mentioned, the layer-oriented technique raises the need to slit the light coming from the reference stars, in order to feed all the WFSs, possibly without decreasing the SNR. A possible solution, implemented in LINC-NIRVANA for LBT, is based on the different superposition of the pupil projections in the directions of the references, accordingly to the conjugation height of the WFS. Such superposition is perfect on the entrance pupil, to which

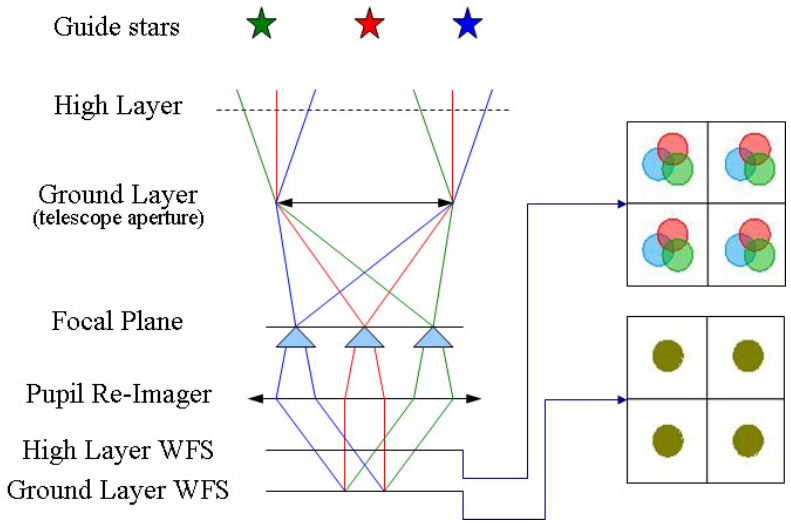

Figure 1.22: Layer-oriented concept with pyramid WFSs.

the Ground layer Wavefront Sensor (GWS) is conjugated, while it decreases for WFSs conjugated to higher and higher layers. The increase in the FoV, inside which a higher number of NGSs can be selected, in order to collect more photons and increase the SNR, translates into a gain in terms of photon density only up to a critical angle, quantified by Ragazzoni [20] as $\theta_\gamma = D/h$ (where D is the telescope aperture diameter and h the maximum height of the considered turbulent layers), above which the photon density tends to stabilize, because for a further FoV enlargement, the telescope pupil projections in the reference stars directions do not overlap anymore and the increasing collected photon number is divided for an also increasing surface.

Please note, however, that considering only the ground layer the critical angle $\theta_\gamma \to \infty$ because the height $h \sim 0$. that is to say that NGSs can be selected in a very wide FoV. This is quite easy to understand, since, for each observed source, the deformation introduced by the ground layer onto the wavefronts is the same, because all the pupil projections (being so close to the actual pupil stop) are perfectly superimposed. Because of this reason, it is possible to retrieve the information about the perturbation introduced in the lower part of the atmosphere looking at references quite far from the science target, which cannot be used for sensing the higher layers, as shown in Figure 1.23.

Another relevant issue is the depth of focus. If a zero FoV was observed, each point along the optical axis would be focused during the observation, that is to say that the depth of focus would be infinite. While the FoV is enlarged, instead, the depth of focus decreases, causing a WFS being sensitive to each scale perturbations introduced at the conjugation height, but only to the large scale distortions introduced by upper and lower layers, since the WFS is not focused on them. This is called *FoV vs thickness rule*. We know that, for each astronomical site, the ground layer is the volume of atmosphere introducing the strongest aberrations on the wavefronts, so it will be for sure conjugated to one of the DMs of the system.

Given such concepts, the *Multiple Field of View* (MFoV) method consists in dividing the light coming from references situated in different FoVs between different WFSs, taking advantage of the LO technique. Considering the LINC-NIRVANA case as an example, the stars in the inner 2' FoV can be used as references for the MHWSs, while a wider 2'-6' annular

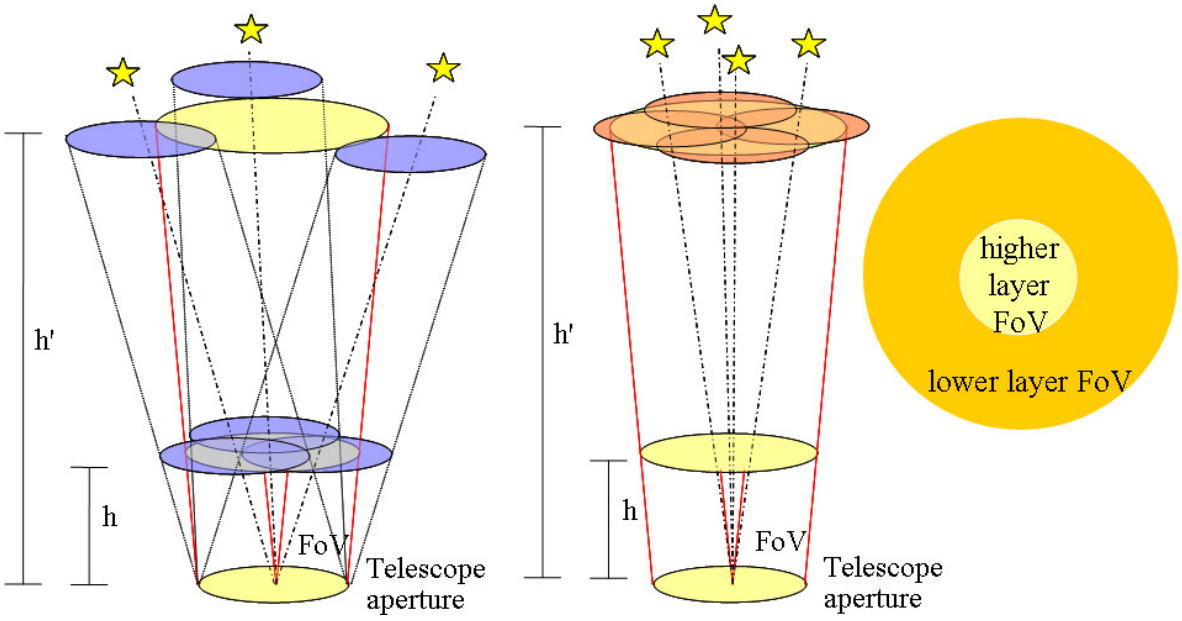

Figure 1.23: *Left*: the metapupil at height h is fully filled by telescope pupil projections in the directions of 3 references very far from the FoV to be corrected; the same projections at a height h' are completely out of the metapupil. *Center*: the metapupil at a height h' is completely filled with telescope pupil projections in the directions of 4 guide stars, selected in a smaller FoV. *Right*: the FoV areas dedicated to the NGSs search for different layers are shown.

FoV is used to select the GWSs guide stars. No beam splitters are then introduced.

In such a way, the limit imposed by the critical angle θ_γ are respected. The GWSs correction is limited to the lower part of atmosphere (a quite thin layer) but it can take advantage of the light coming from a statistically higher number of references, since its FoV is wider, while the MHWSs will be conjugated to a higher height but they will retrieve some information on the wavefront distortion introduced also by the turbulent layers just above or below the conjugation height.

1.4.4 Ground-Layer Adaptive Optics

There is also another AO technique which can be used, considering only the correction to be applied to remove the aberrations introduced in the lower part of the atmosphere, so-called *Ground Layer Adaptive Optics* (GLAO). As we already mentioned, the ground layer usually introduces the main part of the overall perturbations on the incoming wavefronts. Moreover, in some peculiar astronomical sites (such as the Antarctic) the high layers effect is quite negligible. In the other cases, however, a ground-layer-limited correction can be used to considerably reduce the PSF diameter, even if the diffraction limited performance will not be achieved. Because of this, a GLAO system is also known as *seeing reducer*.

As said for the MFoV approach, a GLAO WFS FoV can be very wide, since the distortion introduced by the ground layer on the incoming wavefronts is the same for sources which are very far one from the other. Theoretically speaking, a few well-separated (to focus only on the ground-layer turbulence) NGSs would be enough to retrieve the signal to be sent to

the DM applying the correction, even to correct a quite wide FoV, but an higher number of references allows to take advantage of the optical superposition of the light, increasing the SNR.

The WFS is conjugated at a height just above the telescope entrance pupil and it collects the light coming from the references, re-imaging perfectly superimposed pupils; this allows for a uniform correction over the whole FoV, translating into a uniform PSF. There are several science cases for which a uniform PSF in the FoV is preferable to a very high SR, achieved only in some small areas and strongly varying inside the FoV.

Figure 1.24 shows a comparison between SR maps obtained with a classical AO system (*Single Reference Adaptive Optics*, SRAO), with a GLAO approach and with an MCAO corrector (obtained with MAD, *Multi-conjugate Adaptive optics Demonstrator*, applied to UT3 at VLT). It is clear that the first case correction is really high close to the reference star ($SR > 40\%$), but it goes down below 15% at $\sim 15''$ distance from it. The obtained SR for the central part of the FoV to be corrected is $SR < 5\%$. In the MCAO case, on the right of the picture, the contribution of the 3 NGSs sums up, giving a higher correction on the whole FoV. The 3 NGSs GLAO case, instead, does not allow to reach the very high SR which can be achieved in the other cases, but if a quite large 1' FoV is considered, the Strehl Ratio is always in the range $10\% < SR < 25\%$, giving a more uniform PSF all along the FoV.

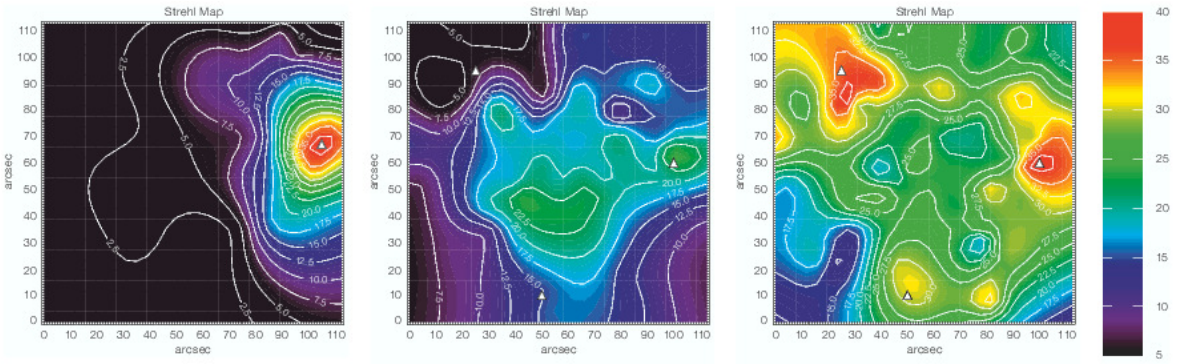

Figure 1.24: Comparison between the SR maps obtained with MAD for SRAO, GLAO and MCAO approaches (from left to right), with the same *seeing*. Credits: C. Arcidiacono.

1.5 Wavefront reconstruction

To correct the wavefront shape, first of all a conversion matrix from the signal sent to the DM and the actual deformation which is reached (that is to say the influence function of the DM) must be computed. Let's consider now a continuous deformable mirror, equipped with actuators on the back of the surface, to modify its shape, like in the LBT DMs. LINC-NIRVANA will use 4 DMs to correct the WF aberrations. The Adaptive Secondary Mirrors (ASM) of LBT will be coupled with the Ground-layer Wavefront Sensors (GWSs), sensing the ground turbulence, and two other commercial piezo-stack mirrors will be conjugated to a 7.1 km height, and guided by the Mid-High Wavefront Sensors (MHWSs). LBT ASMs actuators are, actually, solenoids, coupled with magnets placed on mirror lower surface. Each solenoid creates a magnetic field when driven with electrical current, and the force moving the mirror is created by a gradient in the magnetic field (non-linear). The mirrors conjugated

to the mid-high layer are commercial Xinetics DMs, equipped with Piezo-stack actuators, each consisting of a stack of PZT (lead zirconate titanate) ceramic disks, getting thicker or thinner when a proper electrical potential difference is applied. The overall displacement is linear in voltage. Several other types of DMs exist, some of which are already implemented inside working AO systems (e.g. bimorph mirrors), and others, taking advantage of more exotic new technologies, are under study at the moment (e.g. voice coils and liquid crystals).

Generally speaking, the conversion matrix can be realized measuring the effect of the pushing and pulling of an actuator on a flat incoming WF, sensing the WF shape at the pupil image level (zonal approach); such a procedure must be repeated for each actuator of the DM. The interaction matrix can be obtained by inverting the conversion matrix, to translate the deformation detected by the WFS into a signal to be sent to the DM.

The WF deformation can also be described through the linear combination of analytic expressions:

$$W(x,y) = a_0 Y_0(x,y) + a_1 Y_1(x,y) + ... = \sum_{i=0}^{N} a_i Y_i(x,y) \tag{1.16}$$

where x and y are the spatial coordinates on the pupil, Y_i are the analytic terms and a_i the linear combination coefficients. One of the main decomposition used in optics is the Zernike decomposition, in which the terms are polynomials (Z_n^m) separately describing the known optical aberrations. In polar coordinates the expression for the decomposition is the following:

$$W(\rho,\theta) = \sum C_n^f Z_n^f(\rho,\theta) \quad Z_n^f(\rho,\theta) = \rho^n \cos f\theta \tag{1.17}$$

where C_n^f are the linear decomposition coefficients and n and f are the radial order and the angular frequency, respectively. An advantage in using the Zernike polynomials is that each of them describes a known optical aberration, so they are useful also to detect system misalignments. Figure 1.25 show the main decomposition terms.

The WF reconstruction through polynomial decomposition is called the modal approach. To correct the WF shape in the modal approach, it's necessary to precisely know which actuators have to be push-pulled to reproduce each aberration shape at the level of the DM. A calibration phase is then required, to obtain an interaction matrix translating detected aberration amplitudes to signal to be sent to the deformable mirror.

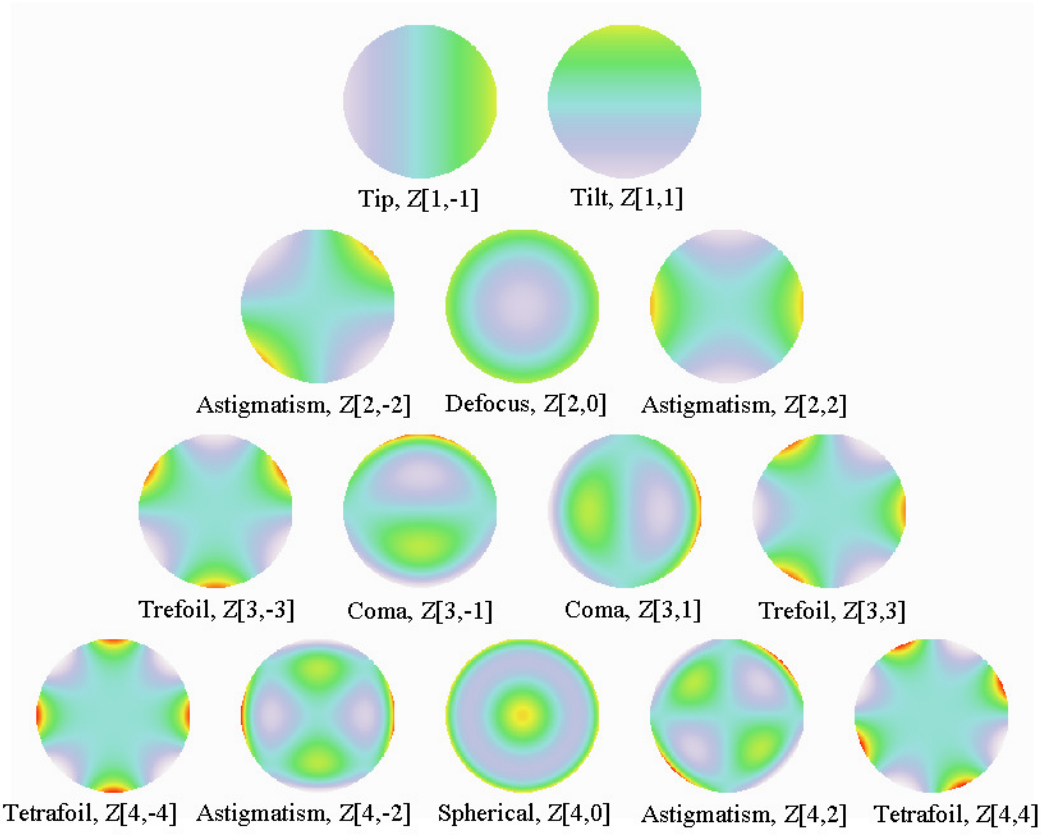

Figure 1.25: Graphical representation of the main aberrations described by Zernike polynomials.

Chapter 2

8m: LINC-NIRVANA and the GWS

LINC-NIRVANA (**L**BT **IN**terferometric **C**amera and **N**ear-**I**nfra**R**ed / **V**isible **A**daptive i**N**terferometer for **A**stronomy) is the near-infrared Fizeau interferometric camera for the Large Binocular Telescope, which has been developed and realized by a consortium of Italian and German institutes, composed of the LBTB (LBT Beteiligungsgesellschaft, a German consortium), INAF (the Italian Istituto Nazionale di Astrofisica), the University of Arizona and the Research Corporation [14]. The aim of the instrument is to acquire $10'' \times 10''$ FoV images [12], with an angular resolution equivalent to that of a 22.8m diameter telescope, taking advantage of the LBT interferometric configuration and acting as a testbed for AO systems to be applied to the future Extremely Large Telescopes (ELTs) [9]. The two apertures of the LBT, indeed, are equivalent to an 11.8 m telescope aperture in terms of collecting area, but their separation allows the possibility to achieve diffraction limited images with a 22.8 m spatial resolution. Since the telescope is ground-based, however, to achieve such a high resolution, Adaptive Optics techniques have to be employed to correct the effects of the seeing, due to the presence of the atmosphere.

This instrument is not only expected to acquire diffraction limited interferometric images, but, thanks to the Multi-Conjugated Adaptive Optics concept, will also correct a wide FoV. This technique, described in Section 1.4, allows for the correction of the wavefront distortions introduced by specific atmospheric layers. A set of wavefront sensors is used to sense the deviation from planarity of the incoming wavefronts, looking at the behavior of the light coming from reference objects on the sky. The MCAO, in particular, is characterized by the use of more reference stars at the same time, in order to increase the corrected FoV. In addition to that, the layer-oriented technique, described in Section 1.4, allows us to sense the distortions introduced by a certain atmospheric layer with a dedicated WFS. It is possible to combine more of these WFSs in order to optimize the wavefront correction, concentrating on the most turbulent layers or conjugating to a proper height between two or more turbulent volumes. The information retrieved by each WFS is used to drive a deformable mirror, conjugated to the same height as the sensor, properly deforming the light inside the instrument optical path in order to correct the atmospheric effects. The layer-oriented technique takes advantage of the optical superposition of the light coming from different NGSs, allowing the selection of fainter stars as references and increasing, in this way, the system sky coverage (reaching 90% at the Galactic equator and 10% at the North pole in the K band). The increase in the

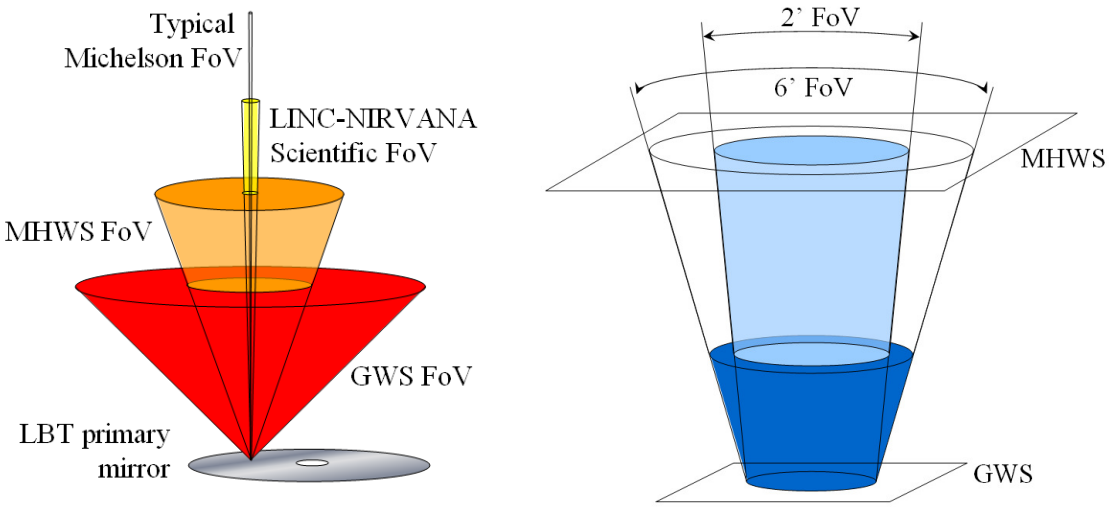

Figure 2.1: The Linc-Nirvana Multiple Field of View concept. The left image shows the different FoVs which are used by Linc-Nirvana: the 2′-6′ annular FoV, in which the GWS selects up to 12 reference stars, the inner 2′ FoV used by MHWS for the selection of other 8 references, and the 10" scientific interferometrically reconstructed FoV, compared with the smaller FoV typical of non-Fizeau interferometers (about 40 mas). The right image shows the effect of projection of one of the apertures of the LBT at different altitudes, at which the sensors are conjugated.

limiting magnitude of a single NGS allows us to select reference up to 20 mag, provided that the integrated magnitude is kept between 14 and 17 mag.

Linc-Nirvana MCAO system is also taking advantage of the Multiple Field of View technique [20] [7], according to which different WFSs are selecting Natural Guide Stars in different FoVs, in order to avoid the splitting of the light coming from a single reference between more sensors. Thanks to the fact that the isoplanatic angle is wider for a lower turbulent layer, a large annular 2′-6′ FoV in diameter is sent to the Ground-layer Wavefront Sensor (GWS), sensing the perturbations introduced by the atmosphere close to the telescope entrance pupil, while the inner 2′ FoV is used by the Mid-High Wavefront Sensor (MHWS) to sense the high altitude turbulence (Figure 2.1). The net result of such a choice is a gain in sky coverage, since fainter references can be selected as guide stars and a larger overall FoV is considered for the NGS search.

The system combines the light coming from the two 8.4 m primary mirrors in a Fizeau interferometric mode [13], which has the advantage that it gives the possibility of getting full imagery and a good coverage of the $u - v$ spatial frequency plane, after a proper restoration process. A restoration of the diffraction limited 10" square Field of View (FoV) image is necessary since the LBT has a binocular collecting area, consisting of two separated pupils, and so it delivers an image with an anisotropic spatial resolution, ranging from $\lambda/8.4$m up to $\lambda/22.8$m and rotating with respect to the sky. For such a reason, the high-resolution image of the astronomical 10" FoV will have to be recovered from a set of interferometric observations corresponding to different parallactic angles [4]. The advantage in terms of amount of data that can be achieved simultaneously by a full FoV interferometric image has to be paid with

a certain number of constraints, e.g. Point Spread Function (PSF) evenness all over the Field of View (FoV) and pupil homotheticity, to take into account in the design of such an interferometer [2].

2.1 Interferometry with the LBT

The Large Binocular Telescope (LBT) is situated on Mount Graham (Arizona), and is composed of two arms in a Gregorian configuration, realized with a 8.4 m primary mirror and a secondary mirror under-dimensioned to minimize the IR thermal background, reducing the entrance pupil to a 8.26 m diameter. The sum of the two apertures is resulting in a total collecting area of / 110 m^2, supported by a common alt-azimuthal mount. The main parameters and technical characteristics of the Telescope are listed in Table 2.1.

Table 2.1: The LBT main parameters and technical characteristics

Weight		700 t
Height	telescope	25 m
	dome	52 m
Mount		alt-azimuthal
Primary mirrors	Center-to-center distance	14.4 m
	Diameter	8.4 m
	Focal Ratio	F/1.14
	Central obstruction diameter	0.889 m
	Edge thickness	0.89 m
	Weight	16 t
Secondary mirrors	Diameter	0.91 m
	Re-dimensioned pupil	8.25 m
	Focal Ratio	F/15
	Thickness	1.6 mm
	Actuators #	672/mirror
Tertiary mirrors	Major axis	0.64 m
	Minor axis	0.5 m
Theoretical angular resolution	V band	0.004”
Pointing precision		0.3”
Operating conditions	wind up to	80 km/h
Temperature working range		$-10°C \div 25°C$

Since the very beginning of its design, the LBT has been conceived to work interferometrically, thanks to the peculiar shape of its pupil, consisting of two separated apertures. It is equipped with three central interferometric stations, in which the light coming from the two apertures can be combined.

The LBT has been designed to work in different operation modes:

- individual beam mode: each arm of the LBT is acting as a single 8.26 m diameter telescope;

- incoherent beam combination mode: the beams are superimposing in a incoherent way, giving a resolving power of an 8.26 m pupil combined with the collecting area of a 11.8 m diameter circular aperture;

- Fizeau coherent beam combination mode: the light coming from the two apertures is coherently combined in an interferometric mode, resulting in a spatial resolution corresponding to the one of a 22.8 m diameter telescope.

- Bracewell nulling mode: the wavefronts from two telescopes are superposed so that at one of them the path difference is exactly half a wave. This method is used by LBTI to suppress the image of a star in order to detect and distinguish the light coming from other small objects close to the star itself (planet finding).

The LBT structure is particularly indicated for Fizeau interferometry, the concept behind Linc-Nirvana optical interferometric design. In Figure 2.2, the Fizeau interferometer concept is compared with the Michelson one; the two configurations are completely different and well-suited for instruments with different characteristics.

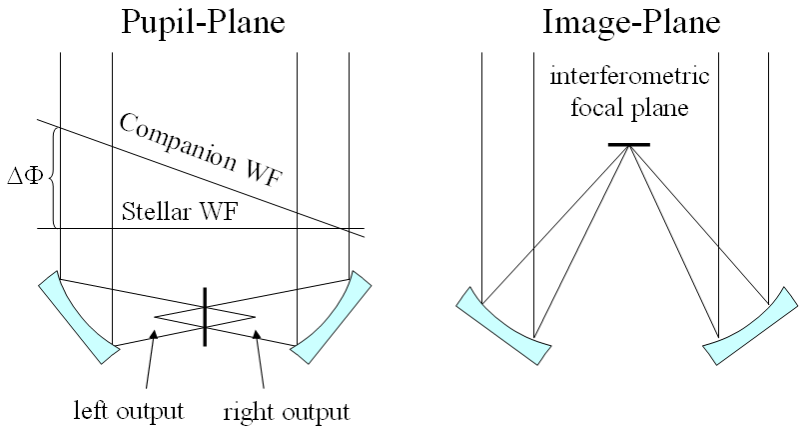

Figure 2.2: Comparison between two different interferometric configurations. On the left, a Michelson (or *pupil plane*) interferometer, in which the light beams combine on the pupil plane, and on the right a Fizeau (or *image plane*) interferometer, in which the interference fringes form in a common focal plane.

In a Michelson interferometer the light combination of the beams occur on a pupil image. To describe the characteristics of the so-retrieved images let's consider a point-like source. A star produces an image on the pupil plane, characterized by a modulation of the intensity as a function of the optical path difference (OPD) of the light coming from the two apertures. In this case, the observable, through which the information about the sources disposition on the FoV is retrieved, is the so-called *visibility*:

$$V = \frac{I_{max} - I_{min}}{I_{max} + I_{min}}$$

where I_{max} and I_{min} are, respectively, the maximum and minimum intensities of the interference pattern. The limit of such a type of interferometer is that it is quite time consuming,

since it allows to retrieve the objects distribution a spatial frequency at a time. Michelson interferometry poses no limits to the baseline length, so it can, in principle, reach an unequaled spatial resolution. On the other hand, in such a technique the FoV is very small: the phase difference between the apertures depends upon the sources distribution ($\Phi = \frac{\theta}{\lambda/B}\lambda$, where θ is the FoV, and B the baseline), and when a source introduces a phase difference with respect to the main source which is higher than the coherence length ($l = \lambda^2/\Delta\lambda$, where $\Delta\lambda$ is the spectral length of the source), the source does not produce fringes anymore. Because of this, the FoV limit is fixed, once the baseline is known: $\theta = \lambda^2/(B \cdot \Delta\lambda)$. Please note that the maximum FoV can be retrieved as the product of the angular and the spectral resolution.

In a Fizeau interferometer, instead, the light beams focus in a common focal plane. In this case, each star image in the focal plane consists of an Airy diffraction pattern, modulated by Young interference fringes. The star image, simulated in Figure 2.4, has two different spatial resolutions along the principal orthogonal axis. Along the Y axis, the resolution is given by the Airy disk dimension (λ/D, where D is the single aperture diameter - 8.26m for the LBT), while along the X axis the resolution is given by the central Young fringe width (λ/B, with B the baseline - 22.8m for the LBT). The result, then in an resolution-anisotropic image.

The central Young fringe width, as already mentioned, depends on the apertures relative distance (λ/B) and represents the minimum resolution element of the system as a whole. Considering a generic field on the sky, the resulting image is, then, a full-field resolution-anisotropic image. To retrieve the an image with λ/B resolution in all directions, the data have to be de-convolved with the point-like source PSF, obtained from the observation of some reference stars (the ones with the higher Signal to Noise Ration, SNR) inside the FoV.

The main limit of Fizeau interferometry is the baseline length. Such an optical system, indeed, presents a blind range for spatial scales ranging from the single aperture resolution (λ/D) and the interferometric one (λ/B). This imposes the choice of a baseline which is comparable with the single aperture diameter, to minimize such a blind zone, and so it creates a limit on the maximum achievable resolution. Another difficulty in the Fizeau interferometry in that the pupil homotheticity requirement, according to which the entrance and exit pupils of the system have to be geometrically similar. For most systems, such a requirement translates into the need to introduce further optical elements inside the system optical path, but in the LBT case, the problem is solved by construction. The common mount on which the two LBT arms are fixed, indeed, provides a time-invariant (and pointing-invariant) input pupil geometry, assuring that once the homotheticity is firstly obtained, such a condition is accomplished for each other pointing.

The main advantage of Fizeau interferometry in the Visible and InfraRed bands is the larger FoV which can be achieved (only limited by atmospheric parameters).

Because of these considerations, the LBT beams will be combined in a Fizeau interferometric configuration, since the telescope structure optimizes such a concept, having a baseline comparable to the single apertures and holding the apertures themselves on a common mount. The theoretical resolution of such a system corresponds to the one of a 22.8m telescope (0.02" in K' band).

2.2 Science with Linc-Nirvana

Table 2.2 lists the theoretical interferometric resolution achievable with Linc-Nirvana at the LBT. The high resolution power is, however, not the only peculiarity of such an instrument.

Table 2.2: Expected LBT AO-corrected performance at different wavelengths

Band	λ [μm]	λ/B [mas]	FoV [as]
R	0.7	6	5
J	1.25	11	10
H	1.65	15	15
K'	2.12	20	20

Other interferometers, in fact, can in principle reach even higher angular resolutions, like VLTI and Keck. Linc-Nirvana uniqueness is related to its true imaging capability, allowing to disentangle structures and effects which could not be easily understood with Michelson interferometry. Moreover, the MCAO correction allows such a high resolution imagery to cover a wide field (10"×10"), which is not achievable with the other high-resolution instruments.

It is easy to imagine, then, how many astrophysical goals such an instrument could try to reach. From a scientific point of view, in fact, such an expected performance increase the present possibilities in many astronomical fields, from extragalactic astrophysics to star formation studies. Generally speaking, Linc-Nirvana will allow the observation of far or faint sources, but above all it will resolve regions up to now not achievable in the IR wavelengths with a FoV which is very wide, with respect to the ones today reachable with other interferometers.

In 2006 a noticeable number of projects has been collected regarding the possible science studies to be carried out with Linc-Nirvana. Such a call revealed a great interest of the community about such an instrument capabilities, which could be applied to a variety of research fields.

Stars

High resolution images of the stars close environment, besides providing a good tool for binary systems detection, are expected to solve several open questions in each phase of their evolution, ranging from their formation and first evolution stages, in which detailed observations of disks and jets could be interpreted with 3-D radiation transfer modeling and hydrodynamic simulations (also providing validation test for new models), to AGB dust shells and evolved super-giant stars (which could, in some cases, even show resolved surface structures), whose outer atmosphere and circumstellar environment exhibit complex and still not completely understood phenomena. Also the final Supernova (SN) phase of massive stars offers several cues to researches to be carried out with Linc-Nirvana, exploiting its high resolution true imagery capability. An example of this is the use of high resolution to derive the distribution of type Ia/b/c and typeII SNe for cosmological distances ($z > 0.05$) but also to confirm the analogous offset already measured for the local universe, discarding the hypothesis of observational biases, e.g. SNe occurring in nuclear regions of starburst galaxies, where a limited angular resolution prevents their detection.

Astrometry: microlensing and planets

Moreover, Linc-Nirvana resolving power is expected to be high enough to use astrometric microlensing to determine isolated stars masses, thanks also to the large FoV and sensitivity, allowing the monitoring of several faint background stars at once. Concerning planets, high resolution and wide field will not only allow for solar system planets surface imagery, but also for extrasolar planets search, pushing the astrometric precision to 0.1 mas (1/100 of the PSF). This would not be an unique astrometric result, nor the best even achieved, but the wide field and true imagery of the instrument increases the likelihood of finding suitable references to improve the accuracy. The same kind of astrometric measurements could be employed in the follow-up of extrasolar planets candidates, allowing for the determination of their orbit and the estimation of their masses.

Galaxies and stellar populations

Concerning external galaxies, a detailed morphological study will be possible, thanks to the high resolution which, coupled with an high sensitivity, will allow to retrieve the structural parameters down to very faint galaxies (sometimes even prevented to be studied with HST because of the long required integration time), to study, for example, the connection between GRBs occurrence and host galaxy properties, or detect, in brighter early-type objects, possible relics of merging events to validate the hierarchical galaxy formation scenario. Moreover, the fitting of detailed galaxies surface brightness profile would allow the precise determination of structural parameters, which are fundamental to define the main scaling relations, and the study of the nuclear regions with a resolution and sensitivity never reached before in the IR domain. A comparison of LN IR data with HST visible data, moreover, would allow to realize color-color diagrams reaching the IR bands, with the aim to more precisely estimate age and metallicity of the nuclear stellar populations, in order to derive their formation history and evolution (already discussed in my degree thesis [25]).

Galactic center

Also our Galaxy inner region would offer several interesting problems to be solved and an ideal laboratory for stellar population study in a nuclear environment. Narrow filters can be used to derive the color and estimate the age of a huge number of stars at the same time, thanks to the wide available field, while astrometric measurements would allow the monitoring of the stellar dynamics in the immediate vicinity of the SgrA* super-massive black hole. Finally, such a black hole emission monitoring, using different colored and polarized filters, would help, together with other campaigns in different bands, to go deeper into the relativistic physics governing the very inner region of our Galaxy. These are only examples of what could be in principle done with an instrument like Linc-Nirvana, working in its interferometric mode.

2.2.1 LINC mode

A subsample of these scientific cases has been recently selected to be studied in the so-called LINC mode. The LINC mode of LN offers on-axis AO corrections while combining the beams of both the LBT 8.4 m mirrors, without performing the 2D image reconstruction. Thus the resulting resolution is equivalent to a 22.8 m telescope in one direction whereas it is equivalent

to a 8.4 m mirror in the perpendicular direction. As in the case of NIRVANA mode, a (near-IR) reference star is required for fringe flexure tracking (FFTS) Similarly to AO on 8m-class telescopes, LINC mode can be defined as:

- Target, AO reference star and FFTS reference star are all the same object (also referred to as early LINC mode)
- Target, AO reference star and/or FFTS reference star are not the same object. However, their distance is less than 5.

Despite the lower performance of LINC mode, several science cases have been identified, in all the research fields already introduced before.

2.3 Adaptive Optics serving interferometry

Interferometric measurements are always characterized by strict technical constraints and high precision requirements, to make the light-beams of interest to correctly interfere and give unique high-resolution results. In this framework, Adaptive Optics (AO) plays a big role, since even a perfect optical co-phasing of the light inside an interferometric instrument, obtained with very precise mechanical adjustments, would completely be destroyed by the action of the atmosphere. Considering a Fizeau interferometer like the LBT, a differential tip-tilt of the wavefront collected by the two apertures, for example, gives a bad superposition of the PSFs in the focal plane, resulting in a motion of the fringes pattern. In addiction to that, the effect of high-order deformations of the wavefronts is an halo composed of speckle-like structures. Linc-Nirvana is so equipped with an advanced Multi-Conjugated Adaptive Optics system, based on Pyramid WaveFront Sensors (WFS), combined according to Layer-Oriented (LO) technique, in order to achieve images close to the diffraction limit in a wide FoV, with a level of correction satisfying interferometry requirements.

As already mentioned, looking to the PSF image shown in Figure 2.4, it is clear that the LBT interferometric configuration produces anisotropic images. The resolution along the telescope baseline is higher, corresponding to the one of a 22.8m aperture, while the resolution in the orthogonal direction is the same one could achieve using only one of the LBT arms. It is, then, required to remove such an anisotropy.

The restoration problem, in the case of the LBT, is basically a multiple image deconvolution problem [18]. The image reconstruction is based on the analysis of the PSF of a reference star, not a priori one of the guide stars used for the wavefront sensing.

A set of interferometric observations corresponding to at least three different parallactic angles is obtained taking advantage of the rotation of the baseline projection on the sky, as the Earth rotates, as a function of the parallactic angle

$$p = \frac{\tan l \cos \delta - \sin \delta \cos H}{\sin H}$$

where l is the site latitude (32°42'05"N), δ the object declination and H the hour angle.

The retrieved field images are de-convolved with a normalized PSF and recombined with proper algorithms, with the aim to reconstruct the high resolution image. In Figure 2.5 the reconstructed images are compared with the original simulated one.

Further problems arise when trying to obtain a quite-wide inteferometric image (with respect to the typical FoV exhibited by non-Fizeau interferometers, which barely exceeds few

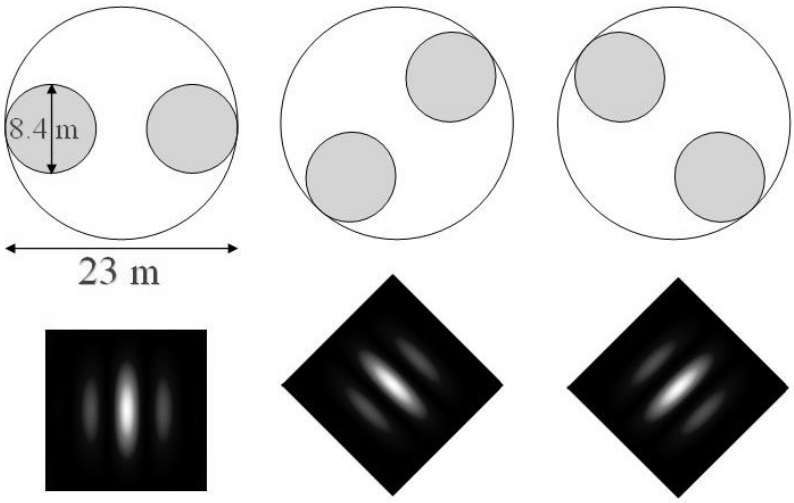

Figure 2.3: Effect of the rotation of the telescope baseline with respect to the sky. Due to the 2-apertures interferometric structure of the LBT, the resulting PSF shows a anisotropic spatial resolution, ranging from the resolution of a single 8.4 m telescope, up to the interferometric 22.8 m aperture spatial resolution in the baseline direction. The rotation of the PSF of each star in the focal plane allows the reconstruction of the high-resolution image of the FoV, if images at different parallactic angles are combined together.

arcseconds), since the PSF shape could in principle change along the FoV itself. This problem has been investigated [3] comparing the effects obtained with a classical AO case and with the MCAO approach. Generally speaking, the usage of more than one reference star results in a more uniform PSF over the whole FoV, which makes easier to find a suitable reference star to be used for the deconvolution and increases the similarity between the objects PSFs and the PSF of the reference star itself. Since the similarity of the PSFs gives better results with respect to the choice of reference PSFs better corrected, but different from the objects PSFs, then an uniform correction all over the FoV is preferred to high Signal to Noise Ratio (SNR) non-uniform corrections. That's why the MCAO approach used by Linc-Nirvana seems to be the best choice for interferometric imagery.

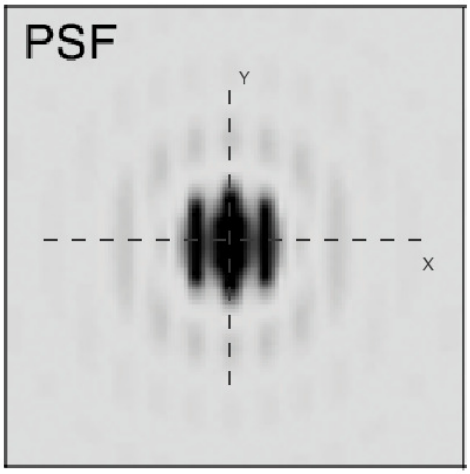

Figure 2.4: Simulated Point Spread Function which will be achieved with Fizeau interferometry on the LBT, equipped with Linc-Nirvana adaptive optics. The classical Airy pattern with a λ/D (D=8.2m) resolution is modulated by Young interference fringe pattern, with λ/B (B=22.3m) resolution.

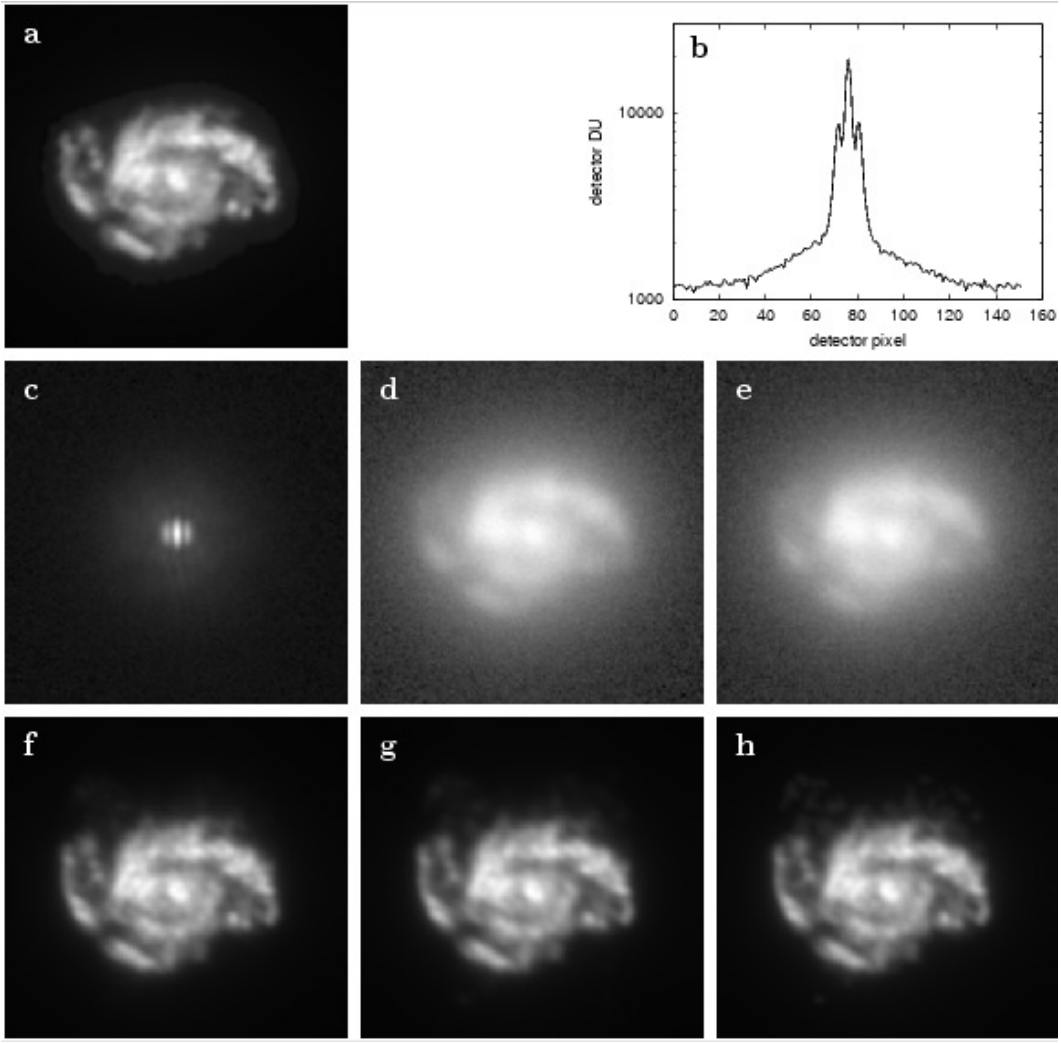

Figure 2.5: Simulated reconstruction process, with three different algorithms. **a**: simulated image with a diffraction-limited resolution of a 22.8m aperture. **b**: PSF intensity profile. **c**: simulated PSF. **d** and **e**: simulated images acquired with the LBT at different position angles, corresponding to 0° and 45°. **f**, **g** and **h**: diffraction-limited reconstructions obtained with different algorithms [24].

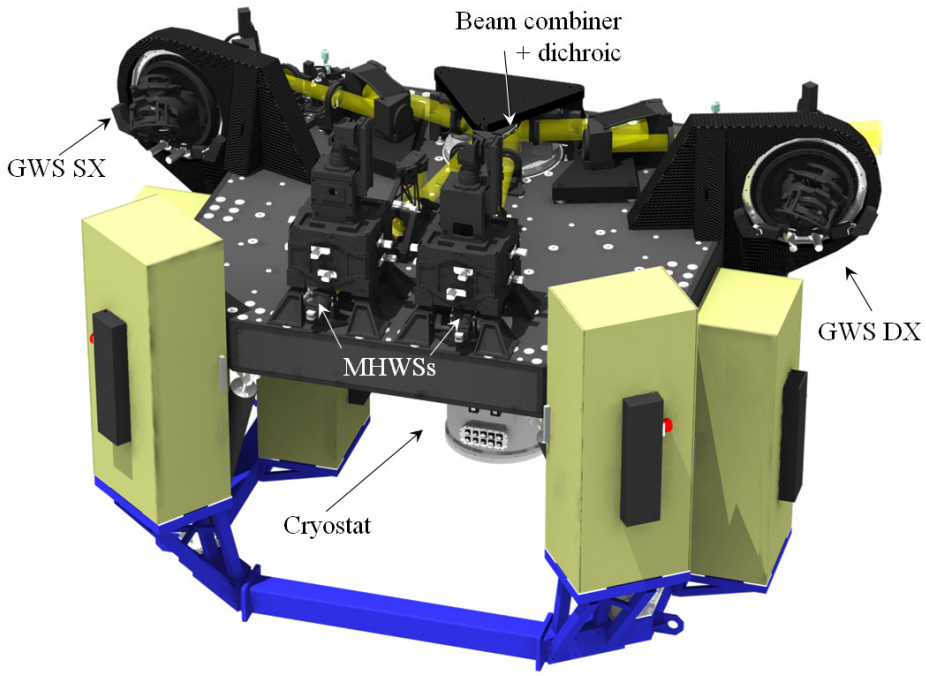

Figure 2.6: The Linc-Nirvana optical bench [11]

2.4 Linc-Nirvana system overview

Due to the binocular configuration of the LBT optics, Linc-Nirvana shows a symmetrical MCAO setup, sensing and correcting the beams coming from the two LBT primary mirrors separately, before they are combined in the common interferometric focal plane. While the interferometric scientific camera works in an IR domain, the AO system is aligned on a visible channel [22]. Figure 2.7 show NIRVANA schematic light and informations flows. The F/15 beam focused by one of the two arms of the LBT is partially reflected by an annular mirror, positioned in a intermediate focal plane, which reflects the outer $2'$-$6'$ annular FoV to the GWS, where the perturbations introduced by the lower part of the atmosphere are retrieved, looking to up to 12 NGSs. The GWS is conjugated at a 100 m altitude, that is to say just above the entrance pupil of the telescope and the corresponding DM is the secondary mirror of the LBT, equipped with 672 actuators, which change the mirror shape to reproduce the opposite of the perturbations introduced by the lower atmosphere, in order to correct them. The light of the inner $2'$ FoV of one arm of the LBT goes through a collimator, since the beams must be well collimated when reaching the beam combining optics, in order to avoid a PSF separation in the common focal plane of the two arms. The pupil geometry must be homothetic to guarantee zero optical path difference across the field. After the collimator, the beam is separated by a dichroic into visible and IR light. The IR light (with a wavelength larger than 1.0 μm), passing through a dichroic mirror, is co-phased with the light coming from the other arm of the LBT by the so-called piston mirror, a wedge-shaped monolithic mirror, acting as the actuator for the fringe tracking loop. Such a recombination mirror compensates for the difference in path between the beams, producing, in the common interferometric focal plane, the characteristic fringe pattern, equal for all the stars in the

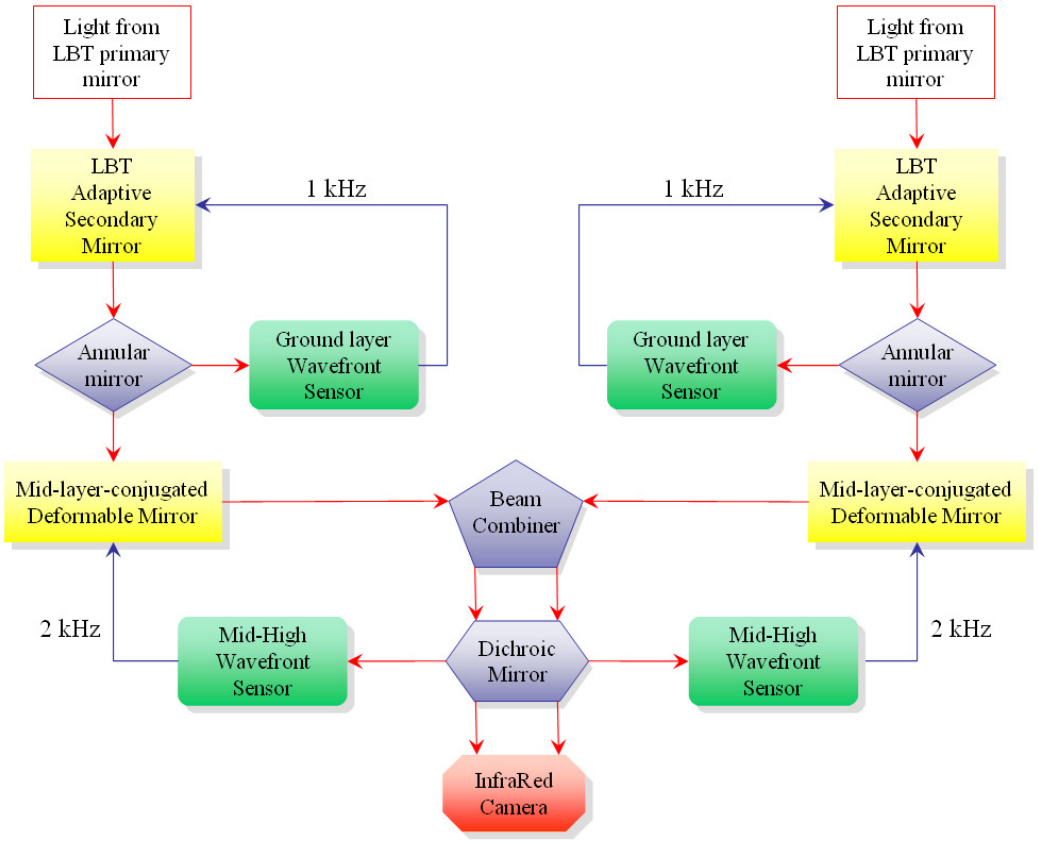

Figure 2.7: NIRVANA conceptual diagram. The red arrows show the light path, while the black ones represent the informations flows between the system components. The WFSs are represented in green, the DMs in yellow and the auxiliary optical elements in grey.

FoV. The scientific images forms on a CCD "HAWAII-2" (2048 × 2048 pixel), kept at a low temperature inside a cryostat together with the Fringe and Flexures Tracking System (FFTS) detector, to minimize the IR thermal background. The FFTS detector takes advantage of a $1' \times 1.5'$ FoV, to select a bright source other than the science object for fringe tracking. The scientific detector is mounted on a de-rotating device, to compensate for the field rotation during exposures. Since the fringes direction is fixed with respect to the LBT mount but the detector is rotating to compensate for the sky movement, the direction of the lowest spatial resolution changes on the detector itself. These effects translate into a maximum de-rotation angle, after which the fringe contrast is too low, corresponding to 30°. The visible beam (with a wavelength shorter than 0.9 μm) inside the $2'$ FoV is re-focused by a F/20 optics at the entrance of the MHWS, conjugated at an height of about 7.1 km and equipped to select up to 8 reference stars. The corrector for the high layer perturbations is a piezostack DM, conjugated at the same height as the MHWS and shaped by 372 actuators to correct the action of the higher part of the atmosphere, trying to achieve flat wavefronts. It is possible to introduce a third DM in the optical path, and shift both the DMs on the bench inside a so-called in "z-configuration", in order to conjugate them at different heights, but at the moment such a third DM has not been implemented. The MHWS is equipped with a second channel to conjugate a second detector to the third DM conjugation height.

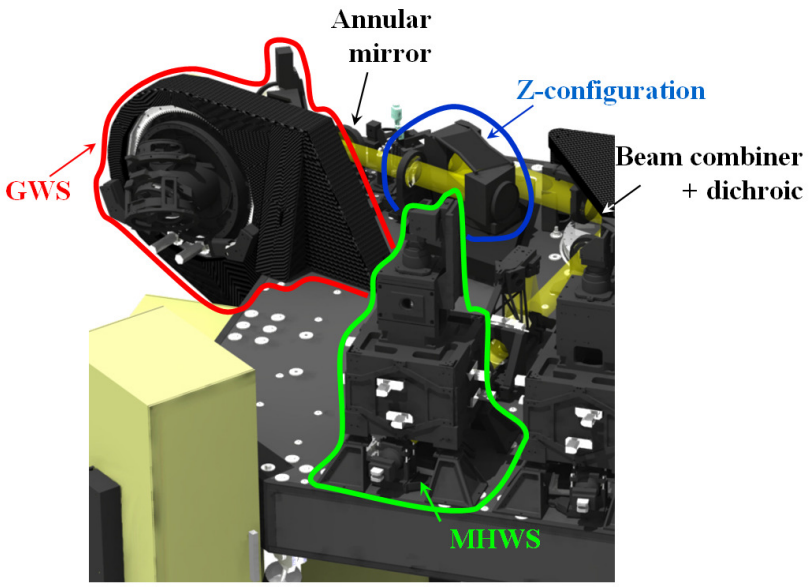

Figure 2.8: NIRVANA half-a-bench.

In correspondence of a combined focus closed to the scientific detector the Fringe-Flexure Tracker (FFT) is placed. It consists of a near IR detector, acquiring $1' \times 1,5'$ FoV images of a bright source to derive the phase difference between the light beams coming from Linc-Nirvana two channels and guide the beam combiner.

The astrometry of the MHWS reference stars can be done thanks to a Patrol Camera, collecting part of the light sent to the MHWS, when a beam splitter is inserted inside the optical path. Because of the LBT alt-azimuthal configuration, the FoV needs to be de-rotated before reach the WFSs. Two optical de-rotators are inserted in the optical path of the visible light focusing in the MHWS F/20 focal plane, while, concerning the GWS, the celestial rotation is compensated by a de-rotating bearing which is part of the GWS mount (see Chapter 6).

2.4.1 Ground-layer Wavefront Sensor

Concerning Linc-Nirvana, my work of thesis is centered on the AIV of the two Ground-layer Wavefront Sensor units, whose aim is the sensing of the deformation introduced on the incoming wavefronts by the atmospheric lower layer, namely about the first 100 m. These systems will guide the Adaptive Secondary Mirrors of the LBT at a 1 kHz frequency, after the wavefronts analysis, performed according to the layer-oriented MCAO MFoV concept. Each GWS can use up to 12 NGSs, to be selected in an annular $2' - 6'$ FoV.

Light optical path

Since the pupil superposition is perfect on the telescope aperture, the NGSs to be used for the lower layer wavefront sensing can be selected, in principle, in a very wide FoV, limited only by the thickness of such a layer. Stars quite far from the FoV to be corrected are still experiencing the same deformation as the scientific FoV stars, since they go through a very similar cylinder of atmosphere, considering only the ground layer. This is the concept behind

the MFoV technique, applied to Linc-Nirvana optical design. The outer part of the F/15 light beam coming from one of the arms of the LBT and entering Linc-Nirvana is reflected by an annular mirror, selecting the $2' - 6'$ diameter FoV, toward the GWS unit. Twelve small probes, called the Star Enlargers (SEs), composed of two lenses and described in the following Section, are moved inside the FoV to select the reference stars and focus their light on the pin of the pyramids. The refractive pyramid is the heart of the WFS, splitting the light in four beams, according to the pyramid WFS concept, as described in Section1.3.2. The light coming from a certain face of each the 12 pyramids is optically superposed, according to layer-oriented technique and, since the WFS is conjugated to the ground layer, the pupils are completely superposed. The pupil re-imaging is performed by a classical Schmidt-camera, called the Pupil Re-Imager (PRI). The beams coming from the SEs are firstly reflected by a flat annular folding mirror and then focused by a parabolic mirror toward a 4-lenses objective, re-imaging the 4 pupils on the CCD.

2.4.2 Main sub-units description

References Selection Unit and Star Enlargers

Generally speaking, a layer-oriented system has to face the difficulty to get both a reasonable diameter of the pupil images on the detector (compatible with available CCDs, with reading speed and noise suitable for an AO loop,in which the correction has to match, at least, the Greenwood frequency) and an acceptable dimension of the optics of the re-imaging camera. The first result can be obtained simply increasing the focal ratio of the beams on the pin of the pyramids, but that would have enlarged the entire FoV, requiring huge, heavy and expensive re-imaging optics. The solution here adopted has been already successfully tested in MAD, the Multi-conjugated Adaptive-optics Demonstrator [16] developed in collaboration with the European Southern Observatory for the Very Large Telescope. The light coming from a reference star, is picked up by a system called the Star Enlarger, composed of two lenses that increase the focal ratio of the incoming beam of a factor 12.5, focusing it on the pin of a pyramid.

Let's consider a layer-oriented pyramid WFS, schematized in Figure 2.9.

The NGSs light beams focuses onto the pins of the pyramids with an F/ratio= F. The following geometric relations are straightforward: $d_l = f_l/F_l$, where d_l, f_l and F_l are the diameter, the focal length and the F/# of the re-imaging lens, respectively, $D = f/F$, regarding the telescope aperture, and $s = f_l/F$, where s is the re-imaged pupil diameter. In such a configuration, the minimum diameter for the re-imaging optics is depending upon the spot diameter in the pyramids focal plane, $f\theta$, where θ is the angular diameter of the FoV, according to the equation:

$$d_l > f\theta + \frac{f_l}{F} \simeq f\theta \tag{2.1}$$

where the second term takes into account for the light beams divergence after the focal plane, but it usually is very small and negligible.

Considering all the previous relations one can easily get the following:

$$s \simeq F_l \theta D\,. \tag{2.2}$$

Considering Linc-Nirvana GWS, since $D \simeq 8.25\,m$, $\theta = 6'$, the resulting re-imaged pupil diameter is $s \simeq F_l \cdot 14.4\,mm$. Please note that we considered only one re-imaged pupil up to

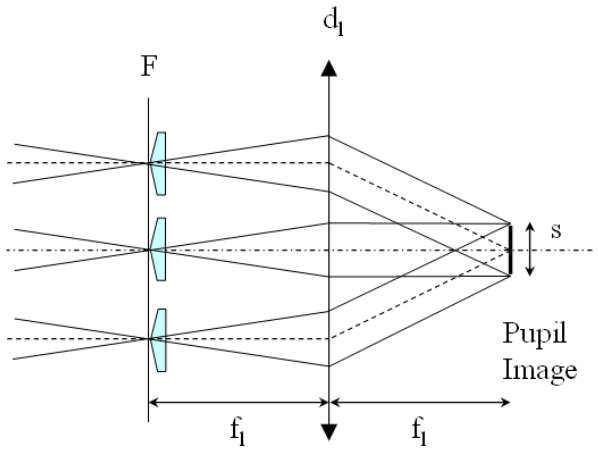

Figure 2.9: Layer-oriented Pyramid WFS scheme. As a semplification, only one of the four beam refracted by the pyramids is shown.

now, but the detector will be filled with a pupils matrix 2×2. Moreover, the spatial resolution of the detector will probably be to high, since the required pupil sampling is $p \simeq F_l \theta r_0$. To reduce the re-imaged pupils size, the F/# on the pin of the pyramids has to be increased. A secondary effect of such an increasing, however, will be the increasing of the FoV image diameter in the focal plane, requiring extremely wide re-imaging optics, since $d_l \simeq f\theta$ and $f = FD$. If $F' = kF$, where F' is the increased F-number, then $d'_l = kd_l$, where d'_l is the new minimum optics diameter required.

The adopted solution to this problem is the introduction of the so-called Star Enlargers. They are small optical systems, to be placed inside the FoV in correspondence of the NGSs to be used for the wavefront sensing. These systems increase the focal ratio of the beams focusing on the pins of the refractive pyramids, selecting only a small portion of the FoV. The result is that in the pyramids focal plane the FoV overall image diameter is linked to F, but the NGSs focused images width depends on $F' = kF$. In other words, the relative distances between the NGSs don't change, but their diameter is increased. The effect on the system is that the minimum re-imaging optics dimension is kept of an acceptable size.

Let's now consider the SEs of Linc-Nirvana GWS.

The optical concept behind the SEs is shown in Figure 2.10. The NGS F/15 beam coming from the LBT is collimated by an achromatic doublet with focal length $f_1 = 13$ mm (and diameter $d_1 = 5$ mm), producing a small pupil image. A second achromatic doublet with focal length $f_2 = 162.5$ mm (and diameter $d_2 = 14.7$ mm) is placed at a distance $f_1 + f_2$ from the first one. In this last lens focal plane an enlarged image of the NGS is produced, with a focal ratio $F' = kF$, where the enlarging factor is $k = f_2/f_1 = 12.5$. The result is then an F/187.5 output beam focusing on the pin of the pyramid. At the end of each SE the refractive pyramid splits the light in four beams, to be analyzed according to the 4-quadrants concept, as described in Section 1.3.2. The divergence angle of the outcoming beams is $\beta = 0.566°$. SEs internal optical alignment is described in Chapter 4.

Speaking of mechanics, the SE optical elements are mounted on cylindrical aluminum holders, optimized in a way to minimize the FoV obstruction and positioned on a V-shaped rail, as shown in Figure 2.11. While the second lens holder is glued to the rail, the first one

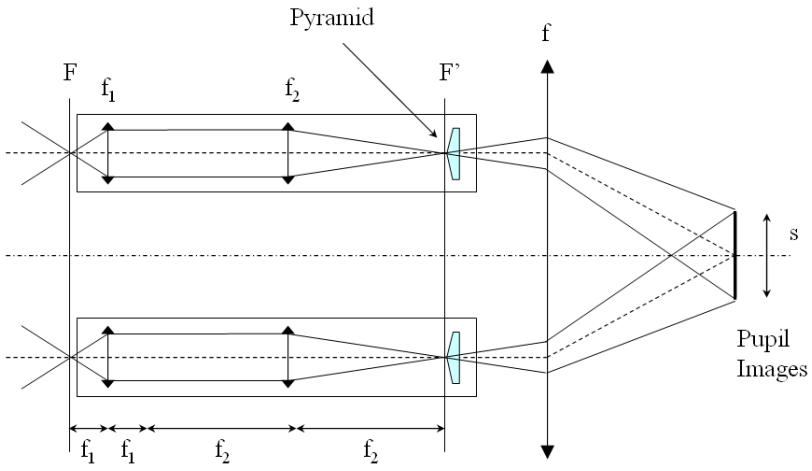

Figure 2.10: Layer-oriented WFS, after the introduction of the SEs.

can be moved along the optical axis in order to focus the beam on the pin of the pyramid.

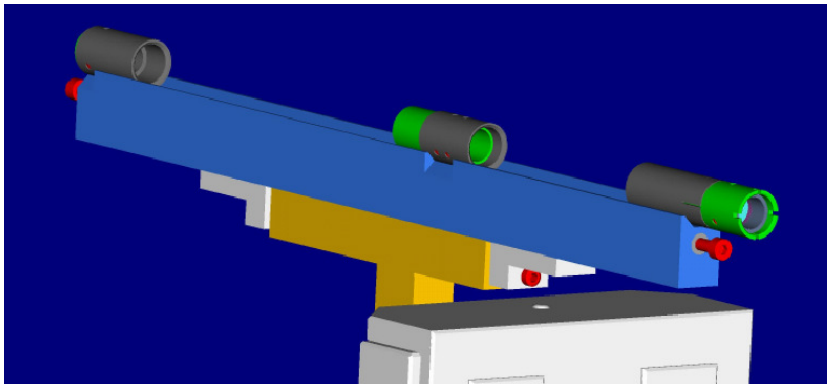

Figure 2.11: The optical elements of a SE, mounted on their mechanics.

Another tricky point concerning the SE is the way they are positioned in the 2′-6′ FoV, which has a 217mm diameter. The SEs overall structure and their arrangement inside the GWS are studied in order to minimize the minimum SE-SE distance that can be reached, to provide an high sky coverage. Of course, the same problem exists also for the MHWS, but in this case the incoming F/# is higher and the number of SEs to be placed inside the FoV is lower. The GWS SEs will pick up the light coming from up to 12 NGSs, being moved on the FoV by 12 XY linear stages, which are custom made in order to minimize their overall weight and ensure a pitch-and-roll wobbling during their positioning inside strict specifications, to minimize the displacement of the pupils created by the 12 SEs on the CCD. The 100×100 mm travel range of the stages permits to cover more than the annular area interested by the sampling with a partial superposition of each individual SE covered area. Since 12 SEs have to be placed inside the FoV, 12 linear stages need to be somehow held inside the reference selection unit. To maximize the SEs movements inside the F/15 focal plane, they will be introduced in the field with small mechanical arms symmetrically disposed around the FoV,

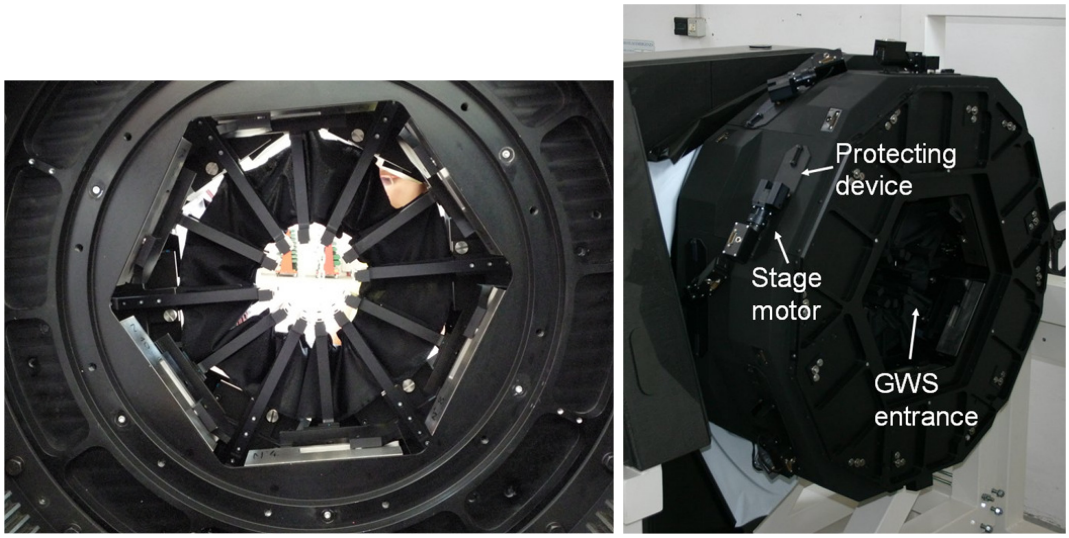

Figure 2.12: *Left*: disposition of the SE arms inside the GWS entrance FoV. One can also notice the light and dust protection made of an elastic soft-cloth material. *Right*: the two plates holding the SEs linear stages. Some stages motors are visible, as they come out from the reference selection unit main structure. The holes in which the motors move are protected from light and dust by particular sliding devices.

as shown in Figure 2.12 (*left*). Since the stages dimension is not so small, to obtain a compact overall structure six XY stages are fixed on a first annular plate, while the other six stages are mounted upside-down to another plate, connected with the first one, as shown in Figure 2.12 (*right*).

The Pupil Re-Imager Unit

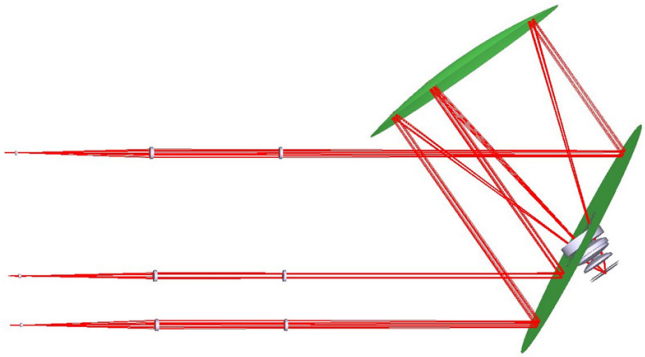

Figure 2.13: Pupil Re-Imager optical design.

The light beams coming from the 12 pyramids go through a system composed of both reflecting and refractive optics, called the Pupil Re-Imager, re-imaging 4 images of the pupil

on the E2V 128 × 128 pixel CCD50. An annular mirror reflects the light toward the power optics and will be used to align the re-imaging optics optical axis to the bearing rotation axis of the GWS. The camera is composed of a parabolic mirror and a refractive system made up of 4 achromatic doublets, placed in the flat mirror central hole, as shown in Figure 2.13, and delivering an F/0.9 output beam. The PRI aperture is 245 mm in diameter and its effective focal length is 220 mm. Speaking about mechanics, the two mirrors are mounted on particular mounts, equipped with various degrees of freedom, to be used during the alignment. The flat mirror, obviously, does not need an accurate centering system, but its mount has tip-tilt capabilities, being fixed to the main structure with three points at a relative distance of 120°.

On the contrary, the parabolic mirror mount is equipped with centering capabilities, which, combined with the tip-tilting mechanism of the objective, allows for the proper relative alignment of the PRI optics. The centering of the parabolic mirror is done thanks to three screws, positioned at a relative distance of 120° all around the mirror mount, acting on the mount itself, allowing the shift of the mirror on a plane perpendicular to the optical axis.

Tolerances, mounting and alignment details are described in Chapter 5.

Table 2.3: Main parameters of the GWS components

star enlarger	d_1	5 mm
	f_1	13 mm
	d_2	14.7 mm
	f_2	162.5 mm
	k	12.5
	travel range	100×100 mm
	FoV	1’
pyramids	β	0.566°
	n	1.53
PRI	f	220 mm
CCD	pixel	128×128
	pixelsize	24 μm

2.4.3 Main mechanical structure

The GWS main mechanical structure has been designed and realized for several purposes. First of all, it obviously keeps all the GWS sub-units in place, in the proper relative positions, once the alignment is done, and acts as an interface between the GWS components and Linc-Nirvana optical bench. Moreover, it is equipped with a de-rotation system, consisting of a bearing fixed on a carbon fiber arm, allowing the whole GWS de-rotation to follow the sky motion (see Figure 2.14).

The SE selection unit consists of two facing flanges, each holding 6 SEs XY linear stages, on which the SEs are fixed, above their tip-tilt plates. The whole unit is then fixed to one side of the rotating part of the bearing, while the PRI is fixed to the other side, with the flat

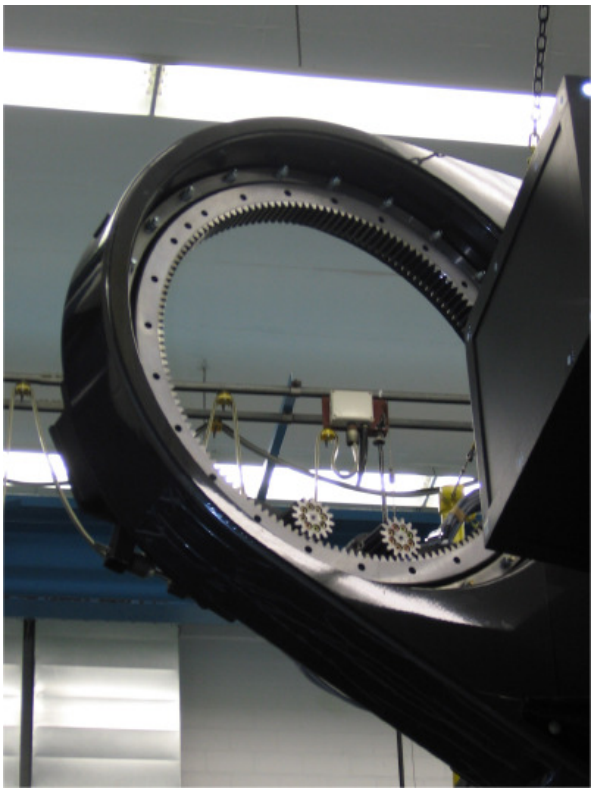

Figure 2.14: GWS carbon fiber arm, mounted on Linc-Nirvana optical bench. In the picture, the bearing allowing the GWS de-rotation is clearly visible.

mirror facing the pyramids on the SEs. The CCD case is mounted on three linear stages in XYZ configuration, allowing the centering and the focusing of the four pupil images onto the detector.

Flexures

The overall weight of each GWS is about 300 kg and this could, in principle, cause some problems in keeping gravity-induced displacements while the telescope pointing changes. Concerning the reference selection unit, the two annular plates (1m of diameter), holding the linear stages, are connected with columns to an additional structural ring, keeping good stiffness characteristics while the cylinder tilts over with the bench. The PRI could, in principle, be affected by flexures stress too, considered the weight of the optics it's composed of and of the linear stages focusing and centering the CCD. In order to minimize this effect on the structure holding the CCD during the GWS de-rotation, three a-static leverages have been introduced on the original mechanical design. These leverages are preloaded to compensate the gravity-induced force acting on the system during an exposure. They are visible as the not blackened mechanical systems in Figure 2.15.

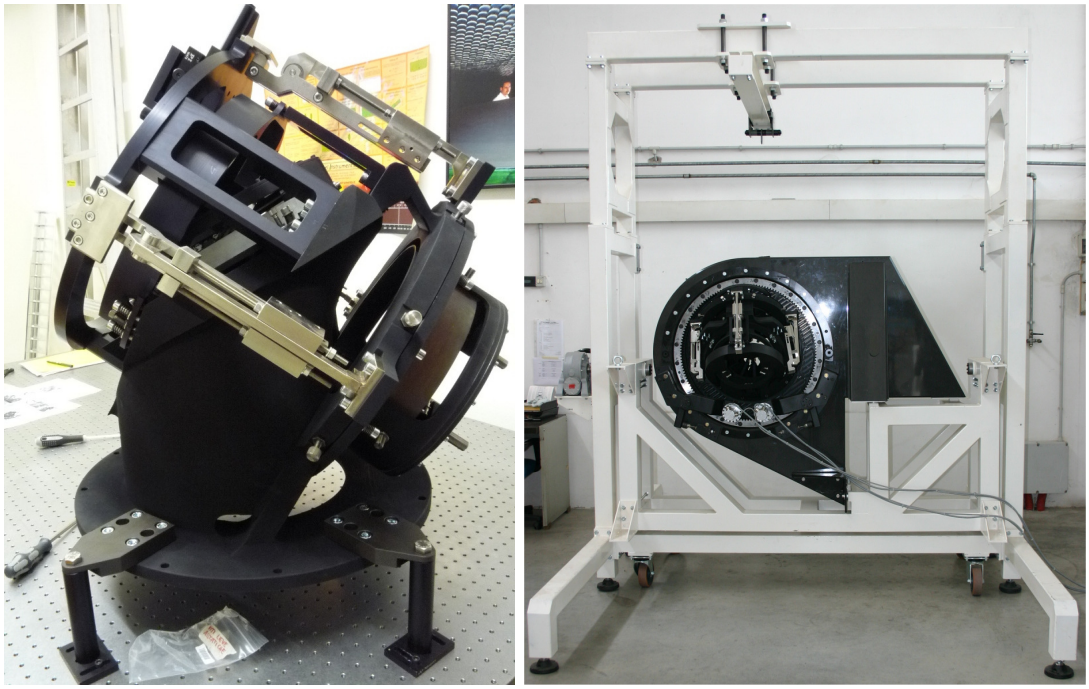

Figure 2.15: *Left*: the assembled PRI. *Right*: the GWS mounted on the carbon-fiber bearing that will allow the rotation of the sensor to compensate the rotation of the sky. Both the GWS and the bearing are held by an huge handling developed and realized to sustain the system during the final alignment procedure.

Handling

During the alignment operations of the GWS as a whole, that take place in the Observatory of Padova, the sensor needs to be somehow held in the same orientation as in the Linc-Nirvana optical bench. Since the weight of the overall sensor is about 300 kg, and it's mounted on its carbon-fiber rotation bearing, which weighs almost 250 kg, the development of a proper handling structure was essential. Figure 2.15 (*right*) shows the huge handling realized for the GWS. The bearing is fixed to a wheels-equipped mechanical cradle, which has several purposes: first of all it is used to tilt the bearing upside-down to mount the PRI and the big plates of the selection unit (lifted with a pulley system) during the assembly, then it holds the entire system during the optical alignment, finally it turns into a parking device to be used in case that the GWS has to be dismounted from Linc-Nirvana. An external big structure is used to fix the handling to the laboratory optical bench with a couple of chains (see Chapter 6 for further details on the GWS assembly and alignment).

2.4.4 GWS first light: pathfinder at the LBT

In the last two years the idea of a preliminary experiment to be led at the LBTO with only the first GWS has been carried on by the Linc-Nirvana consortium, in order to reduce the risk for the project as a whole. The Pathfinder aim is to realize a fully-working GLAO system, to work as a seeing reducer for one arm of the LBT, already equipped with its Adaptive Secondary

Mirror, which recently proved to allow for a high SR correction in its First Light Adaptive Optics (FLAO) mode [6]. The choice of the LBT arm came after a discussion between LBTO and Linc-Nirvana team members, when the possibility to commission the Pathfinder on the DX (right arm) rear port of the LBT in late 2012 arose. Another important issue of the Pathfinder is the verification of the instrument-to-telescope interfaces, both mechanical, optical and software, mainly to prove the ability of the system to control the LBT ASM. Together with the GWS and the annular mirror, the Pathfinder will be composed of an InfraRed Test Camera (IRTC), selected to provide the performance, required to achieve the goal of a GLAO correction for a 13 mag star in H band.

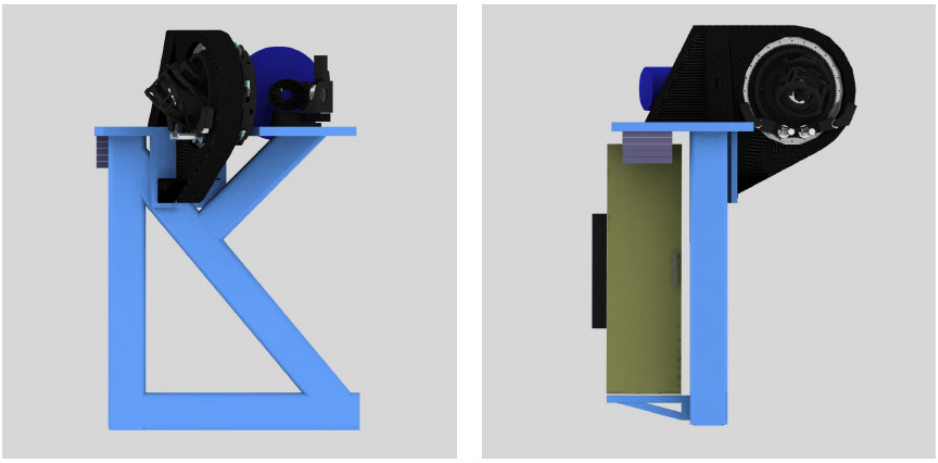

Figure 2.16: Pathfinder on its Support Structure (preliminary design).*Left*: side view. *Right*: end-on view.

Chapter 3

Ground layer Wavefront Sensor Error Budget

The following error budget has been computed to quantify the effect of known errors or uncertainties on the GWS components manufacture, together to uncertainties related to the system alignment procedures. These errors are estimated as blur onto the four re-imaged pupils, which translates in relative shifts of the sub-aperture in which the pupils are divided, which causes (superimposing the light of several pupils coming from different SE) that there will be a "cross-talk" between adjacent sub-apertures, i.e. in a certain sub-aperture there will be some undesired light coming from adjacent sub-apertures. Of course, this shift should be much smaller than the sub-aperture size in order to minimize the undesired "cross-talk".

3.1 GWS components

GWS components performance is crucial for the overall error budget of the system and leads to specifications asked to the providing companies and in some cases to separated test on the components themselves in order to check their compliance with specifications.

- SE diffraction: this effect is due to SE optical design (see Chapter 4), and it is estimated with Zemax computations as a $\mathbf{7}\mu\mathbf{m}$ blur on the pupil.

- Linear stages wobble: The effect on the detector plane both of pitch and of roll of the linear stage which is moving a SE is a shift of the 4 pupils generated by the pyramid held by that star enlarger. A typical specification is that the maximum shift is of the order of 10% of the dimension of the sub-aperture itself, meaning a 25μrad requirement for the linear stages pitch and roll. The real values measured on the SE positioning stages delivered by the providing company, translate in a SE 10" Peak-to-Valley global tilt, assumed 5" RMS (25μrad). These values are documented in test reports, provided by the providing company itself. This a wobble translates into a pupil blur of about $\mathbf{5}\mu\mathbf{m}$.

- Pyramid chromatism: since pyramids are dispersive elements, and they're working with polychromatic light, the chromatism effect has to be taken into account. Pyramid chromatism effect is estimated with Zemax computations, resulting in a pupil blur of $\mathbf{6}\mu\mathbf{m}$.

- Pyramid vertex angle: specifications on the pyramid vertex angle (±17" repeatability and ±58" absolute error), asked to the providing company, allow a maximum blur on the pupil, due to this factor indetermination, of **5μm**. The compliance of that specification is verified in my degree thesis [25], where the divergence angle β between the output beams, which, in the approximation of small angles, is related to the pyramid vertex angle and to the material refractive index n according to the relation $\alpha = \beta/(n-1)$, has been measured. The results are that for one of the 2 sets of 12 pyramids the beam divergence repeatability range (and so, also the vertex angle one) is smaller than required, but for the other set, the repeatability range is just the required one.

- Pyramid faces orthogonality: pyramid faces orthogonality requirement asked to the providing company (±5') can be translated into a maximum pupil blur of 5μm. The providing company test certificate reports a pyramid face orthogonality better than 50" for all the delivered pyramids, translating into a pupil blur lower than **1μm**.

3.2 GWS internal alignment

- SE enlarging factor k: specifications on the enlarging factor k, given in the GWS Opto-Mechanics FDR document, allow a maximum blur on the pupil, due to this factor indetermination, of **5μm**. The compliance of that specification is verified during SE alignment (see Chapter 4 and Figure 3.1, *left*).

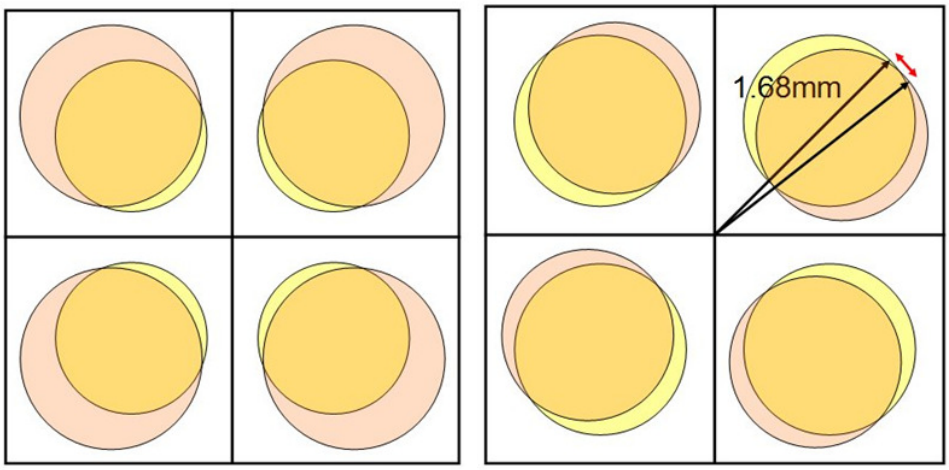

Figure 3.1: Some pupils wrong superposition effects: on the left the effect of a non-uniform SE enlarging factor, on the right a different orientation of the pyramids around the optical axis.

- SE relative tilt: as discussed for the linear stages wobble, the effect of a tilt of a SE with respect to the PR-I is a shift of the 4 pupils generated by the pyramid. A tenth of sub-aperture shift corresponds to a tilt of the SE of about 5 arcsec, that we take as a goal for the SEs tip-tilt alignment with respect to the GWS. This translates into a pupil blur lower than **5μm**.

- Pyramids orientation: a different orientation of the pyramids one respect to the others lead to a wrong superposition of the four pupils on the detector. For geometrical reasons (see Figure 3.1 , *right*), the maximum linear displacement applies to the edges of the pupils, which are 1.68mm far from the center of the rotation. A 1/10 of sub-aperture displacement at the edge of the pupils can be produced by a differential orientation of a pyramid with respect to the others of 10', which we believe to be a mechanically achievable sensibility. This translates into a pupil blur lower than **5μm**.

- Pupil Re-Imager optical quality: PR-I optical quality in terms of blur onto the pupil image can be directly verified on the PR-I itself once it is aligned, considering it as a stand alone camera and measuring the RMS spot radius of the spots in its FoV ($\pm 0.44°$). The previous error budget issue gave a 25μm RMS blur as a specification for the PR-I optical quality. However, measurements on the real PR-I, fed with a wide collimated beam and documented in Chapter 5, gave a maximum RMS spot radius in the edges of the FoV lower than **13μm**.

3.3 Thermal effects

LN and, consequently, the GWS are required to work in a temperature range from -15° to +20° ($\Delta T = 35°$C). However, the detector can be refocused in order to compensate for temperature variations, here we plan to build a look-up table with a 5°C increment.

- SE lenses misalignment due to thermal effects: some misalignments are introduced on SE lenses from thermal effects ($\Delta T = 35°$C), translating into a pupil blur of **4μm**, computed with Zemax simulations. An analogous SE lenses misalignment due to thermal effects for $\Delta T < 5°$C, which is the considered the increment for the look-up table, is negligible with respect to the pupil re-imager optical quality increasing.

- Linear stages wobble in the whole temperature range: SE linear stages pitch and roll has been measured on a first prototype in different thermal conditions (from +15° to -15°), giving a RMS value lower than 5arcsec at each tested temperature, as reported in [25]. No additional wobble is then introduced by temperature variation on the SE linear stages, so there are **no additional blur terms** onto the pupil.

- Pupil Re-Imager optical quality decreasing: The thermal effects on the Pupil Re-Imager optical quality will be compensated refocusing the detector for temperature variation $\Delta T > 5°$C. However, a degradation effect for temperature variation $\Delta T < 5°$C without detector refocusing has to be included in the error budget, resulting in a **7μm** pupil blur.

3.4 GWS misalignment with respect to LN optical bench

- Mismatch DM-WFS: The WFS and the DM can be conjugated to two slightly different layers, resulting in a pupil blur on the WFS detector. The accepted value for this blur is **5μm**, assuming the GWS CCD focusing in order realize a superposition of the spots produced by different sources better of a tenth of sub-aperture, that is to say 1/5 of a pixel of the final CCD camera.

- GWS global defocus: the LBT focal plane is curve, in a way that there is a huge difference in the focal plane position along the optical axis, depending upon the distance from the center of the field. A check on the LBT optical design has been performed with Zemax, resulting in the focal plane positions summarized in Table 3.1.

Table 3.1: Offset of the focal position along the FoV of LBT with respect to the 0° FoV focus. The resulting defocus signals measured by the WFS are listed too.

FoV radius [arcmin]	FP offset [mm]	Defocus RMS [nm]
1	0.66	102
2	2.65	410
3	5.97	922

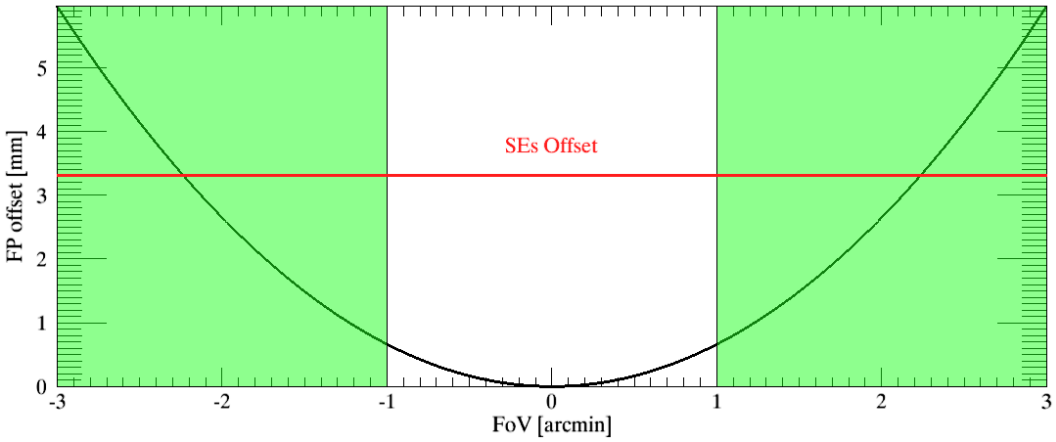

Figure 3.2: Curvature of the LBT focal plane for a 6' FoV. The green areas highlight 2'-6' annular FoV which is re-imaged at the GWS entrance focal plane. The red line represents the FP offset selected in order to minimize the residual WFE in the whole FoV area.

The field curvature is corrected before the MHWSs, in a way to be able to retrieve the defocus signal to be sent to the DMs, but it is still affecting the GWSs, whose defocus signals will not be used in the LINC-NIRVANA AO loop. Considering the values listed in Table 3.1 and plotted in Figure 3.2, an offset value to which align all the whole GWS has been selected, in a way to both divide the annular FoV into two quite equivalent areas, which will respectively be in an intra-focal and in an extra-focal position, and to have a similar residual WFE in the 1' and in the 3' FoV radii. The computed best offset is 3.31 mm, corresponding to put to zero the defocus for the 2.24 arcmin radius in the FoV. In such a configuration the inner 12.57 arcmin^2 are in intra-focal position, while the outer 12.57 arcmin^2 are in extra-focal position. The residual RMS WFE due to defocus is 346 nm in both 1' and 3' position on the FoV. The effective defocus signal retrieved by the WFS is depending on the asterism of the NGSs, and, since it's not used in the AO loop, it's only affecting the WFS capability to retrieve higher order aberrations. What is, then, a reasonably acceptable defocus? The limit is given by the saturated case in which the defocus is so high that only a quarter of each of the four

pupils is illuminated, causing the impossibility to retrieve higher order aberrations. This happens when the NGS diameter increasing due to defocus is of the same order of the correction we want to achieve after the GWS loop closing. The maximum separation between the spherical focal plane delivered by the LBT and the flat plane to which all the SEs are aligned is 2.65 mm in the F/15 focal plane. Such a difference translates into an enlargement of the spot in the SE entrance focal plane of 2.65/15 = 0.18 mm, corresponding to 0.29". This will be the limit of the correction which can be reached with the ground-layer loop, meaning that in case of very good seeing (lower than 30"), the GWS will not be sensitive to the atmospheric aberration. Of course this will only be an extremely conservative limit, that would be effective only in the case of an asterism in which all the NGSs were placed on the outer 6' diameter rings of the FoV. If a slightly better case, in which all the stars are placed in a 5.8' ring, is considered, such a seeing limit would decrease to 0.23". 7% of the FoV exceed the 0.25" *good seeing limit*, here used as a reference also for other consideration. Because of this reasons the tolerance in the GWSs entrance focal plane position with respect to LBT focal plane is very large. The effect of even a huge defocus is **negligible in terms of pupil blur** on the detector and only results in a defocus signal detected by the WFS, which can be subtracted as a static aberration, during the calibration procedures. A limit in the GWS positioning along the optical axis is due to the need of not to introduce a too large static aberration, in order to be sure the WFS will work in its linear regime.

- GWS global tilt: a SE tilt results in a rigid shift of the 4 pupils on the CCD, according with the following expression:

$$Tilt(rad) \cdot \frac{f_{PRI}}{k_{SE}} = pupil\ shift \tag{3.1}$$

where f_{PRI} is the equivalent focal length of the Pupil Re-Imager, and k_{SE} is the Star Enlarger enlarging factor. Since, in our system, f_{PRI} = 225mm and k_{SE} = 12.5, the resulting pupil shift for a given SE tilt is:

$$pupil\ shift(\mu m) = 1.8 \times 10^4 Tilt(rad) \tag{3.2}$$

For a given GWS tilt, the resulting pupil shift is given by $pupil\ shift(\mu m) = 1.8 \times 10^4 Tilt(rad)$. This means that a 1' tilt shall lead to a rigid pupil shift of about a tenth of sub-aperture of the WFS (48μm). Moreover, the annular mirror mount will allow to optimize the tip-tilt alignment of the GWS with respect to the optical axis before each exposure with a precision of 30", translating into a 1' tilt of the beam with respect to the GWS axis. However, a fixed pupil shift has no effect in the wavefront sensing, once their true position is known, in the sense that it can be compensated re-centering the GWS detector, which is equipped with XY positioning remotely controlled stages. Because of this reason, the limit in the GWS alignment in tip-tilt with respect to the beam coming from LBT is only due to the flexures of the overall system, discussed separately. An additional, very small pupil blur is due to the fact that the GWS is working slightly more off-axis than expected. The acceptable indetermination in the tilt of the GWS with respect to the LN bench is retrieved with Zemax computations, in order to limit the pupil blur under a certain value. The maximum RMS blur on the pupil for different values of GWS tilt are summarized in Table 3.2. In other words, since the LBT is delivering an F/15 beam with the exit pupil placed at a distance of 14m,

Table 3.2: Table summarizing the maximum RMS blur on the pupil for different values of GWS tilt.

GWS tilt	Medium RMS blur	Maximum RMS blur
0.00°	6.87 μm	7.01 μm
0.05°	6.94 μm	7.68 μm
0.10°	7.14 μm	8.60 μm

and since the pupil will be sampled with a maximum of 24 sub-aperture on a diameter, to have a shift on the pupil equivalent to one sub-aperture This contribution, however, is **negligible** with respect to the rigid pupil shift.

- GWS global decenter: the effect of a GWS decentering at the level of the pupil is very small (a 50μm decenter produced a pupil shift of 1μm), and the PR-I optical quality degradation starts to be not negligible only for a very large decenter (≈4.8mm). However, there is another reason to keep this type of misalignment as low as possible, which is the SE shift. If we consider seeing-limited conditions and a good seeing (0.25"), the maximum acceptable SE shift should be reasonably lower than the seeing limit. A 15μm displacement, for example, is a factor 10 smaller than the seeing limit. One has to take into account that if the decenter between the GWS bearing rotation axis and the telescope axis is, let's say, ΔX and a SE is perfectly centered on a NGS, after an η degrees de-rotation of the bearing the displacement of the SE with respect to the reference star, Δx(η), will be twice the displacement between the telescope and the bearing axis, multiplied by a factor depending on η (see Figure 3.3):

$$\Delta x(\eta) = 2 \cdot \Delta X \cdot \sin\left(\frac{\eta}{2}\right) \tag{3.3}$$

Of course, to translate this fact into a real requirement, one has to consider the maximum bearing rotation required for a single exposition, depending on the maximum exposure time (10 minutes) and on the maximum field de-rotation speed. The latter can be retrieved, given the minimum zenithal distance z and the site latitude L, with the following expression:

$$\frac{d\eta}{dt} = 0.262\frac{\cos L}{\sin z} \tag{3.4}$$

The mount Graham latitude is L=32.7°, while the minimum zenithal distance for LN on LBT is z =1.5°, resulting in a maximum rotation rate of 8.4 rad/hr. In the very conservative case of a 10 minutes exposure with a 8.4 rad/hr de-rotation speed, the resulting maximum bearing rotation is ≈80°, leading to a maximum SE displacement:

$$\Delta x_{MAX} \approx 1.28\Delta X \tag{3.5}$$

This effect translates in a tip-tilt signal on the WFS, due to a common displacement of all the SEs, which will not be used to perform the wavefront correction, but will be used to re-center the SEs themselves on the reference stars. However, the actual maximum rotation of the bearing during one exposure is driven by the maximum acceptable

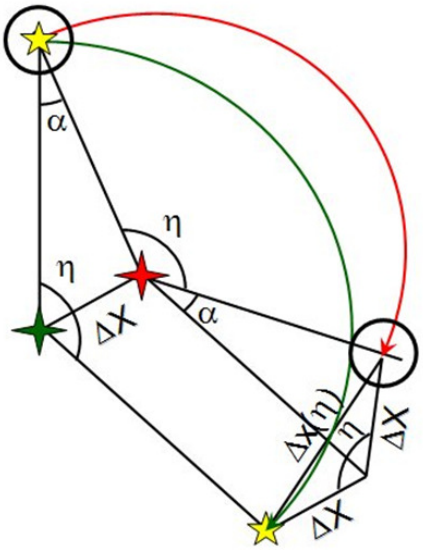

Figure 3.3: An η degrees de-rotation of the bearing. The black circle represents the SE FoV, initially (upper part of the figure) perfectly centered on the NGS. The green and the red crosses are the telescope and the bearing optical axis, respectively. The SE motion is represented by the red arrow, while the reference star motion follows the green arrow.

rotation of the fringes in the heart of the interferometer and corresponds to 60°. If we consider a SE remote re-centering every minute (which is the plan, at the moment of this writing), the maximum bearing rotation decreases of a factor 10, and the maximum not-corrected SE displacement becomes $\Delta x_{MAX} \approx 0.14\Delta X$. According to LN FDR, the maximum accepted GWS misalignment is ΔX=100μm, leading to a maximum SE displacement at the end of the longest exposure of 14μm. The GWS global decenter can be due not only to a GWS misalignment with respect to the LN optical bench, but can derive also from a bearing runout, so the acceptable SEs shift has to be shared between these two sources of indetermination. These effects, however, **do not increase the pupil blur**.

- Pupil matching on WFS: this issue concerns the correspondence of the actual pupils position onto the detector with the expected one, on which the interaction matrix has been computed. Concerning this topic, the main considerations I'll made are based on the operational experience gained by the Adaptive Optics group of the Astronomical Observatory of Arcetri, during the Adaptive Secondary Mirror of LBT test and on the performance of the First Light AO (FLAO) system for LBT. In principle, the system software could compensate for pupil shifting, detecting the positions of the four pupils with a certain time frequency and re-defining the sub-apertures of the WFS. What they already do on the FLAO system is to monitor the pupils movement and, in case it exceeds 1/5 of sub-aperture, to correct such a shift moving the camera lens orthogonally to the optical axis [5]. The median resulting shift during an exposure, if this compensating operation is performed, is 1/10 of sub-aperture. This kind of correction would be quite complicated in the GWS, since it's an MCAO system with very wide and heavy common

path optics. It would be possible, however, to compensate for pupil common shifts via software, provided that, to obey Nyquist theorem, different interaction matrices have been recorded for a shift of the pupils of known fractions of one pixel. Considering the FLAO approach and remembering the GWS minimum sub-aperture size, 2 pixels, additional interaction matrices would be recorded for pupils shifts of 1/5 and 2/5 of a sub-aperture, before going back to the original matrix, with the pupils shifted of an entire pixel. Considering this software correction approach, the resulting median value for the pupil shift is **a tenth of sub-aperture**.

3.5 Bearing contribution

The support structure of the GWS is composed of a Carbon Fiber Resin Plastic (CFRP) structure with an integrated Cross Roller Bearing (CRB) and of a mechanical drive system. The bearing performances affect the WFS measurements in several ways:

- a bearing runout produces a shift of the GWS as a whole, translating into a rigid movement of all the SEs on the FoV as the bearing rotates, which is sensed as a tip-tilt signal for the wavefront sensor;
- bearing wobble translates into a global tilt of the GWS as a whole, varying during an exposition;
- a non-uniform rotation of the bearing causes a tilt signal to be sensed by each SE, according to its distance from the center of the 2'-6' FoV;
- flexures of the CRB with respect to the CFRP.

The bearing flexures and their effect will be analyzed in Section 3.6.

3.5.1 Bearing Wobble

A bearing wobble produces a global tilt of the GWS as a whole and a consequent pupil shift, according to Equation 3.2, varying with time and so resulting in an additional pupil blur. Bearing wobble measurements have been performed by the bearing providing company by means of dial gauges, resulting in a value lower than 40μm over the bearing diameter for both the bearings, resulting in a bearing wobble lower than 12 arcsec, considering a bearing inner diameter of 730mm. According to Equation 3.2, a 12 arcsec tilt of the GWS as a whole produces a consequent pupil shift of about 1μm. The additional pupil blur, due to the fact that the GWS is working slightly more off-axis than expected, is **absolutely negligible**.

3.5.2 Bearing Runout

Bearing radial runout has the same effect as a decenter of the GWS as a whole and so it has to share the permissible GWS displacement with the requirement concerning the GWS alignment on the LN bench (see Section 3.4). Radial runout measurements have been performed by the bearing providing company by means of dial gauges, resulting in the identification of a range of 120° in each bearing rotation global range, in which the radial runout value is lower than 40μm PtV, and to 20μm RMS. The mounting bolts at both the outer and the inner rings have been labeled with 1-24, starting with 1 at the twelve o'clock position and with numbers

increasing in clockwise direction, so as to define univocally the selected ranges, as reported in Figure 3.4. **No additional blur** is introduced at the pupil level. According to Equation 3.5,

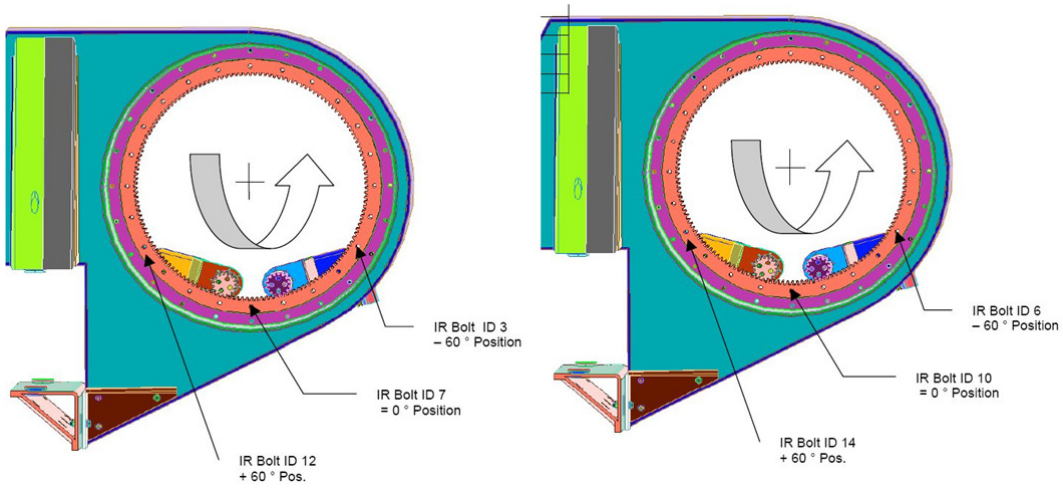

Figure 3.4: GWS bearing rotation ranges in which the radial runout value is lower than the permissible runout of 40μm. *Left*: GWS bearing #1 (LH); *Right*: GWS bearing #2 (RH).

the measured RMS runout shall lead to a SE displacement during one exposure (in the worst case) of $\Delta x_{MAX} = 25.6\mu m$. If we consider, again, a SE remote re-centering every 1 minute, the maximum bearing rotation decreases of a factor 10, and the maximum not-corrected SE displacement translates into a residual tip-tilt signal on the detector, which is not used by the system.

3.5.3 Bearing non-uniform rotation

Non-uniform rotation of the bearing causes a shift of the SEs, translating into a tilt signal to be sent to the WFS by each SE, according to its distance from the center of the 2'-6' FoV. As seen in Section 3.4, the acceptable shift of a SE should be comparable with the telescope tracking accuracy. A 1' indetermination on the rotation of the bearing translates into a shift of a SE placed on the edge of the field of ≈30μm. The bearing non-uniform rotation has been measured and documented, resulting in a in a maximum deviation from the regular motion of 140" for a 120° rotation of the bearing. Considering the maximum bearing rotation in one exposure (60°), the maximum deviation decreases to ≈100", assumed 50" RMS and translating into a shift of a SE placed on the edge of the field of ≈25μm (the true deviation value depending on the selected 120° range). If we consider, once more, a SE remote re-centering every minute, the maximum bearing rotation decreases of a factor 10, and the maximum deviation decreases to ≈40" PtV. The resulting SE displacement on the edge of the field of about 10μm. Again, this has **no effects on the pupil**, except for a differential tip-tilt signal, which, in this case cannot be used as a feedback to adjust the SEs position inside the FoV. The actual tip-tilt signal will depend on the number, position and magnitude of the selected NGS.

3.6 Flexures

3.6.1 GWS flexures

A Finite Element Analysis (FEA) concerning the GWS structure flexures has been carried out by the mechanics providing company. Five bench inclination angles have been considered: 0, 15, 30, 45 and 60 degrees. The worst result in terms of deformation has been obtained at 45 degrees, where the worst deformation is of the order of 0.028mm. A second part of the FEA is dedicated to find a correction factor due to the fact that in the previous FEA the parts where considered as a unique body, while in the reality there are soldered and screwed parts. This correction factor has been found to be 2-2.5, which, multiplied to the worst obtained deformation in the first part of the FEA, results in an estimated deformation of about 0.07mm. Let's now do a couple of conservative considerations:

- Supposing that all this deformation is in defocus, this would entirely translate in a defocus signal, not introducing relevant blur onto the pupil (as already discussed for SE de-focus).
- Supposing that all this deformation is in a direction orthogonal to the optical axis, the effect of such a shift obviously depends upon the point on which we apply it. If we consider this deformation as a 0.07 mm rigid shift of all the GWS with respect to its optical axis (of course this is a very conservative hypothesis) than the overall effect is a GWS decentering, translating into a SE displacement during an exposure. Moreover, if we consider a SE remote re-centering every 1 minute, the maximum not-corrected SE displacement is $\Delta x_{MAX} \approx 0.14 \cdot \Delta X$, translating into a 10$\mu$m blur onto the pupil.
- If we consider this flexure as a rigid tilt of the whole GWS with respect to the bearing, in the most conservative case it would introduce a tilt of the GWS of about 24". According to the consideration made in the GWS tilt paragraph, this would translate into a 2μm pupil blur.

At this stage, the direct sum of such estimated contributions will be considered, to be sure of avoiding underestimations, resulting in a pupil blur of **12μm**. The real effect of the flexures onto the pupils position will be quantified, however, when the system will be delivered at the MPIA in Heidelberg, where the GWS installation on the final LN optical bench, mounted on a tilt platform, will allow the direct measurement of such an effect.

3.6.2 Bearing flexures

A FEA concerning the bearing flexures has been carried out by the bearing providing company, considering 5 bench inclinations: 0, 25, 30, 35 and 60 degrees. The reasons of these angles choice are the following:

- the overall range is driven by the maximum tilt which the bench will experience at the LBT, which is 60°;
- the small 5° steps around the mid-range position are due to the maximum altitude change during the longest scientific exposure. This differential tilt is less than 5 degrees (considering an exposure of 20 minutes, and the impossible but conservative case in which all the movement of the star (15°/hour) is along the altitude movement, during 30 minutes the telescope altitude will move of 5°).

The results of the FEA are expressed as the differential movements of one node, positioned in the GWS center of gravity (see Figure 3.5), which are reported in Table 3.3.

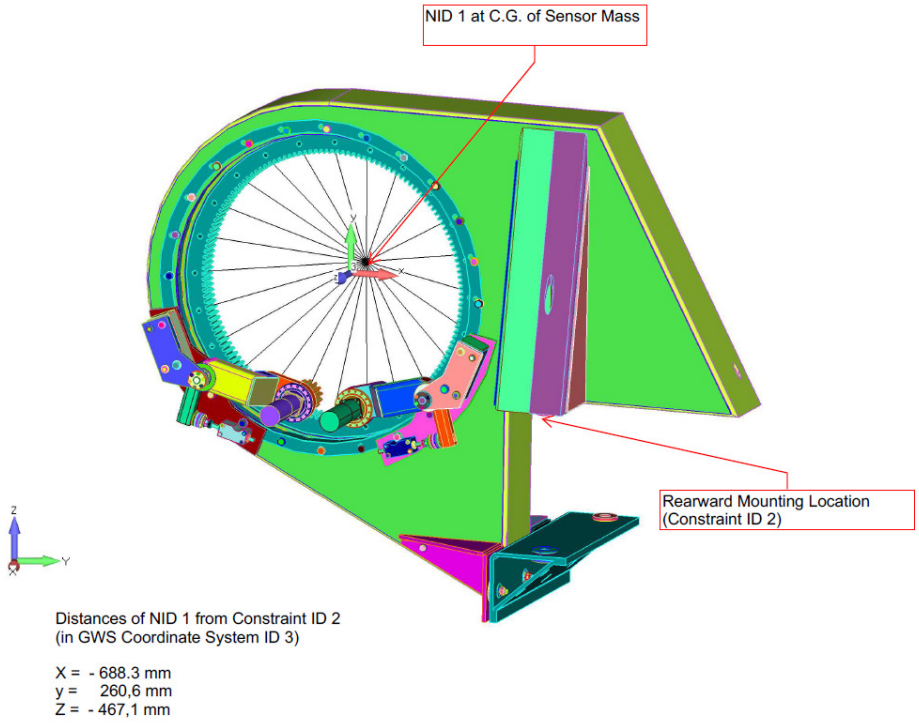

Figure 3.5: Position in the GWS local coordinate system of the reference node (NID1) for the bearing FEA. The position of the constraint closest to such a node is shown too.

The typical differential shift during an exposure is, then, about 15.5 μm for the considered node (the only one we can refer to), corresponding to a differential tilt (estimated considering the distance of the node from the closest constraint in which the bearing is fixed to the bench - 872mm) of 3.7". As usual, in this error budget, we're interested in the differential tilt of the SEs, one with respect to the other. Considering the local tilt of the structure with respect to the coordinate system as linearly increasing with the distance from the constraint, we can assume that the SE fixed at the maximum distance from the bearing-to-bench fixing points (distance $\sim$ 1150 mm) experiences a tilt of 4.9", while the SE which is closest to the bench fixing point (distance $\sim$ 400 mm) experiences a tilt of 1.7", resulting in a differential tilt of about 3.2". The effect on the pupil is a blur of **3.2μm**.

3.6.3 Star Enlargers flexures

- SE tilt due to support flexures: SE support flexures cause 40μrad tilt for 90° rotation. Maximum rotation angle during observation is 60° and SE tilt becomes approximately 2/3 of 40μrad, translating into a **6μm** blur at the level of the pupil.

- SE tilt due to ring flexures: 6 SE experience no tilt due to ring flexures, while the other 6 have 60μrad tilt in a common direction. Differential effect is 30μrad. At 60° rotation, the estimated tilt is approximately 20μrad, corresponding to a **4μm** blur onto the pupil.

Table 3.3: Table summarizing the bearing FEA results in term of shift of the considered reference node.

Inclination range	X	Y	Z
0°-30°	-38 μm	-9 μm	92 μm
30°-25°	-6 μm	-4 μm	14 μm
30° position	0 μm	0 μm	0 μm
30°-35°	7 μm	5 μm	-13 μm
30°-60°	35 μm	40 μm	-66 μm

- SE tilt due to stage flexures: the flexures of the linear and tip-tilt stages coupled together for different orientations with respect to the gravity vector have been measured by the MPIA team in Heidelberg. The highest differential tilt, retrieved for different orientations of the tip-tilt and the linear stage with respect to the inclination axis, is 24 arcsec for a complete 60 degrees range of inclination. This reduces to about 4 arcsec of tilt if the maximum differential inclination which the system can experience during one exposure is considered. The effect of such a differential tilt of the SEs, during an exposure, translates into a pupil blur of $\mathbf{4\mu m}$.

3.6.4 Annular mirror flexures

The requirements for the annular mirror mount flexures are summarized as follows:

- 2' over 60°. Goal: 1' over 60°, with T-T remote adjustment
- 15" over 60°. Goal: 10" over 60°, without T-T remote adjustment

Both these cases result into a pupil blur during an exposure of less than 1/20 of sub-aperture, that is to say 2.4μm. As for the GWS overall tip-tilt, however, such effect can be characterized and compensated, since it affects all the SEs in the same way.

3.7 Overall Error Budget

All the described source of blur on the four re-imaged pupils have been introduced in a complete Error Budget. This computation has been performed assuming conservatively the maximum pupil sampling (24×24), corresponding to the minimum sub-aperture size of 48μm. The conversion from pupil blur to WaveFront Error (WFE) has been accomplished according to the relation shown in Figure 3.6. The overall WFE result allows to estimate the achievable Strehl Ratio in this configuration, according to the following expression:

$$SR(\lambda) = e^{-\left(\frac{2\pi \cdot WFE}{\lambda}\right)^2}$$

One can notice that some of the considered items are, in fact, not introducing any applicable blur onto the pupil, in most of the cases because they are acting on the WFS linearity side, in the sense that such sources of error do not affect the pupil resolution, but introduce a low

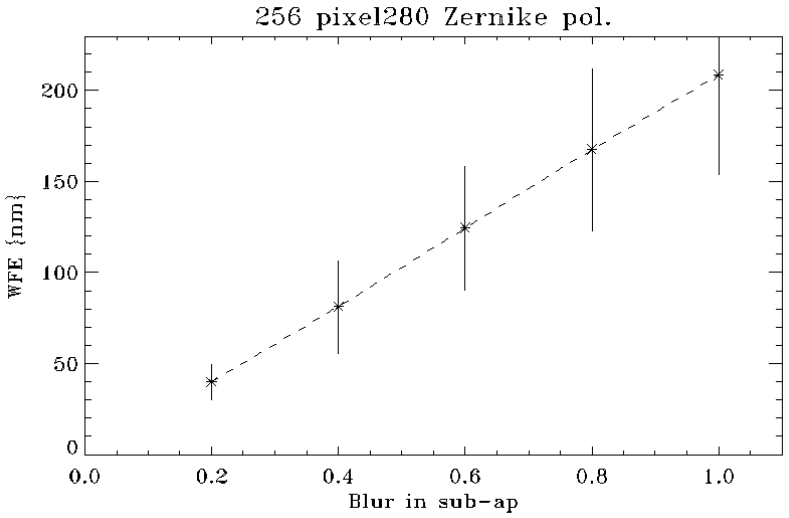

Figure 3.6: Relation between blur in sub-apertures and WFE.

order signal (tip, tilt defocus) onto the WFS, which can be either calibrated and subtracted or simply neglected, since the GWS is not asked to retrieve the very low order aberrations. These sources of error, however, have to be kept under control because they could exceed the linearity range of the WFS. The result of our Error Budget computation is that the expected Strehl Ratio in the J and K bands is 0.71 and 0.89, respectively.

In the next Chapters will be described the test made to verify the compliance of the SEs and PR-I subsystems performance with their requirements, together with all the alignment procedures concepts and characteristics, compared with the goals of each phase.

Table 3.4: GWS pupil blur Error Budget

Error source	blur [μm]	blur[sub-ap]	WFE [nm]
GWS Components			
SE diffraction	7	0.15	30
Linear stages wobble	5	0.10	22
Pyramid chromatism	6	0.13	26
Pyramid vertex angle	5	0.10	22
Pyramid face orthogonality	1	0.02	4
GWS internal alignment			
SE enlarging factor k	5	0.10	22
SE relative tilt	5	0.10	22
Pyramid orientation	5	0.10	22
PR optical quality	13	0.27	57
Thermal effects			
SE lens misalign. (thermal)	4	0.08	18
Linear stage wobble (thermal)	/	/	/
PR optical quality (thermal)	7	0.15	31
GWS misalignment wrt LN optical bench			
Mismatch DM-WFS	5	0.10	22
GWS global defocus	N/A	N/A	N/A
GWS global tilt	N/A	N/A	N/A
GWS global de-center	N/A	N/A	N/A
Pupil matching on WFS	5	0.10	22
Bearing contribution			
Bearing wobble	1	0.02	4
Bearing runout	3	0.06	13
Bearing non-uniform rotation	N/A	N/A	N/A
Flexures			
GWS flexures	12	0.25	53
Bearing flexures	3.2	0.07	14
SE tilt due to support flex.	6	0.13	26
SE tilt due to ring flexures	4	0.08	17
SE tilt due to stage flexures	4	0.08	17
Annular mirror flexures	N/A	N/A	N/A
TOT WFE			**117**
			SR@J $\approx$0.71
			SR@K $\approx$0.89

Chapter 4

Star Enlargers

As described in Section 2.4.2, the Star Enlarger in an optical system used to enlarge the guide star image on the pin of the pyramid, in order to ensure a large linearity range of the WFS, keeping a reasonable pupil image diameter. Each Star Enlarger consists of 2 lenses (SE1, f = 13 mm, and SE2, f = 162.5 mm) and a refractive pyramid, mounted on three different mounts, all aligned on a mechanical support. This Chapter describes the procedure used for the alignment of the 12 SEs of the first GWS (namely the right "DX" GWS of LINC-NIRVANA).

4.1 Star Enlargers alignment concept

SEs alignment tolerances have been obtained after a Zemax Montecarlo analysis, in order to keep the SE performance inside the requirements described in Chapter 3, in terms of SE diffraction, introduced aberration and enlarging factor repeatability. The main SE alignment tolerances are reported in Table 4.1.

The concept behind the procedure used for the SEs internal alignment is to realize a setup in which, in each phase of the alignment, a focused beam is produced on a test CCD, alternatively introducing and removing some setup lenses, according to the SE lenses which are already integrated inside the system in the considered alignment phase.

Table 4.1: SE alignment tolerances.

Item	tolerance
Distance lens 2 pyramid	±21 mm
Distance lens 1 lens 2	±0.1 mm
Relative centering lens 1 lens 2	±0.1 mm

The positioning accuracy of the pyramid with respect to the second lens of the star enlarger has been computed as the corresponding depths of focus (F/187.5 output). The tolerances on the relative separation and centering between the two lenses of the star enlarger are related to the chief ray exit angle at the output of the star enlarger, using the SE global tilt during the overall alignment as a compensator [24].

4.2 Star Enlargers AIV

The Star Enlarger alignment setup components are summarized in the following:

- Laser on a XY mount;
- Beam Expander;
- CCD Camera (Electrim 2000S, 1000x1000 pixels, pixelsize = 8μm) on a mount;
- 1 folding mirror;
- 2 perforated plates (each of them with two holes) on a repositionable holder:
  - first plate holes separation: 3.72 mm;
  - second plate holes separation: 9.89 mm;
- 1 lens f = 76.2 mm (L1, hereafter) on a repositionable linear stage
- 1 lens f = 480 mm (L2, hereafter) on a repositionable linear stage
- 1 lens f = 200 mm (L3, hereafter) on a repositionable linear stage
- Star Enlarger on a xyz-tip-tilt stage

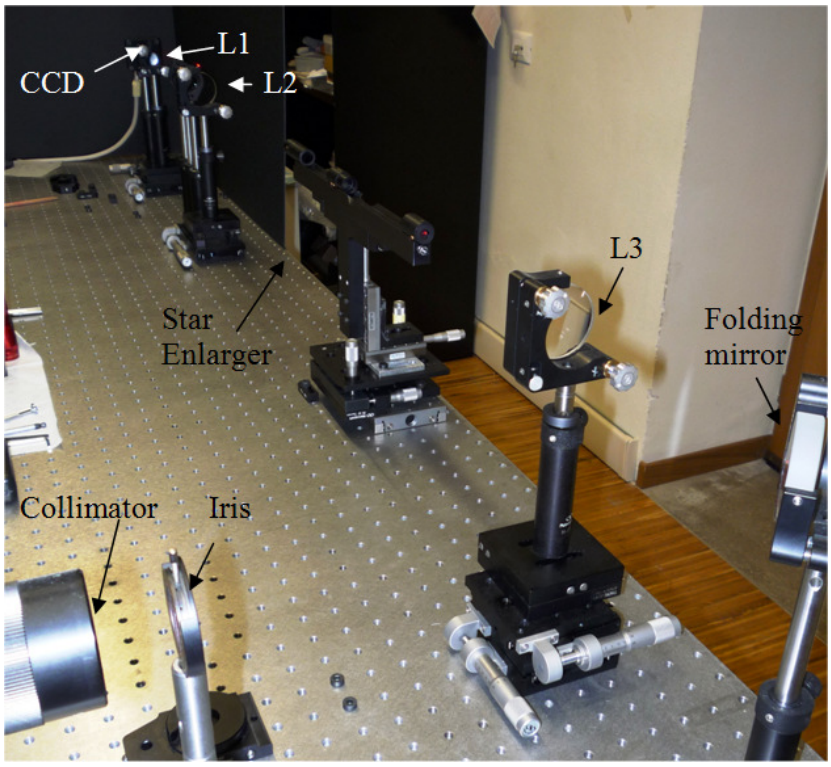

Figure 4.1: Star Enlarger alignment setup

The SE alignment procedure main steps are listed and described in the following, where the tolerances listed in 4.1 are translated into operative requirements for the various phases.

The compliance of the actual alignment with these requirements is verified and reported at the end of this Chapter, in Table 4.2.

1. Laser collimation: we put a plate, with two holes (separation = 3.72 mm) out of the laser beam expander and than put the camera alternatively close to the plate and 2010 mm far, measuring the distance between the two spots, as shown in Figure 4.2. Once the beam is collimated,the distance between the two spots is the same in both the CCD positions. The power of this procedure is its independence from the diffraction effect, since the relative distance between the spots barycenter is considered, and not their diameter. The required precision for the collimation is 4.4 arcsec, to ensure a proper SE lenses relative focus, which translates into a difference between the spots distances measured in the two camera positions higher than 5.3 pixels of our CCD test camera.

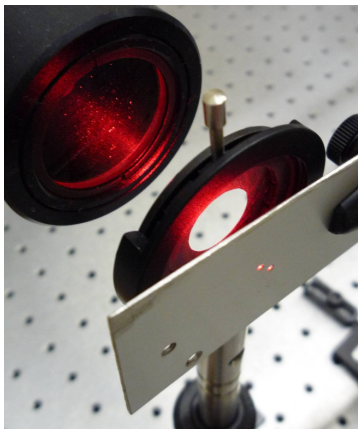

Figure 4.2: The plate with two holes (distance = 3.72 mm) masking the laser beam in the position far from the CCD.

2. We placed L1 in order to focus on the camera and we aligned it (Figure 4.3, a) minimizing the spot diameter, estimated using a gaussian fit on the image, onto the CCD. We define δ_{L1} as the decentering of L1 from the laser beam axis.

3. We then took off L1 and repeated the operation with L2 (Figure 4.3, b). The spot position on the CCD camera should be the same as the previous step (it means that the two lenses of the setup are both aligned respect to the laser beam). δ_{L2} is the decentering of L2 from the laser beam axis.

4. Mechanical alignment of the main part of the star enlarger (i.e. the rail): we fixed the SE rail to the system of stages that controls all the degrees of freedom. Then, we checked that the rail was parallel to the optical axis by moving a pinhole back and forth on the rail itself: the spot on the CCD camera should not move. The centering of the rail respect to the laser beam has been checked with the pyramid inside its holder, since this component has a little range of movement in XY directions inside its mount.

5. Mechanical alignment of SE2 lens inside its holder: we fixed the lens holder, shown in Figure 4.4, on the rail with a couple of drops of glue, in the proper position just measuring it with a ruler. We then inserted SE2 lens into its holder on the rail, and

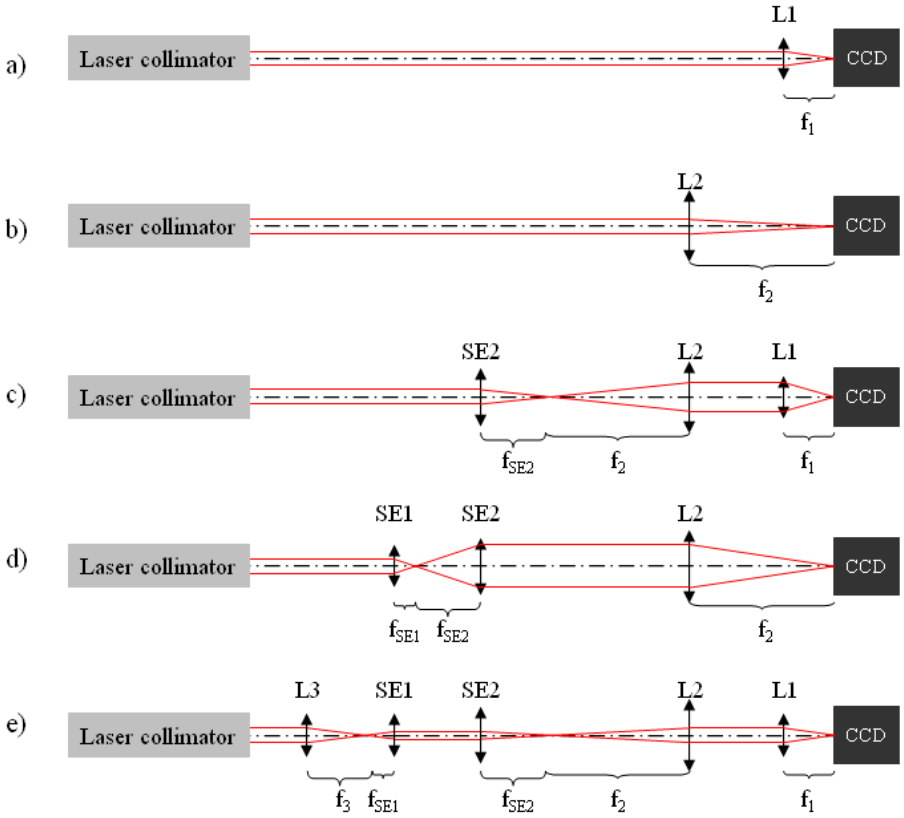

Figure 4.3: SE alignment procedure.

illuminated it with the collimated laser beam. The center of the circular shadow of the external barrel defined the mechanical axis of the SE2 assembly. The central portion of the laser beam was focused by the SE2 into a spot which is supposed to be centered in the shadow of the barrel. The main target is that when the SE2 assembly is put on the rail the focused spot is situated on the optical axis defined by the laser beam and to which all the other setup components are aligned. To check this requirement we put a screen on the rail. We double checked the lens tip-tilt by looking at the back-reflected spots, and we acted on the 6 screws of the barrel in order to minimize the lens tip-tilt.

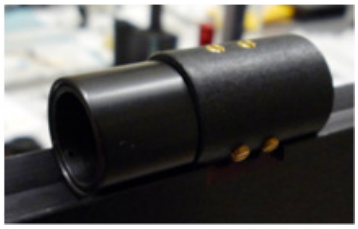

Figure 4.4: An SE2 mount, with the 6 screws used to compensate the decentering of the lens inside its holder.

6. We then put on the optical path both L1 and L2; L2 focal point has to coincide with

SE2 focal point, then we moved the entire rail in order to align in focus SE2 (Figure 4.3, c).

7. We then took off L1, put on the optical path SE1 and aligned it, as shown in Figure 4.3, d. First of all, we checked the tilt of the lens (just to check it was not too big). The lens mount has a focusing and a centering movement. One can act on both of them to align the lens respect to SE2. To achieve the best position along the optical axis, we took a certain number of measurements of the spot diameter at different positions of the lens along z-axis, then the measurements were interpolated with a quadratic curve. In that configuration, Δ_2 is the displacement of the spot on the CCD from the position

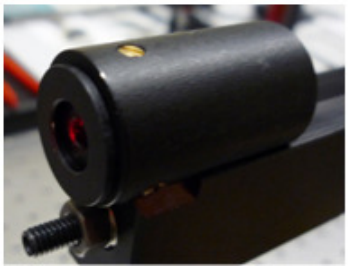

Figure 4.5: An SE1 mount, with the 3 screws used to compensate the decentering of the lens inside its holder; the picture shows also the screw used during the focusing procedure.

of the laser beam axis:

$$\Delta_2 = \frac{\delta_{SE1-SE2} \cdot f_2}{f_{SE2}} + \delta_{L2}$$

we were interested in the $\delta_{SE1} - \delta_{SE2}$ value, that defines the decentering between the two lenses of the SE. Comparing the position of the spot on the CCD in step 3 (δ_{L2}) and in step 7 (Δ_2), one can measure

$$x = \frac{\delta_{SE1-SE2} \cdot f_2}{f_{SE2}}$$

It can be compared with the relative centering tolerance of SE1 and SE2:
$\delta_{SE1-SE2} < 0.1\text{mm} \Rightarrow x < 0.1 \cdot 480/162.5 \Rightarrow x < 0.29\text{mm} \approx 36$ pixel
The so defined x-values for each SE (that is to say for each couple SE1-SE2) were always in specification ($x < 36$pixel).

8. We then put on the optical path L3 in a way that its focal point coincides with SE1 focal point and aligned it, like in Figure 4.3, e.

9. We took off L1, put the perforated plate (distance of the holes = 1263.7 pixels = 10.1mm) just before L3 and measured on the camera the distance between the two spots, to check the magnifying factor (k) of the SE. With the previously used definitions:

$$k = \left(\frac{1263.7}{d}\right)\left(\frac{f_2}{f_3}\right)$$

The required value is k = 12.5.

10. In order to place the pyramid, we placed the pyramid on its holder. The diameter of the beam which illuminated L3 had to be ≈ 13 mm so as to reproduce the correct entrance F/# of the GWS. In that configuration we checked the centering of the pyramid: the four pupils that appeared on the CCD camera had to have the same intensity. The pyramid alignment along the optical axis has not a strict tolerance, because of the very high depth of focus of the incoming beam (F/187.5).

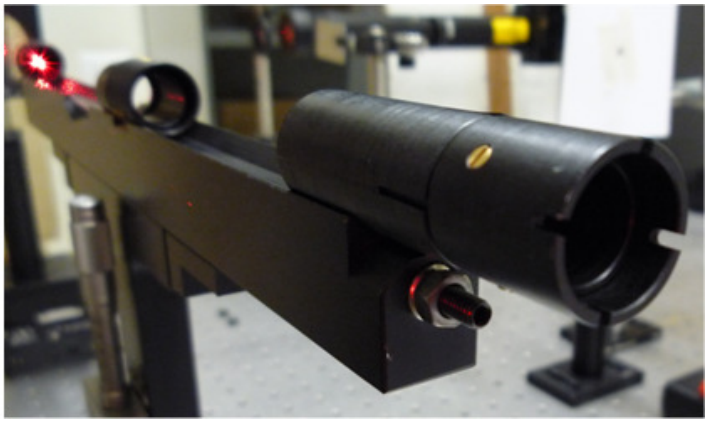

Figure 4.6: SE assembly. In the foreground, the pyramid mount, with the 3 screws for centering (acting directly on the pyramid itself) and the screw for focusing.

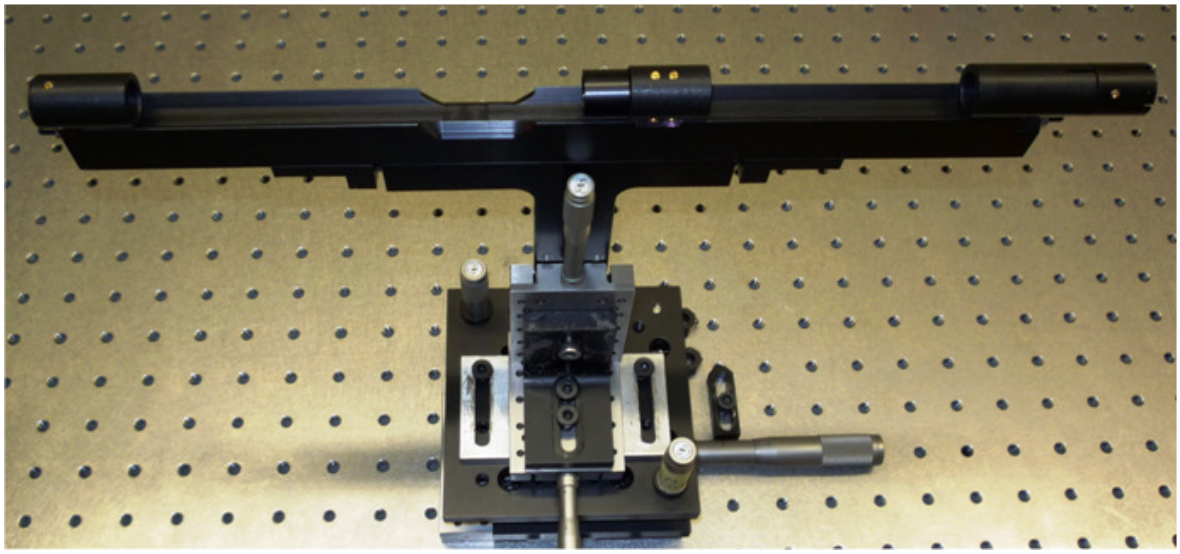

Figure 4.7: SE assembly. Also the x-y-z-tip-tilt system is shown.

4.2.1 Measurements and conclusions

Table 4.2 shows the identification number of each optical component (that is to say the two lenses and the pyramid) of the Star Enlargers and some significant measurements taken during the alignment procedures.

- *collim* is the difference between the distances of the spots as measured in the two position of the camera during the collimating operations described in section 4.2, step 1. Requirements impose this value to be lower then 5.3 pixels.
- *mech* is the distance between the two positions of the spot projected into the camera during the mechanical alignment of the rail, described in section 4.2, step 4.
- x is the parameter which describes the relative centering of SE1 and SE2, as introduced in section 4.2, step 7. This value is required to be smaller then 36 pixels.
- d is the distance between the spots measured in section 4.2, step 9.
- k is the magnification factor of the star enlarger. It is supposed to have a value of 12.5, but the real requirement is its repeatability, which has to be better than 1/240.

Table 4.2: Main verification measurements taken during the SE alignment procedures.

	Components			Δcollim	Δmech.	x	d	k
	SE1	SE2	Pyramid	[pixels]	[pixels]	[pixels]	[pixels]	
SE#1	1	29	F3	3.2	2.2	1.0	242.5	12.51
SE#2	2	2	F4	1.9	1.4	1.0	242.3	12.52
SE#3	3	3	F7	0.2	1.0	1.4	242.0	12.53
SE#4	5	4	F8	1.7	1.4	1.4	241.5	12.55
SE#5	9	23	F21	0.1	1.0	1.0	242.9	12.49
SE#6	22	25	F25	1.3	2.2	1.4	242.3	12.52
SE#7	16	6	F26	3.3	2.0	2.0	242.7	12.50
SE#8	17	12	F30	3.1	2.2	1.0	242.8	12.49
SE#9	21	14	F31	0.2	1.0	1.0	241.7	12.55
SE#10	24	17	F32	3.7	2.0	2.0	242.7	12.50
SE#11	25	22	F18	3.2	1.4	1.0	242.6	12.50
SE#12	30	13	F2	3.4	1.4	2.2	242.3	12.52
Tolerances				<5.3		<36		1/240 rep.

As summarized in Table 4.2, both the requirements about the setup beam collimation the SE lenses relative decenter are fulfilled. Concerning the enlarging factor k, the mean resulting value is $k = 12.51$ and the measured RMS repeatability is 1/605, far lower than the 1/240 requirement.

After the alignment verification, a last test has been performed to check the SE FoV width, required to be higher than 1 arcsec (goal:1.4"). By design, the SE stop surface is placed on the second lens, whose clear aperture is depending on its axial locking cap. The measured

actual cap diameter has been introduced in the Zemax file, as a circular aperture (see Figure 4.8), giving a non-vignetted FoV of 1.3 arcsec and a 50% vignetting level FoV of 1.4 arcsec.

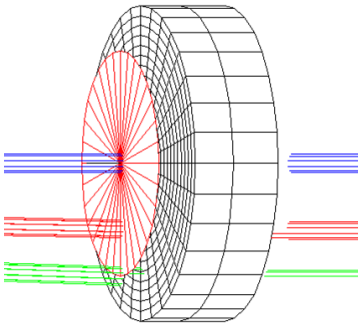

Figure 4.8: SE2 axial locking cap clear aperture is introduced in the Zemax file as a circular aperture 10.5mm wide.

The SE alignment has been completely realized in the Observatory of Padova laboratories, and the performed verification test results are inside the tolerances set before the alignment, to fulfill the requirements listed in the Error Budget (Section 3).

Chapter 5

Pupil Re-Imager

As described in Section 2.4.2, the Pupil Re-imager (PR-I) is a folded Schmidt camera, made up of a parabolic mirror and a refractive prime focus corrector, which optically co-add the light coming from each of the 12 GWS star enlargers, folded by an annular flat mirror. This subsystem re-images the four pupil images on a 128x128 pixel detector (Scimeasure CCD50). The optical design of the PR-I is shown in Figure 5.1. The mechanics of the PR-I is equipped with the following adjusting systems:

- re-centering of the parabolic mirror;
- tip-tilt of the parabolic mirror (notice that it allows to act also on the positioning of the parabolic mirror along the optical axis);
- tip-tilt of the folding mirror;
- tip-tilt of the 4-lenses corrector as a whole;
- tip-tilt of the CCD;
- re-centering of the CCD (motorized);
- re-focusing of the CCD (motorized).

After the components procurement and subsequent tests, a draft version of the Error Budget of the entire GWS was realized. From that estimation, the required Pupil Re-Imager optical quality should lead to a maximum RMS blur of 25μm over the four pupils re-imaged on the CCD. The possible deterioration on the optical quality due to alignment indetermination depends on the combination of defocus, tilt and de-center of the Parabolic mirror with respect to the Prime Focus Corrector. The final blur on the pupils, due to PR-I optical quality, can be verified also without the rest of the GWS. If you feed the PR-I with a wide collimated beam, resembling one of the directions of the rays that will enter the PR-I itself, these rays should focus on a diffraction-limited spot in the focal plane, if the PR-I is perfectly aligned. The tolerance on that spot RMS radius is exactly the same as for the RMS blur of the pupils, as it can be easily verifiable geometrically. The alignment concept is to illuminate the PR-I with a wide collimated beam and to align the Parabolic Mirror with respect to the Prime Focus Corrector in order to optimize the optical quality along the field of view of interest. One should notice that the FoV of the PR-I as a stand alone camera is not the 2' to 6' FoV of

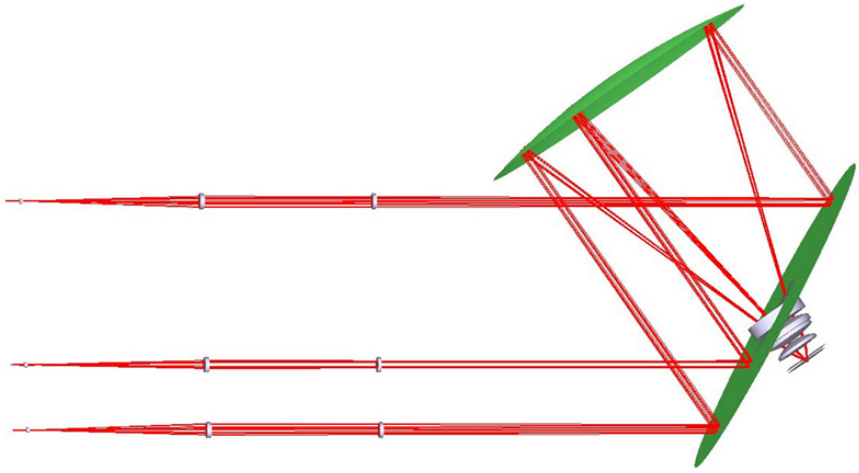

Figure 5.1: Pupil Re-imager optical design.

the GWS. The PR-I FoV, indeed, is depending on the SE exit F/# (187.5) and the divergence angle of the pyramids (about 0.566°), and it corresponds to a 0.88° FoV. Hereafter, we will consider a procedure in which a collimated beam is focused by the PR-I; the goal of this procedure will be to have a RMS spot radius lower than 25μm in a FoV which is 0.88° in diameter.

5.1 Pupil Re-Imager assembly

5.1.1 Mounting of the mechanical supports for both the folding and the parabolic mirrors

The two mounts are very similar. Each mirror had to be glued to three invar pads, placed at 120° on the back of the mirror itself. In Figure 5.2 the mirrors mount assembly is shown. The pads are connected to the main structure with two preloaded springs, keeping the pad itself always in contact with a small sphere, in order to minimize mechanical stress on the glass due to differential thermal expansion between the mirror and the cell. The mirrors are retained in their correct centered position by three centering screws partially made up of a plastic material (delrin) which compensates for different radial thermal expansion between the mirror and the cell. The parabolic mirror cell is composed of two parts, that have been fixed one to each other with 16 M4 screws: the back part of the cell (the one with the three pads) and the barrel. The three screws behind the pads of the parabolic mirror mount are longer than the flat mirror ones, in order to allow a focusing movement of the parabola during the alignment procedure.

5.1.2 Glue the mirrors on their pads

As already said, the back side of each of the two mirrors had to be glued to three invar pads. A two component adhesive was used. First of all we put the mirror on the pads

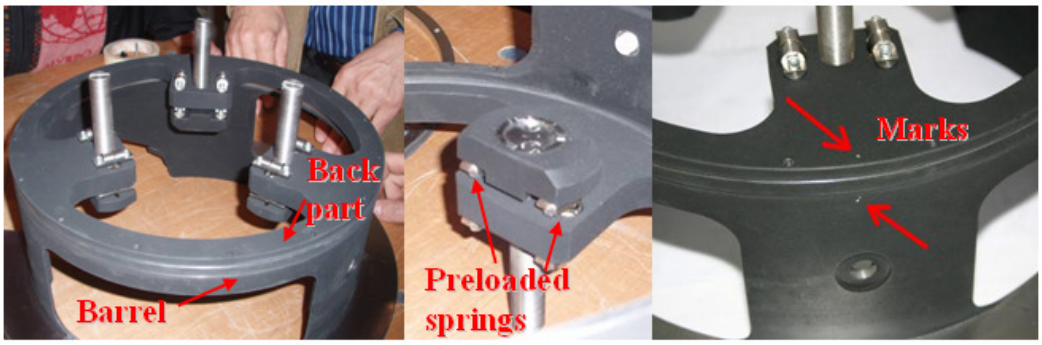

Figure 5.2: On the left, the whole mounting cell for the parabolic mirror is shown. One can see the three long screws connected to the invar pads. In the central figure, one of the invar pads on which the mirror had to be glued. On the right, the marks used to recognize the correct relative position of the cell components during the mounting operations.

(with the springs in their rest position) and regulated the three centering screws in order to approximately center the mirror. After that, we removed the mirror and accurately cleaned the three pads from dust. Then we mixed the two components the glue was made of in a ratio 3/2 in volume and placed them with a spatula in the three arcs between the three points of each pad on which the mirror had to lay. The work life of this mixed material at 22°C is approximately 1.5 hours. We re-put the mirror on the three pads and left it in that position for about 7 days, that was the recommended cure time at 24°C. Concerning the flat mirror, special care had to be used to glue it in the correct position in terms of rotation around the axis orthogonal to the surface, crossing the center of the mirror. This care was due to the fact that the hole in the center of the mirror had a specific orientation respect to the cell. The PR-I mirrors gluing is shown in Figure 5.4.

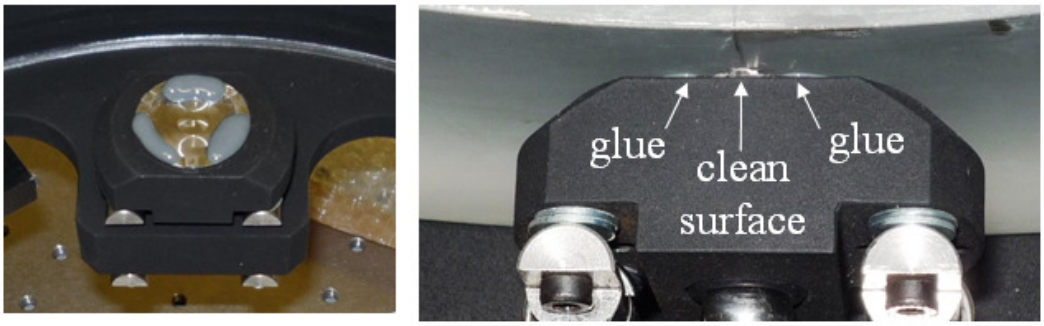

Figure 5.3: Pictures of one of the pads during the gluing procedure. On the left, the glue as it was disposed on the pad; on the right, the pad after the mirror positioning.

5.1.3 Flat mirror mount positioning

The structure holding the folding mirror cell is equipped with a tip-tilt mechanism, realized moving a flange holding the cell to the main structure of the pupil re-imager at three attaching points (placed at an angular distance of 120°), connected to the fixed reference through

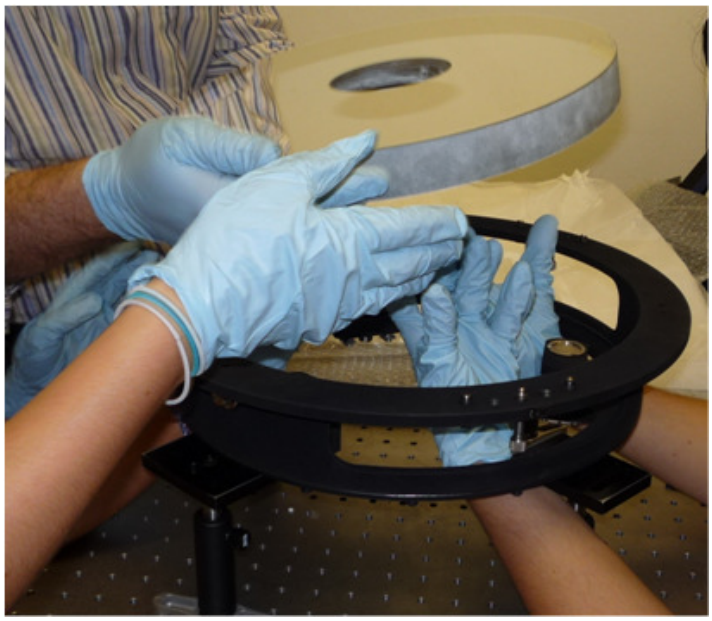

Figure 5.4: Lots of hands holding the folding mirror during its gluing inside the cell. A special care was used to pull it down and glue it in the correct position in terms of rotation.

5 screws. The flange orientation is defined by the labels F1, F2 and F3, incised on both the main structure and the flange itself. Concerning the tip-tilt system, a central M6 screw with a spherical flattened tip is used to initially fix the flange and two M8x35 screws provided with spring washers, are used to pre-load the whole mechanism. The central screw is used to perform the alignment operations (0.35mm step), then two headless screws with a spherical flattened tip are placed in touch with the reference plane to secure the position. The mechanism is shown in Figure 5.5.

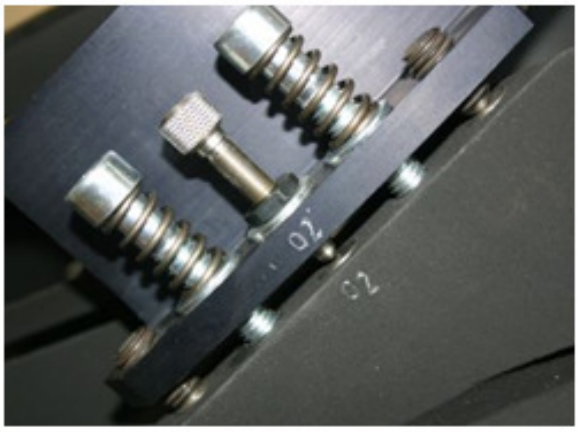

Figure 5.5: The five screws mechanism used for the tip-tilt alignment of the folding mirror and the prime focus corrector.

5.1.4 Prime focus corrector positioning

The barrel holding the 4-lenses corrector is fixed to the flange that keeps it in the correct position inside the hole of the folding mirror with 6 flat head screws, so as to be placed under the flange itself. The flange orientation is defined by the labels O1, O2 and O3, incised on both the main structure and the flange itself. The tip-tilt mechanism is the same used also for the folding mirror holding structure (see Figure 5.6).

Figure 5.6: On the left, the flange holding the prime focus corrector, on the right the same flange already mounted on the pupil re-imager main structure.

5.1.5 Parabolic mirror positioning

The mounting cell first has to be fixed to the bottom part of the pupil re-imager main structure with six M8 micrometric centering screws, as shown in Figure 5.7, taking into account that the correct orientation of the cell with respect to the main structure is defined by the incised marks. To allow the centering operation of the parabolic mirror, keeping the mirror mount in contact with the main body of the pupil re-imager, a blocking flange (whose orientation is defined by the labels P1, P2 and P3) had to be fixed with 4 preloaded M8x45 screws. When the centering operation are finished, 6 blocking M8x25 screws are introduced to secure the flange.

5.1.6 CCD holding structure positioning

The CCD holding structure is composed of an annular flange, held by three supports fixed on the pupil re-imager main structure with 4 M8x30 screws, and an XYZ system of linear stages, that will be used for the centering and focusing operations. The correct orientation of the structure is defined by the labels S1, S2 and S3. In order to minimize the flexure stress on the structure holding the CCD during the GWS de-rotation, three astatic levers have been introduced on the original mechanical design. In condition of not acting gravity the a-static levers have not to be preloaded in the direction of the support of the CCD.

Figure 5.7: On the left the bottom part of the pupil re-imager is shown; on the right, there is the flange used to keep the parabolic mirror cell in contact with the main structure during the centering operations.

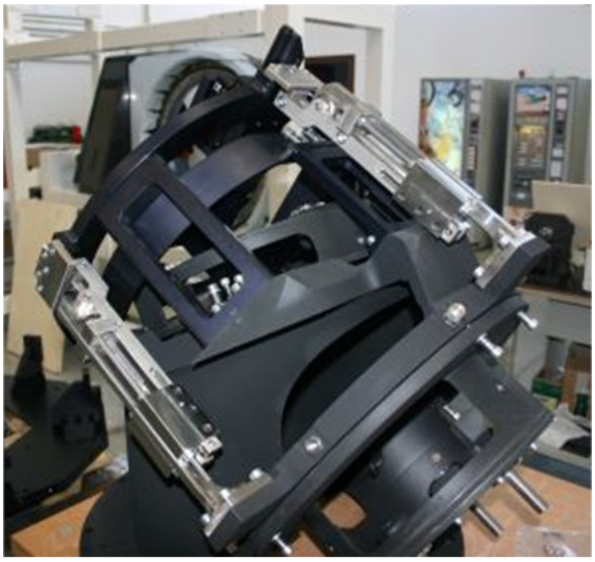

Figure 5.8: Pupil re-imager unit.

5.2 Pupil Re-Imager Alignment concept

As already said, the Pupil Re-Imager optical quality was required to guarantee a RMS spot radius lower than 25μm over the complete FoV of the PR-I intended as a stand-alone camera. We explored several ways to check separately defocus, tip-tilt and de-centering of the Parabolic Mirror with respect to the Prime Focus Corrector, to define the best-achievable combination of tolerances for the three of them in order to be sure we can reach the goal we set at the beginning. We fixed the focus tolerance at 0.5mm, which is achievable with mechanical positioning of the Parabola. The alignment procedure explained in the following should allow us to reach a final alignment better than 0.1mm in de-centering and 0.02° in tip-tilt.

The procedure is divided into 6 main Phases, described in the following sections. The overall idea is to illuminate the PR-I with a collimated beam and to align the Parabola to

the Objective (Prime Focus Corrector) by checking the optical quality over the FoV and the amount of coma on a de-focused image of the reference spot on axis. This fact poses a problem: we need to have a reference spot, within a certain precision, close to the center of the field, being the aberrations field dependent. This means that there must be a preliminary procedure that has the purpose to align the reference beam arriving on the parabola (which means the 2 flat mirrors which are folding the light towards the Parabola, as it will be clearer in the following, and as it can be seen from Figure 5.20 where the optical setup that will be used is shown). From Zemax computation we have taken as a maximum off axis error $\pm 0.3°$, which is compatible with having a RMS spot radius lower than 25μm over the complete FoV ($0.88°$, at the edges of the four pupils re-imaged on the final CCD), once all the other source of error are added and the CCD focus is optimized, as it can be seen in Figure 5.11 and Figure 5.10. The off axis of the reference incoming beam is produced by several sources of error, which are dependent on the particular procedure adopted for the alignment, and will be shown in the following sections. This is why, to define this procedure, we firstly double-checked each error source, when possible with optical test on the bench, otherwise with Zemax computation, in a way to have a total budget in agreement with the maximum acceptable off-axis of the reference beam of $\pm 0.3°$. To better understand the various sources of error, we have to outline the concept of the alignment, that will be developed in 6 different Phases, and by the means of an optical setup which foresees the usage of an additional flat folding mirror (with the aim of folding the light toward the PR-I), of an optical fiber (acting as reference source) and of an off-axis parabolic mirror (collimating the beam).

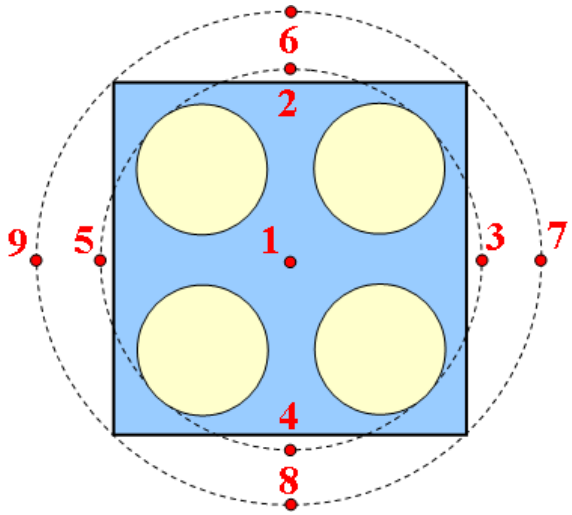

Figure 5.9: Locations of the field considered in Figures 5.10 and 5.11. The circles represent the 4 pupils positions and the blue square the CCD50 area.

The optical setup is composed of an optical fiber illuminating an off-axis parabolic mirror, which is collimating the beam toward the PR-I itself, and a wide flat mirror folding the beam inside the PR-I itself; this folding mirror has tip-tilt capabilities, in order to move the reference created by the fiber along the whole PR-I field of view. A test camera, with a very high spatial sampling is used instead of the final CCD EEV50, in order to have the highest possible resolution for the evaluation of the images affected by the coma during the alignment procedure.

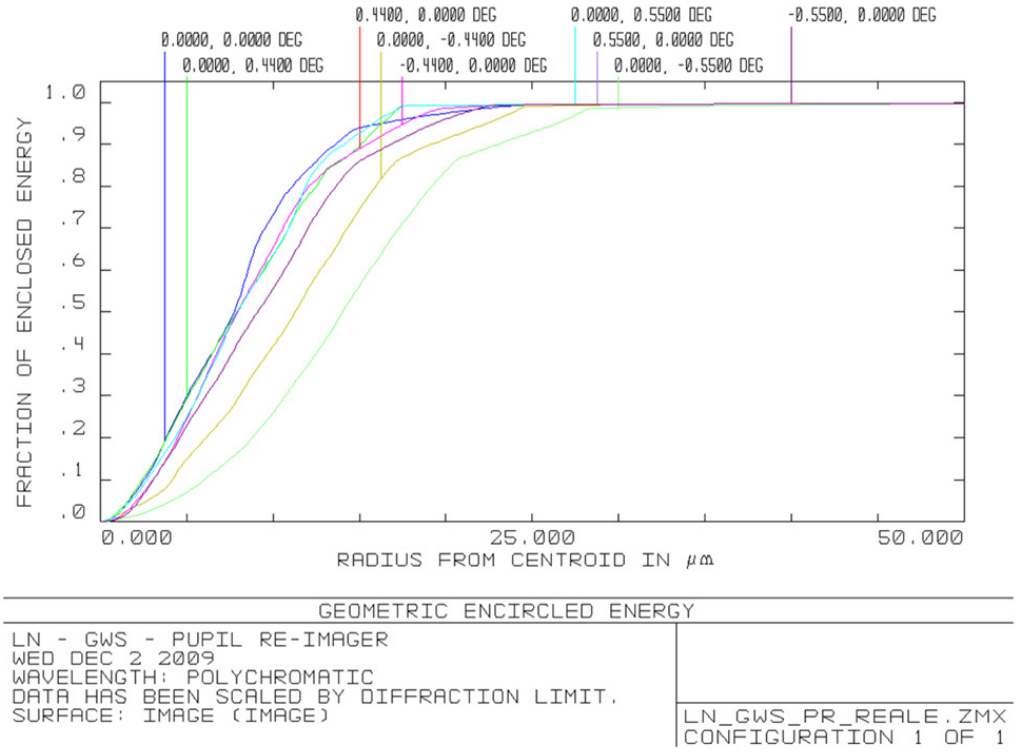

Figure 5.10: Geometric encircled energy in the entire FoV, with 0.5mm of defocus and an alignment obtained with a 0.3 off-axis of the reference incoming beam. The CCD focus has been optimized minimizing the RMS spot radius on the whole FoV. Field 1 represents the on-axis beam, fields from 2 to 5 represent the edges of the four pupils that will be re-imaged by the PR-I on the final CCD, while fields from 6 to 9 are the four corners of the CCD (so, they are already outside the utilized FoV - see also Figure 5.9). Other error sources introduced during Phase 4 and Phase 5 of the alignment procedure are not considered in this spot diagram. These sources introduce an RMS blur contribution smaller than the ones already considered.

The different phases of the alignment are outlined in the following sections, and they reflect what was just mentioned above: the real alignment of the PR-I Parabola is performed in Phase 4 and Phase 5, in Phase 3 is performed the alignment of the two flat mirrors, which must precede the fine-alignment of the Parabola and must be preceded by a pre-alignment, at least in the sense of direction of the beam, of the Parabolic mirror itself. In a certain sense, in the first two Phases of pre-alignment of the Parabola, we do not care about the optical quality in the focal plane and we care instead of the beam direction, treating the Parabola like it is a flat mirror.

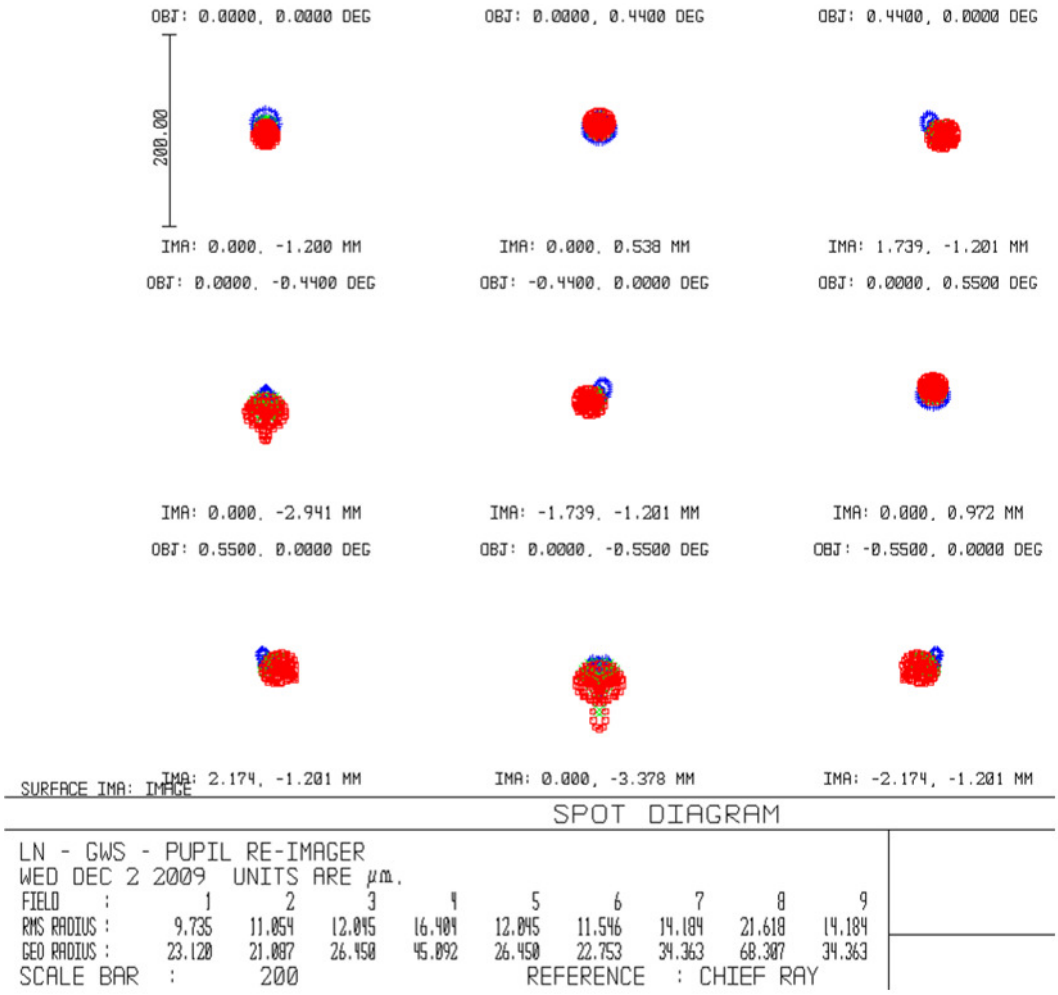

Figure 5.11: RMS spot radius in the entire FoV, with 0.5mm of defocus and an alignment obtained with a 0.3° off-axis of the reference incoming beam. The CCD focus has been optimized minimizing the RMS spot radius on the whole FoV. Field 1 represents the on-axis beam, fields from 2 to 5 represent the edges of the four pupils that will be re-imaged by the PR-I on the final CCD, while fields from 6 to 9 are the four corners of the CCD (so, they are already outside the utilized FoV - see also Figure 5.9). Other error sources introduced during Phase 4 and Phase 5 of the alignment procedure are not considered in this spot diagram. These sources introduce an RMS blur contribution smaller than the ones already considered.

5.3 Pupil Re-Imager alignment

Pupil Re-Imager alignment procedure is described in detail hereafter. Once mounted on the GWS, the pupil re-imager rotates together with the bearing. Beams with a focal ratio F/187.5, coming from the SE, re-form the 4 pupils on the CCD plane, no matter which part of the parabolic mirror reflects them. Because the pupil re-imager rotates together with the pyramids (that is to say the SEs), the positions of the 4 pupils on the CCD are fixed during the rotation. It is not fundamental that the pupil re-imager optical axis matches the bearing rotation axis. They are only required to be parallel. And this can be simply done moving the folding mirror in tip-tilt. The goal of the Pupil Re-imager alignment procedure is therefore to make the parabolic mirror optical axis perfectly match the prime focus corrector optical axis. Obviously, also the distance between the parabolic mirror and the 4-lenses group has to be the nominal one, within a certain tolerance included in the error budget. Otherwise, the distance between the parabolic mirror and the SE is not so strictly defined, since the entrance pupil is set close to infinite. Since the very central part of the parabola can be approximated with a sphere, which obviously doesn't have a unique optical axis, it is necessary to explore a wide area of the parabolic mirror to be able to identify the optical axis itself. The overall idea is to illuminate the PR-I with a collimated beam and to align the Parabola to the Objective (the small Prime Focus) by checking the optical quality over the FoV and the amount of coma on a de-focused image of the reference spot on axis.

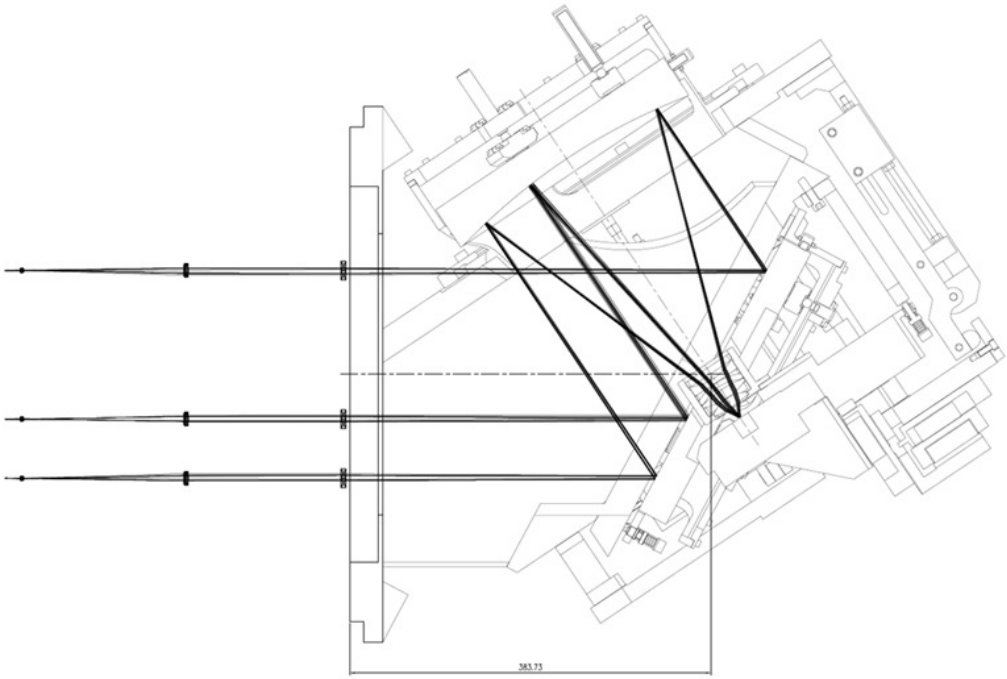

Figure 5.12: Pupil Re-imager opto-mechanical design.

5.3.1 Phase 1: On axis reference definition on the test camera

This phase has the purpose to align and center a test camera to the objective optical axis materialized by a laser beam and, in particular, to define on the CCD the objective optical axis projection. The main steps are the following:

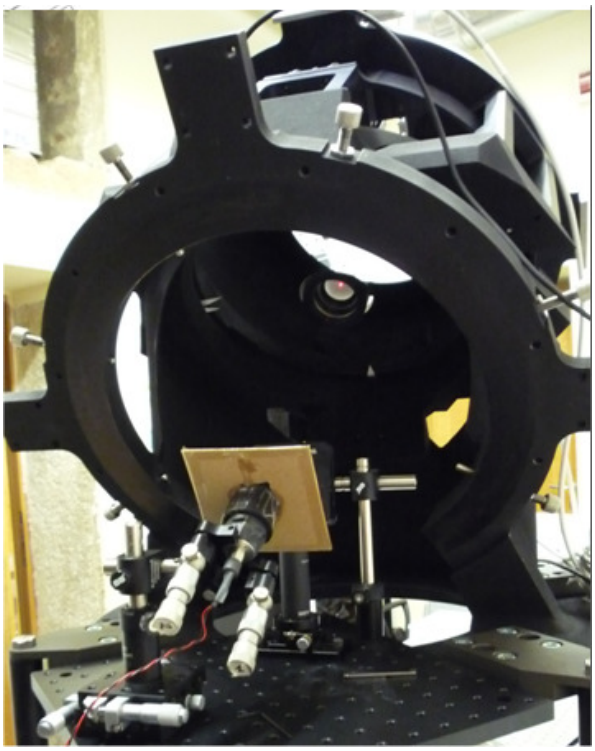

Figure 5.13: Laser source materializing the Prime Focus Corrector optical axis in phase 1A.

A Materialize the optical axis of the objective with a laser source positioned on the optical bench (see Figure 5.13), with a precision of 27μm in centering and 29arcsec in tilt.

- mount a laser on the optical bench with centering and tip-tilt capabilities from the side of the removed PR-I parabola; centering micrometers sensibility: 0.01mm ("shift y" actuator values need to be multiplied by cos(56.2°) in order to obtain the true shift in the y axis), tip-tilt micrometer sensibility: 0.05μm = 0.029 arcsec.
- by observing the back reflected spots materialize the objective optical axis. In order to minimize the alignment error, the alignment has been performed 15 times and the mean values of centering and tip-tilt positions have been used:

Considering the standard deviation of the data ($\pm 1\sigma$):
Centering indetermination: $\pm 32\mu$m
Tip-tilt indetermination: $\pm 3.9\mu$m = ± 22.5 arcsec
Considering the mean values, the corresponding indeterminations are: $st.dev./\sqrt{15}$
Centering indetermination: $\pm 8.3\mu$m
Tip-tilt indetermination: $\pm 1.0\mu$m = ± 5.76 arcsec
Resulting movement of the spot on the CCD: $\pm 5\mu$m

Table 5.1: Test value of the actuators positions, concerning tip-tilt (1μm = 5.8arcsec) and decentering. Please consider that "shift y" actuator values need to be multiplied by cos(56.2°) in order to obtain the true shift in the y axis!

	Tilt x (μm)	Tilt y (μm)	Shift x (mm)	Shift y (mm)
1	103.5	141.0	10.61	6.31
2	104.5	139.5	10.60	6.35
3	103.5	137.5	10.61	6.30
4	105.5	131.0	10.58	6.41
5	103.5	140.0	10.60	6.32
6	105.0	132.5	10.58	6.39
7	105.0	133.5	10.58	6.37
8	105.0	133.5	10.58	6.38
9	104.0	137.0	10.59	6.32
10	104.5	137.5	10.58	6.31
11	102.5	140.5	10.63	6.29
12	106.0	142.5	10.57	6.23
13	104.0	135.0	10.59	6.33
14	101.5	132.0	10.62	6.41
15	102.5	133.0	10.60	6.36
Mean value	104.0	136.5	10.59	6.34
Standard dev.	1.23	3.73	0.017	0.049
Max dev.	2.5	6.1	0.03	0.11

B Center the test camera with the objective optical axis, materialized by the laser, and focus it; record the position of the spot on the CCD (see Figure 5.14). The test camera is mounted on a magnetic re-positionable base, defining the spot position with a maximum error of ±0.55mm. We have to notice that the X and Y axis of the test camera chip are inverted with respect to the definitions of the X-Y axis of the translating motorized system used to move the camera itself. Since we're interested in absolute values of centering and tip-tilt this point is not crucial. This phase required further test.

- Test on re-positionability of the test camera on its magnetic base plate: the graphs in Figure 5.15 show the results of the test on the repeatability of the test camera positioning on its magnetic base plate. A fixed laser beam was going trough the prime focus corrector and formed a spot on the CCD. The camera has been removed and repositioned 10 times and the spot centroid position was computed at each repositioning. The spot centroid moved in a range of 3.26 pixels in the camera x-direction and 5.43 pixels in the y-direction, corresponding respectively to a 7.2μm and a 11.9μ m ranges.
- Test on the movement of the spot due to motorized stages repositioning: the test camera is mounted on a linear motorized stage system in XYZ configuration (1μm=283.298 counts). During the test, each of the three stages has been re-initialized and sent to a specific position 10 times and the position of the spot on the CCD has been computed. Considering all the three contributions in their

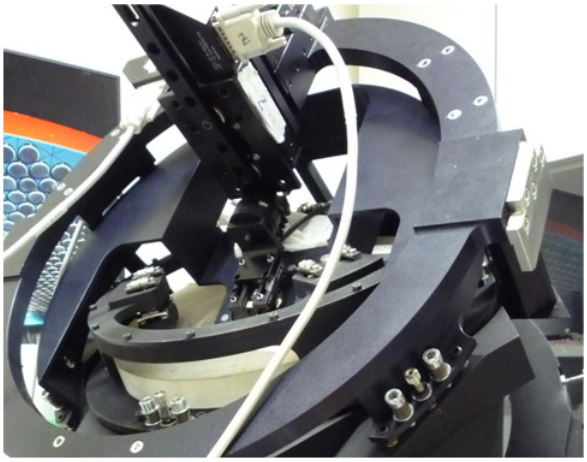

Figure 5.14: Test camera mounted on a repositionable magnetic base plate, which can be moved with the CCD motorized stages in XYZ configuration.

worst possible combination, the spot centroid should move in a range of less than 2 pixels in the camera x-direction and 3 pixels in the y-direction, corresponding respectively to a 4.4μm and a 6.6μm ranges (see Figure 5.16).

- Characterization of the angle between the Prime Focus Corrector optical axis and the z-stage movement axis: This test provides the movement of the spot on the CCD camera during a long (2,500,000 counts = 8.825mm) travel along the direction of movement of the z-stage (resembling the objective optical axis), to characterize the angle between the true movement of the stage and the Prime Focus Corrector optical axis itself. The considered range is far larger than what expected as necessary for the following procedure phases (focusing of the test camera) (see Figure 5.17). The movements of the spot between position500000 (x =1316.39, y =1239.38) and position-2000000 (x =1330.84, y =1223.52) are 15.15 pixels in the x-direction and 16.24 in the y-direction, corresponding respectively to a 33.3μm and a 35.7μm ranges. These values are still far inside the required precision in the camera positioning, even if the 8.825mm range considered is really wide.

The total indetermination on the optical axis definition on the CCD for Phase 1, considering a conservative sum of all the described contributions is $\pm$78μm, corresponding to 14% of the repositioning required precision, which is $\pm$0.55mm.

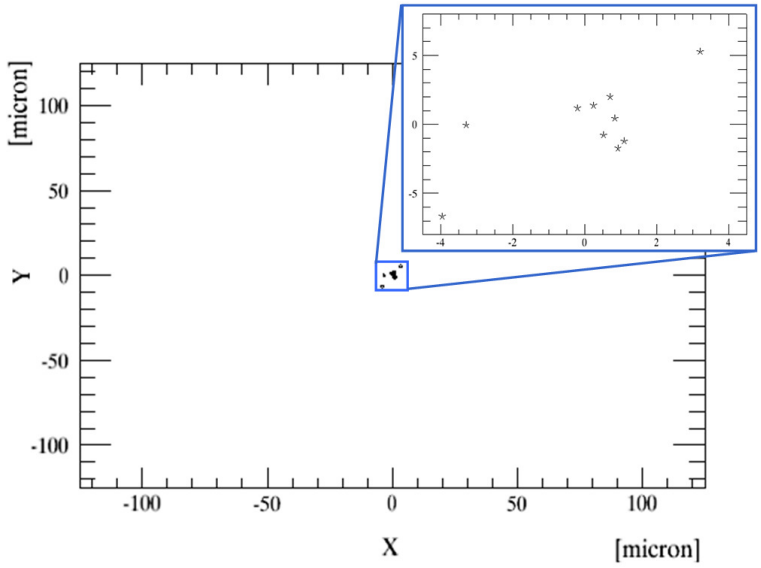

Figure 5.15: Graphs showing the results of the test on the re-positionability of the test camera. The values of x and y position of the spot on the CCD are expressed in μm. The bigger graph is dimensioned on the required camera positioning repeatability (0.55mm).

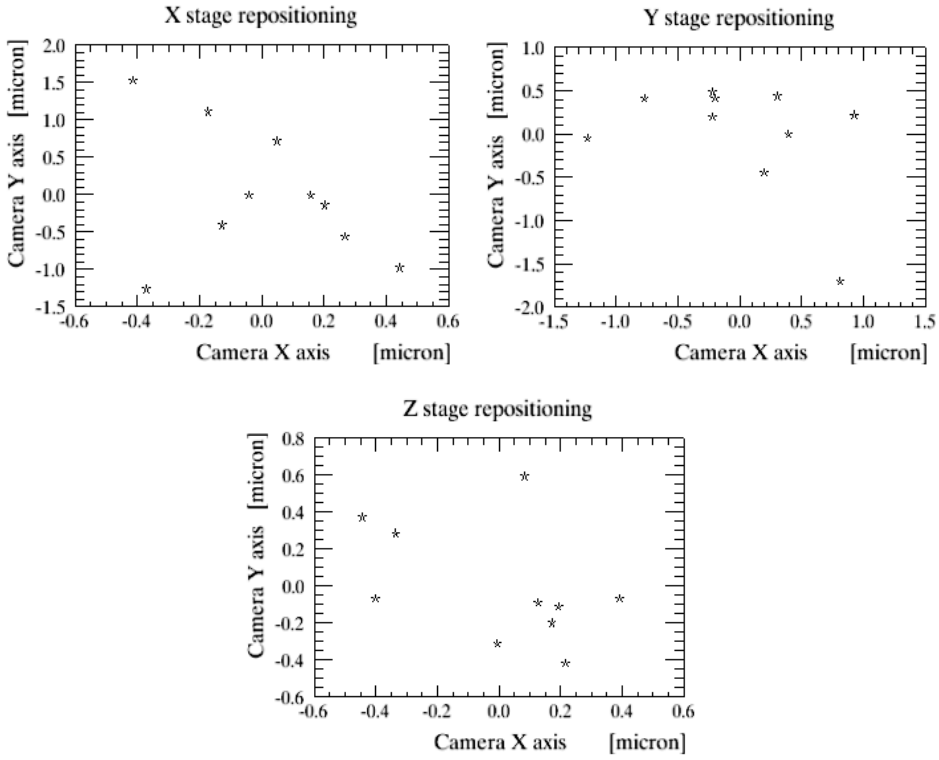

Figure 5.16: Results of the test on the re-positionability of the motorized stages in the three axis. The overall maximum displacement has been retrieved as the sum of the three resulting ranges.

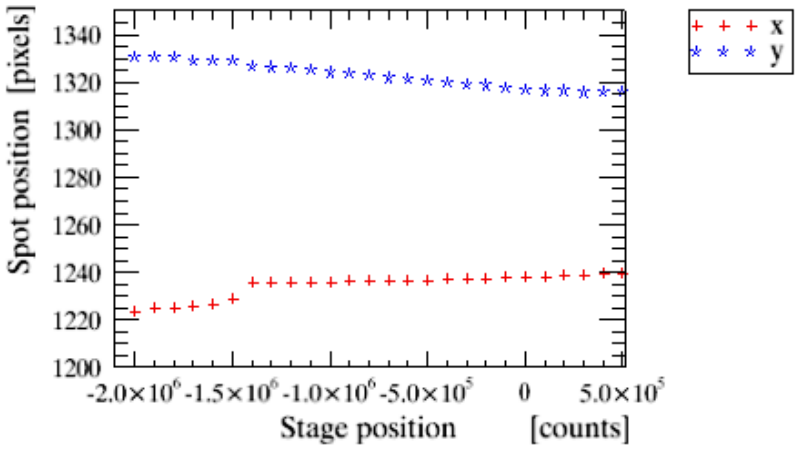

Figure 5.17: x and y positions on the test camera (in the CCD reference system), changing the position of the camera itself along the Z axis with the motorized stage. 2,500,000 counts correspond to a 8.825mm range.

5.3.2 Phase 2: Alignment on axis between the objective and the parabola

This Phase has the purpose to make a rough pre-alignment of the Parabola to the Objective, in order to accomplish, during Phase 3, the alignment of the 2 flat mirrors. We call it "rough pre-alignment" since, at this stage, having only one observable described in the following, it is impossible to distinguish between the decenter and the tilt of the Parabola.

A Align a laser source, positioned instead of the test camera, to the Objective: the parabolic mirror is mounted on the PR-I main structure and positioned at its nominal focal place, with a mechanical precision which should fulfill the tolerance of 0.5mm in focus. The nominal distances of the parabola and the flat mirror of the PR-I inside their mount cells are summarized in Figure 5.18. At this stage, the test camera has been

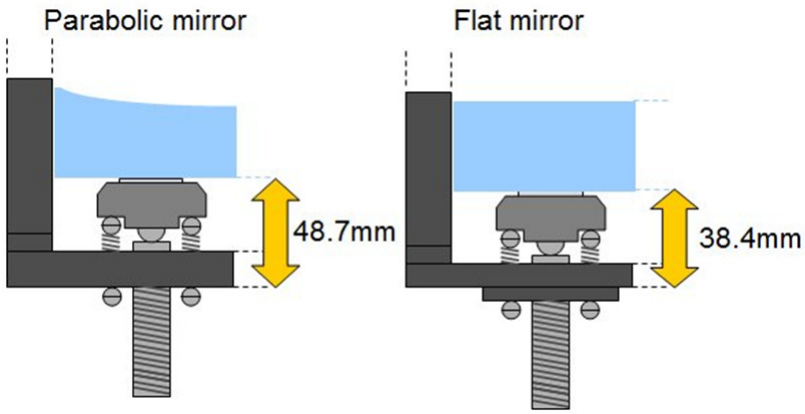

Figure 5.18: Focus nominal positions of the parabolic and flat mirrors inside their mount cells.

dismounted, and this operation has been performed with the possibility to re-mount the test camera with a repeatability of less than 15μm (see previous Section). Next step is to mount a laser source shining the light toward the objective, from the CCD side, with centering and tip-tilt adjustments, and to align the laser with the objective in a way to materialize the objective optical axis, by observing the back reflected spots (masking the parabola with a black screen). This operation has been achieved with a precision of $\pm$120μm in centering and $\pm$60 arcsec in tilt (see Figure 5.19).

B Remove the black screen from the parabola, and align the parabola with the laser materializing the objective optical axis. Of course, shining a laser on the center of the Parabola, we can only align the parabola surface normal with the incoming laser beam, since there will always be a tilt compensating a certain amount of decenter (and vice versa). This operation has been achieved with a precision of 0.6mm in centering and 0.06° in tilt.

The total indetermination of the alignment of the Parabola surface normal with respect to the Objective optical axis is the sum of the errors in aligning the Parabola (0.6mm and 0.06°) and the propagation of the errors in materializing the Objective optical axis with the laser beam (120μm and 60 arcsec). They give a total error (in the conservative case of a simple sum of the two contributions) of 1.75mm in centering or 0.15° in tilt.

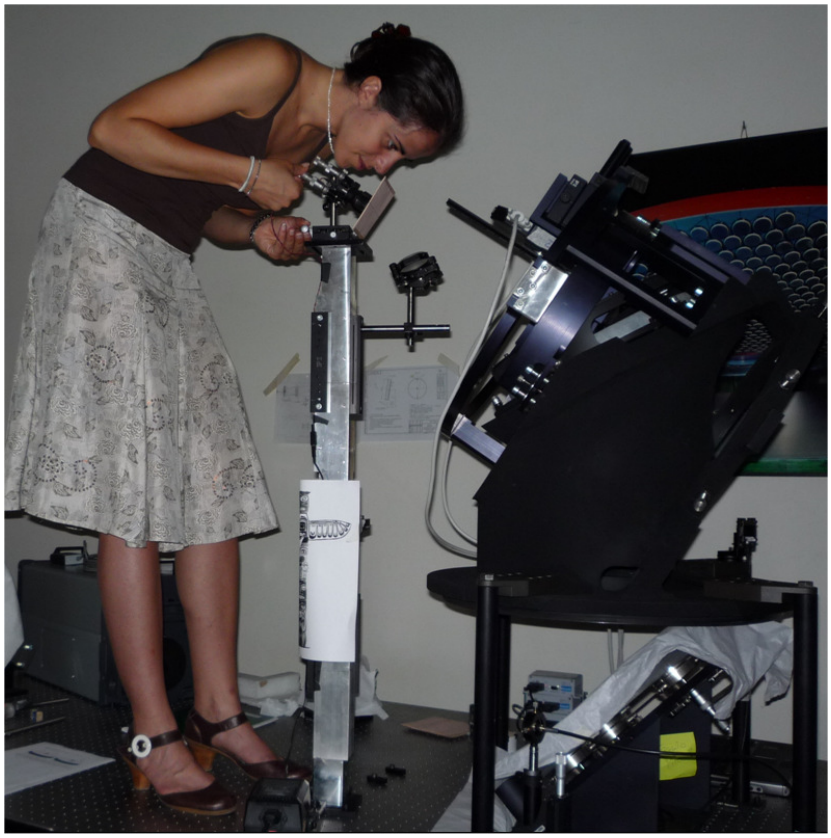

Figure 5.19: Alignment of the laser source to materialize the Prime Focus Corrector optical axis in Phase 2A.

5.3.3 Phase 3: Alignment of the two flat mirrors

This Phase has the purpose to feed the PR-I with an extended collimated beam, resembling the on-axis beam coming from the star enlargers. When the beam reaches the Parabola, it has to be parallel to the Objective optical axis. Once this configuration is reached, there will be only one way to align the Parabola minimizing the coma effect and keeping the spot fixed on the recorded position on the CCD (Phase 4 and Phase 5). This optical setup is shown in Figure 5.20, and it is made in this way:

- a 100μm-core optical fiber (mounted on a X-Y-Z stage for alignment purposes) is used as reference light for the alignment;
- an Off-Axis Parabolic mirror (OAP), mounted on a custom tip-tilt mount, collimates the beam coming from the optical fiber, directing it toward the PR-I;
- an additional flat folding mirror, positioned below the PR-I, sends the collimated beam inside the PR-I itself; this folding mirror has tip-tilt adjustment capabilities (using actuators with differential micrometers, with a resolution of 1μm, corresponding to 1.16 arcsec), in order to move the reference created by the fiber along the whole PR-I field of view;
- the test camera, with a very high spatial sampling (2.2μm of pixel size) is used instead of

the final CCD EEV50, in order to have the highest possible resolution for the evaluation of the images affected by the coma during the alignment procedure.

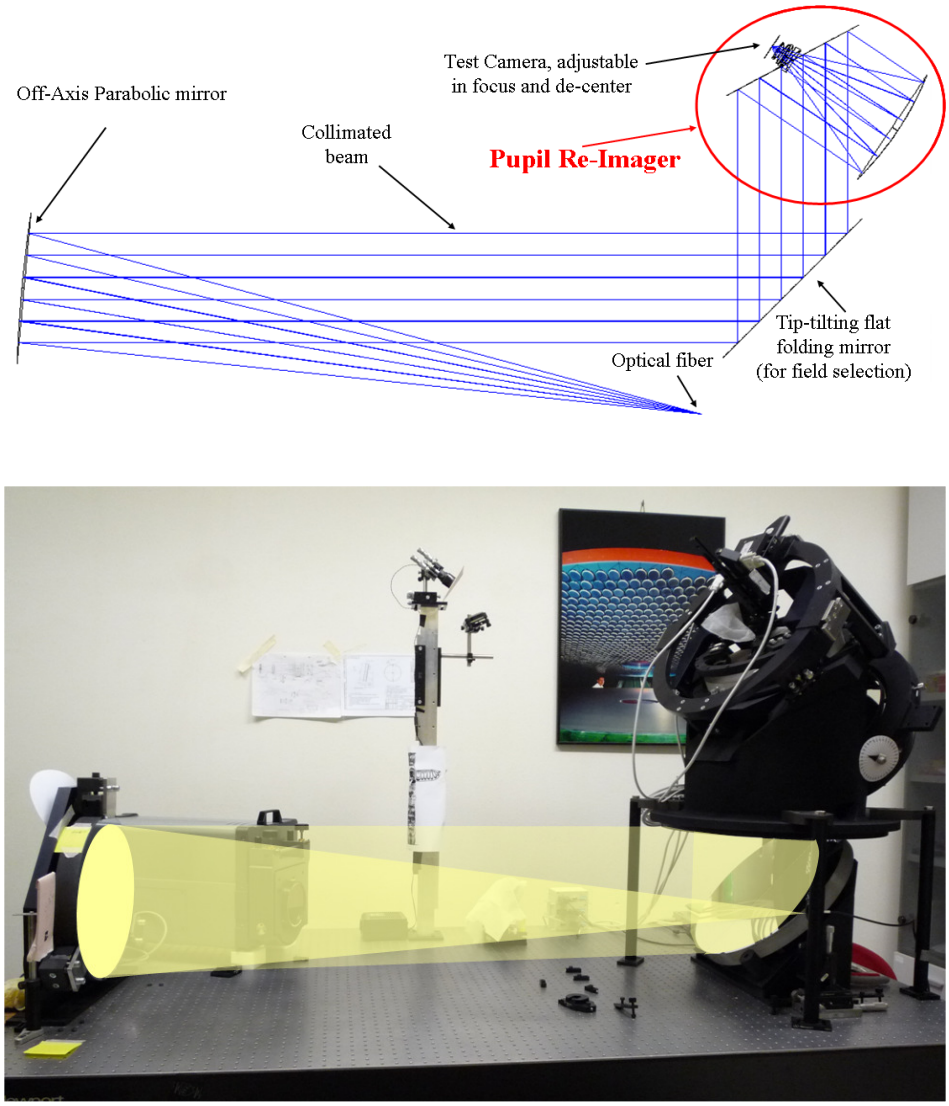

Figure 5.20: The optical setup used to align the Pupil Re-Imager (design, *above*, and actual setup, *below*). The required precision in the OAP alignment with respect to the fiber is ±3mm in de-center. In this way an eventual coma effect introduced on the spot on Phase 4 and Phase 5 by the OAP is smaller than the minimum coma we want to detect on the CCD.

OAP Alignment

The setup OAP alignment consists of a relative orientation and centering of the optical fiber and the OAP itself. Namely, the optical fiber has to be placed on the focal point of the OAP, along the optical axis of its parent parabola. The required precision in the positioning of the fiber in the focal plane of the OAP was ±3mm in de-center. In this way an eventual coma effect introduced on the spot on Phase 4 and Phase 5 by the OAP is smaller than the

minimum coma we want to detect on the CCD. The focusing precision is not defined since the beam will not be used for focusing purposes. The alignment procedure can be summarized as follows:

- a collimated, 100mm in diameter, beam has been reflected by the OAP and focused on a CCD camera. The relative orientation of the incoming beam and the OAP has been modified in all the three rotation axis in order to minimize the dimension of the spot on the camera, reducing the coma effect to zero, within a certain error (40arcsec for the inclination of the incoming beam with respect to the OAP parent parabola optical axis).
- in such a way, the position of the focused spot defined the focal point of the OAP within a certain error, which is ±0.3mm in the two directions.
- the optical fiber has then been placed so as to be coincident with the focused spot, with an indetermination lower than ±0.5mm in the two directions. The total indetermination in the fiber positioning in the OAP focal plane is then lower than ±0.8mm in both directions, which is far inside our requirements.
- the focal position of the optical fiber has been checked with an auto-collimation procedure, resulting in an indetermination of the fiber position along the optical axis lower than ±2.5mm (remember the long focal distance of the OAP).

The last step of Phase 3 is to tip-tilt adjust the flat folding mirror below the PR-I in a way to superimpose the spot to the reference, recorded on the CCD during Phase 1, within an accuracy of 0.001° (corresponding on a shift of the spot on the CCD of 7μm, that is to say almost 3 pixels).

Table 5.2: Incoming beam off-axis error budget.

Error source	Accuracy	Consequent max flat mirror misalignment	Consequent max incoming beam tilt
Phase 1: Reference definition on the test camera	0.078 mm	0.011deg	0.022deg
Phase 2: Parabola prealignment	1.75mm, 0.15deg	0.142deg	0.284deg
Phase 3: Flat mirror alignment	0.003deg	0.003deg	0.006deg
Total off-axis amount			0.312deg

Table 5.2 reports the incoming beam off-axis Error Budget. All the uncertainties regarding the various alignment phases are listed and the sum of them is considered as the worst possible off-axis amount, concerning the wide white-light collimated beam inclination with respect to the Objective optical axis.

5.3.4 Phase 4: Alignment of the PR-I

At this point of the procedure the PR-I is fed with a wide collimated beam corresponding to the on-axis beam of the PR-I FoV, within the already described uncertainties. Please note that the PR-I in this procedure is not oriented as it will be on the LINC-NIRVANA optical bench. This, of course, implies that the gravity vector direction is different from the PR-I working one. Please note, however, that the PR-I will work in several gravity conditions, since it will rotate around its optical axis to de-rotate the FoV and it will be tilted together with the overall bench to follow the source in the sky. Moreover, the working conditions will be, from the flexures point of view, worse than the one adopted for the internal alignment. Because of this, the effect of the gravity on the mirrors and the test CCD, in this particular configuration, is not expected to introduce additional errors on the PR-I alignment. There will be only one way to align the Parabola minimizing the coma effect and keeping the spot fixed on the recorded position on the CCD, which is the preliminary "center of the field", used as a reference for the alignment phase. The camera is then de-focused in the intra-focal direction of an amount of 62000 steps of the focusing linear stage, corresponding to 0.22 mm (see Figure 5.21). The resulting image shows a central dark "hole" due to the central obscuration of the PR-I. To measure the coma, the position of the central obstruction with respect to the whole de-focused reference image is determined. Using an IDL procedure interpolating the contours of the outer and inner ellipses (they are not exactly circles, because of an astigmatism effect, discussed in the following), the de-centering between the two ellipses is computed and then translated in a coma measurement.

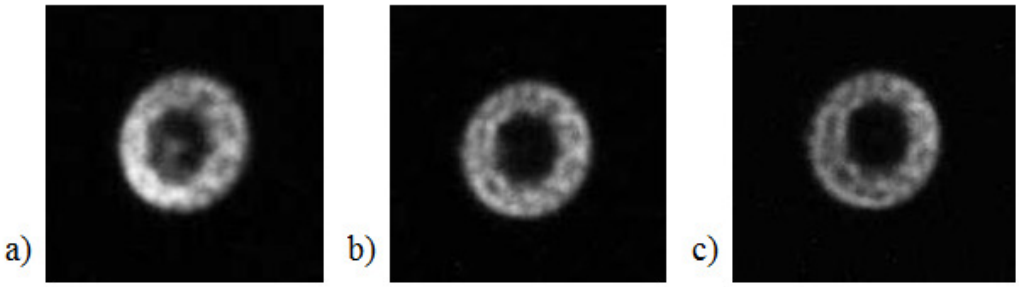

Figure 5.21: Defocused images of the spot (0.22 mm intra-focal direction). Image a) and c) show a de-centering between the inner and outer ellipses of 3 pixels (in opposite directions), while image b) shows a de-centering of less than 0.5 pixels.

The goal is to iteratively adjust tip-tilt and centering of the parabolic mirror, in order to minimize the de-centering between the two ellipses without changing the position of the focused spot on the CCD camera. According to the error budget of the PR-I internal alignment, the misalignment accepted in this phase between the Parabolic mirror and the Prime Focus Corrector shall be smaller than 0.17mm in de-centering (and 0.014° of tilt).

Since the Parabolic mirror - prime focus corrector de-centering is required to be smaller than 0.17mm, the de-centering between the ellipses has to be smaller than 1 pixel of the test camera, that is to say 2.2 μm. The reached value for the de-centering of the two ellipses after the iterative procedure is 0.25±0.25 pixels ($<$ 1 pixel), corresponding to 0.69±0.69 arcsec of coma.

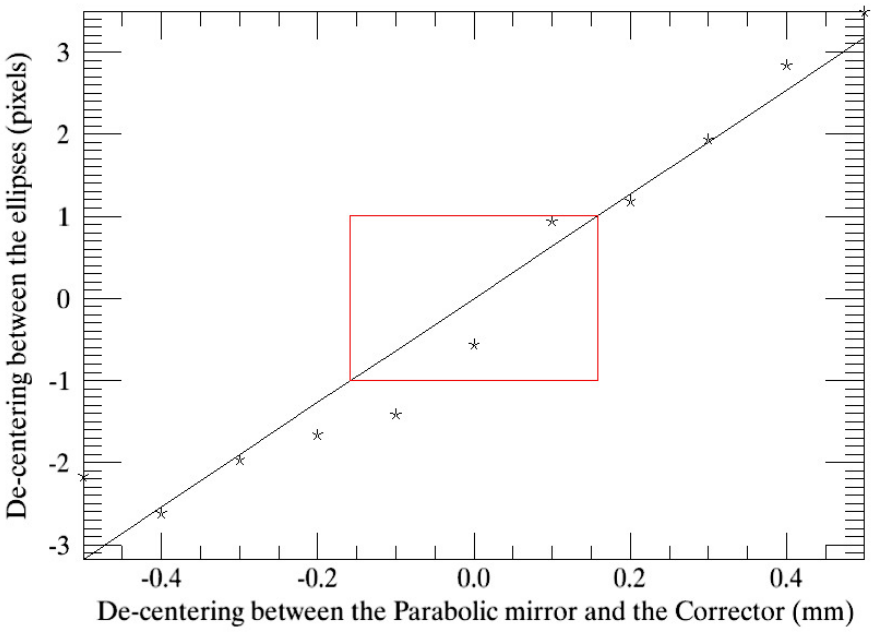

Figure 5.22: Measured values of de-centering between the inner and outer ellipses, corresponding to different physical de-centering of the parabolic mirror, compensated with a tilt to keep the focused spot in the defined position (center of the field) on the test camera. The red rectangle represents the specification range.

Astigmatism contribution:
The images obtained in Phase 4 show an astigmatism component, which could, in principle, either depend on the PR-I optics (prime focus corrector internal misalignments, each optical component manufacturing, etc.) or on the test setup. Measuring the outer ellipses eccentricity, the resulting astigmatism component is 5.5 arcsec. To check the effect of such an aberration on the PR-I optical quality, the whole amount of astigmatism is considered as introduced by the PR-I (in particular by the Parabolic mirror surface) and the resulting RMS blur is computed. The resulting RMS spot radii are 8.0μm, 9.4μm and 10.8μm in the center of the FoV, at 0.44° and at 0.55° from the center, respectively (see Table 5.3).

5.3.5 Phase 5: final focus adjustment of the PR-I

A manually operated measurement arm that measures the surface of real physical objects, tracing the exact coordinates of space, is used to check the distance between the parabolic mirror and the prime focus corrector.

The reference planes are the rear of the Parabolic mirror and the flange holding the Prime Focus Corrector (see also Figure 5.23).

The nominal distance (considering Zemax and CAD drawings) is 353.68 mm. The measured distance is 353.62 mm. The focal positioning requirement (0.5 mm) is then fulfilled.

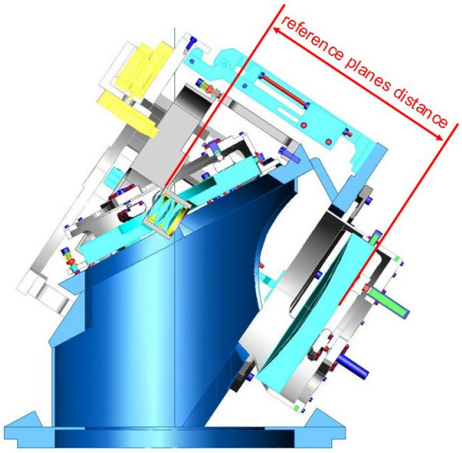

Figure 5.23: The reference planes for the mechanical measurement of the distance between the optics inside the PR-I are shown.

Table 5.3: Error budget summarizing the various contributions to the total RMS blur, measured as the RMS spot radius, obtained optimizing the focus position of the CCD over the full FoV with polychromatic light.

	Ref. Section	On axis	0.44° off-axis	0.55° off-axis
RMS nominal spot radius	5.2	5.6μm	7.4μm	8.9μm
Maximum defocus (0.1mm)	5.3.5	6.2μm	7.7μm	9.2μm
Maximum off-axis alignment (0.3°)	5.3.3	7.0μm	11.9μm	15.6μm
Internal alignment (0.025mm, 0.005°)	5.3.4	5.9μm	7.8μm	9.3μm
Measured astigmatism (5.5")	5.3.4	8.0μm	9.4μm	10.8μm
Total RMS spot radius		**9.6**μm	**13.6**μm	**17.1**μm

5.3.6 Phase 6: final PR-I optical quality check

By tilting the additional flat folding mirror below the PR-I, the optical quality off axis is checked. The limit of the PR-I FoV (±0.44°) is reached tilting the Flat mirror of 0.22° in several directions. The flat folding setup mirror is tilted using three manual actuators, positioned on the rear of the mirror, with 120° of relative separation. A 0.22° tilt corresponds to a 0.7mm travel of one of the actuators. First of all, the test camera is precisely positioned in the focal plane, minimizing the spot radius of the image at the center of the FoV, both considered as the width of the Gaussian curve fitting the spot bi-dimensional profile and the RMS spot radius (see Figure 5.24).

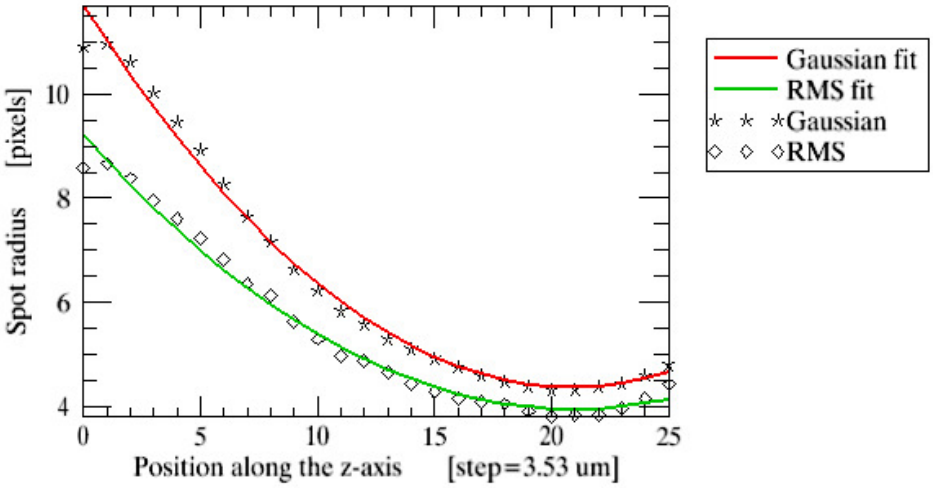

Figure 5.24: Through focus values of the spot radius.

The camera is fixed at the focal position, and a set measurements of the RMS spot radius all over the FoV (see Figure 5.25) of the PR-I, is taken. The RMS spot radius is computed on each image, considering only the pixel values over a threshold of 5% of the peak intensity of the spot at the centre of the FoV.

All the RMS spot radii of the sampled spots are lower than 25 μm, so the alignment satisfies the requirements. A new value of 13 μm RMS radius is then introduced as a PR-I optical quality measurement in the revised Error Budget (Chapter 3).

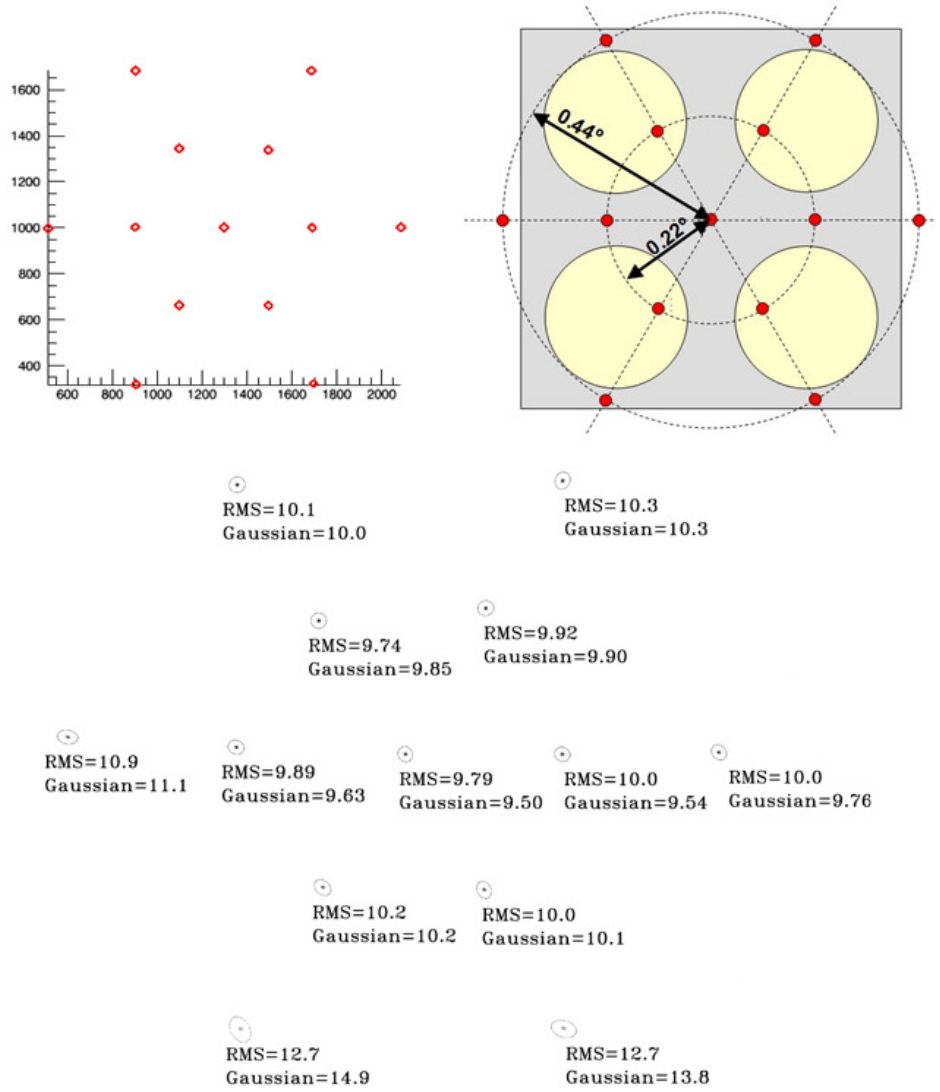

Figure 5.25: Positions over the FoV for the set of measurements of RMS spot radius. Upper left image: spots positions on the test CCD (scale:pixels). Upper right image: corresponding positions on the final CCD. The red dots indicate the sampled positions, plotted over a representation of the pupil images on the final CCD. Lower image: real images on the test CCD (μm).

Chapter 6

Ground layer Wavefront Sensor AIV

In the previous Chapters the AIV of the subsystems including optical elements, namely the 12 Star Enlargers and the Pupil Re-Imager, has been described, resulting in each case inside the requirements. At that stage, the next step was the integration of the subsystems in the GWS, and their alignment to the mechanical axis of the bearing, which allows to compensate for the rotation of the sky. Concerning the SEs, the main requirement is their relative alignment, as already discussed in Chapter 3, which is critical in terms of blur introduced onto the pupils. On the PR-I hand, instead, it will be aligned to the bearing rotation axis using its internal flat folding mirror, in order to make the center of the PR-I field of view coincident to the rotation axis projection. As for the already described subsystems, the main part of the Ground-layer Wavefront Sensors AIV is being realized in the laboratories of the Astronomical Observatory of Padova.

6.1 GWS assembly

The integration of the 12 X-Y linear stages (one of them shown in Figure 6.1, *left*) moving the SEs inside the FoV on the SE Unit main mechanical structure have been realized at the providing company premises (Tomelleri S.r.l.), together with the alignment of the stages to a common reference in order to move the SEs along the same plane. To avoid mechanical stress, each stage is fixed to the structure on three points, two of them composed of a push-pull system in which a screw is used to regulate the linear stage inclination and two pre-loaded springs are keeping it in contact with the screw itself (Figure 6.1, *right*).

On each linear stage is fixed a tip-tilt stage, used to make all the SEs parallel, in order to avoid differential shifts of the pupils on the detector. Also these stages have been integrated in the SE unit before its arrival in Padova.

Because of the GWS weight and size, a mechanical handling has been realized in order to both assembly and hold the system during the internal alignment procedure. Such an handling is equipped with shelves and chains to keep a standard optical bench integral with the handling itself, to avoid differential movements during the alignment. After the GWS handling mounting, the carbon fiber arm is held inside a trolley (which will act as a parking device for the GWS as a whole, after the alignment), fixed to the rest of the handling itself through a pivoting mechanism, allowing the 180 degrees rotation of the whole trolley and

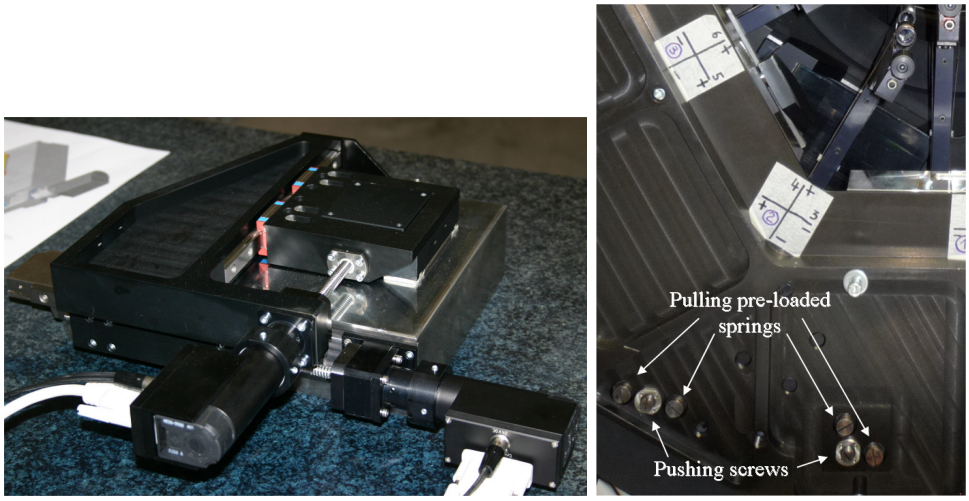

Figure 6.1: *Left*: one of the linear stages moving the SE inside the FoV. *Right*: the two push-pulling systems used for the SE#2 linear stage alignment to its holding flange.

carbon fiber arm, in order to mount the GWS PR-I and SE Unit.

To mount the SE Unit (called also the *GWS lower part*) on the bearing, the whole carbon fiber arm has to be rotated to have its light entrance facing the ground. The GWS lower part is then positioned just below the carbon fiber arm, thanks to a proper trolley, which allows also the SE Unit rotation, to reach the same orientation of the bearing. Chains are then used to lift the lower part of the GWS and hold it during its mounting (see Figure 6.2).

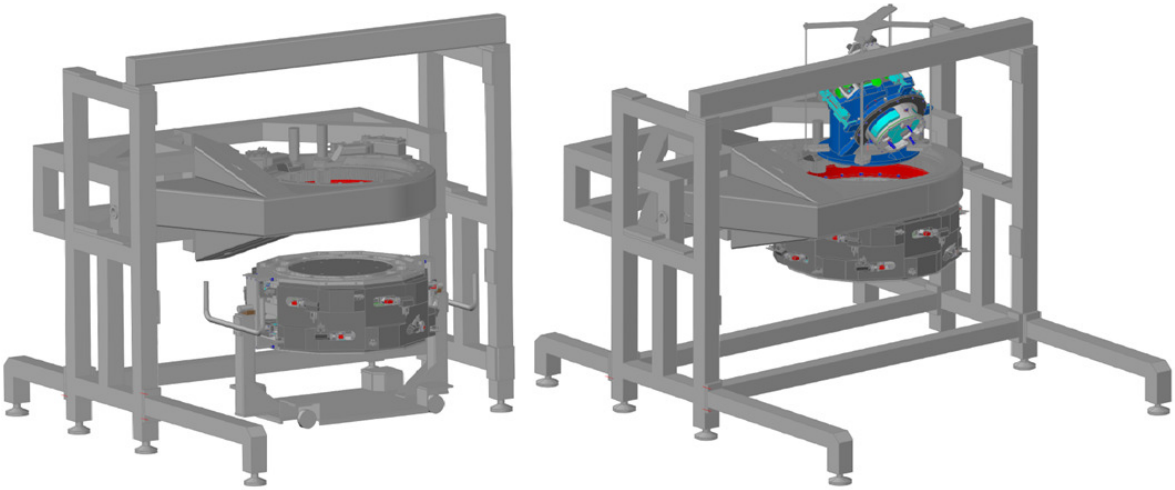

Figure 6.2: *Left*: the GWS lower part, placed under the carbon fiber arm, to be lifted and fixed to the bearing. *Right*: the PR-I is lowered on the carbon fiber arm.

In Figure 6.3, *left*, is shown the GWS lower part fixing operation, performed through 24 M12 screws. The PR-I is then lifted with the crane, thanks to a proper cross-shaped lifting device, and positioned just above the bearing, as shown in Figure 6.3, *right*. The PR-I mounting is then performed with 12 M8 screws. At this stage the GWS main parts are

Figure 6.3: *Left*: GWS lower part fixing operation. *Right*: PR-I positioning on the carbon fiber arm.

assembled on the carbon fiber arm. The next step is to make the optical bench be integral with the handling structure, to avoid differential flexures and movements.

Figure 6.4: GWS completely assembled inside its handling.

The GWS trolley is re-rotated in order to reach its operational zero position, i.e. with the bearing rotation axis parallel to the ground. Such a position is then kept with a blocking bar, which is screwed to the trolley and equipped with an hole and two screws. A M12 screw is inserted in the hole, from the handling structure side and fixed on the blocking bar side with a bolt, while the two screws are screwed pushing on the handling structure to reach a complete blocking.

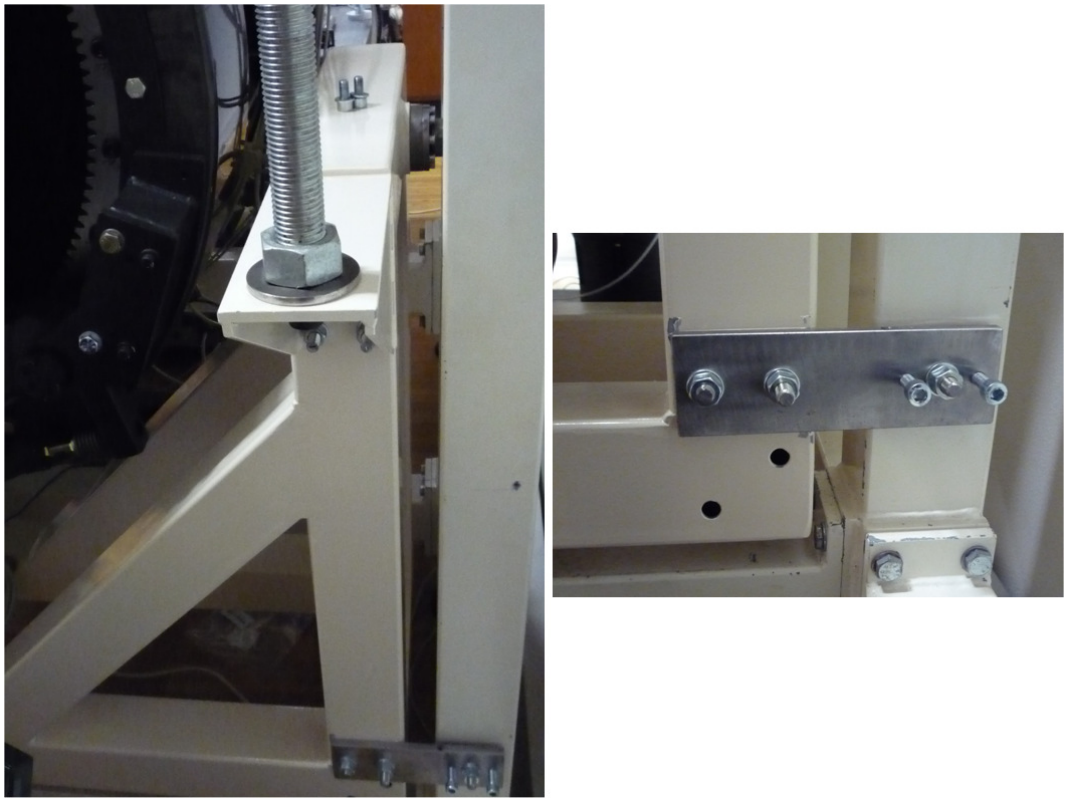

Figure 6.5: *Left*: GWS trolley blocking system (bottom of the picture), in the picture also the rotation axis is visible on the upper part. *Right*: blocking system enlargement.

The last sub-systems to be assembled in the GWS are the 12 SEs. Before the insertion inside the WFS lower part, the SEs have to be coupled to their T-arms and positioned in the middle of their focus range. Two headless screws, pushing the SE in two opposite directions along the rail on which the SE is coupled with its T-arm, are used to change the position of the SE along the optical axis. Two blocking screws, one of them is shown in Figure 6.6, are used to block the SE in the proper focal position during the fine-alignment phase.

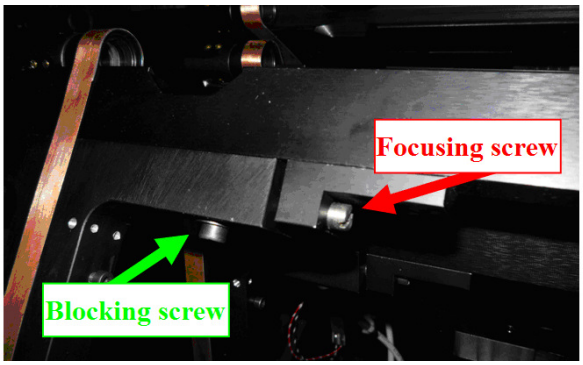

Figure 6.6: One of the two couples of focusing and blocking screws of a SE.

A copper stripe is following the profile of each SE, as seen from the entrance of the GWS,

and all of them are connected together in a collision control system, with the aim of blocking the SEs motors once a collision between two of them accidentally occurs. Each Collision Control stripe is coupled to its SE, and screwed with 4 (2 for each side) teflon screws to the SE T-arm. Finally, the SEs are inserted inside the GWS lower part and fixed to the tip-tilt stages with 3 M4 screws (see Figure 6.7).

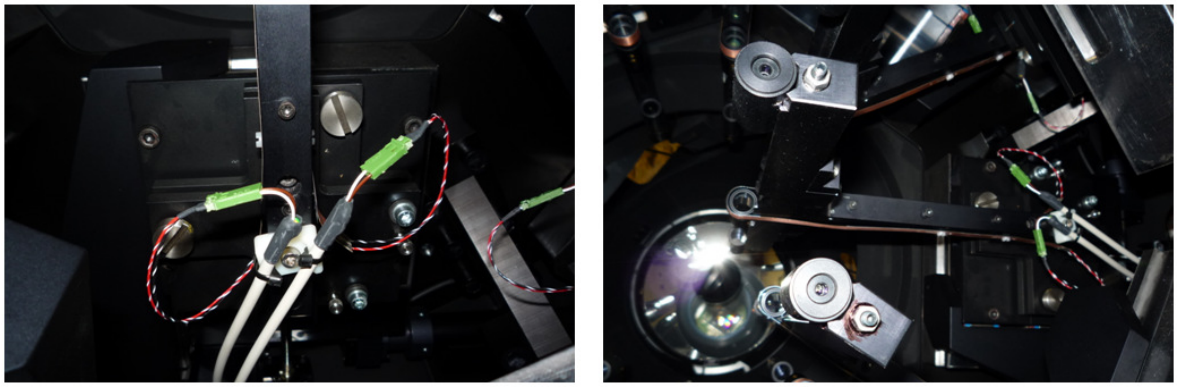

Figure 6.7: SE mounting inside the GWS lower part. Each SE T-arm is fixed to the respective tip-tilt stage with three M4 screws, one of them holding also a plastic device keeping the Collision Control cables connectors on the proper position, to be connected to the SE Collision Control stripe.

Finally, the whole system is assembled, except for the CCD50 camera, which is, at this stage, replaced by the test CCD still keeping a reference for the PR-I *center of the field*.

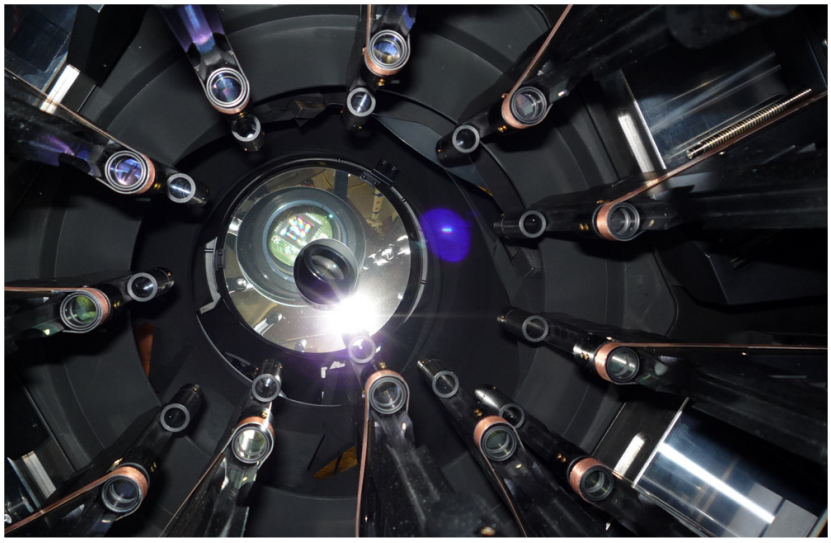

Figure 6.8: 12 SEs mounted inside the GWS. On the background, the flat folding mirror can be seen, and the reflected image of the objective and the test CCD is visible too.

Figure 6.8 shows the 12 SEs integrated on the GWS. Through the PR-I mirror, the test CCD chip is visible too.

6.1.1 Optical bench positioning

A 2.10×2.40 m optical bench by Newport is positioned with the shorter side facing the GWS light entrance. In Figure 6.9 the procedure to fix the optical bench to the handling is shown. First of all, the bench is positioned close to the handling, with its short side in correspondence of two white plates, equipped with holes, to which two small black plates with shelves are fixed. The bench is positioned just above these shelves and leaned on them varying the bench legs height. Two L-shaped secure plates, are fixed both to the handling, through the plates equipped with shelves, and to the upper face of the bench, to avoid its sliding off the shelves during the lifting operations. Two small circular plates, with 8 M6 holes in a configuration which corresponds to the bench threaded holes and equipped with an eye-bolt, to which the chains will be fixed, are positioned and fixed on the bench, at a 1.9m distance from the handling. The chains are fixed to the handling, on one side, and to the eye-bolt on the bench on the other, through a turnbuckle, which allows to tighten the chain. The bench legs are then lowered and separated from the bench upper part, which is held by the GWS handling structure.

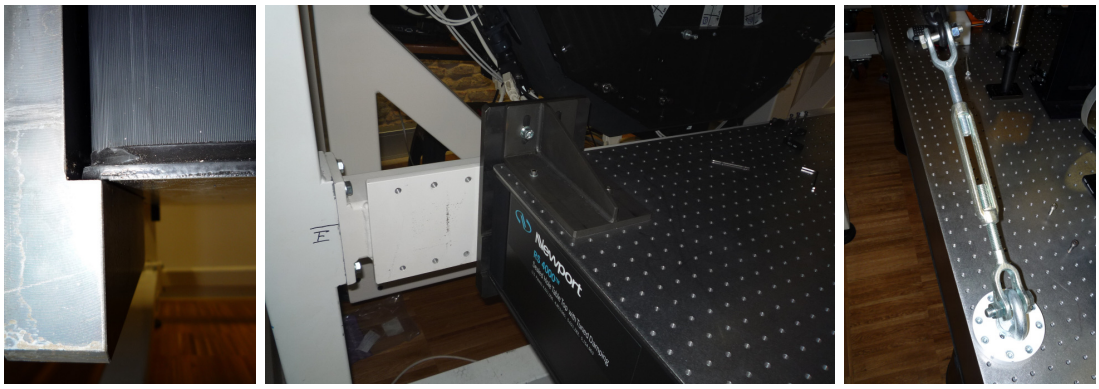

Figure 6.9: Procedure to fix the optical bench to the handling. *Left*: the bench is positioned (varying the bench legs height) just above the shelves, in order to lean on them. *Center*: the L-shaped secure plates, to be fixed both to the handling and to the upper part of the bench, to avoid its sliding off the shelves. *Right*: one of the chain fixing device, blocked with 8 M6 screws on the optical bench surface. Also the turnbuckle system, used to tighten the chains is visible.

6.2 GWS internal alignment

As already said, the GWS internal alignment consists of the relative alignment of the SEs, to avoid a wrong pupil superposition on the detector, the alignment of the PR-I optical axis to the bearing rotation axis, performed with the flat folding mirror at the entrance of the PR-I itself, and the proper positioning of the SE entrance focal plane with respect to a mechanical reference representing the nominal position of the LBT focal plane. All these alignment steps have to be followed by a verification of the performance, in order to match all the Error Budget requirements.

Figure 6.10: The optical bench completely held by the handling. The legs of the bench are separated from the upper part.

6.2.1 PR-I flat mirror alignment

To adjust the tip-tilt position of the PR-I flat mirror, in order to make the GWS rotation axis parallel to the center of the PR-I field of view, defined during the PR-I alignment, a collimated beam, materializing the rotation axis direction, is required. An Off-Axis Parabolic mirror has been lighted with an 100μm core optical fiber and aligned to it in order to produce a collimated 330 mm wide white beam. The OAP alignment procedure is analogous to the one already described for the PR-I internal alignment (see Section 5.3.3), and the precision reached in this case for the optical fiber positioning are the following: $\pm$0.3 mm x-y positioning in the focal plane and $\pm$0.5 mm along the optical axis. These precisions have been verified in Zemax to introduce an aberration on the GWS re-imaged spot, which is negligible with respect to the spot aberrations produced by the PR-I (whose internal alignment is inside specifications). The collimated beam produced with the parabolic mirror has been folded with a 430 mm wide flat mirror toward the GWS entrance. The inclination of such a setup mirror has been adjusted in order to keep the spot fixed on the test CCD for a complete $\pm$60° GWS rotation.

Figure 6.11 shows the minimum spot movement (*red line*) obtained, that is to say the residual shift onto the CCD for the on-axis beam, included in a 28×9 pixel range. Being the PR-I effective focal length 220 mm and the test camera pixelsize 2.2μm, this range translates into a 58×18 arcsec range. This residual motion is a combination of the bearing wobble and the GWS flexures with the test CCD flexures, which have been estimated to dominate in this

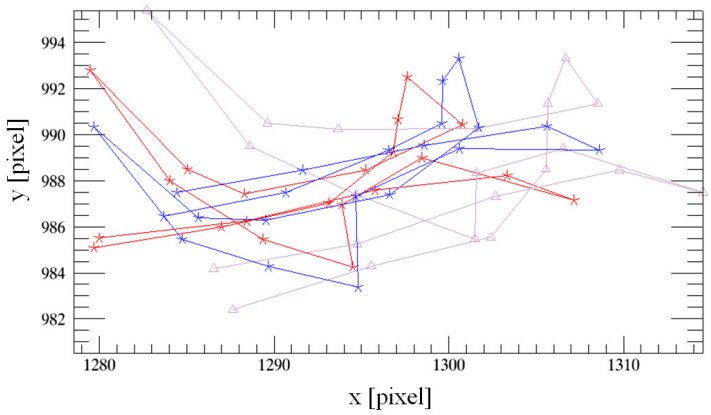

Figure 6.11: Movements of the focused spot barycenter on the test camera for a complete ±60° GWS rotations. The three lines correspond to three different positions of the setup folding mirror. The *red line* shows the minimum retrieved spot movement (i.e. the final on-axis position), while the *blue* and the *violet lines* show, respectively, the movements of the spot for incoming beams with a ±6" tilt with respect to the on-axis position. The X axis of the test CCD corresponds to the direction of the gravity vector in the middle of the GWS rotation range (0° position). It is not surprising, then, that most of the residual spot movement (please note also that the graph scales are different for X and Y axis), after the setup alignment, occurs in the X direction and that the spot path extreme positions correspond to the 0° (last point on the right of the graph) and ±60° (points on the left of the graph) positions of the bearing. Scale: ~ 2"/pixel.

configuration. CCD flexures will be measured with the final CCD.

To align the internal flat mirror of the PR-I, the GWS rotation axis has to be made parallel to the beam defining the *center of the field* inside the PR-I ±0.44° FoV (see Section 5.3.4). Operatively, the flat mirror inclination has to be adjusted in order to achieve a field (rotating the GWS) in which the optical quality is center-symmetric. The center of the field corresponds to the GWS rotation axis.

The results obtained after of such an alignment are shown in Figure 6.12. The PR-I quality along its FoV has been measured as the dimension of the focused spot of a collimated incoming beam, mapping the whole FoV. The values in Figure 6.12 refer to the Gaussian fit width in test camera pixels unit. The measurements have been repeated in three configurations, corresponding to 0°, +60° and −60° rotation angle of the bearing. These results translates into an optical quality, expressed in RMS value, which is lower than 13μm in the whole PR-I FoV, as expected from the PR-I alignment results.

6.2.2 Star Enlargers alignment inside the GWS

Concept and main setup

To align the SE to the GWS mechanics, the setup shown in Figure 6.13 has been realized. The idea is to use a wide collimated laser beam, coming from a commercial interferometer, as a reference, aligned to the GWS so as to be parallel to the GWS optical and rotation axis (now coincident). A commercial $f = 500$ mm, 2 inches diameter lens is used to focus part of

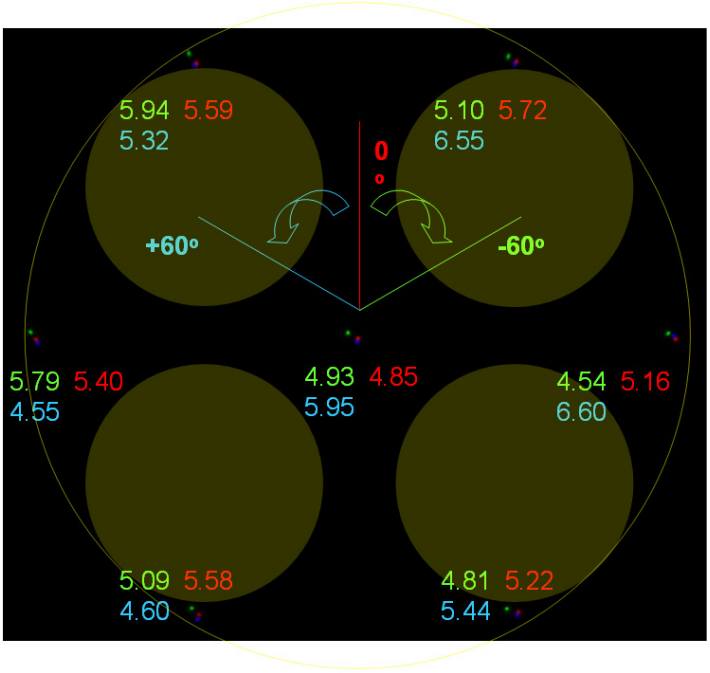

Figure 6.12: PR-I quality along its FoV, measured as the dimension of the focused spot of a collimated incoming beam, mapping the whole FoV. The numbers refer to the Gaussian fit width in test camera pixels unit. The *red*, *blue* and *green* configurations correspond, respectively, to 0°, +60° and −60° rotation of the bearing. The corresponding RMS values are lower than 13μm, as expected from the PR-I alignment results.

the wide beam in the nominal focal plane, defined by the mechanics of the GWS itself, and a physical stop positioned at the proper distance from the focusing lens (according to the entrance pupil position at LBT: 14 m) defines an F/15 beam. The focused beam (the *green* beam in Figure 6.13), once passed through a SE, produces four images of the pupil stop on the test CCD. The part of the beam which is not focused by the lens reaches the GWS optics still collimated (the *red* beams in Figure 6.13). If this collimated beam passes through a SE, on the test CCD 4 spots will be produced, whose barycenters are defining the positions of the 4 pupils re-imaged when the same SE is reached by a the beam focused in its entrance focal plane. The part of the collimated beam entering the GWS where no SEs are present focuses on the center of the PR-I FoV.

Component	Characteristic	value
Interferometer	Beam diameter	100 mm
	Beam collimation	better than 1 arcsec
	Wavelength	633 nm
Pupil stop	diameter	33 mm
	distance from the lens FP	17 mm
Focusing lens	focal length	500 mm
	resulting F/#	F/15

Table 6.1: Setup components main parameters

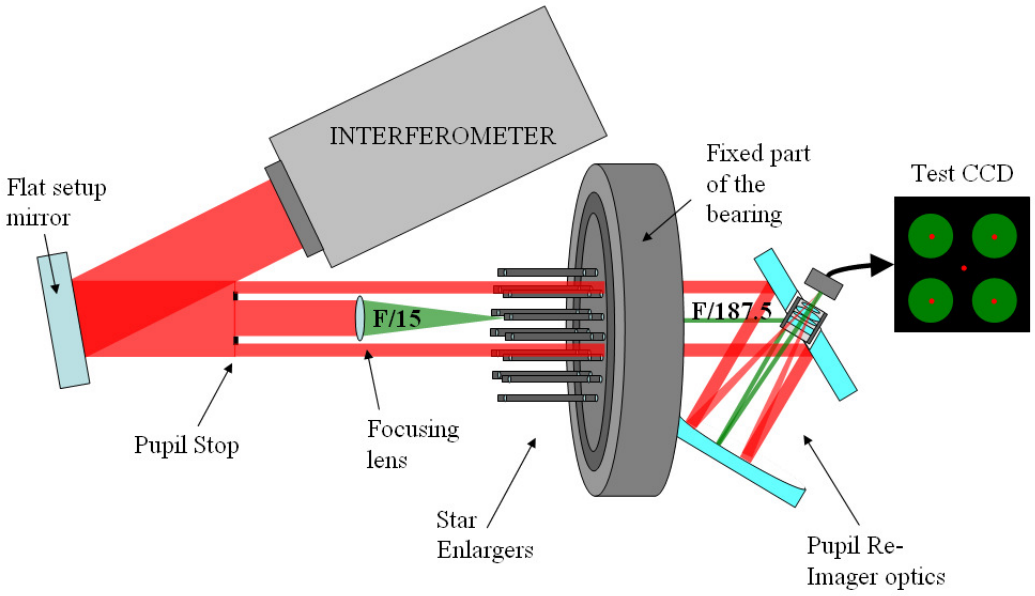

Figure 6.13: A wide collimated beam, materializing the GWS rotation axis, is used to align the SEs to the GWS mechanics. Part of this beam is focused in the nominal mechanical focal plane, producing an F/15 beam which will be used to focus the SEs, looking at the four pupils re-imaged on the test CCD (*green* beam). The beams which enter the GWS still collimated will produce a spot centered on the center of the field. When this beam goes through the SE, 4 spots are produced on the test CCD, that will be used to align the rotation angle of the pyramid and the SE tip-tilt (*red* beam).

Mechanical rotation axis materialization

The wide collimated beam is firstly aligned to the GWS mechanics in order to materialize the bearing rotation axis, which, at this stage, coincides with the optical axis defining the center of the field of the PR-I (see Section 6.2.1). To perform such an alignment, the beam coming from the interferometer is folded by the flat setup mirror, to make it easier to be tip-tilted, toward the GWS entrance and focused by the PR-I onto the test CCD. The position defining the rotation axis on the CCD has been retrieved during the PR-I flat mirror alignment and corresponds to the pixel [1301, 940] of the test CCD, with an indetermination of 5 pixels, corresponding to ∼10", since the scale of the test CCD inside the PR-I is 2"/pixel. The flat setup mirror is then tip-tilted in order to position the focused spot, produced by the wide collimated beam entering the PR-I, on the reference, with an error lower than 2 pixels (4").

F/15 beam focusing

A 2 inches wide lens with a 500 mm focal length is used to focus a F/15 beam at the entrance of the GWS, to reproduce the LBT focal plane, in order to properly align the SEs in focus. This lens has been aligned in auto-collimation, placing a reference mirror in the GWS nominal mechanical entrance focal plane, with a $100\mu m$ accuracy. Figure 6.14 shows the auto-collimation setup used to focus the F/15 lens: the collimated beam coming from the interferometer is divided by a beam splitter into two separated beams, one reflected by a

mirror toward a setup lens focusing it on a test camera (*yellow* beam in Figure 6.14) and the other passing through the F/15 focusing lens, being reflected by the reference mirror in the GWS focal plane and auto-collimating back on the beam splitter (*red* beam in Figure 6.14), which reflects it toward the same test camera collecting the spot coming from the first beam.

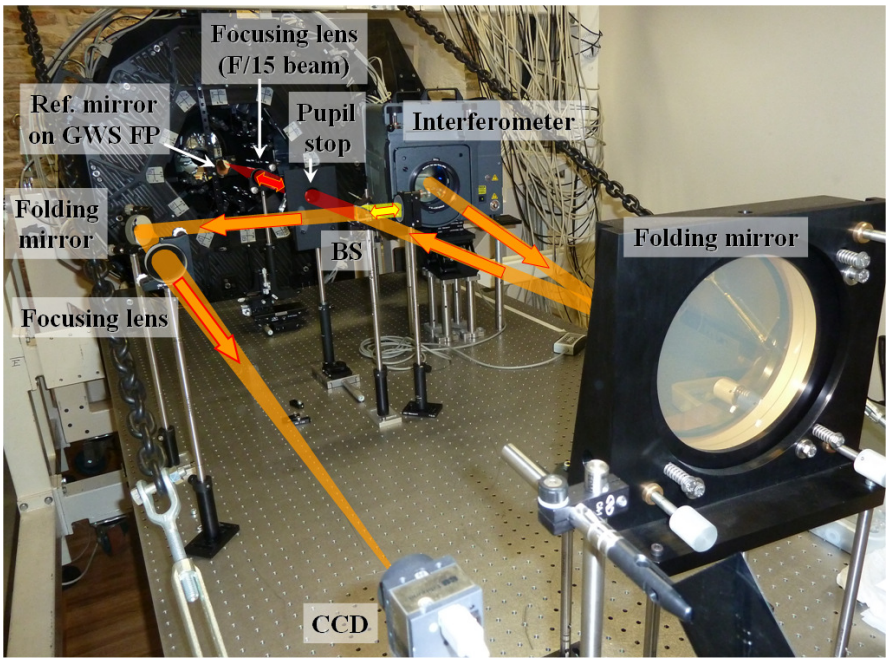

Figure 6.14: Setup for the F/15 beam focusing in the nominal GWS entrance focal plane. In *red*, the light going to the reference mirror placed in the GWS entrance focal plane, in *yellow* the light of the interferometer, acting as a reference for the CCD alignment in focus. In *orange* the common path is shown.

The setup lens focusing onto the test camera is moved along its optical axis to optimize the focusing of the first beam and the retrieved spot size measurements are shown in Figure 6.15, *left*. Once the focusing lens is positioned in order to minimize the first beam spot size, the second beam is considered. The lens focusing the F/15 beam at the entrance of GWS is moved through focus in order to find the position minimizing the size of the spot focused onto the test camera, in auto-collimation. The obtained measurements are shown in Figure 6.15, *right*, giving a precision of less than 50 μm.

Following the described procedure, the F/15 beam which will be used as a reference for the SEs alignment is focused in the nominal mechanical entrance focal plane of the GWS, with a precision which can be estimated combining the indetermination in the reference mirror mechanical positioning and in the best focus position of the F/15 focusing lens: $\sqrt{100^2 + 50^2} = 112$ μm. An error of such an amount in the GWS focal plane positioning would introduce a ~ 18 nm WFE defocus signal onto the GWS, which is still far from bringing the WFS out of its linear regime.

SE complete alignment

A F/15 beam is focused in the GWS entrance nominal focal plane, following the procedure described in the previous Section, in correspondence of a X-Y position inside the FoV which

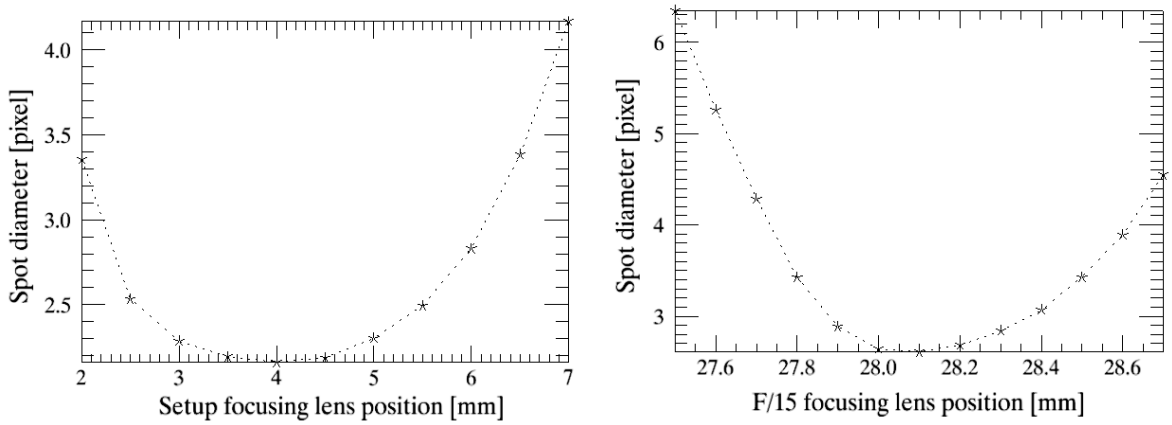

Figure 6.15: Measurements of spots sizes during the F/15 focusing lens alignment procedure. On the *left*, the focus curve obtained for the setup lens alignment to the test camera, on the *right*, the F/15 focusing lens measurements.

could be reached by four SEs, in order to change the lens position and re-perform the focus alignment only three times, to align all the SEs.

The SE alignment to the rest of the GWS is an iterative procedure, performed as follows:

- Pyramid rotation: as discussed in Chapter 3, the goal for the precision in the pyramid rotation alignment is 10', leading to a displacement of the sub-apertures, which are at the outer edges of the pupils, in the direction of the CCD corners, of 1/10 of sub-aperture. To measure the residual rotation after the alignment, the barycenter positions of the four spots obtained illuminating the SEs with a collimated beam (as shown in Figure 6.16) have been considered. Because of small defects in the pyramids faces orthogonality, the rotation angle has been measured considering 6 different diagonals, shown in Figure 6.17, and their mean deviation from the 45° has been taken as a rotation measurement.

- Tip-tilt adjustment: as shown in Figure 6.16, when a collimated beam goes through the SE, four spots appear on the test CCD. The relative distances between the spots depends upon the pyramid vertex angle and faces orthogonality, but the position of the overall barycenter can be used as a measurement of the tilt of the SE with respect to the incoming beam. As already discussed in Chapter 3, the main effect of a tilt of the SE is a lateral shift of the pupils, produced when a focused beam is reaching the pyramid, on the CCD which, in this case, can be quantified as the shift of the four spots on the test camera. Before measuring such a tilt, the interferometer beam, used as a reference, has to be adjusted in tip-tilt in order to focus on the *center of the field*, defined on the camera during the PR-I alignment and corresponding also to the GWS rotation axis projection. This adjustment has to be done with a precision which is far better than the required GWS global tilt, since such a beam will act as a reference for all the SEs alignment. The PR-I scale with respect to the test camera is about 2"/pixel. The effect of a tilt of the incoming beam on the four spots position is reduced by the SE enlargement of a factor k=12.5. As reported in Chapter 3, the usual goal of a tenth

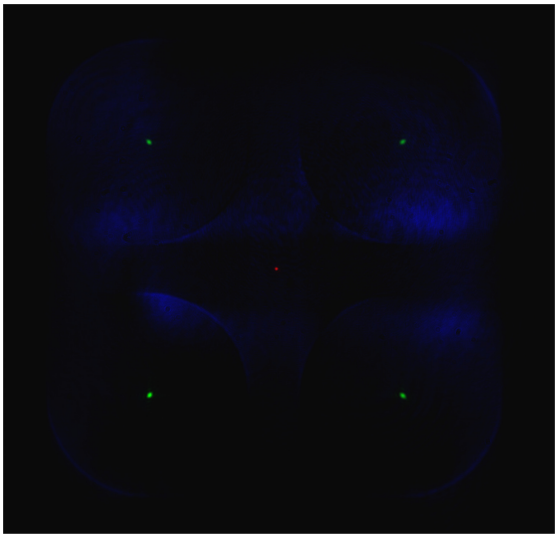

Figure 6.16: Superposed real images obtained with the setup configurations shown in Figure 6.13. In *red*, the spot obtained with the collimated beam going through the PR-I, without the SE. In *green*, the SE is introduced between the interferometer and the PR-I. In *blue*, the four pupils re-imaged illuminating the SE with the F/15 beam.

of sub-aperture shift of the pupils is reached with a tilt of the SE lower than 5 arcsec, corresponding to a shift of our spots on the test CCD of less than 2.2 pixels. On the other hand, a tilt of the reference incoming beam of 5", corresponding to a shift of the focused central spot, produced by the light not passing through the SEs, of 2.5 pixels of the test CCD, will translate into an error in the SE tip-tilt measurement of about a 2.5/12.5=0.2 pixels, corresponding to a hundredth of sub-aperture, which is totally negligible in terms of error budget.

- Defocus alignment: to position the SEs in the optical path along the optical axis, the defocus signal retrieved by the wavefront sensor has to be minimized. The F/15 beam passing through one SE is then re-collimated by the pupil re-imager and produces 4 images of the pupil onto the test CCD. Figure 6.18 shows three 4-pupils frames obtained in different focus conditions. The wavefront shape is retrieved comparing the intensities of the four pupils using the quad-cell equations with very small 2.2×2.2 μm (the test CCD pixelsize) sub-apertures. Once the wavefront is computed, it is de-composed into Zernike polynomials and the defocus term is considered. Figure 6.19 shows the typical behavior of the retrieved Zernike defocus coefficient for a complete sweep in focus of the SE. These coefficients are normalized according to Noll, 1976 [17], so as to always have a standard deviation equal to 1, so their units are not expressed in the usual standard *cgs* system. To convert them into metric values, a converting factor has been retrieved using the following procedure: a spatial range along the z axis, centered on the best focus position, is defined and the defocus coefficient is measured for both the extreme intra-focal and extra-focal positions (which are symmetric with respect to the

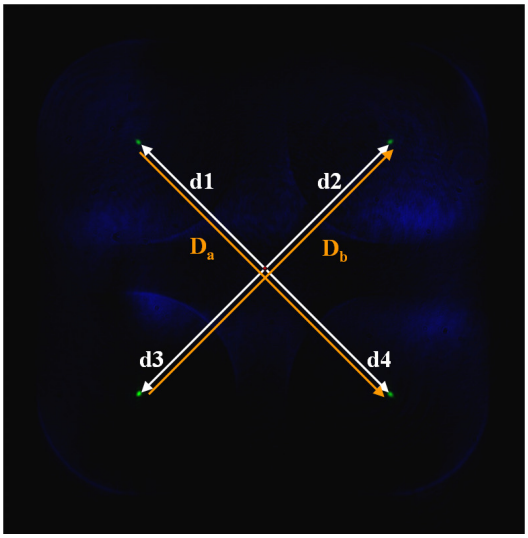

Figure 6.17: The considered diagonals to measure the pyramid rotation with respect to the CCD X and Y directions. $d1$, $d2$, $d3$ and $d4$ represent the directions between the overall image barycenter and the four spots, while D_a and D_b are the diagonals of the quadrilateral defined by the four spots.

best focus). The converting factor can be retrieved as

$$Con_{def} = \frac{1}{8 \cdot 2\sqrt{3}} \cdot \frac{1}{F^2} \cdot \frac{\Delta l}{\Delta c}$$

where F is the incoming beam F/#, Δl is the used range along z, $\Delta c = Z_{def,intra} - Z_{def,extra}$ is the difference between the measured defocus coefficients in the intra and extra-focal positions. The factor $2\sqrt{3}$ is an approximation which allows to convert from RMS to PtV values. The retrieved converting factor for the SEs, illuminated with the light coming from the interferometer ($\lambda = 633$ nm), is $Con_{def} = 0.074$ nm, being $\Delta l/\Delta c \sim 1/2160$ mm. This factor has then been multiplied to the retrieved Zernike defocus coefficients in order to obtain the residual defocus WaveFront Error (WFE) in nanometers. As discussed in Chapter 3, the tolerance for the GWS focal plane position is quite high, however the goal for the SEs relative alignment in defocus is to keep them inside the GWS focus depth, leading to a defocus RMS equal to $\lambda/28$, corresponding to a residual WFE of 20 nm for the considered wavelength.

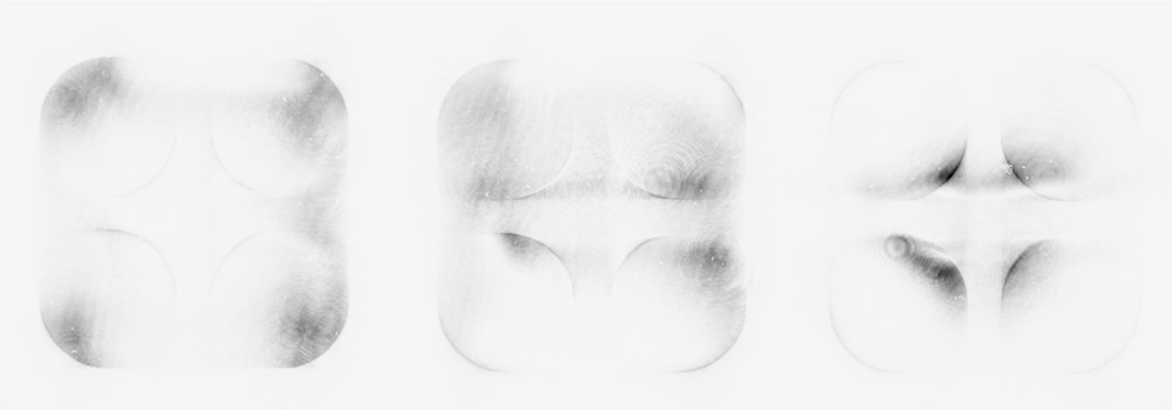

Figure 6.18: Effect of different defocus signals on the four pupils on the test CCD. This effect is amplified because, for alignment purposes, a monochromatic red laser light is used, producing a very small spot on the pin of the pyramid.

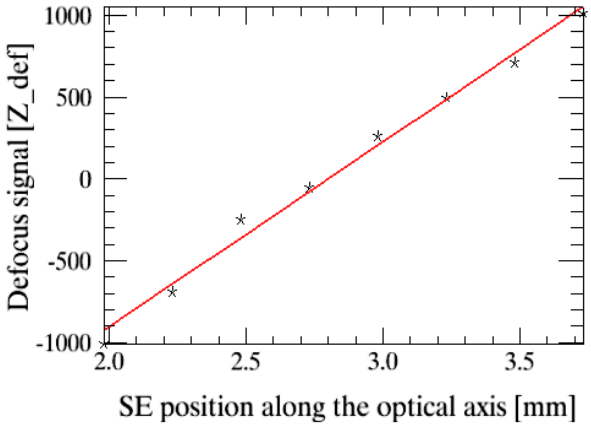

Figure 6.19: Typical behavior of the retrieved Zernike defocus coefficient for a complete sweep in focus of the SE. Zernike coefficient is normalized according to Noll, 1976 [17]. The steepness of the fitted line is due to the fact that the measurements have been carried out with monochromatic light, which allows a greater sensitivity.

Table 6.2 summarizes our alignment goals concerning this phase.

Item	Measured Effect	Goal max value	Effect on Error Budget
Pyramid rotation	Four spots rotation	10'	1/10 sub-aperture
Reference beam tilt	Central spot shift	2.5 pixels	Negligible
Star Enlarger tip-tilt	Four spots overall shift	2.2 pixels	1/10 sub-aperture
Star Enlarger defocus	Defocus signal	20 nm WFE	/

Table 6.2: SE alignment procedure goals

SE alignment results

Table 6.3 summarizes the results obtained during the SEs alignment, concerning the tolerances discussed in Chapter 3 and in the previous Section.

SE ID	Reference beam tilt [pixel, pixel]	SE tip-tilt [pixel, pixel]	Pyramid rotation [arcmin]	SE defocus [nm WFE]
SE01	0.4, 2.0	-0.7, -0.4	0.0	4.3
SE02	0.3, 2.0	1.2, 1.7	-0.8	3.0
SE03	0.7, 0.2	-1.6, -0.6	-0.1	2.1
SE04	0.5, 1.7	-0.4, 0.7	-0.8	4.1
SE05	0.0, 0.1	-1.8, -0.2	-1.0	7.3
SE06	-0.2, 1.0	0.7, 1.4	1.2	8.3
SE07	0.1, 1.4	-0.8, -0.3	1.6	1.8
SE08	-0.2, 2.0	-0.9, 0.8	-1.3	0.4
SE09	-0.2, 1.7	-1.2, -0.5	-0.2	6.5
SE10	0.2, 1.3	1.8, 1.1	0.8	3.2
SE11	0.9, 1.6	-0.4, -0.7	0.4	2.9
SE12	0.3, 1.9	-0.5, 1.5	-0.5	4.6

Table 6.3: SE alignment with respect to the overall GWS results.

Comparing the results reported in Table 6.3 with the tolerances listed in Table 6.2, one can notice that all the verified items about the SEs alignment are resulting to be inside the requirements discussed in Chapter 3.

6.2.3 Other verifications

After the GWS internal alignment, some verifications have been performed, in order to double-check the alignment result and the overall system optical quality.

Pupil blur

The first verification, performed at the end of the SEs alignment, has been the pupil blur static measurement. A calibrated USAF resolution test chart (see Figure 6.20) has been used as a reference for the measurement of the Modulation Transfer Function of the system.

This target presents different triplets of lines, with increasing width and separation, which are divided into groups of 6 elements. Table 6.4 summarizes the spatial frequencies of the

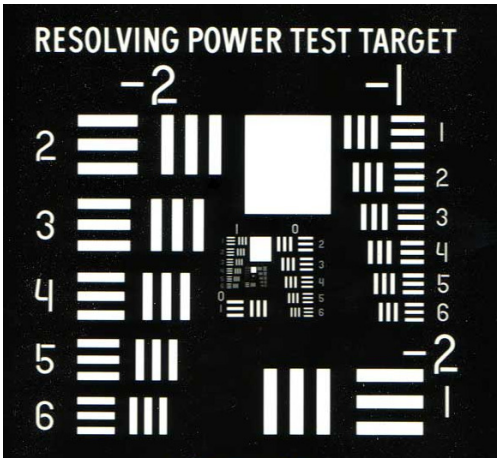

Figure 6.20: Typical USAF target.

triplets contained in a complete USAF target, according to the expression:

$$R(lp/mm) = 2 \times G + (E-1)/6$$

where R is the resolution of the considered triplet and G and E the group and the element numbers, respectively.

E / G	**-2**	**-1**	**0**	**1**	**2**	**3**	**4**	**5**	**6**	**7**	**8**	**9**
1	0.250	0.500	1.00	2.00	4.00	8.00	16.00	32.0	64.0	128.0	256.0	512.0
2	0.280	0.561	1.12	2.24	4.49	8.98	17.95	36.0	71.8	144.0	287.0	575.0
3	0.315	0.630	1.26	2.52	5.04	10.10	20.16	40.3	80.6	161.0	323.0	645.0
4	0.353	0.707	1.41	2.83	5.66	11.30	22.62	45.3	90.5	181.0	362.0	—
5	0.397	0.793	1.59	3.17	6.35	12.70	25.39	50.8	102.0	203.0	406.0	—
6	0.445	0.891	1.78	3.56	7.13	14.30	28.50	57.0	114.0	228.0	456.0	—

Table 6.4: Number of Line Pairs / mm in USAF Resolving Power Test Target 1951.

Since the lowest group number in our target is **0**, the lowest spatial frequency we can take into account is 1 mm spacing between the lines. The target has been positioned in the setup pupil stop position and illuminated with the collimated white light produced with a 600 μm core optical fiber. For all the elements composing group 0, we retrieved the profiles of the re-imaged lines and measured the MTF as the contrast between light and dark regions, according to the following expression:

$$MTF(f) = \frac{Peak - Valley}{Peak + Valley} \tag{6.1}$$

Figure 6.21 shows the obtained MTF (since we have no reason to identify one SE as the worst performing one, SE04 has been used as a representative). We define our resolution limit as the spatial frequency at which the MTF reach the 0.5 value, corresponding to a line width of 0.5 mm, re-imaged as $0.5 \times 16.8 \times 2.2 = 18.5$ μm onto the test CCD.

In Figure 6.22, the convolution of a top-hat repeated pattern, representing the physical lines width re-imaged onto the CCD, with a gaussian profile, with a 18.5 μm width (*blue*

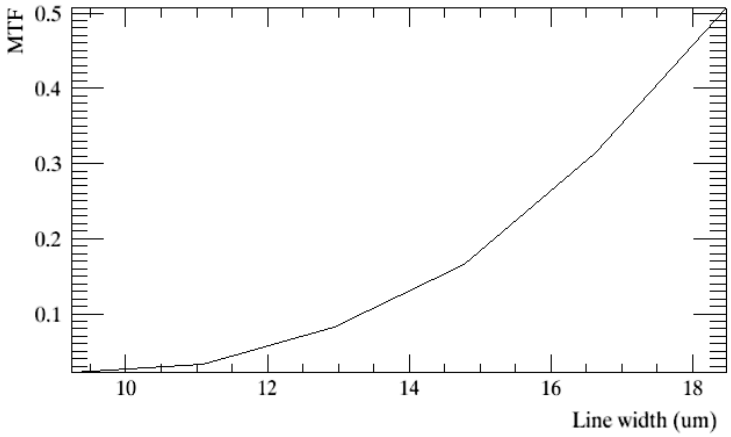

Figure 6.21: Measured MTF of the GWS through SE04.

line), has been superposed to the retrieved profiles of the 0.5 mm wide lines triplet so as to compare the two shapes. It is evident that the contrast of the computed profile is lower than the measured one. Because of that, a third profile has been introduced in Figure 6.22, representing the convolution of the same pattern with a 15.8 μm wide gaussian function (*green line*), showing a much better agreement with the measured profile. This is due to the fact that the MTF=0.5 threshold is an arbitrary value. The retrieved value of 18.5 μm will be considered as an upper limit for the GWS pupil blur, hereafter. An analogous graph is shown in Figure 6.23 for higher spatial order triplets, which are more affected by the noise.

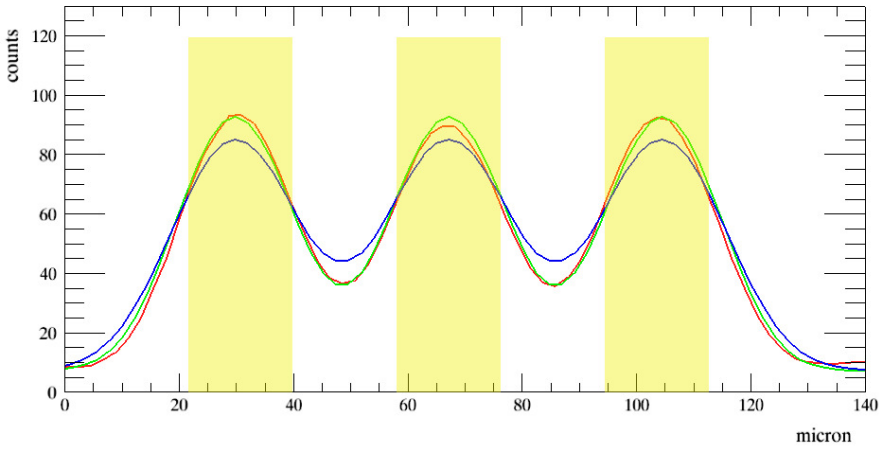

Figure 6.22: Top-hat pattern convolution with a gaussian profile (gaussian width = 18.5 μm) for the higher order (USAF, group#0, element#1). The yellow areas show the top-hat pattern, the *red* line represents the measured profile, while the *green* and the *blue* ones are the computed profiles with a gaussian width of 15.8 μm and 18.5 μm, respectively.

As a further check, a 600 μm pinhole has been positioned on the pupil stop and a SE has been centered onto the focused F/15 beam. The re-imaged four spots show a small elongation

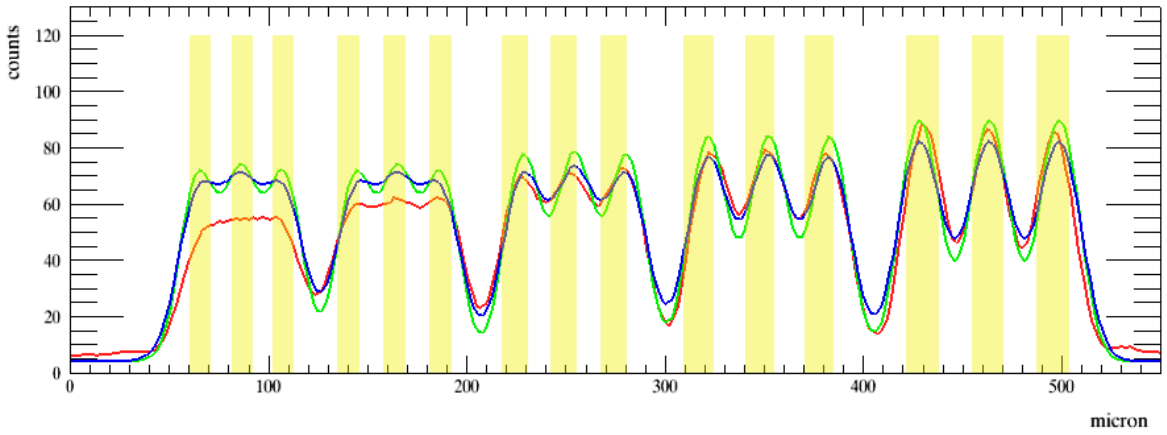

Figure 6.23: Top-hat pattern convolution with a gaussian profile (gaussian width = 18.5 μm) for the higher order (USAF, group#0, elements from 2 -*right*- to 6 -*left*-). The yellow areas show the top-hat pattern, the *red* line represents the measured profile, while the *green* and the *blue* ones are the computed profiles with a gaussian width of 15.8 μm and 18.5 μm, respectively.

(less than 13%) toward the center. A gaussian fit has been carried out on these spots, giving a standard deviation of about 12 μm. After the pinhole dimension subtraction, performed as $\sqrt{(2*\sigma)^2 - (d_{pinhole} \times pixelscale)}$, the resulting pupil blur is about 13 μm. However, this result is strongly depending on uncertainties, since the error propagation for the square root subtraction is high. This value will be considered only a check to be confident the retrieved 15.8 μm blur value was not an underestimation.

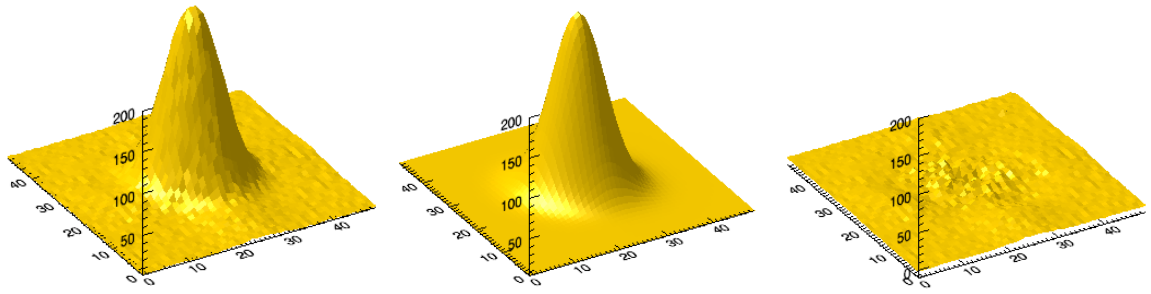

Figure 6.24: *Left*: profile of the image of a 600 μm pinhole, positioned on the pupil stop. *Center*: profile of the gaussian fit carried out on the pinhole image, giving a standard deviation of about 12 μm. *Right*: residual of the two profiles subtraction.

Pupil image cosmetics

A further check realized on the aligned GWS is the verification of the pupil images cosmetics, to verify they do not show relevant features. Images of all the pupils re-imaged by the 12 star

enlargers are shown in Figure 6.25.

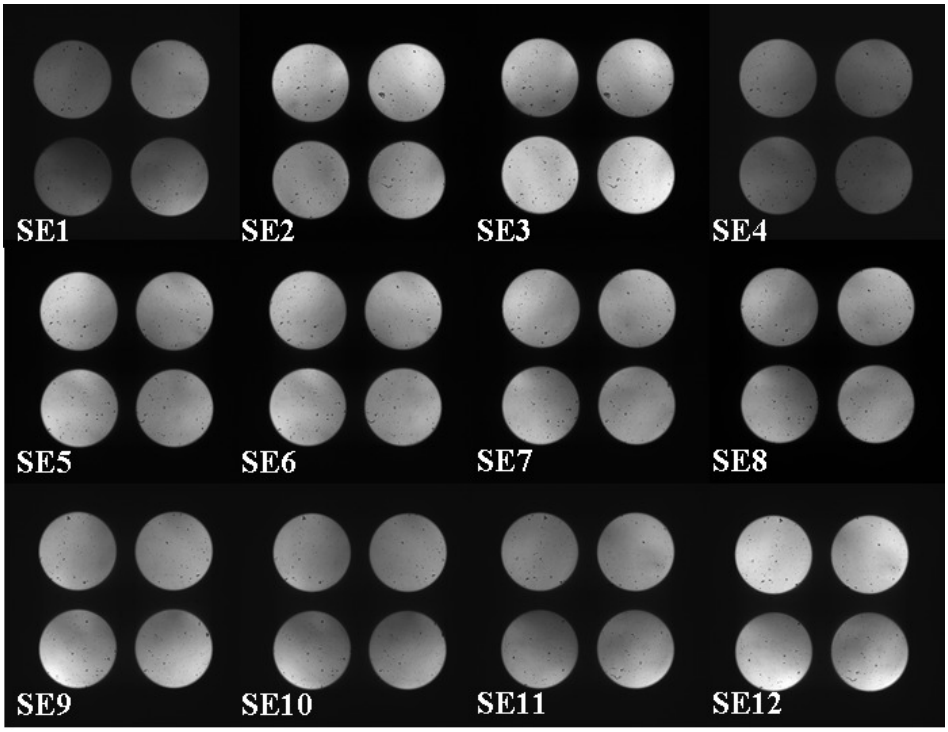

Figure 6.25: Pupil images taken with all the SEs.

Some features appear to all the re-imaged pupils, passing through different star enlargers, revealing their dependency upon the alignment setup. Black dots are due to the diffraction of dust on the test CCD. However, the cosmetics look good.

6.3 System test as a whole and next steps

After the described alignment phases, in which each sub-system has been separately aligned and tested and the GWS has been completely assembled and internally aligned in a static configuration, some test on the system performance as a whole have been carried out, to measure the pupils stability during the bearing rotation. As it is described in the previous Chapters, despite being only one of the four wavefront sensors of Linc-Nirvana, the GWS reveals a noticeable internal opto-mechanical complexity, mainly due to the presence of 12 small devices, with 3 optical components each, moving in a wide annular FoV and sending the light to a common pupil re-imager. The need to obtain and keep a very good super-imposition of the pupil images on the CCD camera, requires an overall alignment procedure in which more than a hundred of degrees of freedom have to be contemporary adjusted. The rotation of the entire WFS to compensate for the sky movement, moreover, introduces a further difficulty in ensuring the required pupil superposition stability. Because of this complexity, it's hardly surprising to find some surprises when testing the behavior of the complete system, since the overall performance includes a combination of all the items included in the error budget, together with unexpected effects (not necessary unsolvable, but simply unknown) and the

result of not yet compensated terms.

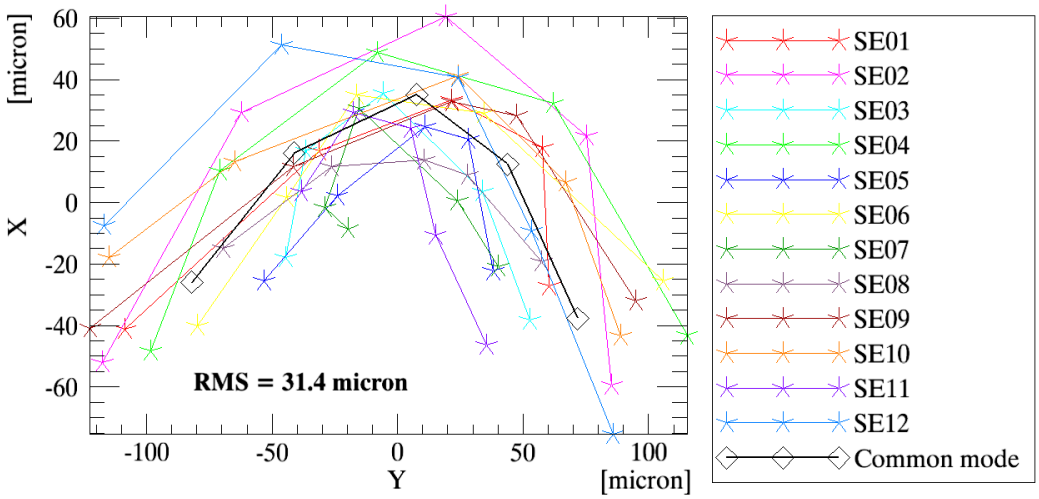

Figure 6.26: Pupils movements on the test CCD for a complete 120 degrees rotation of the GWS. Test CCD X and Y axis are inverted to reproduce a vertical orientation of the gravity vector when the bearing is in the 0° position.

Considering the pupils superposition stability, a substantial discrepancy with expectations has been found out when rotating the bearing, as shown in Figure 6.26. All the previously listed items combine in a way that it is very difficult to completely disentangle them, but it's important to be able to separate at least the common part of such a motion, due to the bearing wobble and to the Pupil Re-Imager and CCD (moreover, this is not the final CCD50, but only the test CCD, mounted in a way which is in part different from the final one) flexures, which can be compensated moving the CCD on its plane, using a look-up table and fine-tuning it as discussed for the pupil matching on WFS issue (see Chapter 3 and Figure 6.27).

Moreover, part of the measured pupil shifts can be due to mechanical problems which could be somehow solved but they first need to be found out, disentangling their effects from the overall pupils movements. This is exactly what happened, since, after many test with the aim to isolate different contributions (linear and tip-tilt stages, flanges flexures, SEs differential behavior, etc..), we discovered that part of the measured differential behavior of the SEs was due to the fact that in some SEs the lenses (namely $SE1$ and $SE2$) were sliding inside their barrel during the rotation. In this case, metal shims have been inserted between the lens and its barrel to ensure a better stability during the rotation, instead of only keeping them pressed between two elastic o-rings. After the lenses fixing the RMS of the spots differential movement was not reduced since, in some cases, the lens shift were somehow compensating the effect of flexures (see Figure 6.28).

The residual shift RMS, measured after the lenses fixing, is not a surprising number, since it includes the effect on the SEs differential tilt of the flexures of the stages, the ring plate holding the stages and the SEs supports. If we consider the sum in quadrature of those effects, as reported in Table 3.4, the expected spots movement was about 14.5 μm. Moreover, despite its capability to perform a 120 degrees rotation, the system is required to rotate for a

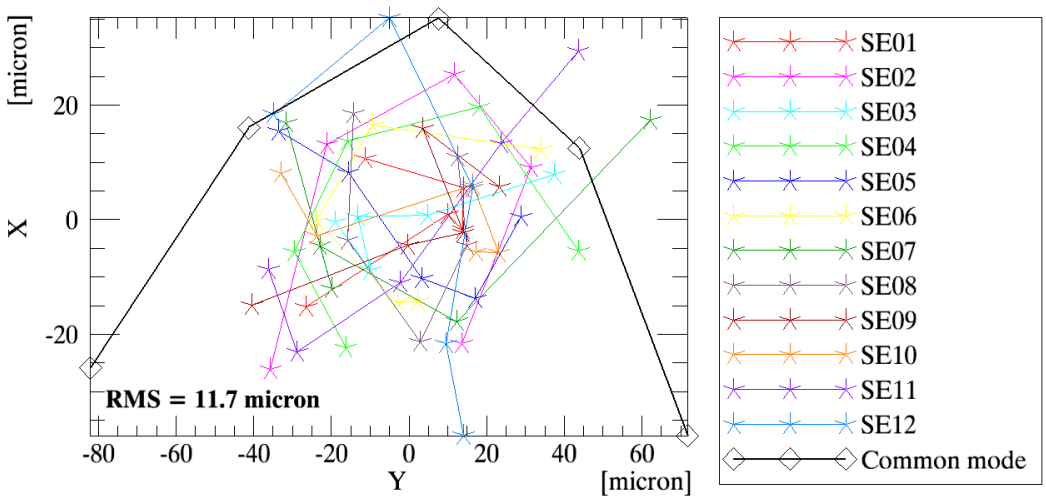

Figure 6.27: Pupils movements on the test CCD for a complete 120 degrees rotation of the GWS, after the subtraction of the common mode, which can be compensated moving the CCD. Test CCD X and Y axis are inverted to reproduce a vertical orientation of the gravity vector when the bearing is in the 0° position.

maximum of 60 degrees inside an observation, because of the limit in the fringes rotation in the interferometric focal plane. A best 60 degrees range can then be selected, to reduce even more the residual differential movements of the pupils produced by the 12 SEs, as shown in Figure 6.29.

I cannot report the very final results of the test of the system as a whole, since the final adjustments concerning the described issues on pupils stability are still on-going.

There's still another point to be discussed. A final decision on how to tackle the issue of the curved focal plane, described in Chapter 3, is on-going in the coming weeks at the time of writing. Possible options are to accept the degradation due to the mis-matching, to tilt all the linear stages of the SEs, in order to minimize the residual defocus detected during the SE movement inside the FoV and to divide the SEs in groups, focused on slightly different planes, in order to be used in different FoV rings, again to minimize the residual defocus, and reduce the size of the seeing disk below which the system is no more sensitive to the high order perturbations, because of saturation of the defocus signal.

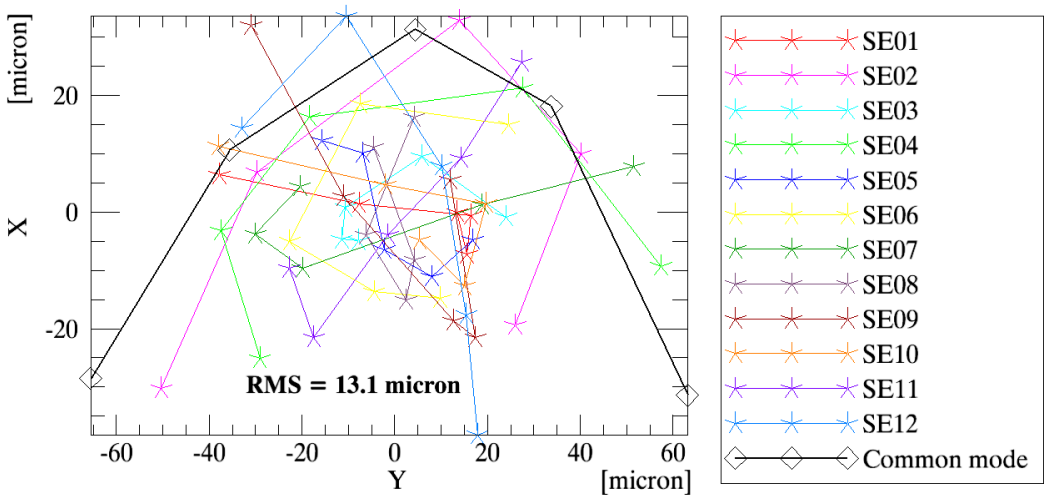

Figure 6.28: Pupils differential residual movements on the test CCD for a complete 120 degrees rotation of the GWS, after the SE2 gluing, when necessary. Test CCD X and Y axis are inverted to reproduce a vertical orientation of the gravity vector when the bearing is in the 0° position.

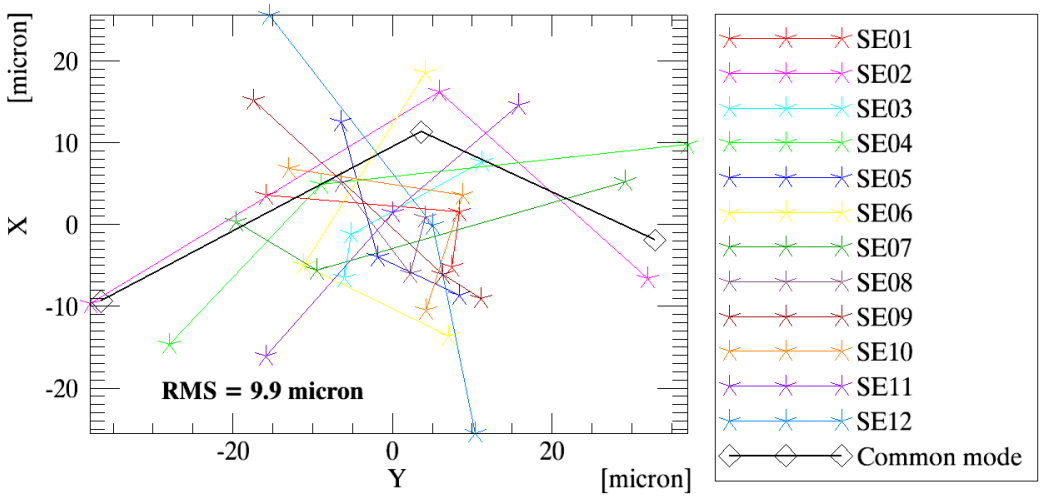

Figure 6.29: Pupils differential residual movements on the test CCD for a 60 degrees rotation of the GWS. Test CCD X and Y axis are inverted to reproduce a vertical orientation of the gravity vector when the bearing is in the 0° position.

6.4 Conclusions

The first Ground-layer Wavefront Sensor of Linc-Nirvana has been completely aligned and verified, and it passed all the performed verifications in its static configuration. The subsystems, whose AIV was already described in detail in Chapters 4 and 5, have been integrated into the main mechanical structure, fixed to the rotating bearing, and each optical subsystem has been optically aligned to the mechanical references in the main structure (nominal focal plane and bearing rotation axis). A procedure for the alignment has been wrote down, taking into account the requirements listed in Chapter 3, the results obtained in the subsystems alignment, and computations made with Zemax or in an analytic way. The compliance of the system performance to the expectations validates the procedure, which will be employed also for the second GWS alignment. All the test have been performed in a static configuration, that is to say without rotating the GWS bearing, since it was not required by the procedure and, above all, to avoid the introduction of uncertainties due to the bearing wobble into the SEs relative alignment.

Test on the system as a whole, including rotation, have been carried out and the final adjustments to ensure an acceptable pupils stability are still on-going at the time of writing, even if the main failures have been already identified and fixed.

Flexures test will be performed at the MPIA, in Heidelberg, to verify the compliance of the actual movements with the expectations and, in case of very good results, to revise the Error Budget again.

Chapter 7

8mm: IntraOcular Lenses test demonstrator

It frequently happens that some knowledges and skills, developed for a particular field of research, can be the solution to other kind of needs in apparently completely different frameworks. Concerning Italian Astronomy, the development and realization of both ground-based and space experiments and projects allowed to reach a very good level of skillness and increase the know-how in a number of different technological areas. These fields have been interpreted by the Italian Institute for Astrophysics (INAF) as the starting point for a constant and well-regulated technology transfer activity. The goal of such an activity is the development of new knowledges and technologies and the establishment of collaborative working relationships between research institutes and local industries, in order to support the professional growth of the staff of these industries, for the creation of innovative products or of spin-offs for the exploitation of the intellectual property.

The technology transfer program, active at the Astronomical Observatory of Padova (OAPd), includes projects supported by the Italian Ministry of University and Research (MIUR), the INAF Office for Technological Innovation (INAF-UIT) and the Industry.

In this framework, a collaboration between OAPd and one Italian ophthalmology industry has been started. As it will be clearer in the following, several similarities exist between Adaptive Optics for Astronomy and for the Visual Science. This deep similarity gives the great chance of injecting into the eye care industry the concepts, ideas and technologies developed for astronomical instrumentations. In particular the three dimensional technologies in wavefront sensing developed to assess wide field diffraction limited imaging in large telescopes, being developed to recognize from which altitude a certain aberration is coming from, offers the unique opportunity to develop sensors for the medical eye care industry able to disentangle the aberrations from the lens, the cornea and the retina shape itself.

A working group has been formed in order to define three prototypes of optical systems for eye care measurements that have been implemented at conceptual level in the laboratory of the Astronomical Observatory of Padova and will be engineered by the industry. The program has been funded by MIUR and the Italian Physical Society (SIF) starting mid 2007.

During my PhD, I realized and characterized a prototype wavefront sensor for the analysis of intra-ocular lenses, used in the transplant of human crystalline lens, described in the following.

7.1 Astro vs Ophto

7.1.1 The human eye: our personal optical system

The human eye is an optical system in all respects. It is composed of two lenses, named *cornea* and *crystalline* lens, like a basic telescope, and two fluids, called the *vitreous* and the *aqueous humor*, which have a physiological protection and retaining function but also introduce distortions on the light passing through them. The crystalline lens can change its shape, so as to adjust the focal length of the eye in order to focus on objects at various distances, in a process called *accommodation*. The lens curvature is controlled thanks to a small muscle, called the *ciliary muscle*, which contracts to achieve short focal distances, increasing the crystalline lens curvature, and relaxes to focus to objects placed at infinity, flattening the lens.

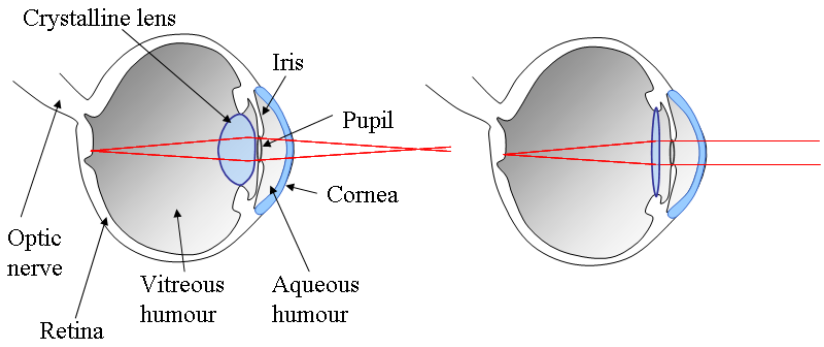

Figure 7.1: The human eye scheme, in two different crystalline lens accomodation positions. *Left*: the lens thickens after the ciliary muscle contraction, increasing its refracting power; *right*: the ciliary muscle is relaxed and the crystalline lens focuses to infinity.

The crystalline lens is made of particular transparent proteins which can, mainly because of the age, progressively oxidize and increases the opaqueness of the crystalline lens itself, causing a common disease known as *cataract*. A total cataract makes one quite completely blind, but it can be surgically nursed, replacing the damaged crystalline lens with a artificial IntraOcular Lens (IOL).

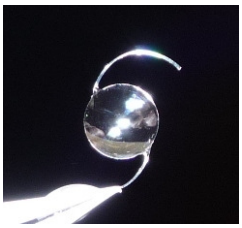

Figure 7.2: IntraOcular Lens.

The first artificial crystalline lens implantation was performed by Dr. Harold Ridley in England, and dates back to November 27^{th}, 1947. The idea came from one of his assistants, who, during a cataract removal operation, asked him why a so important lens was going to be removed without a replacement. In the last half a century, the technology used to realize the artificial crystallines and the replacement procedure have been developed using

new materials and techniques, and those kind of surgery is nowadays well known and it's become an ordinary operation. Even if the production techniques have been developed too (moulding from a casting, etc.), it's still difficult to realize artificial crystallines with a high optical quality and an a priori well known dioptric power. It is therefore worthwhile to test the IOL optical quality, starting from the optical power measurement, before implant it in the patient eye. Nowadays, however, only sample surveys are regularly done, both because the optical quality required to the IOL to be effective in the cataract disease treatment is not so high and because the precise measurement is time expensive and requires a certain skillness in optical alignment. The aim of this part of my PhD work was then to realize a demonstrator of a small, easy to use, low-cost optical system completely made up of commercial components, able to measure the IOLs optical power with a sensitivity far higher than the accuracy which can today be reached in the IOL manufacturing, to quickly and easily test **each** IOL before the implantation.

7.2 IOL quality test demonstrator

7.2.1 The demonstrator concept

We realized a prototype of a WaveFront Sensor with the aim to analyze the optical quality of IntraOcular Lenses, used to replace a damaged crystalline lens, and increase the accuracy in the dioptric power measurement up to ± 0.125 diopters. Such a prototype has been completely aligned and tested in the Adaptive Optics laboratory of the Astronomical Observatory of Padova. For the realization of this particular prototype, a pyramid WFS was selected as the heart of the testing device, but it could, in principle, be substituted by any other pupil-plane WFS. The prototype concept, shown in Figure 7.3, consists of illuminating the IOL to be tested with a white-light collimated beam and analyzing the transmitted light with a pyramid WFS.

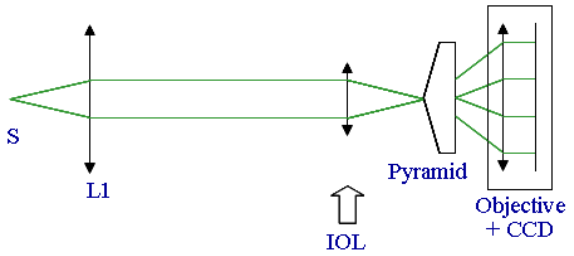

Figure 7.3: IOL testing prototype concept; an optical fiber and a collimating lens (L1) produce a collimated beam, which is focused by the IOL on the pin of the pyramid of the WFS.

The main steps of the demonstrator development are listed in the following:

- Optimization of the holder used to keep the IOL in a fixed position. Since the measurement of the optical power of the lens (defocus of the wavefront) is fundamental, the position of the lens along the optical axis need to be somehow fixed or known.
- Accurate measurement of the static aberrations introduced by the setup: once they have been characterized, it has been possible to ignore them since they turned out to be negligible with respect to the measured wavefronts.

- Optimization of the phase concerning the alignment of the pyramid with respect to the lens, whose position in the x-y plane is extremely variable, since it is immersed in a liquid. De-centering, tip-tilt and de-focus of the pyramid with respect to the lens have to be measured and minimized, and these operations will be completely automated in the next steps, thanks to motorized remotely controlled stages and a control software.

- Measurement of the wavefront produced by pre-characterized lenses in order to have a comparison for the lab measurements and to fix a zero-point for the focal length determination.

7.2.2 The real setup

In order to preserve the IOL sterility and elasticity characteristics, the lens has to be always immersed in a physiological solution. This implied the introduction of a proper holder for the IOL itself, which could be filled with a liquid. The definition and introduction of such an holder imposed some constraint on the system:

- to avoid the distortion of the wavefront, the surfaces of the physiological solution medium, which the light will pass through, need to be flat. Because of that, the liquid solution volume has to be limited by characterized flat optical windows, since a direct transition from air to the physiological solution (or viceversa) produces a curved surface, due to the surface tension of the liquid.

- to define the position of the IOL along the optical axis inside the solution, the lens is kept horizontal, to take advantage of gravity and make the lower optical window act as a reference plane on which the IOL leans.

- since the IOL is immersed into a liquid, it is not possible to align with the asked precision the lens to the WFS.

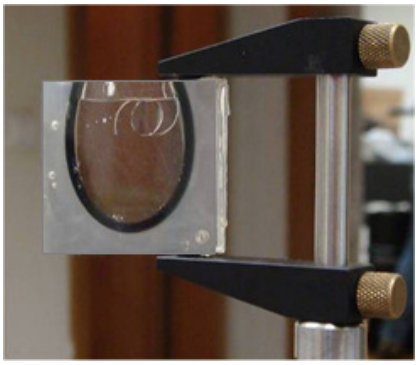

Figure 7.4: IOL holder.

The realized IOL holder, shown in Figure 7.4, is composed of two $\lambda/4$ quality optical windows, separated by an o-ring which maintains them at a fixed relative distance of 2mm. A silicon glue keeps the surface together and avoids any liquid leakage. On one side, both the o-ring and the glue are open, so it is possible to fill the holder with the physiological solution and insert the IOL. The surface tension on the open side is enough to keep the liquid inside

the holder, when it is positioned horizontally. A further setup modification consists of the insertion of a Star Enlarger system (see Section 2.4.2), just in front of the refractive pyramid, which is necessary to obtain non-overlapping pupil images on the CCD. This problem is due to the fact that we used a refractive pyramid which was not custom made for this experiment, and its vertex angle was too small to ensure the pupil separation for the complete range of IOL diopters.

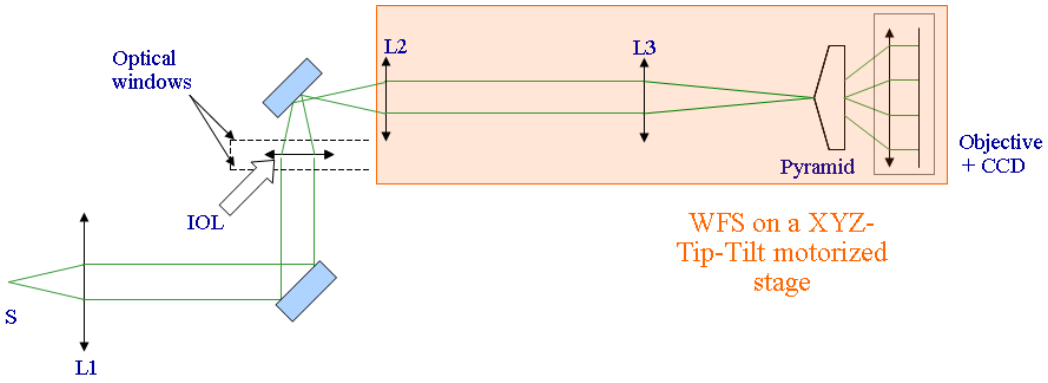

Figure 7.5: Demonstrator modified concept.

Figure 7.5 shows the setup modified concept. The idea is to have a sensor which can be aligned with respect to the position of the IOL to be tested, thanks to a 3-axis mechanical movement system, allowing the minimization of the relative de-centering and a correct focusing the whole system. This both solves the IOL positioning problem, due to the fact the lens is immersed in a liquid solution and so it lays on the optical window in an unknown XY position, and goes in the direction of a real commercial test instrument, in which the IOLs can be inserted quickly, without any particular care, to perform the measurements. Once the IOL is inserted in its holder, it can be put inside the optical path of the light on the bench, the WFS can be aligned and the wavefront shape retrieved. The static aberrations, introduced by the setup components and little misalignments between them, have to be subtracted to what the WFS is measuring.

7.2.3 Setup details

To minimize time and money cost of the prototype realization, commercial off-the-shelf available optical components have been used. In particular, the pyramid vertex angle imposed the introduction of a Star Enlarger system between the IOL and the WFS, to avoid the pupils superposition on the CCD.

Table 7.1 summarizes the main optical characteristics of the commercial components used to realize the optical setup, shown in Figure 7.6 and described in the following:

- a laser head (not in Figure 7.6) has been used as a tool for the optical components alignment, in terms of centering and tip-tilt;
- the source S is an optical fiber, fed with white light, mounted on a kinematic magnetic base plate, to be easily removable and repositionable, when an alignment check with the laser beam is required;

Table 7.1: Optical commercial components used to realize the prototype

	Component	Characteristic
S	Source: optical fiber	core $s = 200$ μm
L1	Collimating lens 1	Focal length $f_{L1} = 76$ mm
L2	Star Enlarger lens 1	Focal length $f_{L2} = 9$ mm
L3	Star Enlarger lens 2	Focal length $f_{L3} = 125$ mm
Pyr	Refractive pyramid	Vertex angle $\alpha = 1°$
Obj	Objective	Focal length $f_{obj} = 75$mm
CCD	CCD AVT Pike F145B	1388x1038 pixel, pixelsize = 6.45 μm

- the collimating lens L1 collimates the optical beam coming from the source, to illuminate the IOL with flat wavefronts;
- the IOL, inserted in its holder and immersed into the physiological solution to maintain its flexibility, is positioned horizontally in an area in which the optical axis is vertically folded by two flat mirrors;
- the pyramid WFS position is remotely adjusted in order to make the IOL focal plane fall on the vertex of the pyramid. A Star Enlarger (composed of lenses L2 and L3), increases the spot diameter on the pin of the pyramid in order to decrease the pupils dimension on the CCD, to avoid their superposition, due to a small pyramid vertex angle, and to increase the WFS linearity range;
- a commercial photographic objective re-images a pupil plane onto the detector, which is the last component of the prototype.

Enlargement

The spot diameter on the pin of the pyramid ($s_{pyramid}$), once the parameters in Table 7.1 are fixed, is related to the focal length of the lens to be tested:

$$s_{pyramid} = s \cdot \frac{f_{IOL}}{f_{L1}} \cdot k$$

where $k = f_{L3}/f_{L2}$ is the SE enlarging factor.

Table 7.2: IOL focal range

	MIN	MAX
f_{IOL}	30 mm (33 diopters)	200 mm (5 diopters)
$s_{pyramid}$	1.12 mm	7.31 mm

Table 7.2 reports the IOL focal length range which our prototype is asked to analyze and the relative spot diameter range on the pin of the pyramid.

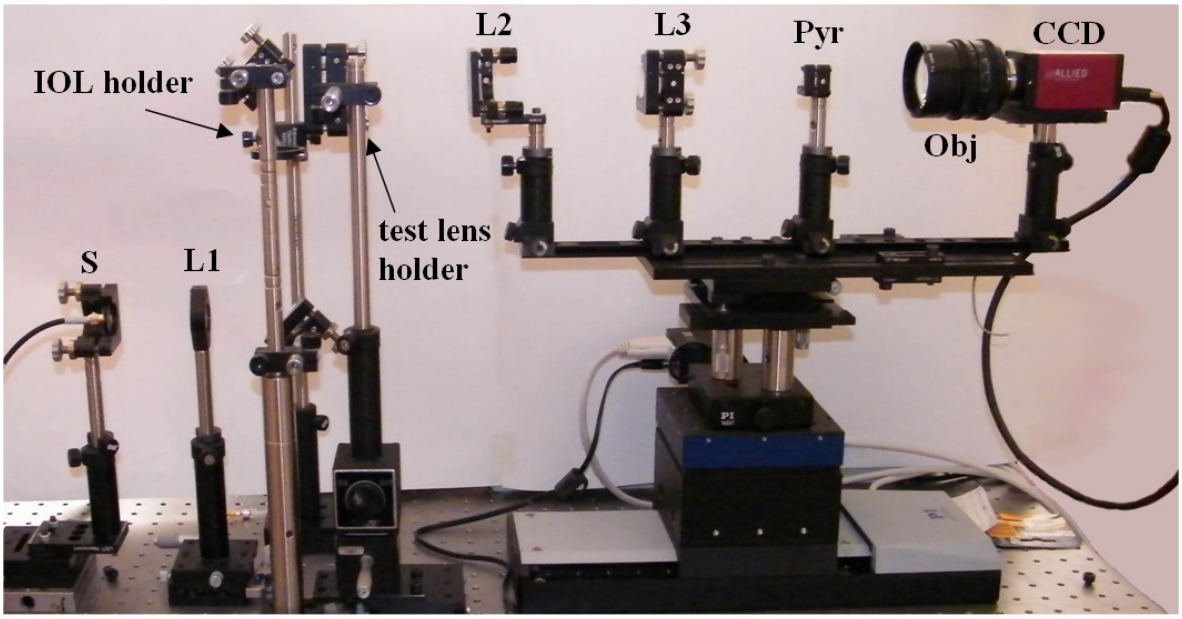

Figure 7.6: Prototype setup.

Motorized linear stages

Table 7.3: WFS motorized axis characteristics

Axis	Name	Travel range [mm]	Resolution [μm/step]	Repeatability [μm]
Z	Newport: M-511.DG	102	0.033	1.15
Y	Newport: M-501.DG	12.5	0.0056	2.33
X	Newport: M-126.PD1	25	04125	3.62

Table 7.3 lists the main characteristics of the motorized linear stage by Newport company used to align the WFS to the IOL inside the prototype. Each stage has an internal reference (defined with Hall effect), corresponding to the zero value of the encoder. While the stages resolutions are by-design values, the positioning repeatability has been estimated through a statistic analysis based on 10 determinations for each stage.

7.3 WFS linearity range

7.3.1 Characterization of the relation between Zernike defocus coefficient, diopters and focal lengths

First of all, the prototype is asked to measure the dioptric power of the lens which is tested. Because of that, the first test we performed had the aim to obtain the IOL focal plane position from the defocus coefficient measurement, retrieved by the WFS, through the Zernike

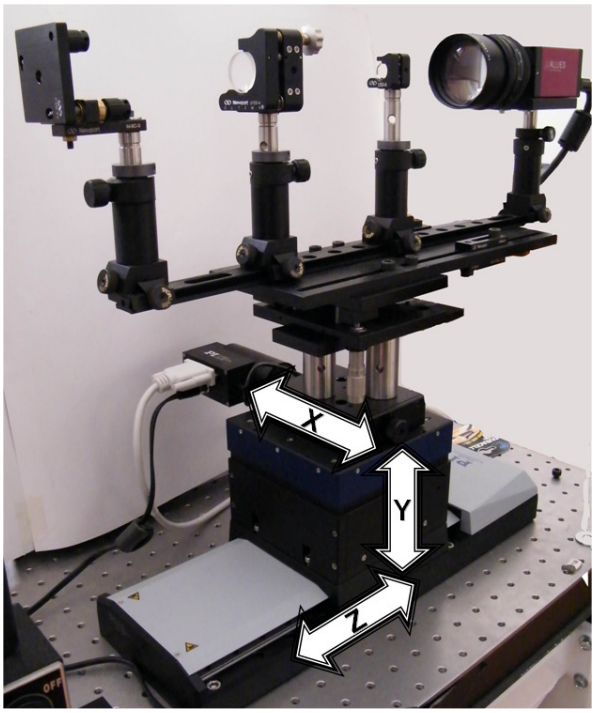

Figure 7.7: WFS motorized axis.

polynomials analysis. The focal plane position is expressed in mm as the distance from a reference position of the focusing stage. The following step will be the calibration of such a reference position. The test procedure consists of:

- take a set of measurements of the defocus coefficient ($C_{defocus}$) for a test lens, varying the WFS position (Z_{WFS}) along the optical axis, in order to map the aberration caustic;
- plot the defocus coefficients versus the WFS positions along the optical axis and compute a linear interpolation to retrieve the linear best fit, defining the empiric law that will be used to link the defocus coefficient to the position of the linear focusing stage: $Z_{WFS} = m(f) \cdot C_{defocus} + q(f)$, which is peculiar of the lens focal length (an analogous expression exists as a function of the dioptric power);
- once the best fit is retrieved, the position of the WFS corresponding to a zero defocus coefficient can be computed, and the WFS is moved to reach such a position;
- the defocus coefficient is measured again and the procedure is iterated 2 times; in an ideal situation the measured defocus coefficient should be null, but the real measurement can be useful to quantify the indetermination $\delta C_{defocus}$ and the related error in the WFS position $\delta Z_{WFS} = \delta C_{defocus} \cdot m(f)$. δZ_{WFS} can be converted in diopters, remembering that

  $$d = \frac{1}{f} \qquad \pm \Delta d = \frac{1}{f^2} \cdot \Delta f$$

  where f and Δf are the focal length and the error to be associated to it in mm, respectively, and d and Δd are the dioptric power and its indetermination, due to the error of the WFS positioning with respect to the lens focal plane.

- The obtained expression can be easily inverted to obtain:

$$\pm\Delta f = \Delta d \cdot f^2$$

Substituting $\Delta d = 0.125$ the maximum acceptable indetermination on the focal length measurement is then retrieved.

7.3.2 Defocus measurements linearity and sensitivity

Since the empiric law retrieved in the previous section is depending upon the lens focal length, the whole procedure has been repeated with test lenses (both IOL and commercial glass lenses) with different focal lengths. Table 7.4 reports the retrieved angular coefficients for a complete set of lenses with different focal lengths. The same results are shown in Figure 7.8 too, as a function of the lens dioptric power.

Table 7.4: The empiric law angular coefficients for a set of test lenses with different focal lengths. The last column lists the computed tolerances for the focal length measurements in mm, corresponding to ±0.125 diopters. IOLs are labeled with an asterisk, while the other lenses are commercial glass lenses, used to have a complete set of focal lengths.

Focal length [mm]	Dioptric power	m [mm]	Δf_{max} [mm]
49*	20.4	0.004	0.30
61*	16.4	0.006	0.47
76.2	13.1	0.008	0.73
82.5*	12.4	0.014	0.86
95.2*	10.5	0.020	1.15
100	10	0.023	1.25
125*	8	0.054	1.98
150	6.7	0.113	2.81

The next step is to verify the stability of the described procedure and define what happens when the WFS starting position is very far from the IOL focal plane. From this point of view, the maximum distance from the focal plane in which the WFS is working properly represents the linearity range of the sensor itself and depends also upon the focal length of the lens to be tested. In Figure 7.9, the defocus Zernike coefficient is plotted as a function of the WFS position along the optical axis (with respect to the best focus position), for a lens with a focal length of 100 mm. One can notice that the retrieved plot shape clearly deviates from linearity for a WFS distance from the best focus higher than 6 mm.

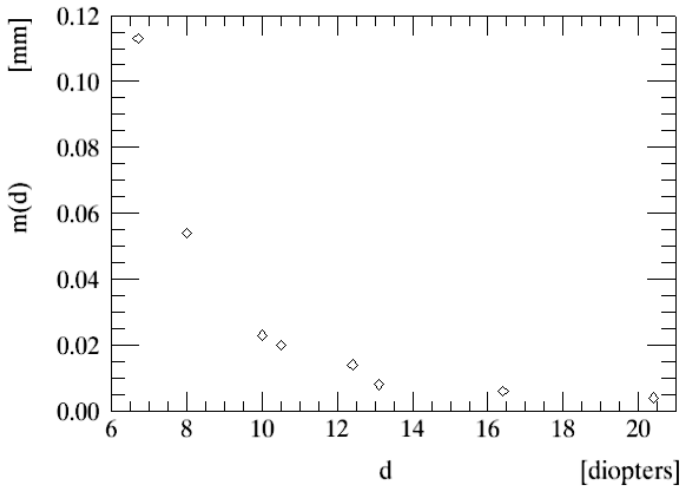

Figure 7.8: Empiric law angular coefficient, as a function of the dioptric power of the lenses.

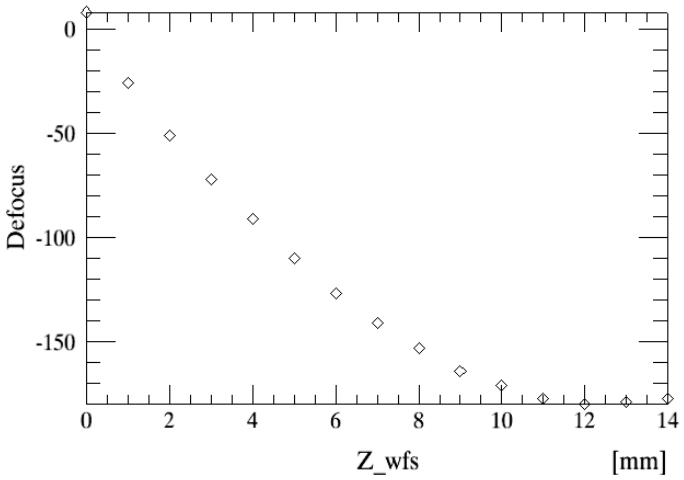

Figure 7.9: Defocus coefficients for a lens with $f = 100$ mm as a function of the distance of the WFS from the best focus position (in mm). The total range is of course symmetric, but the graph shows only the WFS movement on one direction. The linear behavior of the WFS is maintained up to a 6 mm distance from the best focus position, while for bigger distances the WFS reaches the saturation of the signal.

7.3.3 Tip-tilt measurements linearity and sensitivity

The WFS centering with respect to the optical axis defined by the IOL is realized minimizing the tip and tilt coefficients retrieved by the WFS in the Zernike polynomials analysis. The centering procedure is analogous to the focusing one, described in Section 7.3.1. The aim of this test is the characterization of the linearity range and the sensitivity of the WFS concerning the tip-tilt measurements. Table 7.5 shows the linearity ranges computed in geometric approximation for each considered focal length. These values have to be compared with the corresponding values obtained experimentally.

Table 7.5: Results of the geometric computation of the WFS linearity range, depending upon the source diameter, the star enlarger enlarging factor and the collimating lens focal length. IOLs are labeled with an asterisk, while the other lenses are commercial glass lenses, used to have a complete set of focal lengths.

Focal length [mm]	Dioptric power	Tiptilt linearity range [mm]
49*	20.4	0.13
61*	16.4	0.16
76.2	13.1	0.20
82.5*	12.4	0.22
95.2*	10.5	0.25
100	10	0.26
125*	8	0.33
150	6.7	0.40

Glass test lenses

To have a sensitivity estimation, we used two already characterized commercial lenses with a 2 inches diameter, to minimize the errors due to the aberrations introduced by the lens to be tested. The focal lengths of the lenses are 150mm and 100mm, respectively. A procedure analogous to the test performed on the defocus coefficients has been used. First of all, a set of measurements of the Tip and Tilt coefficients, varying the WFS X (tip) and Y (tilt) positions has been taken for each of the two test lenses; then the best linear fit has been computed on the values of the positions of the WFS along the x and y axis versus the tip and tilt coefficients, respectively, to retrieve the empiric law describing the link between WFS position and measured Zernike coefficient. The obtained angular coefficients of the best linear fit were expected to be the same for the two direction, for each lens. The result are shown in Table 7.6.

As an example, Figure 7.10 shows the trend of the retrieved Tip coefficient, in the 150mm focal length test lens case, as a function of the WFS X position. It's been verified, and it is visible in this Figure, that the WFS behavior is linear in a 0.3mm wide range, centered on the zero-tip position of the WFS, where the four pupils are uniformly and equally illuminated.

If the WFS at the beginning of the measurements is already inside its linearity range, it can adjust its position automatically, simply minimizing the tip and tilt coefficients. If, on the contrary, the WFS is outside the linearity range, the acquisition range can be increased

Table 7.6: Results of the test on the conversion of the WFS positions along the x and y axis to the tip and tilt retrieved coefficients. As expected, the angular coefficients of the best linear fit are similar for the x and y direction, once the test lens is fixed.

Focal length [mm]	m_{tip} [mm]	m_{tilt} [mm]
150	0.0011	0.0010
100	0.00047	0.00046

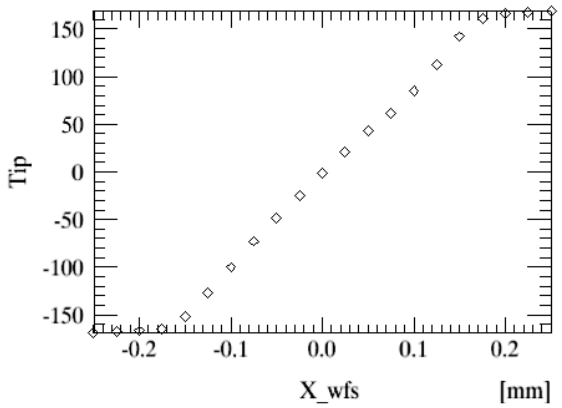

Figure 7.10: Tip coefficient of the 150 mm focal length test lens, as a function of the WFS x position.

verifying which of the pupils are illuminated and moving the WFS step-by-step in the correct direction in order to enter the linearity range.

Linearity test with an IOL

The same linearity test performed with the glass test lenses have been repeated with an IOL, to validate the procedure itself. The linearity ranges have been measured for an IOL with focal length equal to 95.2 mm, in all the three axis. The results are shown in Figure 7.11, and the obtained linearity ranges are about 5 mm for the defocus and 0.2 mm for the tip and tilt.

These ranges are compatible with the computations reported in Table 7.5 and are far wider than the minimum ranges we required to perform our measurements.

7.4 Wavefront computation and conversion in nanometers

The WFS computes the aberrations as the linear combination of a set of polynomials (see Zernike polynomials description in Section 1.5), whose coefficients vary according to the entity of each type of aberration. We decided to stop the reconstruction at the 14th Zernike polynomial. These coefficients are normalized according to Noll, 1976 [17], so as to always have a standard deviation equal to 1. The first step we performed before each measurement was the centering and focusing of the WFS minimizing the tip, tilt and defocus terms retrieved

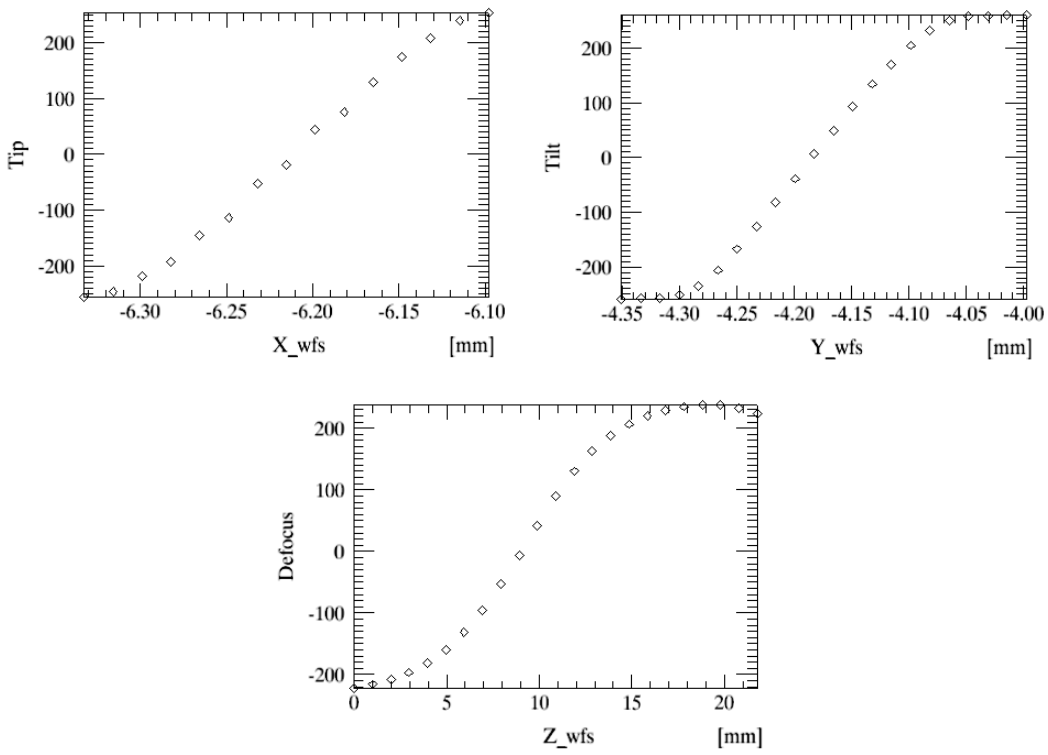

Figure 7.11: Tip, tilt and defocus coefficient trends for the 95.2 mm focal length IOL, as a function of the WFS position along x, y and z axis, respectively.

with a preliminary analysis. The residual tip, tilt and defocus term will be subtracted by the measured wavefront. Since the coefficients are not expressed in physical units in the WF computation, it is necessary to convert them in order to quantify the aberrations in term of nanometers PtV on the wavefront. A spatial range along the z axis, centered on the best focus position, is defined and the defocus coefficient is measured for both the extreme intra-focal and extrafocal positions (which are symmetric with respect to the best focus). The converting factor can be easily retrieved as follows:

$$Con_{defocus} = \frac{1}{8 \cdot 2\sqrt{3}} \cdot \frac{D^2}{f^2} \cdot \frac{\Delta l}{\Delta c}$$

where D is the IOL diameter (6 mm), f is its focal length, Δl is the used range along z, $\Delta c = C_{intra} - C_{extra}$ is the difference between the measured defocus coefficients in the intra and extrafocal positions. The factor $2\sqrt{3}$ is an approximation which allows to convert from RMS to PtV values. Since such a converting factor is obtained with only two determinations, we increased the robustness of the result repeating the described procedure for several couples of intra and extrafocal positions defocus coefficients determinations. All the measurements have been repeated for each of the lens in the sample, and the results are summarized in Table 7.7.

Table 7.7: Focal lengths of the lenses sample and the factors to convert the Zernike coefficients in mm. IOLs are labeled with an asterisk, while the other lenses are commercial glass lenses, used to have a complete set of focal lengths.

Focal length [mm]	Dioptric power	$Con_{defocus}$ [nm]
49*	20.4	2.2
61*	16.4	2.0
76.2	13.1	1.9
82.5*	12.4	2.7
95.2*	10.5	2.9
100	10	3.2
125*	8	4.5
150	6.7	6.5

7.5 Calibration lines

As explained in the previous Section, two defocus measurements, taken in intra and extra-focal positions, can be used to retrieve the calibration line for the conversion of the computed Zernike coefficients in nanometers of WFE.

7.5.1 Through focus reliable range for the calibration lines determination

The couple of measurements used to determine the calibration line shall not be taken in too close positions, since errors in the defocus coefficients computation translate into an indetermination in the calibration line slope which is increasing while the intra and extrafocal positions distance decreases. On the other hand, this distance shall not exceed the linearity range, discussed in Section 7.3.2. Finally, an error in the calibration line angular coefficient propagates into the determination of the test lens focal plane position and, consequently, into the dioptric power measurement. Which are, then, the minimum and the maximum spatial ranges along the optical axis inside which the WFS can be moved to properly determine the test lens focal plane position? Moreover, we want to define the range and the number of images, which are suitable for a reliable computation of the conversion coefficient described in Section 7.4. Since the conversion coefficient is in direct ratio to the calibration line angular coefficient, the indetermination in the latter propagates into the former. Similar test have been performed using two laboratory lenses, $f = 100$ mm and $f = 150$ mm, respectively, and an IOL in the same focal range ($f = 95.2$ mm), to verify the obtained results were compatible.

Glass test lenses

Table 7.8 shows a set of measurements of the calibration line slope and of the conversion coefficient, taken for different distances of the intra and extra-focal positions of the WFS (ΔZ), for both the glass test lenses considered. Reference represents a reliable focal plane position measurement, i.e. the mean value of 13 determinations, obtained with a set of 13 couples of images taken with relative distances ranging from 0.1 mm to 1.2 mm with a 0.1 mm step, and considered as a reference position for the other measurements. All the other ΔZ

ranges in Table 7.8 are centered in such a reliable focus position, and the reported δz and δd represent, respectively, the difference between the position of the retrieved focal plane and the dioptric power, with respect to the reference. A check on the reliability of the measurements has been performed recomputing both the coefficients using 10 different couples of images, with a fixed ΔZ. The obtained coefficients are very stable, presenting totally negligible fluctuations.

Figure 7.12 and 7.13 show the variation of the coefficients and the residual dioptric power measured considering different ranges ΔZ. The required precision for the prototype in the measurement of the dioptric power is 0.125 diopters, translating, for the considered $f = 100$ mm and $f = 150$ mm lenses, into a 1.27 mm and 2.81 mm precision in the definition of the test lens focal plane position, respectively. We can notice that all the retrieved measurements are inside such a requirement. However, we arbitrarily decided to limit the acquisition range, in a way that the indetermination on the retrieved coefficients is lower than the $\pm 5\%$. This leads to a range between 0.1 mm and 4 mm for the $f = 100$ mm lens and between 0.07 mm and 0.25 mm for the $f = 100$ mm lens.

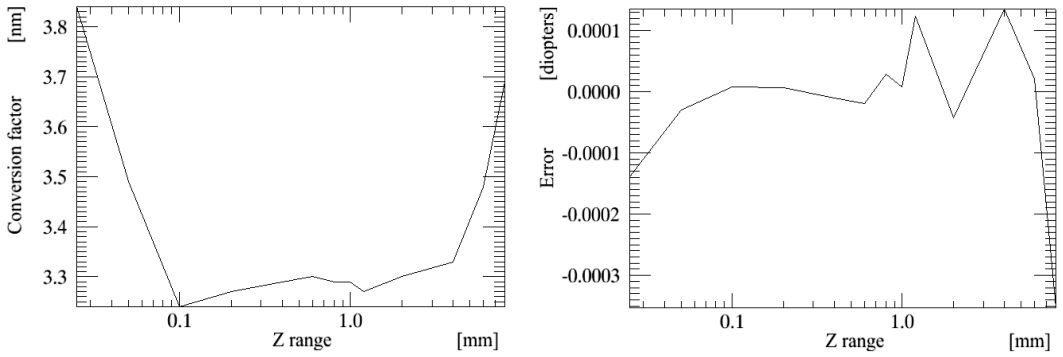

Figure 7.12: Test lens with $f = 100$ mm. Conversion coefficient and dioptric power residual measurements, experimentally resulting for different ranges ΔZ.

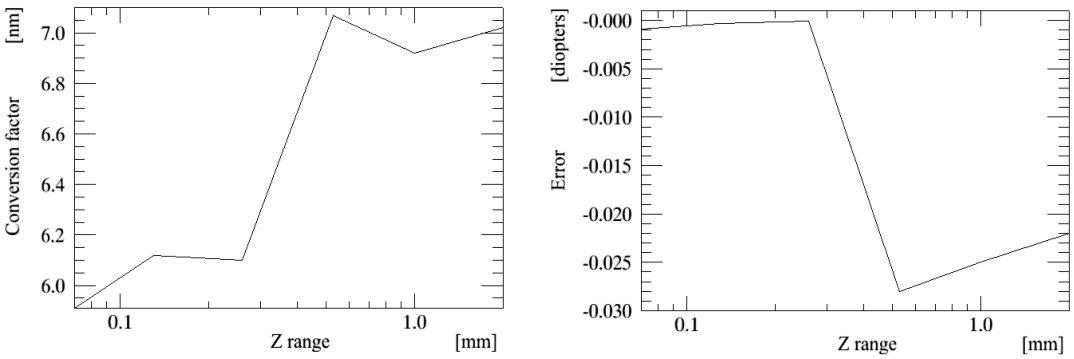

Figure 7.13: Test lens with $f = 150$ mm. Conversion coefficient and dioptric power residual measurements, experimentally resulting for different ranges ΔZ.

Finally, we checked the stability of the obtained conversion coefficient measuring it in different days and daytimes for the lens with $f = 100$ mm. For a complete set of measurements, the coefficients varies between 2.9 nm and 3.3 nm. Considering that the mean value of the static aberration due to the setup (see next Sections) is about 100 nm, this indetermination, translating into an error of about 13 nm, still allowed a WF reconstruction with a precision better than $\lambda/50$.

IOL: f = 95.2mm

Analogous test have been performed on a IOL in the same focal range as the glass laboratory lenses used to verify the best acquisition ranges. In Table 7.9, the results of this test are listed, with the same definition used in the previous paragraph. As obtained for the glass $f = 100$ mm lens, the minimum distance between the couple of images, to compute the focal plane position, is 0.1 mm. Concerning the conversion coefficient stability, however, the 5% indetermination is exceeded for $\Delta Z < 0.2$ mm.

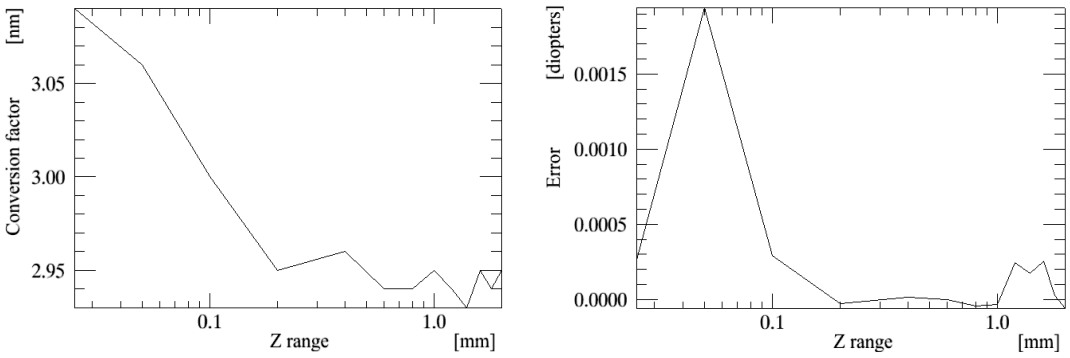

Figure 7.14: IOL with $f = 95.2$ mm. Conversion coefficient and dioptric power residual measurements, experimentally resulting for different ranges ΔZ.

Table 7.8: Calibration line angular coefficients (m_cal), measured with different ΔZ ranges, centered in the reference focal position. The reported δz and δd represent, respectively, the residual shift of the focal plane and the dioptric power, with respect to the reference. Last column lists the retrieved conversion coefficients.

Test lens: $f = 100$ mm

ΔZ [mm]	m_{cal}	δz [μm]	δd [diopters]	$Con_{defocus}$ [nm]
0.025	-33.83	-5.51	$-1.39\cdot10^{-4}$	3.84
0.05	-37.21	-1.19	$-3.00\cdot10^{-5}$	3.49
0.1	-40.05	0.33	$8.33\cdot10^{-6}$	3.24
0.2	-39.77	0.26	$6.67\cdot10^{-6}$	3.27
0.4	-39.53	-0.40	$-1.00\cdot10^{-5}$	3.29
0.6	-39.35	-0.76	$-1.92\cdot10^{-5}$	3.30
0.8	-39.49	1.16	$2.92\cdot10^{-5}$	3.29
1	-39.46	0.33	$8.33\cdot10^{-6}$	3.29
1.2	-39.73	4.92	$1.24\cdot10^{-4}$	3.27
2	-39.42	-1.72	$-4.33\cdot10^{-5}$	3.30
4	-39.05	5.35	$1.35\cdot10^{-4}$	3.33
6	-37.31	0.83	$2.08\cdot10^{-5}$	3.48
8	-35.22	-13.99	$-3.53\cdot10^{-4}$	3.69
Reference	-39.60	0	0	3.28

Test lens: $f = 150$ mm

ΔZ [mm]	m_{cal}	δz [μm]	δd [diopters]	$Con_{defocus}$ [nm]
0.07	-9.77	-5.94	$-9.0\cdot10^{-4}$	5.91
0.13	-9.42	-2.11	$-3.2\cdot10^{-4}$	6.12
0.26	-9.47	-0.26	$-4.0\cdot10^{-5}$	6.10
0.53	-8.16	-181.53	$-2.8\cdot10^{-2}$	7.07
1	-8.34	-162.69	$-2.5\cdot10^{-2}$	6.92
2	-8.21	-142.79	$-2.2\cdot10^{-2}$	7.02
Reference	-8.87	0	0	6.51

Table 7.9: Calibration line angular coefficients (m), measured with different ΔZ ranges, centered in the reference focal position. The reported δz and δd represent, respectively, the residual shift of the focal plane and the dioptric power, with respect to the reference. Last column lists the retrieved conversion coefficients.

IOL: $f = 95.2$ mm

ΔZ [mm]	m_{cal}	δz [μm]	δd [diopters]	$Con_{defocus}$ [nm]
0.025	-46.35	11.96	$2.63 \cdot 10^{-4}$	3.09
0.5	-46.77	88.23	$1.94 \cdot 10^{-3}$	3.06
0.1	-47.83	13.17	$2.90 \cdot 10^{-4}$	3.00
0.2	-48.52	-1.28	$-2.81 \cdot 10^{-5}$	2.95
0.4	-48.50	0.69	$1.52 \cdot 10^{-5}$	2.96
0.6	-48.76	-0.04	$-8.34 \cdot 10^{-7}$	2.94
0.8	-48.74	-2.00	$-4.39 \cdot 10^{-5}$	2.94
1	-48.67	-1.62	$-3.55 \cdot 10^{-5}$	2.95
1.2	-48.79	10.94	$2.41 \cdot 10^{-4}$	2.94
1.4	-48.93	7.83	$1.72 \cdot 10^{-4}$	2.93
1.6	-48.67	11.64	$2.56 \cdot 10^{-4}$	2.95
1.8	-48.74	1.19	$2.62 \cdot 10^{-5}$	2.94
2	-48.66	-2.70	$-5.94 \cdot 10^{-5}$	2.95
Reference	-48.74	0	0	2.94

7.6 Wavefront analysis

After the characterization of the procedure for the WFS alignment with respect to the IOL, the first WaveFronts can be retrieved. These measurements, however, will include also the aberrations introduced by the setup. Because of this reason, this static aberrations have to be quantified, to determine if they have to be subtracted or they can be simply neglected.

7.6.1 Static aberration

To measure the IOLs optical quality with our demonstrator, the first step was to characterize the static aberrations introduced by the setup itself. Since the optical elements to be analyzed by the prototype have a non-negligible optical power, we could not simply measure the aberrations of the setup, retrieved removing the IOL from the optical path, since in such a configuration the light does not focus on the pin of the pyramid WFS. So, to characterize the setup static aberration we had to replace the IOL with another focusing optical element. Calibrated achromatic doublets have been selected to perform this analysis, in order to introduce on the WF only negligible aberrations. Moreover, the test lenses had a 50.8 mm diameter, and only the inner part (6 mm) were selected by a diaphragm in order to work in quasi-paraxial conditions and to limit the diameter to the actual IOL diameter. There are several possible source of error in determining the static aberration introduced by the setup. First of all we want to be sure that this aberration is actually static, that is to say that we will not accidentally change it during operations on the setup. During the test on the IOL, in fact, some setup components are sometimes moved or removed to check the alignment of the setup or to disentangle one component from another. The setup alignment is regularly checked with the laser beam, and during this operation the optical fiber is removed using the magnetic base plate on which it is fixed. Moreover, we could sometimes change the optical fiber itself. In both this cases, the effect should not be the introduction of aberrations on the setup, since the only aberrations directly depending upon the optical fiber position are the tiptilt, which is automatically subtracted, and the defocus, always minimized before each measurement. In case the fiber does not deliver an uniform and spheric WF, however, the repositioning of the fiber itself could change the static aberration of the setup. The positioning of the test lens could, in principle, be another source of error. Its position could vary in x-y directions, again acting on the tip-tilt coefficients, or along the optical axis, slightly changing the focus position. But, again, these are contributes which are subtracted or minimized. However, if the lens itself is not center-symmetric or the 6 mm area selected by the diaphragm is changing, some unknown aberrations could be introduced. Moreover, also the environment conditions should be taken into account, since different temperature-pressure on the setup could change the performance and the static aberration itself. Finally, also the choice of the test lens could introduce some systematic errors on the static aberration measurement. More than one lens should be used. The result of this discussion is that what we are calling static aberration is, in fact, non-static at all. What we want to know, now, is whether it is static enough to be simply subtracted by the measured IOL wavefronts or, better, if we could simply consider it as negligible, or none of them. In Table 7.10 are summarized the Zernike coefficients (tiptilt is automatically subtracted) and the overall Peak-to-Valley (PtV) aberrations, obtained in various configurations, to possibly disentangle aberrations which could be introduced during any operation on the setup. The configurations taken into account are the following;

- Test 1: first coefficients determination. The used test lens has $f = 100$ mm, the WFS

Table 7.10: Zernike coefficients measured in different setup conditions, to verify the stability of the aberration introduced by the demonstrator itself and quantify it.

C_i [nm]	3	4	5	6	7	8	9	10	11	12	13	PtV
Test 1	11	2	10	17	2	4	49	29	2	7	12	83
Test 2	30	3	32	2	7	13	38	6	6	7	13	74
Test 3	11	23	17	3	17	25	54	1	4	6	8	73
Test 4	3	41	15	2	14	23	44	9	1	5	7	69
Test 5	22	3	34	3	13	9	40	7	5	9	15	71
Test 6	17	0	35	3	16	11	40	6	4	8	15	74
Test 7	18	5	29	10	17	8	30	20	5	13	15	69
Test 8	19	1	32	11	18	10	31	17	4	8	14	71
Test 9	13	30	21	10	16	9	59	0	1	6	11	84
Test 10	48	8	15	10	13	2	14	15	10	1	6	89
Test 11	4	49	19	13	14	13	10	3	20	1	3	85

is centered and focused with respect to the lens;

- Test 2: the centering and focusing procedures are repeated, to verify they are not introducing an unexpectedly variable and high aberration;
- Test 3: the same as Test 1, but repeated in other conditions (another day and daytime);
- Test 4: the same as Test 2, but repeated in other conditions (another day and daytime);
- Test 5: the optical fiber is removed from its holder and then replaced;
- Test 6: same as test 5;
- Test 7: the kinematic base used to reposition the optical fiber after laser alignment verification is removed and repositioned;
- Test 8: the $f = 100$ mm lens is axially rotated of 90°;
- Test 9: the $f = 100$ mm lens is rotated of 180° (reversed with respect to the optical axis);
- Test 10: the same as Test 1, with the $f = 150$ mm lens replacing the $f = 100$ mm one;
- Test 11: the same as Test 2, with the $f = 150$ mm lens replacing the $f = 100$mm one;

The first thing to be noticed about the results reported in Table 7.10 and Figure 7.15 is that, even if the Zernike coefficients can vary, the system introduces a PtV aberration which is always of the same order of magnitude. There is not a significant variation of the Zernike coefficients for one of the performed Test with respect to the other, but all the Test results are varying in the same range. The rotation of the test lens (Test 8 and Test 9), for example, does not change the measured WF aberrations more than the reperforming of the whole procedure (see Test 1 to Test 4). The repositioning of the optical fiber, in particular, seems not the change the results at all. The more powerful Zernike polynomial turned to

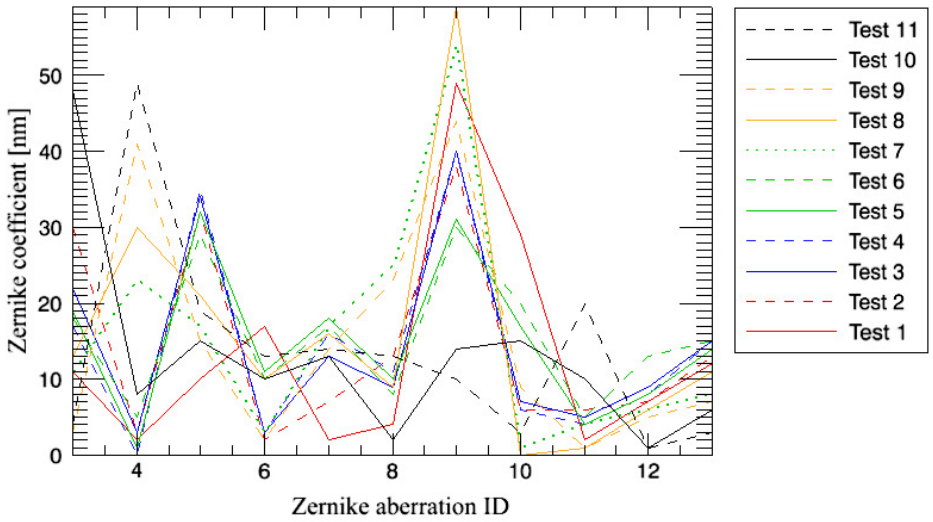

Figure 7.15: Zernike coefficients, reported in Table 7.10, measured in different setup conditions, to verify the stability of the aberration introduced by the demonstrator itself and quantify it.

be the spherical one (Zernike coefficient ID #9). However, this does not mean that the demonstrator is introducing an high spherical aberration, since such a term is decreasing when using the $f = 150$ mm focal length lens instead of the $f = 100$ mm one. This is, in fact, an expected variation, due to the decreasing of the mean curvature of the lens surfaces. However, this underlines the slow-dependency of such a parameter by the prototype setup, being more related to the test lens itself. Lets try now to quantify the static aberration. For all the performed test, the PtV aberration has turned to be smaller than 90 nm, that is to say lower than $\lambda/6$ (considering the light peak at about 550 nm). We can, then, neglect the static aberration effect and still retrieve the IOL dioptric power with the required precision. A $\lambda/4$ shape of the WF delivered by the IOL can be measured too.

7.6.2 Measurement of the aberrations introduced by the IOL holder

With the test described in the previous Section, the prototype static aberration has been quantified for the complete setup but the IOL holder, composed of two flat optical window with a nominal $\lambda/4$ optical quality. The test performed to verify if the aberrations introduced by the such an holder are non-negligible consists of introducing the holder itself, filled with the physiological solution, in the collimated beam just before the $f = 100$ mm glass test lens, whose WF was already known. The static WF has been subtracted by the one measured with the holder inside the optical path, before compute the polynomial fit with the Zernike terms. In Figure 7.16 are reported the 3D shapes of the following WFs: static aberration without the IOL holder, static aberration with the holder and the residual of the subtraction between the two. Table 7.11 summarizes the measured aberration coefficients, reported also in Figure 7.17. The result of such a test is that the IOL holder is introducing about 50 nm of astigmatism (Zernike coefficients ID #3 and #4), probably due to a small curvature of one of the windows. Also this aberration, however, is negligible, since it is of the same order of

Table 7.11: Zernike coefficients measured with and without the IOL holder, to quantify the aberration introduced by it.

C_i [nm]	3	4	5	6	7	8	9	10	11	12	13	PtV
Static	29	9	30	9	11	3	44	6	6	6	15	92
Static + IOL holder	68	46	37	3	3	0	44	12	8	4	10	116
IOL holder (WF subtraction)	38	37	8	6	13	4	1	7	14	3	5	87

magnitude of the static aberrations.

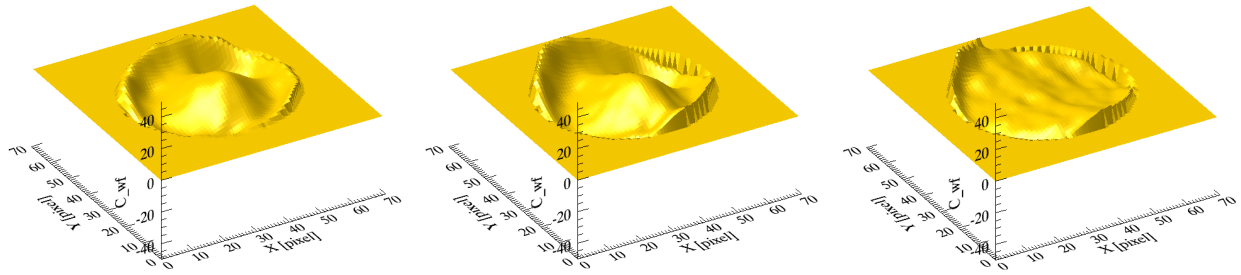

Figure 7.16: 3D representation of the WFs retrieved without (*left*) and with (*center*) the IOL holder inside the optical path. The right image shows the residual of the subtraction between the two of them, corresponding to our estimation of the IOL holder contribution. The Zernike coefficient scale is still in normalized units, not converted in nm, and the ±50 range represents the required 0.125 diopters precision.

7.7 Test IOL WF measurements repeatability

The IOL selected for the test has a nominal focal length $f = 95.2$ mm, i.e. 10.5 diopters. The test consists of repeating the WF measurements, starting from the IOL positioning, 10 times, in order to verify the measurements repeatability. Before each measurement, the WFS is aligned to the IOL, minimizing the tip-tilt and defocus terms. The IOL holder is equipped with a tip-tilt mount, which is adjusted in order to be orthogonal to the beam with a precision of 0.3°. For each of the WF measurements, the focal plane position is retrieved, as explained in Section 7.5. The resulting residual displacements from the 10 measurements mean value, taken as a reference, are reported in Table 7.12. The requirement for the precision of the dioptric power determination is 0.125 diopters, that is to say 1.15 mm indetermination in the measurement of the focal plane position, for the considered test IOL. The retrieved measurements statistical 3σ range is 0.2% of the lens focal length, corresponding to 0.02 diopters, which is far inside the requirement (all the measurements are inside a 255 μm range, which is, again, inside what required).

To verify the WF measurement repeatability, since the IOL is immersed in a liquid and is not always in exactly the same position with respect to a x-y reference, it is possible to rotate the retrieved WFs before compare them. The rotation angle can be computed maximizing

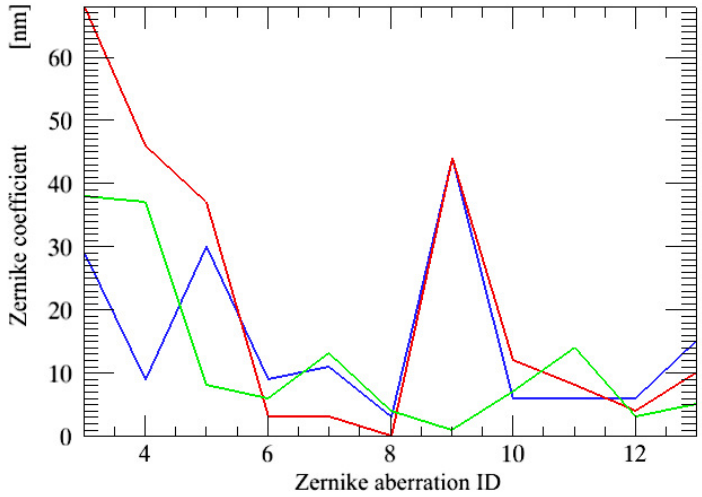

Figure 7.17: Zernike coefficients, reported in Table 7.11, measured to verify the aberration introduced by the IOL holder. The *blue* and *red* lines represent the static aberrations measured without and with the IOL holder, respectively. The *green* line shows the residuals of the subtraction between the two measured wavefronts.

Table 7.12: Residual focal plane shifts, with respect to the mean focal position. The focal plane position measurements gives values in a 255μm range. The statistical 30 range is 210μm wide, corresponding to an indetermination on the focal length of 0.2%, corresponding to 0.02 diopters.

Measurement ID	WF1	WF2	WF3	WF4	WF5	WF6	WF7	WF8	WF9	WF10
FP shift [μm]	2	27	-17	171	-65	-84	24	-9	-51	-14

the correlation factor of two WFs, as a function of the rotation angle of one of them. We used the first retrieved WF as a reference and optimized the rotation of the other WFs along the optical axis.

Figure 7.18 and Table 7.13 show, respectively, the obtained WFs and the correlation factors between each WF (without tip-tilt and defocus terms) and the mean of the ten measurements.

In Figure 7.19 the Zernike polynomials coefficients of the 10 already rotated WF s fits are shown.

In Figure 7.20 the conversion factor in nanometers is shown as a function of the nominal focal length of the lenses. An error of 5mm on the focal length of the IOL translates in an indetermination on the conversion factor of about $0.3 \cdot 10^{-6}$ nm, which is corresponding to a PtV variation on the WF measurement of about 20nm (from 170 to 190nm).

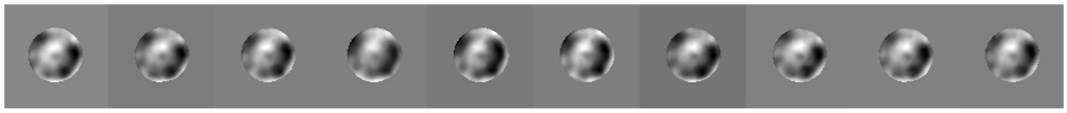

Figure 7.18: WFs retrieved with 10 different measurements.

Table 7.13: Correlation factors between each measured WF and the mean of all the WF sample.

WF1	WF2	WF3	WF4	WF5	WF6	WF7	WF8	WF9	WF10
0.98	0.99	0.99	0.94	0.97	0.96	0.99	0.97	0.98	0.98

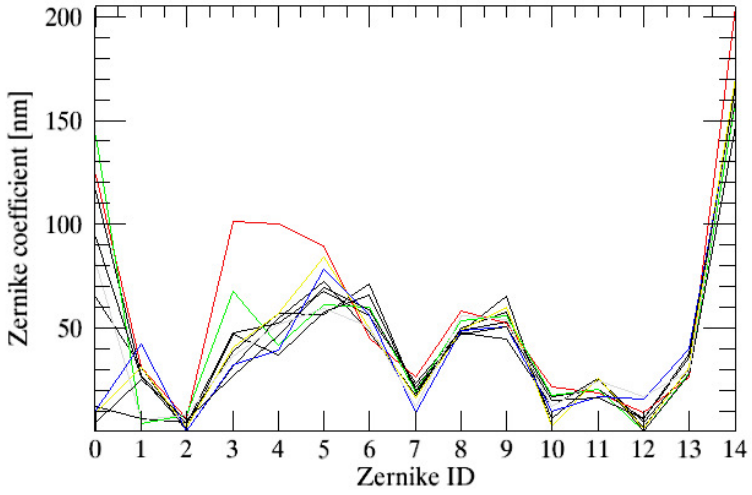

Figure 7.19: WFs polynomial fit coefficients retrieved with 10 different measurements.

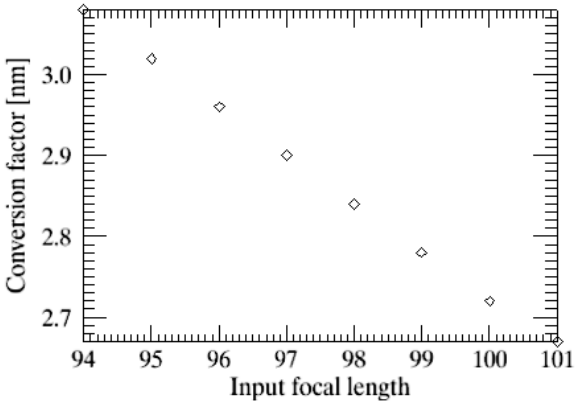

Figure 7.20: Conversion factor in nanometers is shown as a function of the nominal focal length of the lenses.

Table 7.14: Nominal characteristics of the IOL received from the providing company. n is the refractive index, P and P_{eff} are, respectively, the nominal power of the lens and the effective power measured with a less sensitive WFS. All the lenses are biconvex and the surfaces radius and central thickness are reported in the sixth and seventh column of the Table, respectively.

Sample	ID	n	P [diopters]	P_{eff} [diopters]
1	1204028000	1.4603	20.00	20.35-20.46
2	1204028005	1.4603	20.00	20.35-20.46
3	1011008485	1.4602	16.00	16.00-16.18
4	1106018502	1.4603	16.00	16.32-16.46
5	1109023005	1.4603	12.00	11.99-12.24
6	1109023006	1.4603	12.00	11.99-12.24
7	1012009783	1.4602	08.00	08.17-08.27
8	1012009412	1.4602	08.00	08.11-08.29

7.8 IOL focal length measurement

Table 7.14 lists the nominal characteristics of the test IOLs received from the providing company. One should notice that the lens nominal dioptric power P, is in fact very different from the effective dioptric power range which has been measured by the providing company, P_{eff}, for the calibrated lenses of the sample. This is not a surprise, since, as already said, it's still difficult to realize artificial crystallines with a high optical quality and an a priori well known dioptric power. The goal of this test is to measure the IOLs focal length, and so their dioptric power, with an error lower than 0.125 diopters, with respect to the range of P_{eff}, declared by the providing company.

Table 7.15 shows the results obtained from the IOLs focal length measurement. The dioptric power P_{eff} is reported again, as the mean value of the range provided by the company to which half of such a range is coupled as an indetermination. This power is translated into a focal length f_{eff}, which is reported in Table 7.15 too. The last column reports the positions of the linear focusing stage, after the WFS alignment, with respect to an arbitrary reference. The reference position should be calibrated using an IOL whose focal length is precisely known, simply retrieving the position of the linear focusing stage after the WFS alignment and subtracting it from the calibrated focal length of the lens. Since the IOLs in the sample had different indetermination to be associated with their nominal focal lengths f_{eff}, all the lenses have been used as calibration lenses for the system, and the final reference position has been retrieved as an average between all the retrieved reference positions, weighted according to the inverse of each lens focal length f_{eff} indetermination. The resulting reference position is then 86.87 mm.

7.9 Comments to the results and conclusions

Figure 7.21 shows the resulting dioptric power measurements, P_{mea}, already calibrated according to what explained in Section 7.8, to which the nominal powers P_{eff} have been subtracted. The yellow area in the plot represents the indetermination in the dioptric power nominal value, claimed by the IOLs providing company. The error bars, associated to each power

Table 7.15: Obtained results of the IOLs focal length measurements.

Sample	IOL ID	P_{eff} [diopters]	f_{eff} [mm]	position [mm]
1	1204028000	20.40±0.06	49.02±0.14	38.09
2	1204028005	20.40±0.06	49.02±0.14	38.28
3	1011008485	16.09±0.09	62.15±0.35	25.52
4	1106018502	16.39±0.07	61.01±0.26	24.99
5	1109023005	12.115±0.12	82.54±0.81	4.36
6	1109023006	12.115±0.12	82.54±0.81	4.69
7	1012009783	8.22±0.05	121.65±0.74	-37.14
8	1012009412	8.2±0.09	121.95±1.32	-36.84

measurement value, are ±0.125 diopters wide, and represent the maximum acceptable error to fulfill our precision requirement. All the bars are entering the yellow area, that is to say that we have no evidence that any of our measurements is out of specifications, considering the indetermination in the calibration nominal focal lengths we had from the providing company.

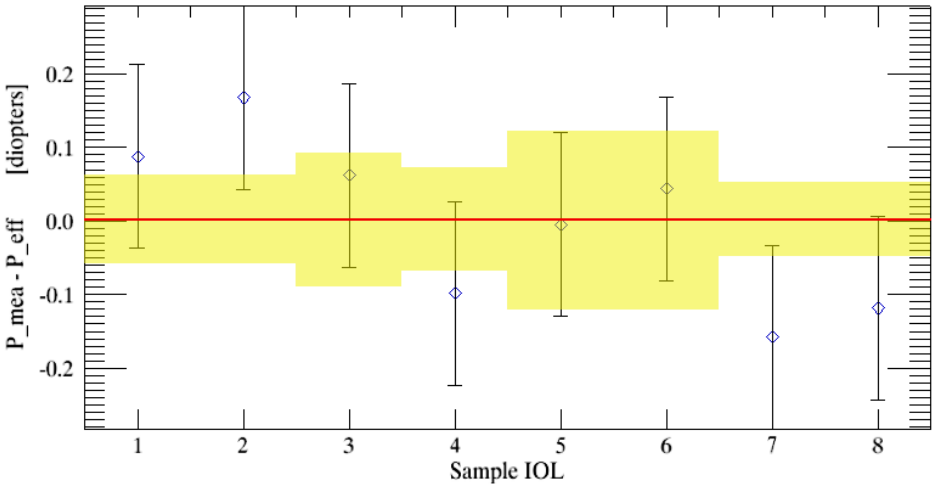

Figure 7.21: Dioptric power measurements performed with the demonstrator, to which the dioptric power claimed by the providing company has been subtracted. The yellow area represents the indetermination in the nominal dioptric power value, while the error bars associated to our measurements are ±0.125 diopters wide, to verify the compliance of our measurements with our goal.

In conclusion, we realized a laboratory demonstrator of a WaveFront Sensor to perform optical quality test and dioptric power measurement of IntraOcular Lenses, in a easy, fast and cheap way. The goal of measuring the optical power of the lenses with an error lower than 0.125 diopters has been reached for all the calibrated IOLs in the sample. The power of this sensor is its ability to automatically align itself to the IOL, minimizing the defocus and tip-tilt signals, instead of performing a complicated alignment of the lens to be tested. In

such a way, no particular optical knowledge or skillness in alignment procedures is required to perform the test. Moreover, the system is completely composed of commercial optics and mechanics and the whole setup is compact. Further improvements are still possible, such as the implementation of an optical trap to remove the spurious light coming from the collimated beam and not passing through the IOL, in order to increase the collimated beam diameter and furtherly reduce the precision required to position the IOL inside its holder. We have realized the demonstrator using optics and mechanics which were already present in the AO Laboratory of the Astronomical Observatory of Padova, but the optimization of some optical components parameters, such as the pyramid vertex angle and the setup lenses focal lengths, could allow to obtain a even more compact opto-mechanical system.

Chapter 8

Conclusions

The regions where light forms the caustics, produced by a converging bundle of rays, are governed by Maxwell equations regardless of how the light has been generated and collected, which are the positions and distances of the regions that perturbed such light, and the way it has been converged. In particular, the light produced from hydrogen burning several billion of years ago, later deformed by the complex, but local, structure of the terrestrial atmosphere, and collected by state of the arts, multi-tons glass mirrors, and the light collected by one of the most marvelous production of nature, the human eye, are of the same nature.

While the obvious difference in the scale of the entrance pupil is also recalled in the title of this PhD Thesis, it is remarkable that this is not the only fundamental difference in terms of scales, neither the only extreme similarity in terms of importance. In fact the position, along the line of propagation, where the perturbation of the light occurs plays a significant role. In Astronomy, this translates into gather information on where, along the column of turbulence lasting about 10 km, the degradation of the image occurs to proper compensate for it. In the Wavefront Sensor depicted in this work, the sensor is substantially aiming to isolate the turbulence occurring very close to the entrance pupil, the so called ground-layer turbulence, in contrast with high altitude turbulence, the latter being responsible of scintillation and field of view dependent aberrations, compensated elsewhere in Linc-Nirvana. At the same time, it is important to recall that the IOL, a real prosthesis that is nowadays improving the quality of life of millions of people, is responsible of the perturbation of the light produced in the middle of the about 24 mm of light path inside the human eye, from the outer edge of the cornea to the retina. While the system worked out in this Thesis is unable to distinguish the occurrence of the aberration along Z (and, on the other hand, it does not need for that), it is remarkable that a proper compensation with the right choice of an IOL would require to distinguish which eye deficiencies arise from the cornea and which from the lens.

In this Thesis, two different Wavefront Sensors, based on the same optical concepts, have been realized, aligned and characterized, pointing out the peculiarities, the advantages and the limits of both of them. The importance of the here implemented new Adaptive Optics techniques development is quite evident in Astronomy, both because in principle they will allow to deliver high quality imagery over a much wider field of view and because they are expected to be implemented also in the next generation Extremely Large Telescopes (ELTs), so, in this framework, our system could act as a pathfinder. Considering the ophthalmic research field, on the other hand, the realization of a compact, easy to use and completely made up of commercial components demonstrator paves the way to a new generation of quite

cheap but fully functional opto-mechanical systems to perform IOLs quality test in a quick and mostly automatic way, in order to verify the compliance of each produced lens with the requirements set out by each patient disease.

Socio-political implications of this kind of work have to be considered too, since one of the aim of my PhD Thesis is to connect two different scientific communities, which are often making similar kind of studies without the proper communication, trying to empower the interdisciplinarity of the research, considered as a global concept, to optimize its progress.

Bibliography

[1] J. M. Beckers. Increasing the size of the isoplanatic patch with multiconjugate adaptive optics. In *ESO Conference on Very Large Telescopes and their Instrumentation*, volume 2, pages 693–703, 1988.

[2] P. Bizenberger, E. Diolaiti, S. Egner, T. M. Herbst, R. Ragazzoni, D. Reymann, and W. Xu. LINC-NIRVANA: optical design of an interferometric imaging camera. In *Proc. SPIE*, volume 6269, 2006.

[3] M. Carbillet, S. Correia, P. Boccacci, and M. Bertero. Restoration of interferometric images. II. The case-study of the Large Binocular Telescope. *Astronomy & Astrophysics*, 387:744–757, 2002.

[4] S. Correia, M. Carbillet, P. Boccacci, M. Bertero, and L. Fini. Restoration of interferometric images. I. The software package AIRY. *Astronomy & Astrophysics*, 387:733–743, 2002.

[5] S. Esposito, A. Riccardi, L. Fini, A. Puglisi, E. Pinna, M. Xompero, R. Briguglio, F. Quirs-Pacheco, P. Stefanini, J.C. Guerra, L. Busoni, A. Tozzi, F. Pieralli, G. Agapito, C. Arcidiacono, Salinari P., G. Brusa-Zappellini, R. Demers, and J. Brynnel. First light AO (FLAO) system for LBT: final integration, acceptance test in Europe, and preliminary on-sky commissioning results. In *Proc. SPIE*, volume 736, 773609, 2010.

[6] S. Esposito, A. Riccardi, F. Quirs-Pacheco, E. Pinna, A. Puglisi, M. Xompero, R. Briguglio, L. Busoni, L. Fini, P. Stefanini, G. Brusa, A. Tozzi, P. Ranfagni, F. Pieralli, J.C. Guerra, C. Arcidiacono, and P. Salinari. Laboratory characterization and performance of the high-order adaptive optics system for the Large Binocular Telescope. 49 issue 31, pag.G174:G174, 2010.

[7] J. Farinato, R. Ragazzoni, C. Arcidiacono, A. Brunelli, M. Dima, G. Gentile, V. Viotto, E. Diolaiti, I. Foppiani, M. Lombini, L. Schreiber, P. Bizenberger, F. De Bonis, S. Egner, W. Gässler, T. Herbst, M. Kürster, L. Mohr, and R.-R. Rohloff. The Multiple Field of View Layer Oriented wavefront sensing system of LINC-NIRVANA: two arcminutes of corrected field using solely Natural Guide Stars. In *Proc. SPIE*, volume 7015, 2008.

[8] R. Foy and A. Labeyrie. Feasibility of adaptive telescope with laser probe. *Astronomy & Astrophysics*, 152:L29–L31, 1895.

[9] W. Gaessler, C. Arcidiacono, S. Egner, T. M. Herbst, D. Andersen, H. Baumeister, P. Bizenberger, H. Boehnhardt, F. Briegel, M. Kuerster, W. Laun, L. Mohr, B. Grimm,

H.-W. Rix, R.-R. Rohloff, R. Soci, C. Storz, W. Xu, R. Ragazzoni, P. Salinari, E. Diolaiti, J. Farinato, M. Carbillet, L. Schreiber, A. Eckart, T. Bertram, C. Straubmeier, Y. Wang, L. Zealouk, G. Weigelt, U. Beckmann, J. Behrend, T. Driebe, M. Heininger, K.-H. Hofmann, E. Nu$\sigma_\star$baum, D. Schertel, and E. Masciadri. LINC-NIRVANA: MCAO toward Extremely Large Telescopes. *Comptes Rendus Physique*, 6:1129–1138, 2005.

[10] E. Gaviola. On the quantitative use of the foucault knife-edge test. *J. Opt. Soc. Am., vol.26, p.163-169*, 1936.

[11] T. M. Herbst, R. Ragazzoni, A. Eckart, and D. Weigelt. Imaging beyond the fringe: an update on the LINC-NIRVANA Fizeau interferometer for the LBT. In *Proc. SPIE*, volume 7734, 773407, 2010.

[12] T. M. Herbst, R. Ragazzoni, A. Eckart, and G. Weigelt. LINC-NIRVANA: achieving 10 mas imagery on the Large Binocular Telescope. In *Proc. SPIE*, volume 7014, 2008.

[13] T. M. Herbst, R. Ragazzoni, A. Eckart, and G. Weigelt. LINC-NIRVANA: the Fizeau interferometer for the Large Binocular Telescope. In *Proc. SPIE*, volume 7013, 2008.

[14] J. M. Hill and P. Salinari. Large Binocular Telescope project. In *Proc. SPIE*, volume 4004, pages 36–46, 2000.

[15] A. Kolmogorov. The local structure of turbulence in incompressible viscous fluid for very large reynolds' numbers. *Dokl. Akad. Nauk SSSR, vol.30, p.301-305*, 1941.

[16] E. Marchetti, N. N. Hubin, E. Fedrigo, J. Brynnel, B. Delabre, R. Donaldson, F. Franza, R. Conan, M. Le Louarn, C. Cavadore, A. Balestra, D. Baade, J.-L. Lizon, R. Gilmozzi, G. J. Monnet, R. Ragazzoni, C. Arcidiacono, A. Baruffolo, E. Diolaiti, J. Farinato, E. Vernet-Viard, D. J. Butler, S. Hippler, and A. Amorin. MAD the ESO multi-conjugate adaptive optics demonstrator. In *Proc. SPIE*, volume 4839, pages 317–328, 2003.

[17] R. J. Noll. Zernike polynomials and atmospheric turbulence. 66:207–211, 1976.

[18] M. Piana and M. Bertero. Regularized deconvolution of multiple images of the same object. *J. Opt. Soc. Am. A*, 13(7):1516–1523, 1996.

[19] R. Ragazzoni. Pupil plane wavefront sensing with an oscillating prism. *Journal of Modern Optics*, 43:289–293, 1996.

[20] R. Ragazzoni, E. Diolaiti, J. Farinato, E. Fedrigo, E. Marchetti, M. Tordi, and D. Kirkman. Multiple field of view layer-oriented adaptive optics. Nearly whole sky coverage on 8 m class telescopes and beyond. *Astronomy & Astrophysics*, 396:731–744, 2002.

[21] R. Ragazzoni, J. Farinato, and E. Marchetti. Adaptive optics for 100-m-class telescopes: new challenges require new solutions. In *Proc. SPIE*, volume 4007, pages 1076–1087, 2000.

[22] R. Ragazzoni, T. M. Herbst, W. Gaessler, D. Andersen, C. Arcidiacono, A. Baruffolo, H. Baumeister, P. Bizenberger, E. Diolaiti, S. Esposito, J. Farinato, H. W. Rix, R.-R. Rohloff, A. Riccardi, P. Salinari, R. Soci, E. Vernet-Viard, and W. Xu. A visible MCAO channel for NIRVANA at the LBT. In *Proc. SPIE*, volume 4839, pages 536–543, 2003.

[23] F. Roddier. The Effects of Atmospheric Turbulence in Optical Astronomy. *Prog. Optics*, 19:281–376, 1981.

[24] LINC-NIRVANA team. *LINC-NIRVANA Final Design Review.* 2005.

[25] V. Viotto. *Interferometria di Fizeau con LBT di galassie della Vergine: caratterizzazione dei sensori di fronte d'onda a 12 stelle.* 2007.